A complete redshift sample of galaxies

Bean, Adrian John

A COMPLETE REDSHIFT SAMPLE OF GALAXIES

by

Adrian John Bean

JUNE 1983

Being an account of work done at the Department of Physics and submitted to the University of Durham in accordance with the regulations for admission to the degree of Doctor of Philosophy

To Jocelyn Elizabeth Bean

Born: 25th June 1983.

.....He has put eternity into man's mind, yet so that he cannot find out what God has done from the beginning to the end.

Ecclesiastes

Chapter 3, Verse 11.

CONTENTS

PREFACE

The work describes in this thesis has not been submitted for any degree, diploma or other qualification at any other university. The work has been carried out in collaboration with Drs. R.S.Ellis, T. Shanks and R. Fong at Durham, Dr. G. Efsthathiou at Cambridge and Dr. B.A.Peterson at Stromlo, but the majority is the author's own work.

Certain results have been submitted to the Mon.Not. Roy.Astr. Soc and Astrophysical Journal for publication.

ABSTRACT

Adrian John Bean

A COMPLETE REDSHIFT SAMPLE OF GALAXIES

The role of complete redshift samples is discussed with particular attention focused on the need for new deeper and better controlled surveys for statistical clustering and dynamical studies. The compilation of one such catalogue, along with simulated samples, is described, this 'AARS' survey consisting of 322 accurate galaxy velocities and magnitudes in five small, well separated fields.

An estimate of the galaxy luminosity function is made, with and without assuming spatial homogeneity, and fitted with a standard parameterised form the characteristic luminosity of which is found to be some 0.5 magnitudes brighter than from most previous samples.

Evidence that the sample may be fairly representative comes from the number magnitude and redshift counts that are compared with models which assume spatial homogeneity. Plots of the galaxy distributions, though, vividly demonstrate the clustering of galaxies at small scales.

The AARS and other surveys are used to estimate redshift two and three point galaxy correlation functions. The two point function is generally consistent with homogeneity at scales beyond 10 MPC although there is some evidence for anti-clustering. At smaller scales the projected form agrees well in shape and amplitude with the -0.8 powerlaw found from projected catalogues with a 'break' in the powerlaw also occurring at a similar scale. The unsmoothed spatial function, however, exhibits a strong rise above the usual powerlaw behaviour at scales smaller than the break.

The two point function is also used to estimate the relative peculiar velocity dispersion between close galaxy pairs. The dispersion of $\sim$ 200 km/sec, roughly independent of separation, is found to be considerably smaller than most previous estimates, however a reanalysis of these samples suggest the data may, in fact, be compatible. This dispersion along with the spatial correlation functions provides a 'Cosmic Virial Estimate' of the Cosmic Density Parameter of $0.1 < \Omega < 0.2$, the universe only being closed if most of the matter is considerably less clustered than galaxies.

The new statistical results are discussed in detail and used to constrain theories of galaxy formation.

CHAPTER ONE

INTRODUCTION

1.1 GENERAL

Ever since the discovery of the microwave background radiation (Penzias and Wilson, 65) gave strong support for the hot big bang theory, there has been much effort to determine the cosmic density parameter Ω* and to understand the nature and distribution of matter and how it has evolved in the expanding universe.

Since the largest visible structures are clusters of galaxies, there has naturally been much study of the galaxy distributions on the sky. In particular, with the advent of high speed computers, detailed statistical analyses of galaxy catalogues have given insight into the apparently complex structure visible to the eye and to the possible processes responsible for its formation. More recently, with the further growth of technology, it has been made possible to obtain accurate optical galaxy redshifts in large numbers which, as well as providing a much clearer view of the three dimensional distribution, can give information on the typical peculiar velocities in the clusters. Assuming that these motions are induced by the gravitational potential associated with the clustering distribution and the latter is statistically stable, one can estimate the total mass density associated with galaxies, thus providing a lower bound to Ω.

The primary aim in this thesis is to study statistically the peculiar velocities and clustering of galaxies by means of a recently compiled redshift catalogue. This catalogue, denoted as the AARS (Anglo Australian Redshift Sample), consists of over 300 high accuracy redshifts in five small, high galactic fields of typically $4^{\circ} \times 4^{\circ}$ and complete to around 16.75 in apparent magnitude. Since the fields are deep and well separated, it is hoped they may, perhaps for the first time, provide a reasonably representative

---

* $\Omega \left(= \frac{\rho}{\rho_c} \right)$ is the ratio of mean to the critical density required to close the universe in the standard Friedmann model with $\Lambda = 0$.

sample of the universe as a whole.

As well as the statistical studies, the redshift and magnitude information is used to investigate the form of luminosity function of galaxies outside rich clusters, comparison with which may provide insight into the processes by which galaxies and clusters formed.

The two sections of this chapter that follow give a brief review of the most popular clustering and dynamical studies of the galaxy distribution, the aim being to show the important role statistical studies with complete redshift samples have to play in these fields. The section after gives details of the previous available redshift data and points the need for deeper and better controlled surveys. The AARS is introduced in the final section along with a description of its role and the aim and layout of this thesis.

1.2 CLUSTERING STUDIES

The homogeneity and isotropy of the universe on the largest scales are important assumptions in modern cosmology. Early indications of these came from Hubble's work (Hubble, 29) on the distance and recession velocities of galaxies and also evidence for the homogeneity of the galaxy distribution came from his study of the scaling of galaxy counts as a function of apparent magnitude (Hubble, 34). More recent and detailed observations bear out this early work on the Hubble law (Sandage and Tammann, 75) and homogeneous models now give good fits to deep number counts over the range of magnitude 15-25 (Kron, 78, Tyson and Jarvis, 79). Also, evidence for the isotropy assumption has come from the observed isotropy of the microwave background (e.g.Partridge and Wilkinson, 67).

Although these and other observations strongly suggest overall homogeneity on scales of many hundreds of MPCS, there has yet been little

observational evidence for the minimum scale length at which this can be said to safely hold. Indeed at small scales it has long been known that the matter distribution is inhomogeneous because of the existence of galaxy clusters.

The earliest objective support for the small scale clustering of galaxies came from the statistical work of Shapley (35) and others who studied the angular distribution of galaxies on early magnitude limited samples. With the compilation of more consistent and larger catalogues, such as those of Zwicky (Zwicky et al, 61-68) and the deeper Lick Survey (Shane and Wirtanen, 67), more thorough statistical studies were made possible that still dominate our thinking on galaxy clustering today.

The most popular statistic used here has been the two point angular correlation function $\omega(\theta)$ that has been especially powerful because a linear integral relation exists between it and its spatial equivalent, $\xi(r)$. Analyses from several catalogues (Peebles and Groth, 75, Groth and Peebles (GP), 77) have suggested galaxies are typically clustered on scales r from 0.05 to at least 3.0 MPC*, with $\xi(r)$ following a powerlaw of slope around -1.8. At larger scales though the estimates vary; here GP have found evidence from the Lick catalogue for a break away from a powerlaw slope at 9 MPC whereas the Durham group (Shanks et al, 80a) found a 'break' occurring at only 3.0 MPC.

Naturally the presence and position of any real feature in $\xi(r)$ is likely to have profound effects on our understanding of cluster and galaxy formation. However the problem with these observations is that, at the scales of interest, the real density contrast is low (around unity) and seen in projection is lower still so that noise and systematic effects in the catalogues, such as galactic obscuration, can hide the real clustering distribution.

* Throughout this thesis distances quoted are calculated assuming a Hubble constant H of 100 km/sec/MPC.

Although the studies described above show the distribution of galaxies appears to be reasonably understood on scales of several MPC and on the largest scales, where the universe is homogeneous and isotropic, over the intermediate range of separations the typical extent and strength of clustering is highly uncertain. Statistical studies of the angular distributions of Abell Clusters (Hauser and Peebles, 73) on the one hand, has shown correlations of order unity on scales $\sim$ 30 MPC and local structure on this scale is evident from the angular distribution and number magnitude counts (e.g. Peterson, 73) of shallow catalogues. On the other hand, recent 'redshift maps' of the distribution, although often showing clustering of large extent, also show prominent holes (e.g. Einasto et al, 80) that suggest anticlustering could be present over scales 10-50 MPC.

More objective estimates of the clustering over these scales can come from direct estimates of the spatial correlation function in three dimensions using complete redshift information. Although at small scales redshift separation will be a poor measure of distance because of peculiar velocities, at larger scales (around the suspected break and beyond) it should be adequate and should enable any weak clustering features present to be picked up, that would be undetectable above the noise in the angular studies.

Up until now though little, if any, of the available redshift data has been suitable for reliable statistical studies, being either incomplete or biased by local inhomogeneities or else specially selected to be close to rich clusters.

In section 5 we consider how deep complete redshift samples in small fields can be of use here, especially for studies of the distribution on the larger scales.

1.3 VIRIAL ESTIMATES OF THE MEAN MASS DENSITY

At the same time as astronomers have been trying to understand and describe the distribution of galaxies on the sky, much effort has been

directed towards determining the typical masses of galaxies and determining their contribution to the mean mass density.

Here the most valuable tool has been the virial theorem which can be applied to a bound and, on average, stable self gravitating system to provide a measure of its total mass. To do so requires measuring the total internal kinetic energy and balancing this with one half of the mean potential energy stored in the system.

Applying this principle to our galaxy and the Andromeda nebula M31, Öpik (22) found a ratio of mass to luminosity $\frac{M}{L} \sim 3.0$ (in units of the solar quantity), in good agreement with that expected from galaxies composed of stars like the sun. Recent estimates for spirals give $\frac{M}{L}$ in the range 1 to 10 (Burbidge and Burbidge, 75), the masses of these galaxies thus having changed little since the 1970's.

With a mean $\frac{M}{L}$ and mean luminosity density ρ_L for the universe we can, of course, estimate the contribution to Ω from galaxies. Taking a mean $\frac{M}{L}$ of 20 (to include the higher $\frac{M}{L}$ of ellipticals) and adopting $\rho_L \approx 1.0 \times 10^8 \; L_\odot \; MPC^{-3}$ (1.1) (Davis and Huchra, 82), we get a mean density $\rho = 2.0 \times 10^9 \; L_\odot \; MPC^{-3}$. Since the critical density $\rho_c = \frac{3 H^2}{8\pi G} \simeq 2.8 \times 10^{11} M_\odot \; MPC^{-3}$ (1.2), we get $\Omega \sim 0.007$ (1.3) (independent of the true value of H), a number, while significantly less than unity, large enough to suggest that gravitation has something to do with the expansion of the universe.

Although these 'conventional' masses and $\frac{M}{L}$ agreed (and still do) with that expected from the known mix and mass of stars within galaxies, it was soon realised the internal dynamics did not take account of any other mass distributed beyond the luminous parts of galaxies, which could allow Ω to be closer to unity than in eqn. 1.3 above. To detect such matter gravitationally, it was necessary to consider the dynamics of whole systems of galaxies. In the case of the virial theorem, this required an estimate of the total kinetic energy of systems from the radial velocities of member

galaxies and their potential energy from their positions on the sky, averaged in a way to account for projection effects.

The most obvious candidates for such a study were compact clusters whose smooth profiles suggested an equilibrium situation. Applying the virial theorem to Coma, Zwicky (33) found the total mass of the cluster far exceeded the sum of the conventional masses of the member galaxies suggesting a serious, 'virial mass discrepancy'. Indeed more recent estimates from many rich clusters (see Faber and Gallagher (79) for a review) give $\frac{M}{L} \sim 650$ (1.4) which, if typical for all galaxies, from eqns 1.1 and 1.2 would make $\Omega \sim 0.2$ (1.5) ; well above the estimate in eqn 1.3.

Support for the 'dark matter' suggested by Zwicky has come more recently from the outer rotation curves of some nearby spirals (e.g. Shostak and Rogstad, 73) which, instead of falling with increasing radius (as expected for convergent masses), remain flat to the limits of observation, which is in some cases out to 50 KPC. The usual interpretation of this behaviour is that bright spirals, at least, are embedded in massive, dark isothermal halos with density varying as $\rho(r) \sim \frac{1}{r^2}$, the mass rising linearly with radius to the scales above (Ostriker et al, 74).

Taking an average rotation velocity V_c = 200 km/sec and assuming a halo extent r_H = 50 KPC, in this way one gets a typical galaxy mass of $V_c^2 \frac{r_H}{G} \sim 5 \times 10^{11} M_\odot$. If we further take the mean space density of such galaxies as $n = 0.01\ MPC^{-3}$ we get from eqn 1.2, $\Omega \simeq 0.02$ (1.6). This is above the estimate in eqn 1.3 but still well below the extrapolation used in eqn 1.5 from rich clusters.

While many observations seem to bear out these mass estimates in rich clusters and from spiral rotation curves, which are now generally accepted, more controversial has been the question of whether the amount of dark matter per typical bright galaxy is comparable to that found for galaxies in rich clusters. Masses here generally come from the application

of the virial theorem to loose groups where the low density contrast along with projection effects can make the assigning of galaxies to particular dynamical units a serious problem (Faber and Gallagher, 79). In addition, large redshift measurement errors can cause the observed velocity dispersions (and hence virial masses) to be artificially raised. Together these problems are probably responsible for the large differences in $\frac{M}{L}$ reported by different observers, giving rise to corresponding variations in Ω that vary between those from conventional masses and rich clusters in eqns 1.3 and 1.5 above.

An alternative 'statistical virial theorem' approach that avoids the projection and membership problem has been developed by Peebles (76a). This is based on the two and three point correlation functions that provide a useful estimate of the gravitational potential associated with the small scale clustering. Balancing the 'pressure' of the rms, relative, radial peculiar velocity dispersion $\langle V^2(r) \rangle$ between all pairs at scale r with the force from this potential, can provide both an estimate of Ω and a consistency test of how well galaxies trace out the matter distribution at small scales. For this 'cosmic virial theorem' (CVT) to give reliable results though, one needs a fairly large sample of accurate redshifts in a representative sample of the universe, an issue to which we now turn.

1.4 COMPLETE REDSHIFT SAMPLES

For many years observers have been measuring galaxy redshifts in special parts of the sky to study the dynamics of rich clusters and groups or merely to plot out galaxy distributions in particular regions of the sky. While for some of these and other purposes strict completeness (or high redshift accuracy) may not be necessary, for the statistical clustering and velocity studies mentioned earlier, complete and accurate redshift information is needed in a fair sample of the universe. Although, in turn, this requires considerably more painstaking observational work the rewards are much greater.

Details of four such samples are given in Table 1.1, the first two of which are discussed below.

Until recently the only approximation to a complete redshift survey has been the second reference catalogue (SRC) of bright galaxies (De Vaucouleurs et al, 76) which is based on the all sky Shapley Ames (1932) catalogue, now complete to B = 13.0 (Sandage, 78). The Huchra sample in Table 1.1 is a survey in turn based on the SRC and which was used by Davis, Geller and Huchra (78) to make estimates of the luminosity function of galaxies and statistical studies in three dimensions for application of the Cosmic Virial Theorem.

The results from these studies though, can only be regarded as preliminary since comparison of the number magnitude counts with deeper surveys imply the northern sample, in particular, (with a depth of only around 30 MPC) is grossly biased by the Virgo local supercluster. At these depths too, large scale motions may complicate using redshifts as distance indicators. In addition, the redshifts and magnitudes for this sample come from a variety of sources which may contain serious random and systematic errors.

To provide a fairer and more homogeneous catalogue, the group at Harvard set out to remeasure the redshifts of all galaxies with very poor quality velocities and extend the sample in the north and part of the south to B = 14.5. This CFA (Centre for Astrophysics) catalogue, recently completed (Huchra et al, 83), contains over 2,000 galaxies and is likely to make a tremendous impact on our knowledge of the local supercluster and beyond. Recently, Press and Davis (82) have used the survey to make well controlled virial studies of groups, while at larger scales the sample provides a useful data bank for studies of the velocity field around Virgo (Davis and Huchra,82) to provide an alternative dynamical estimate of Ω.

Despite the obvious value of the survey, it rests at its limit on the Zwicky magnitude system which contains large random and occasional

TABLE 1.1: COMPLETE REDSHIFT SAMPLES

Sample	Observers Limit[a]	B_J	Area of Sky	Nos of Velocities	rms velocity error km/sec	Reference
HUCHRA	B = 13.0	13.2	$BII \geq 40^o, BII < -40^o$	593	75	Davis et al, 78
CfA	B = 14.5	14.7	$\delta > 0$ $BII \geq 40^o, BII \leq -30^o$	2440	50[c]	Huchra et al, 83
KOS	$J_{KOS} \simeq 15.0$[b]	15.45	120 deg^2 (8 fields)	171	100	Kirshner et al, 78
AARS	$B_J \simeq 16.75$[b]	16.75	70 deg^2 (5 fields)	322	70[c]	Peterson et al, 83

Notes :

a B =II ao + GG385, J_{KOS} = III aJ + Wr 4, B_J = III aJ + 66395

b J_{KOS} are total while B_J are isophotal

c For the CfA 60% have rms errors of 35 km/sec or less ;

for the AARS around two thirds have rms errors less than 50 km/sec.

systematic errors (Huchra,75) and, as with every large angular catalogue, may be seriously affected by variations in galactic obscuration. Also, although Davis and Geller (76) claimed the sample to 14.5 is fair, Peterson (73) has noted from projected plots of the Zwicky catalogue, that considerable 'mottled' structure is visible on scales of 20 degrees, even at $15.0 < B < 15.7$. This corresponds to structure on scales of 30 MPC or so. Similar inhomogeneities are suggested from the Zwicky number counts at these magnitudes (Kirschner et al, 79).

More direct evidence for inhomogeneities on the scale of the sample come from the number redshift distributions for the CFA (Davis and Huchra,82) which in the north appear to be dominated by galaxies in the Virgo and Coma (see Gregory and Thompson,78) superclusters, with a prominent void between.

Thus, while the volumes surveyed are large, the presence of structure on scales comparable to the survey depth, of around 60 MPC, suggests deeper surveys may be necessary for reliable statistical studies at these and smaller scales.

Before we turn to such surveys, two others deserve a brief mention. Firstly, the highly accurate 21 cm redshift catalogue of nearby large late type galaxies by Fisher and Tully (81), although not magnitude limited, will provide further information on group structures and dynamics in the local supercluster. Also, Rood (82) has used such compilations to provide a shallow catalogue of optical redshifts with realistic velocity errors.

1.5 DEEP REDSHIFT SURVEYS AND THE A.A.R.S

An alternative to compiling shallow, wide angle redshift catalogues is to measure redshifts in small fields to fainter magnitudes so the depth along the line of sight is much larger than the clustering length of galaxies. Choosing several such fields, in well separated parts of the sky, further increases the chance of sampling a fair volume of the universe.

In the first such survey (Table 1.1), Kirshner, Oemler and Schecter (78), (KoS (78), (Henceforward the KOS Survey) measured around 170 redshifts

in eight small fields of typically 4^{o} x 4^{o}, complete to around $J_{KOS} = 15.0$, for luminosity and clustering studies. Despite the characteristic depth of around 100 MPC these observers (Kirschner et al, 79) claimed the four northern fields were dominated by a supercluster comparable to their sample depth, which was also visible in the Zwicky counts at similar magnitudes. To examine the large scale structure further, these authors (Kirshner et al, 81 ; Henceforth KOSS) have extended three of the original northern fields in smaller patches of 1.4^{o} square but to deeper magnitudes of R = 16.3.

Since the original KOS survey was small and apparently unrepresentative, the Durham group were also motivated to measure redshifts for a larger sample of galaxies, to still fainter magnitudes and, for reliable dynamical studies, with better precision.

The basic aims of this survey were to :

(1) Estimate the galaxy luminosity function and mean luminosity density.

(2) To present plots of the galaxy distributions in 'redshift space'.

(3) To estimate spatial correlation functions using redshift information to examine the clustering of galaxies.

(4) To estimate the rms peculiar velocities of galaxies by means of correlation functions in angular and redshift coordinates which, with the information in (3), allows a Cosmic Virial Theorem estimate of Ω.

The program for (1) and (3) has been discussed for the KOS sample by Kirshner et al (79) (KOS(79). and (4) by Peebles (79). However, as Table 1.1 indicates, since the AARS has roughly double the number of galaxies, twice the sample depth and generally twice the redshift accuracy of the KOS sample, it should be better suited for all these studies.

The main purpose of this thesis is thus to report on the compilation of the AARS and on the analyses of the program (1-4) above. In most cases the analyses techniques have been repeated on the KOS survey, in order to compare with the original studies, and on one or two occasions other redshift samples have been studied.

To understand the random and possible systematic errors in the methods used, most of the analyses have been repeated on simulated catalogues designed to match features of the observed catalogue as closely as possible. In addition, the sample is large enough for subsamples to provide an alternative estimate of the sampling errors involved ; in most studies the survey has been split into a northern (two fields) and southern (three fields) subsample for such purposes.

Turning to a more specific layout of the thesis ; Chapter 3 gives a background to the survey and gives details of the magnitude and velocity measurements and their associated errors. Some basic features of the catalogue are also briefly discussed and the compilation of the simulated catalogues described.

Chapter 4 is devoted to carrying out (1) above, which is a fundamental interest in many areas of cosmology. However, most previous estimates have either come from rich clusters or else from estimates using complete redshift samples assuming spatial homogeneity. In the analyses for the AARS though, the luminosity function is estimated both assuming and dropping the latter assumption, the results being fitted by standard Schecter functions and compared with fits from the KOS and other surveys. The luminosity denisty is also estimated which, with an estimate of Ω, puts constraints on the $\frac{M}{L}$ of any low luminosity constituents of the universe.

The analyses in Chapter 5 is intended as a 'bridge' between Chapter 4 and the statistical studies in Chapter 6 and describes the galaxy distribution in the redshift volumes in both quantitative and qualitative terms. The

chapter is split into two main parts, the first of which uses the number magnitude and redshift counts, along with models estimated from Chapter 4, to examine the radial density fluctuations in the AARS volumes and thus test how representative they may be of the universe. The number magnitude counts also provide an absolute normalisation of the luminosity function and luminosity density for Chapter 4, while the number redshift models provide a measure of the mean 'background' density of galaxies needed for the later statistical studies. The second half of the chapter is concerned with carrying out (2) above, which provides subjective but important information on the clustering and peculiar velocities of galaxies, which may be missed in the correlation analyses.

Perhaps the most interesting and valuable application of the sample comes from the statistical clustering and dynamical studies in Chapter 6 (3 and 4 above). The depth of the fields are large enough to examine reliably, perhaps for the first time, the two point correlation function on scales of tens of MPCS to test for the existence of any large scale inhomogeneities in the universe. At smaller separations three dimensional correlation functions provide information on the small scale clustering of galaxies which, in turn, provides a measure of the cluster potential energy for the Cosmic Virial Theorem. At these scales the correlation functions also allow a statistical estimate of $\langle v^2 \rangle$ for use in the virial theorem. As discussed later, most previous estimates here have come from samples that have been either biased, poorly controlled, or too small to provide believable results.

Since the main motivation for the survey was to measure high quality redshifts for the dynamical studies, much of Chapter 7 is spent in discussing the Cosmic Virial Theorem application and comparing the results from other dynamical studies, which together may be starting to provide more definite information on the distribution of 'dark matter'. At the end of the chapter

the results from the clustering and dynamical studies are used to strongly constrain the present theories of galaxy and cluster formation, in turn, suggesting we might look for new scenarios.

Chapter 8 concludes the discussion with a summary of the basic conclusions, pointing the need for further redshift samples. Also discussed are present and future studies in other related areas of cosmology. The appendix gives details of the transforms between the AARS B_J magnitude system and other systems and also lists the complete redshift catalogue.

In a thesis of this type, studying several diverse and involved subjects, it is natural that a considerable amount of space is occupied in review and discussion of the theory and observations. Thus, before following the program above, the next chapter is devoted to reviewing further the clustering and dynamical studies of the galaxy distribution that are too involved to discuss fully in a brief introductory chapter.

CHAPTER TWO

REVIEW OF STATISTICS TO INVESTIGATE THE DISTRIBUTION AND MASSES OF GALAXIES

2.1 CLUSTERING CORRELATION FUNCTIONS

In the last chapter we discussed the importance of statistical studies in understanding both the clustering of galaxies and overall homogeneity of the universe and, in particular, noted the powerful role correlation functions have had to play in the analysis of projected catalogues.

In this section we first consider in more detail the observational data on the two and three point angular correlation functions and discuss how they can constrain models for galaxy clustering and galaxy formation. Since the angular correlation functions are inevitably smoothed versions of the real spatial functions, we also discuss how correlation functions estimated with redshift and angular information can provide a more direct estimate of the spatial clustering, especially at large scales, where we may expect any clustering features to be especially weak in projection.

2.1.1 Angular Studies

Many statistics have been used to analyse the distribution of galaxies on the sky but perhaps the most useful has been the two point angular correlation function $\omega(\theta)$. This is defined through the probability dp of finding a galaxy in an element of solid angle $d\Omega$ at an angular separation θ from a randomly chosen galaxy in an apparent magnitude limited sample. The relation is $dp = N\,(1 + \omega(\theta)d\Omega$ (2.1), where N is the mean galaxy surface density.

Peebles and his collaborators in Princeton have analysed several catalogues with this statistic and have found from both the Zwicky and deeper

Lick samples (Peebles and Groth 75, Groth and Peebles, 77) that to good approximation, $\omega(\theta) = \frac{A}{\theta^{\sigma}}$ with $\sigma \simeq 0.8$, (2.2), at small angular scales. Furthermore, the amplitude A varies between catalogues in the way expected for their different characteristic depths, suggesting the estimates are not seriously affected by variable obscuration and true clustering is being measured. As $\omega(\theta)$ is related to the three dimensional statistic $\xi(r)$ by a simple linear integral relation, $\xi(r)$ itself may be expected to have a power-law form, but with powerlaw index $\sigma + 1$, so that $\xi(r) = \left(\frac{r_o}{r}\right)^{\gamma}$ * with $\gamma \simeq 1.8$ (2.3). The amplitude r_o here is related to A by a factor that requires the distribution of distances of galaxies in the sample. Using an assumed luminosity function to calculate the latter, Groth and Peebles (77), find averaging over both catalogues, $r_o = 4.7$ MPC with 'reasonable' errors in the luminosity function making this uncertain by a factor two or so.

As discussed in the introduction, at large angular separations estimates of $\omega(\theta)$ vary because the clustering density contrast is so low seen in projection, making the behaviour of $\xi(r)$ at scales greater than about 3 MPC uncertain. While the scaling between catalogues of different depths suggests over scales of about 50 MPC and greater the universe is close to homogeneous, the angular studies provide little reliable information on the behaviour of $\xi(r)$ over the large range of intermediate scales.

Although the two point correlation function provides some information on the clustering of galaxies at small scales, more comes from the angular three point correlation function that is defined in an analagous manner to $\omega(\theta)$ and measures the excess probability that a galaxy chosen at random has two close neighbours.

* The amplitude of $\xi(r)$, $r_o^{1.8}$ used in this thesis is often denoted as B.

From the same angular catalogues as were used to estimate $\omega(\theta)$, Peebles and Groth (75) have found the three point spatial correlation function is well modelled by

$$\zeta(r,z,|r-z|) = Q(\xi(r)\,\xi(z) + \xi(r)\,\xi|r-z| + \xi(|r-z|)\,\xi(z)) \quad (2.4)$$

over the scales $0.05 < r < 5$ MPC, where $\xi(r)$ comes from eqn. 2.3 and r, z, and $|r-z|$ are distances separating three galaxies in space.

The estimate of the amplitude Q here, like r_o, requires an assumed luminosity function, the average value from the catalogues giving $\bar{Q} = 1.29$ (Groth and Peebles,77).

The simple forms of the two and three point angular correlation functions implied from these catalogues suggest the underlying distribution of galaxies may also have a simple explanation. The usual and most straightforward is that galaxies are generally clustered in a scale invariant hierachy extending from scales of tens of KPCS to several MPCS. However, studies of projected samples using other statistics, such as those considered by Shanks (79) and more recently Kuhn and Uson (82), have shown this interpretation cannot account for all features of the distribution and other models for galaxy clustering may give equally good representations of the data.

While the correlation functions at small scales do provide important constraints for models of the galaxy distribution perhaps their main interest at present is that their simple forms provide an elegant measure of the potential energy associated with the clustering pattern needed for an application of the Cosmic Virial Theorem.

2.1.2 Probing Theories of Galaxy Formation

As well as being relatively simple to estimate, $\xi(r)$ (and $\zeta(r,r,r)$) is a useful tool to test models of galaxy clustering and in turn how it may have developed in the expanding universe. Two such theories of galaxy and cluster formation have been extensively discussed,both based on

'Gravitational Instability', which we consider now.

(a) The Isothermal Theory

Since, intuitively we might expect the smallest scale structure to form first and as gravity is scale free, an attractive explanation for the powerlaw correlation functions is that galaxies formed early on and clustered hierarchically to form small groups that formed supergroups and so on (Peebles,74). The correlation functions can be understood more quantitatively in this light by simple linear perturbation theory in the following picture described in Peebles (74).

It is assumed at recombination that fluctuations on mass scales larger than individual galaxies are isothermal and have a power spectrum of the form ; $< |\delta K|^2 > \propto K^n$ ($-3 \leq n < 4$), the initial condensations that fragment out of the fireball having masses 10^5-10^6 $M_\odot$. These are assumed to cluster gravitationally by linear theory, the perturbations fragmenting out of the expansion at density contrasts of around unity to form bound, stable systems. If no relaxation takes place these will have characteristic densities on scale r of $\rho(r) \sim r^{-\gamma}$ where $\gamma = \left(\frac{9 + 3n}{5 + n}\right)^*$. Since $\xi(r)$ is a measure of this density on scale r, we find that with n = 0, corresponding to a simple white noise spectrum at recombination, we can explain the observed powerlaw slope of -1.8 quite naturally. As well as being good support for the isothermal theory with white noise initial conditions, the form of $\xi(r)$ has also been interpreted as evidence for a high density universe. If Ω is close to unity more detailed theory (Davis and Peebles,77) suggest that a shoulder should occur in $\xi(r)$ at a similar scale to observed in projected catalogues, where the perturbations are around unity. If instead $\Omega \ll 1$, a break away from a powerlaw is expected at much smaller scales (where $\xi \gg 1$) because linear perturbations stop growing at an early epoch and a powerlaw cannot be maintained for long (Davis et al,77). However possible alternatives have been discussed by

* Although numerical N body simulations (Gott et al,79) roughly bear out these predictions, thermodynamic arguments (Saslaw,80) and studies of relaxation processes (Press and Lightman,78) suggest a slope of $\xi(r)$ similar to observed can evolve from gravitational interactions, independent of initial conditions.

Gott and Rees (75) and others who argue that an initial spectrum with $n < 0$ may allow an approximate powerlaw, similar to observed, in a low density universe. Thus, while the gravitational clustering picture appears to be able to account for a powerlaw correlation function, the use of $\xi(r)$ as a probe to Ω and the index n is less satisfactory. As discussed later in this chapter, a more reliable probe of Ω using the correlation functions is likely to come from the dynamical studies which, within the assumptions, do not depend on the process by which galaxies and clusters formed.

(b) The Adiabatic Theory

Although the isothermal picture is still, perhaps, the most popular theory for galaxy formation and the easiest to bring to observational test, an alternative scenario has been discussed extensively by some Soviet astronomers. In this 'pancake theory' of the Moscow group, fluctuations are assumed to be adiabatic with no structure on scales less than 10^{13}-10^{15} $M_{\odot}$ (Doroshkevich et al, 74), comparable to the typical masses of present day superclusters. Larger structures then grow by gravity, collapsing in a gaseous state to form pancakes out of which galaxies fragment due to cooling behind the shocks produced.

Although harder to identify with the observed correlation functions than the isothermal theory, one might associate the preferred mass scales with features seen in $\xi(r)$. Theory (e.g. Doroshkevich and Shandarin, 78, Peebles, 80a, p.386) suggests that if Ω is close to unity, the preferred length scale should correspond to around 2 MPC, while for a low density universe the scale may be tens of MPCS. At present the only special scale suggested by the angular observations is the 'break' in $\omega(\theta)$. However other features may possibly exist at smaller scales in $\xi(r)$ that are not seen in $\omega(\theta)$ due to projection effects. At larger scales if this picture is correct, one might also expect $\xi(r)$ to show statistical evidence for the holes that

may be expected to form around pancakes where no galaxies are able to form.

In Chapter 7 we rediscuss this picture and the isothermal theory in the light of new data on the correlation functions from redshift samples and discuss how other observations from such surveys can further constrain the theories.

2.1.3 Correlation Functions with Redshift Information

We have seen that, while the angular correlation functions give information on the spatial correlation function at scales of a few MPCS, at larger scales, that are of particular interest for constraining theories of galaxy formation, the estimates are uncertain.

As discussed in Chapter 1, complete redshift samples are of importance here. Since at large separations the redshift separation 's' between pairs should be an almost direct measure of distance, the two point correlation function $\xi_s(s)$ estimated with redshifts should be almost equivalent to the spatial function $\varepsilon(r)$.

In a fairly recent analyses of the KOS catalogue KOS(79) have claimed that, instead of exhibiting a shoulder on scales of several MPCS, $\xi_s(s)$ for this survey has a long tail with correlations of order unity on separations of 30 MPC. However, as noted in Chapter 1, the sample is small and possibly unrepresentative so the results are only preliminary.

Although peculiar velocities affect using direct redshift separation as a distance indicator at the smallest separations, information on the small scale form of $\xi(r)$ can come from the redshift two point correlation function $\xi_v(\sigma,\pi)$, (Peebles,79) split into redshift separation coordinates σ and π perpendicular and parallel to the line of sight. While the distribution of velocity differences along the line of sight provides an estimate of the peculiar velocities between pairs, the integral of $\xi_v(\sigma,\pi)$ along the line of sight provides a projected estimate of $\xi(r)$, similar to that obtained from $\omega(\theta)$, but less smoothed. In addition the statistic allows a more direct

estimate of r_o than from $\omega(\theta)$ because the distances to galaxies in the sample are known through their redshifts.

Estimates of $\xi(r)$ from $\xi_v(\sigma,\pi)$ from the KOS sample by Peebles (79) give $r_o = 4.1$ with a similar value coming from the Rood catalogue (Peebles, 81) ; both rather smaller than found for the Zwicky and Lick catalogues.

Such samples can also provide an estimate of the three point correlation function and its amplitude Q which, like r_o, can be estimated through projected separations using redshift as a distance indicator. Preliminary analysis from the Rood catalogue (Peebles, 81) gives $Q \simeq 0.7$, considerably smaller than from projected estimates but, since the sample is small and probably unrepresentative, the difference is not unexpected.

In Chapter 6 we estimate the shape and amplitude of $\xi(r)$ for the AARS by means of $\xi_s(s)$ and $\xi_v(\sigma,\pi)$ and repeat the analysis on the KOS survey. Since the AARS fields are deep and sample larger than the KOS or Rood catalogues it is more likely to provide a reliable estimate of $\xi(r)$. We also compare the findings with the newly published results of the CfA catalogue given in Davis and Peebles (82). In the same chapter we also estimate Q for both the AARS and KOS sample which, with r_o and $\langle v^2 \rangle$, allow a consistent application of the Cosmic Virial Theorem.

Finally, it may be noted that, although $\xi(r)$ and $\zeta(r,r,r)$ are useful for the dynamical studies, (as discussed earlier) they provide only limited information of the clustering distribution. With redshifts other statistics that have complicated projection properties (e.g. Gott and Turner 77a) may be useful when measured in three dimensions, although the effects of peculiar velocities still need to be controlled.

2.2 STATISTICAL DYNAMICAL THEOREMS

As outlined in the last chapter, although dynamical studies of the general galaxy distribution have an important role in estimating Ω, the study of individual bound systems is hampered by projection problems.

In this section we consider these and other difficulties in more detail and point the need for a statistical solution to the problem. Two such approaches are discussed, based on the powerlaw correlation functions in section 1, the first being a 'cosmic energy eqn' and the second the 'Cosmic Virial Theorem', mentioned in Chapter 1. The latter is discussed in some detail and tests on N body simulations are reported on. As well as their role as an estimate of the potential in the clustering, the use of correlation functions for estimating the velocity dispersions is described, with particular emphasis on the role that the AARS has to play here.

2.2.1 Virial Studies of Groups

The problems with applying the virial theorem to galaxy groups were briefly mentioned in Chapter 1.3 and have been discussed by many authors (see Faber and Gallagher, 79, for a review). In these studies one has first to assign galaxies to groups, normally with just redshifts and angular coordinates on the sky, and then assume they act as isolated dynamical units of point particles satisfying the virial theorem.

Probably the biggest danger in this procedure is due to projection effects. Groups picked out by just redshifts and positions on the sky may be easily contaminated by foreground or background galaxies or worse still by two or more separate groups at different distances seen overlapping in projection. In these cases Hubble velocities can grossly inflate the velocity dispersions leading to spuriously high virial masses. On the otherhand rejecting all high velocity galaxies in groups as accidentals can artificially truncate the velocity dispersions and cause the masses to be underestimated. Similarly, the fact one can split a wide group quite naturally into subgroups both on the sky and in redshift need not deny the reality of the whole system as a bound entity (Rood and Dickel, 78). Even when membership has been well defined one still has to use correction factors to convert projected separations and line of sight velocity dispersions to three dimensions. In a small group at a given instant these

factors along with the time average needed in the virial theorem can be incorrect by an order of magnitude.

Apart from these projection effects there is still the possibility some low density systems, although associated in space, may be unstable and unbound ; in these cases the kinetic energy is due to Hubble velocities and the virial masses spurious (Turner and Sargent, 74). On the otherhand for bound groups beginning their collapse most of the total energy may be in the form of potential so the virial theorem may actually underestimate the mass (Tully,80). In loose groups too, where we may expect low velocity dispersions, redshift errors can masquerade as high peculiar velocities again leading to meaningless results (Sandage,78). Indeed it requires only a small proportion of poor redshifts in a group study to seriously compromise the results. While these uncertainties may not be too serious in rich clusters and compact groups, in the more common, looser groups they can make the virial masses vary by several orders of magnitude even if the real mass per bright galaxy is constant.

There are two main approaches to this problem. The first is to use a well defined group detection algorithm to select systems and to calibrate systematic errors in the $\frac{M}{L}$ values by repeating the analysis on catalogues prepared from N body simulations of galaxy motions and clustering in an expanding universe. This line has been followed by Gott and Turner (77b) and more recently by Press and Davis (82) but still has the problem of relying on the models describing the real universe in details important for the estimate of $\frac{M}{L}$. The alternative is to abandon even nominal identification of specific groups and treat the projection and stability problems statistically.

2.2.2 The Cosmic Energy Equation

In 1973 Geller and Peebles (73) developed a statistical virial theorem to deal with the problems of projection in group studies. Using

the incomplete Shapley Ames catalogue these authors compiled a relative velocity histogram between all pairs within a certain angular separation of each other. Then, subtracting off a histogram of background uncorrelated pair, they estimated the total rms relative velocity dispersion $\langle V_T^2 \rangle$ between all correlated pairs of galaxies in the sample. To measure the total correlation potential energy of these pairs, they calculated a similar corrected histogram of projected angular separations on the sky. Assuming that $\frac{3}{2} \langle V_T^2 \rangle$ was a measure of the mean kinetic energy (T) of a typical group galaxy and the correlation energy (W) was a measure of the average total potential, Geller and Peebles balanced the two, assuming stability $T = \frac{1}{2} W$, to obtain a mean mass per galaxy for the sample.

As pointed out by Fall (76) though, the fact that two galaxies are correlated does not make them part of the same stable group, even in a statistical sense, since not all inhomogeneities are stable or even bound. This affects the analysis in two ways, both of which will cause the masses to be over-estimated. Firstly, the relative peculiar velocity dispersion will be over-estimated as it includes pairs expanding with the universe, and secondly, since the clusters are not all bound, $T > \frac{1}{2} W$.

Noting that the excess potential energy in the clustering can be given by an integral over $\xi(r)$, Fall (76) modified the original approach and related this potential to the absolute rms peculiar velocity $\langle V_p^2 \rangle$ of a random galaxy. The relation is

$$\frac{1}{2} \langle V_p^2 \rangle = \frac{2}{3} \rho \int_0^\infty \frac{1}{2} \xi(r) \, 4\pi r^2 \, \frac{G}{r} \, dr, \qquad (2.5)$$

Since this equation does not assume statistical stability it has been referred to as the 'Cosmic Energy Equation' ; the factor of $\frac{2}{3}$ replacing the usual $\frac{1}{2}$ of the virial theorem. (As Fall notes, although this factor is estimated from linear perturbation theory, it appears to roughly hold in some nonlinear situations as well).

With eqn. 1.2 we see eqn . 2.5 can be used to determine Ω with just an estimate of $\langle V_p^2 \rangle$ and $\xi(r)$, without involving either the mean luminosity density or the assumption that the clustering be stable. In addition, unlike the usual studies in part 1, eqn. 2.5 does not require assigning individual galaxies to particular groups.

However, there is the practical problem of having to estimate the absolute velocities of galaxies $\langle V_p^2 \rangle$ from the observable relative pair weighted dispersion $\langle V^2 \rangle$. While on the one hand the small scale contribution to $\langle V_p^2 \rangle$ may be overestimated from $\langle V^2 \rangle$ (which is weighted to denser regions) ; on the other, $\langle V^2 \rangle$ does not include the contribution to $\langle V_p^2 \rangle$ from large scale motions which, at present, are poorly understood. Related to the latter is the uncertainty of the potential in eqn. 2.5 due to the uncertain behaviour of $\xi(r)$ at scales beyond a few MPCS.

Although redshift samples can help determine $\xi(r)$ at large scales, a more hopeful approach using correlation functions is the Cosmic Virial Theorem of Peebles which relates $\langle V^2 \rangle$ directly to the potential in the clustering through the three point correlation function.

2.2.3 The Cosmic Virial Theorem (CVT)

As discussed in Peebles (76a), although the two point correlation function measures the mean number of neighbours $\langle N \rangle$ around a random galaxy, we require the mean square of this number (given by the three point function) to estimate the potential associated with the grouping. This can be seen as follows : if a galaxy has a velocity V_i because of N_i neighbours within a clustering length R then $V_i^2 \sim G \frac{N_i M}{R}$ and since $\langle V^2 \rangle$ is weighted by the number of pairs we get

$$\langle V^2 \rangle = \frac{\langle N^2 \rangle}{\langle N \rangle} \frac{GM}{R} \quad \text{(Peebles,80b).}$$

A more rigorous relation comes from balancing the 'pressure gradient' of the pair supported velocity dispersion with the gravitational acceleration of all

neighbouring galaxies of each pair whose average abundance is measured by the three point mass correlation function $\zeta_\rho(r,r,r)$. This can be expressed in polar coordinates (Peebles, 76b) as

$$\frac{\partial}{\partial r}\left(\xi \langle v^2\rangle\right) + \frac{\xi 2}{r}\langle v^2 - v_t^2\rangle = -\frac{2Gm\xi}{r^2} - \frac{2G\rho}{r}\int d^3z \,\frac{\underline{r}\cdot\underline{z}}{z^3}\,\zeta_\rho(r, z, |r-z|) \tag{2.6}$$

where $\rho = nm$ is the mean mass density with n the mean number density of galaxies of mass m. $\langle v_t^2\rangle$ here refers to the one dimensional transverse dispersion. In a fuller treatment there are also time dependent linear terms that are excluded because it is assumed the clustering is statistically stable. Using the assumptions discussed shortly one can also exclude the second term on the left-hand side and the first term on the right-hand side which leaves the relation

$$\langle v^2(r)\rangle = \frac{2G\rho}{\xi(r)}\int_r^\infty \frac{dr}{r}\int d^3z \,\frac{\underline{r}\cdot\underline{z}}{z^3}\,\zeta_\rho(r, z, |r-z|) \tag{2.7}$$

Taking $\zeta(r,r,r)$ from eqn. 2.4, estimated from angular studies of galaxies, we find after a complicated integral: $\langle v^2\rangle = C\gamma\, Q\, B\, r^{2-\gamma}\, \Omega$ (2.8) where $C\gamma$ is a constant. Thus taking $\gamma = 1.8$ we expect to find $\langle v^2\rangle \sim r^{0.2}$ over the region where the clustering is stable.

Although the theory appears complicated it can be understood easily in terms of the usual virial theorem $v^2(r) \sim G\frac{M}{r}$ in the clustering hierarchy picture (Peebles, 76a). Since the mass on scale r here is given by $M(r) \propto \rho\,\xi(r)\,r^3$, the typical mean square velocity of the sublumps within a cluster is $\langle v^2\rangle \sim \rho\,\frac{\xi(r)}{r}\,r^3$, in agreement with eqn (2.8). The main contribution to $\langle v^2\rangle$ here comes from clusters on scale r. Of course individual subclusters do not really act as point particles (they are

extended and overlap each other) but Peebles (78) has shown that adjusting the velocities according to eqn (2.8) in the sublevels of a dynamical hierarchy simulation, can give rise to a stable clustering pattern.

As mentioned above the theory is based on a number of assumptions and requirements that are listed and discussed briefly below (Peebles,76b).

The scale r needs to be small enough that

(1) $\langle V^2 \rangle >> (H\ r)^2$

(2) The peculiar velocity is isotropic : $\langle V_t^2 \rangle = \langle V^2 \rangle$

(3) $\bar{\zeta}(r,r,r) >> \xi(r) >> 1$

The scale is large enough that

(4) $n\ \bar{\xi}\ r^3 >> 1$

(5) The clustering correlation functions trace out the matter distributions, so $\bar{\zeta}\rho(r,r,r) \simeq \bar{\zeta}(r,r,r)$.

Assumptions (1-3) suggest a stability criterion similar to assumed in individual group studies, in which the characteristic time for evolution of structure on scale r is much longer than the dynamical times. This is reasonable at small scales where the crossing times $\sim \frac{r}{\langle V^2 \rangle^{\frac{1}{2}}}$ are much smaller than the Hubble time $\frac{1}{H}$ (point 1) and the density contrast is high (point 3). Assumption (2) is necessary to remove the second term on the left-hand side of eqn 2.6 but also seems physically reasonable if the clustering is in equilibrium.

Assumptions (4-5) are concerned with the distribution of matter. Implicit in (5) is the assumption that bright galaxies visible in magnitude limited samples trace out the fainter galaxies and other matter. If galaxies masses instead depend on clustering environment systematic effects may occur.

Assumption (5) also requires that the mass is localised in galaxies of mass m. If instead galaxies have massive isothermal halos so $m \propto r$ we would expect from eqn 2.8 that $\langle V^2 \rangle \sim r^{1.2}$ (2.9), if assumptions (1-4) hold. If though most of the mass is localised in the brightest galaxies

(which have a small space density n) the 'discreteness' interaction term on the right-hand side of eqn 2.6 may dominate the collective term in which case we would expect (in which case (4) does not hold)

$$\langle v^2 \rangle \sim \frac{Gm}{r} \quad (2.10)$$ at small scales. (Turner, 76)

As we discuss in Chapter 7, tests of the stability of the distribution can come from the typical observed crossing times at small scales, while tests of the distribution of matter can, in principle, come from the observed scaling of $\langle v^2 \rangle$ with scale r.

Although this statistical approach requires stability and is quite sensitive to the distribution of matter at small scales, it is much less sensitive to both the large scale clustering and velocity of galaxies than the cosmic energy equation in eqn 2.5 above. While the approach has also the advantage over the traditional group studies in that one does not have to physically assign particular galaxies to groups, to estimate $\langle v^2 \rangle$, one still has the problem of deciding what proportion of pairs on the sky are physically associated. In part 5 we consider how correlation functions with redshift information can also provide a statistical estimate of this quantity.

2.2.4 Tests on N Body Simulations

As a test of the Cosmic Virial Theorem and the assumptions it requires, it is interesting and instructive to see how well it applies to numerical N body simulations of the expanding universe that are dynamically self consistent and which allow a direct estimate of the kinetic and potential energies associated with the clustering in three dimensions.

Such simulations have been carried out by several authors but here we consider those described in Efsthathiou and Eastwood (81) (Henceforth EE) who have presented results from simulations using both 1000 and 20000

particles. Although the observed results for $\langle v^2 \rangle$ and $\xi(r)$ are fairly similar in both sets to test the theory it is preferable to consider the ensemble estimates from six of the smaller simulations since these use a higher accuracy code and a smaller softening parameter in the potential which (unlike the larger simulations) is independent of time.

As EE discuss, for these simulations (with $\Omega = 1$ and poisson initial conditions) the three point correlation function is adequately given by eqn 2.4, that was used for the CVT in part 3. However, as these authors note, a test of the latter is complicated because $\zeta(r)$ does not have a simple powerlaw behaviour. In order to allow for this, $\xi(r)$ was modelled by the author from fig 2a of EE by a softened powerlaw of the form

$$\xi(r) = \frac{B}{(r + r_c)^{\gamma}} \qquad (2.11)$$

where the coordinates are in proper distance. The resultant least squares fit yielded the three parameters, $B = 2.88$, $r_c = 0.044$, and $\gamma = 2.78$; which gives as good a fit to the observed $\xi(r)$ as the four parameter fit used by EE. This model was then substituted into $\zeta(r,r,r)$ of eqn 2.4 with $\Omega = 1.2$, which was then used in the integral in eqn 2.7. Since the simulations also used a softened potential of the form ;

$$\phi(r) = \frac{G M_i M_j}{(r^2 + E_o^2)^{\frac{1}{2}}}$$

this was also incorporated into eqn 2.7 using the mean softening of the ensemble of $E_o \simeq 0.017$.

The results of $\langle v^2 \rangle^{\frac{1}{2}}$ as a function of r from the numerical integration of the triple integral in eqn 2.7, with these particular models for $\zeta(r,r,r)$, $\xi(r)$ and the force, are given as the solid line in Fig 2.1. The filled circles are the observed estimates of $\langle v^2 \rangle^{\frac{1}{2}}$ (radial dispersion) taken at small scales from fig 3.a of EE (ensemble 1), with the crosses referring to the one dimensional transverse component $\langle v_t^2 \rangle^{\frac{1}{2}}$. The dashed line is

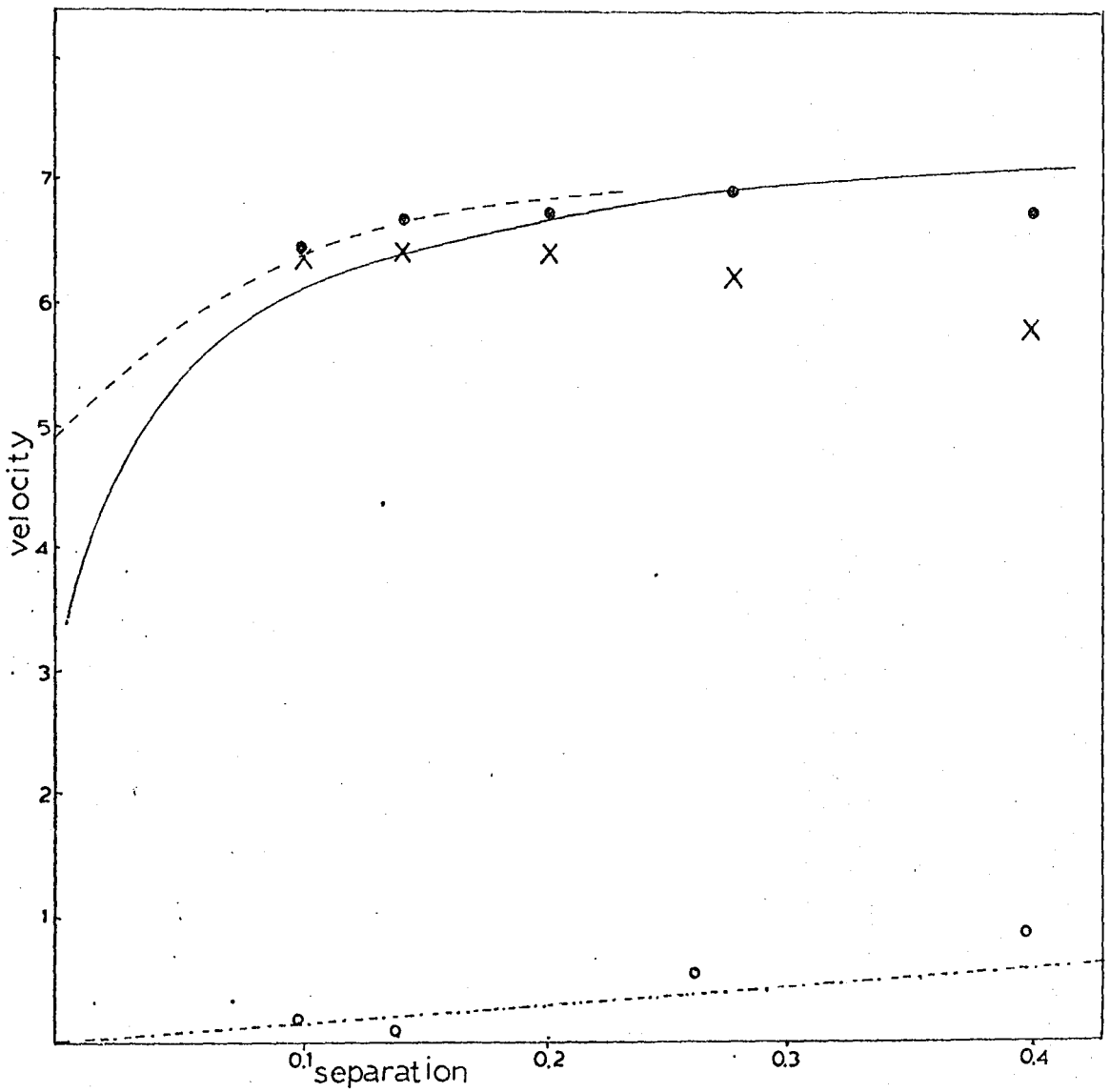

FIGURE 2.1: Velocities as a function of separation for the ensemble 1000 N body simulations of Efsthathiou and Eastwood. The observed rms radial dispersion $\langle V^2 \rangle$ (solid circles) and the transverse components (crosses) are shown against a model based on collective interactions (solid curve) and including the pair interaction term (dashed curve). The observed mean relative velocity $\langle V_r \rangle$ (open circles) is shown against pure Hubble flow (dotted line).

the result of adding the interaction term in eqn 2.6 to the collective force given by the solid line. Also at the foot of the figure are the observed estimates of $\langle V_r \rangle$ (open circles) taken from the same figure of EE ; the dotted curve here corresponding to the velocity $\langle Hr \rangle$ expected if the clustering were in free expansion.

We see from this figure that the results from the integration are in good agreement with that observed. Of course this is to be expected if our model for $\bar{\xi}(r,r,r)$ is reasonable and the assumptions discussed in Part 3 hold. At the scales of interest ($0.2 > r > 0.1$) the agreement between the solid and dashed curves show the velocity dispersions are supported by many pairs so assumption 4 holds. At small scales we see the observed velocity dispersions are also close to isotropy (assumption 2) and the solid curve lies well above the dotted line (assumption 1) and at those scales $\xi(r) >> 1$ (assumption 3) ; all suggesting the clustering is close to equilibrium. Further support for this comes from the observed estimates of $\langle V_r \rangle$, which at small scales cancels the Hubble flow.

While the CVT is applicable at small scales, at larger separations ($r > 0.2$) the velocity dispersions are larger in the radial than tangential directions suggesting the clusters are collapsing. This can be seen directly from the estimate at $\langle V_r \rangle$, which rises significantly above the Hubble flow line in Fig 2.1, consistent with slowly forming clusters. As EE discuss, this behaviour as consistent with the observed shape of $\xi(r)$ assuming it evolves in the expected way in a self similar universe.

Although this study has shown the assumptions are reasonable and the CVT could be accurately applied to the simulations to estimate the input mean density, we have no guarantee this need be the case for the real universe. Here too we still need to be able to estimate $\langle V^2 \rangle$ (and $\xi(r)$ and $\bar{\xi}(r,r,r)$) from just redshift and angular positions on the sky ; an issue we now turn to.

2.2.5 Estimating $\langle V^2 \rangle$

As well as being intimately related on dynamical grounds, the peculiar velocities and clustering of galaxies are connected on observational grounds. For example, a clue to the reality of dynamical systems comes from an examination of the galaxy distribution in redshift space where peculiar velocities should make virialised groups appear elongated along the line of sight (Jackson, 72). Although not very useful for distinguishing individual systems it does suggest a statistical method for estimating $\langle V^2 \rangle$ by measuring the elongation of the clustering pattern along the line of sight.

To do this for complete redshift samples, Peeble (79) has used the two point correlation function $\xi_v(\sigma,\pi)$ which, as mentioned in section 1.3 has components σ and π perpendicular and parallel to the line of sight. The advantage of this statistic over the original Geller and Peebles approach is that the'background correction' for uncorrelated pairs is more stable and the statistic allows a visual demonstration of the effects of peculiar velocities in distorting the clustering along the π relative to the σ direction. To estimate $\langle V^2 \rangle$ as a function of projected separation one can then exploit knowledge of the spatial clustering, by convolving $\xi(r)$ with model distribution functions to match the observed velocity broadening in $\xi_v(\sigma,\pi)$ at different σ. Alternatively the second moment of $\xi_v(\sigma,\pi)$ along the line of sight provides a direct estimate of $\langle V^2 \rangle$ which can be corrected for Hubble velocities statistically by means of $\xi(r)$. From the theory in Part 3 we expect $\langle V^2 \rangle$ to scale as $\sigma^{0.2}$ like the scaling with spatial separation in eqn 2.8.

In the statistical virial theorem analysis discussed in Part 2, Geller and Peebles (73) found $\langle V^2 \rangle^{\frac{1}{2}} = 290$ km/sec at projected separations< IMPC from the Shapley Ames catalogue. A very similar value was found by Davis et al, (78) from the Huchra catalogue using a similar method, although these authors did correct the velocity dispersions for the Hubble expansion contribution. More recently Peebles has found considerably higher values of

$\langle V^2 \rangle^{\frac{1}{2}} \sim$ 500 km/sec using $\xi_v(\sigma,\pi)$ from the KOS (Peebles (79) and Rood catalogues (Peebles, 81) and also the southern Huchra sample (Peebles, 80b). With $r_o \sim 4.0$ in each case (also estimated from $\xi_v(\sigma,\pi)$) and Q around unity these give a CVT estimate of $\Omega \sim$ 0.5.

However, these values, especially for $\langle V^2 \rangle$, can only be regarded as preliminary. The KOS sample is small and so is subject to large statistical fluctuations and the other two are based on the SRC which is certainly a biased catalogue. Also the latter is incomplete and, being a compilation of many sources, probably contains some quite inaccurate redshifts. For the estimate of $\langle V^2 \rangle$ an important requirement is that the redshifts should have accuracies smaller than the expected peculiar velocities of galaxies. In nearby loose groups these are typically 50-100 km/sec (Tully,82) but since $\langle V^2 \rangle$ is pair weighted to the denser regions, where velocities should be higher, accuracies of this order are probably tolerable.

In Chapter 6 we consider an estimate of $\langle V^2 \rangle$ and r_o using $\xi_v(\sigma,\pi)$ from the AARS. Since this sample consists of several deep and well separated fields and contains over three hundred redshifts with accuracies comparable to those dicussed above, it should provide more reliable results than previously found. A reanalysis of the previous data is also presented and a comparison made with the newly published results from the CfA catalogue. In Chapter 7 the estimates of $\langle V^2 \rangle$, r_o and Q are used to estimate Ω by the CVT.

For the present we now turn to the compilation of the catalogue, in particular focusing attention on the velocity error analysis, needed for a full understanding of the dynamical results.

CHAPTER THREE

THE ANGLO AUSTRALIAN REDSHIFT SAMPLE

3.1 INTRODUCTION

The first two chapters have outlined the important and powerful role that complete redshift samples have to play in modern cosmology and, in particular, have pointed the need for a new, deep survey to provide a reliable estimate of the peculiar velocities between pairs and to study the large scale form of the correlation function.

In this chapter is given a detailed account of the compilation of the AARS catalogue along with a brief discussion of its general features. The next section gives a brief background to the survey and how the fields were chosen with section 3 giving more details on the present status of the data. Sections 4 and 5 give details of the measurements of the magnitudes and redshifts with particular attention given to the assessment of the errors. In section 6 basic features of the survey are presented and briefly discussed before the more detailed analysis in subsequent chapters. Finally the last section describes the preparation of simulated catalogues which are used throughout this thesis to test the methods of analyses for random and systematic errors. As noted in Chapter 1.5, the full redshift catalogue is presented in the appendix at the end of this thesis.

3.2 BACKGROUND TO THE SURVEY

The AARS was started in 1979 with the view of providing a large number of redshifts (spanning a fair volume of the universe) by sampling galaxies in several deep, well separated fields, unbiased by local inhomogeneities. Since the survey was primarily intended for correlation and luminosity studies the basic requirement for realistic analysis (which was also a practical possibility) was to obtain complete photometry and redshifts for at least two hundred galaxies. For the luminosity function estimates ,

accurate photometry and strict completeness were important although fairly large errors in the velocities were tolerable. As discussed in Chapter 2.2, for the dynamical studies the accuracy of the redshifts needed to be below the expected peculiar velocities of galaxies so that rms errors around 50 km/sec seemed desirable.

Apart from these requirements the following choices were still left open.

(a) The limiting magnitude of the survey.

(b) The angular size and shape of each field.

(c) The number of fields.

(d) The final choice of fields on the sky.

The choice a, b and c together naturally fix the total number of galaxies in the survey which was the biggest constraint due to the shortage of observing time for measuring high quality redshifts. The main other constraint was the availability of plate material for preparing the sample prior to measuring redshifts.

Since the Durham group at the time were examining the galaxy distribution around the south galactic pole by means of catalogues prepared from U.K. Schmidt plates, it seemed appropriate to start by focusing attention on this region and to use the Anglo Australian Telescope (AAT) for the spectroscopic work.

With these constraints (a) - (c) were chosen as follows :

Since the Zwicky and KOS number magnitude counts still showed evidence for inhomogeneities at B = 15.5 it seemed desirable to go deeper than a limiting magnitude 16.0. As the unvignetted region of a UKST plate is typically $4^{o} \times 4^{o}$ and to $B_J = 16.5$ one expects to find around fifty galaxies it appeared that a reasonably fair sample could be formed with four or more well separated plates. Thus the choice (a)-(c) seemed quite natural. Furthermore, with an optimal observing setup on the AAT, it was

estimated one could measure the redshift of a typical sample galaxy to an accuracy of better than 50 km/sec in 15 to 20 minutes. Thus,measuring redshifts for a minimum sample of 200 galaxies would occupy seven or eight nights ; a reasonable demand on the AAT.

Going to much deeper magnitudes would have considerably increased the exposure time needed for the redshifts and at increasing depths K dimming and curvature effects increasingly complicate the analyses. Similarly, reducing the angular size of the fields, although allowing more fields to be studied, would have reduced the number of pairs contributing to the correlation functions and increased the observational work for the photometry. Also (as discussed later in the thesis) if the width across a field of its characteristic depth had been smaller than the correlation length $r_o \sim 5$ MPC, statistical fluctuations in the redshift distribution would have been considerably increased.

Lastly, there was still the problem (point d) of choosing the fields to be surveyed. To test for any possible north-south differences still present at the depth of the sample it was aimed to study some fields in the north as well as the southern galaxtic cap, parts of which are accessible from the AAT.

Beyond this the fields were chosen to satisfy several basic criteria to ensure the maximum chance of obtaining a fair sample of the universe. Firstly the areas were to be free from small scale ($\sim$ 1 deg) galactic absorption as delineated by the distribution of very faint galaxies ($B_J < 22$) and secondly the preliminary number counts (if available) should be representative of the entire sky at that limit. Also the fields needed to be sufficiently well separated to reduce the chance of large scale inhomogeneities biasing the total sample.

In Fig 3.1 are shown the positions of the five chosen AARS fields as boxes (not to scale). Also shown are the eight original KOS fields (circles)

KEY

AARS FIELDS

[1] = GSA

[2] = GSD

[3] = GSF

[4] = GNA

[5] = GNB

KOS FIELDS

① = NP4

② = NP5 *

③ = NP6

④ = NP7 *

⑤ = SP3

⑥ = SP4

⑦ = SP5

⑧ = SP6

◉ = NP8 (KOSS)

CLUSTERS

Ⓥ = VIRGO

Ⓒ = COMA

Ⓕ = FORNAX

FIGURE 3.1

POSITION OF REDSHIFT FIELDS

IN

EQUATORIAL COORDINATES

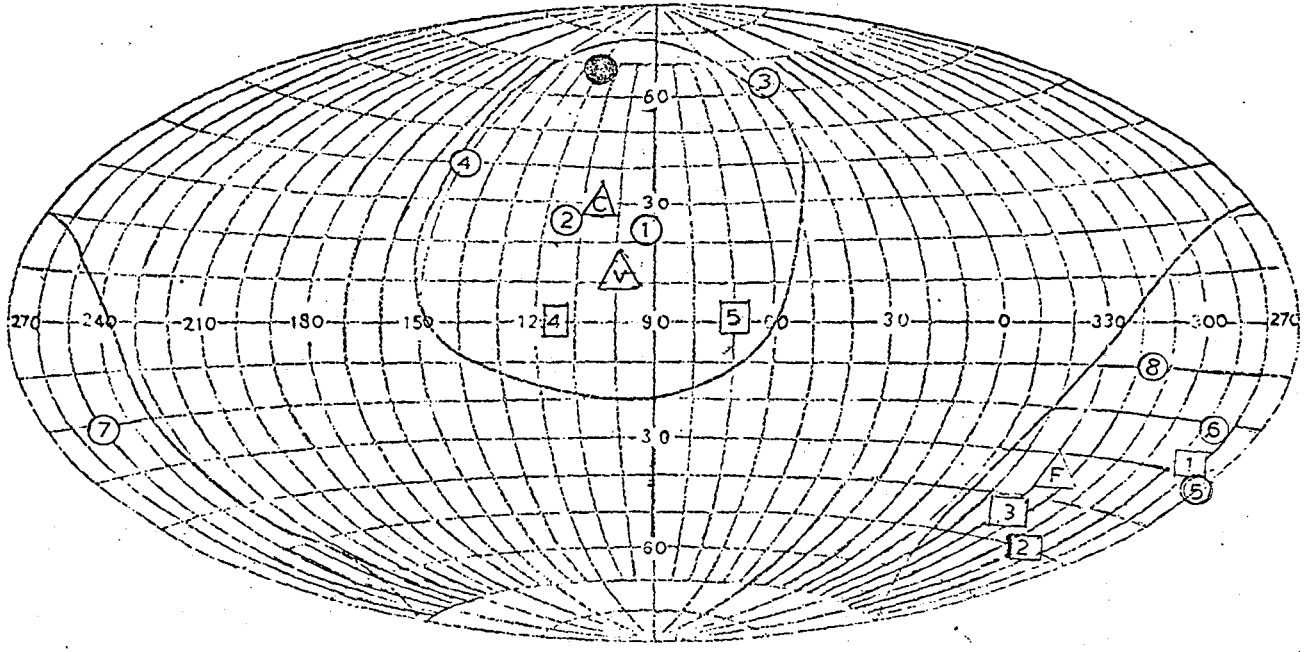

* ALSO IN KOSS SURVEY

and the clusters Virgo and Coma in the north and Fornax in the south (triangles). The remaining symbol (filled circle) refers to field NP8 which, along with small subregions of the fields NP5 and NP7 (see Key on Fig 3.1) of KOS, make up the KOSS survey mentioned in Chapter 1.5.

We see the AARS fields are all at high galactic latitude to avoid, at least, the known band of galactic obscuration (enclosed by solid line). In the south each of the fields are separated by at least 20^{o} so galaxies in different fields at the characteristic depth of the sample are always greater than 70 MPC apart. In the north the corresponding distance is around twice that.

Since both the characteristic depth and separations of the fields are larger than the usually accepted clustering length of galaxies, the AARS may be a reasonable approximation to a fair sample of the universe.

In this context it may be finally noted that, apart from avoiding obvious nearby rich clusters such as those shown in Fig 3.1 (where faint galaxies would dominate the counts), the fields were not deliberately chosen to exclude any rich areas which should be fairly represented in a 'random' sample of the universe. Although in a large sample the 'fairness' of the clustering sampled could be tested by a comparison of $\omega(\theta)$ for the sample with deeper catalogues (see Chapter 2.1) the AARS is too small for such a study (However see Chapter 6.4).

A further description of the gross properties of the survey is given in section 6 of this chapter with some of the points discussed above, being taken up again in Chapter 5.

3.3 OUTLINE OF THE DATA

The observations for the AARS considered in this thesis were taken in the three years 79-81 during which interval sufficient observing time on the AAT was available to measure over three hundred velocities, providing complete redshift information in some of the fields to $B_J = 16.75$.

Details of the present data for the survey are given in Table 3.1.

TABLE 3.1: The Anglo Australian Redshift Sample

Field	Field Centres			Adopted limit	Numbers to limit		Area
	α	δ	B_{II}	B_J	Total	With Redshifts	deg^2
GSA	00 57	-28 02	-90	16.74	76	74	14.06
GSD	02 01	-49 42	-63	16.75	64	62	13.95
GSF	03 44	-45 06	-56	16.50	50	50	14.44
GNA	13 41	+ 0 00	60	16.61	70	68	13.95
GNB	10 40	+ 0 00	49	16.76	69	68	13.91

We summarize now, more fully, the available (a) magnitude and (b) redshift data for the survey used to follow the program discussed in Chapter 1.5, briefly indicating other observations and other possible uses of the data.

(a) As shown in Table 3.1, complete magnitude information exists at the time of writing in all fields to at least 16.50 (the actual limit varying from field to field) with reliable magnitude data in some fields existing to beyond the limits shown. The magnitudes have all been measured photographically from short exposure U.K.Schmidt plates (III a J) of the fields taken through a GG 395 filter, corresponding to what we call a photoelectric B_J band lying between 4000 and 5500 Å. The plates were all scanned by the Epping PDS machine, the isophote chosen corresponding to a surface brightness of around 24 mag/(arcsec)^2 with rms errors on the magnitudes estimated to be around 0.05.

Further details of the photometry and comparisons with other systems are given in the next section.

(b) As shown in Table 3.1, the redshift data is complete, apart from seven galaxies, to the magnitude limits adopted for the sample. Although a further sixteen redshifts exist for fainter galaxies, due to incompleteness they are not included in the survey. The spectra were all taken at the AAT and cross correlated with the spectra of template objects with known or inferred velocities to give absorption velocities. Normally working at high dispersion (33 Å /mm) this gave errors generally less than 50 km/sec. However, a small proportion of spectra (20%) were taken at lower dispersion giving errors nearer 100 km/sec, the rms error for the total sample being 50-100 km/sec. More details of the velocity measurements and, in particular the error analysis, are given in section 3.5.

In addition to measuring magnitudes and redshifts, classifying galaxies according to morphological type is important for luminosity function studies since at the depth of the sample K dimming is non-negligible and varies between galaxy types. A full de Vaucouleurs classification for four

fields was done by eye from blue plates in Durham by H. Corwin with the poorer plate for field GNB typed by several members of the Durham group. Abbreviated types for the whole survey are given in the appendix.

Apart from the studies in this thesis the data discussed above has other important uses. Most of the spectra, for example, have been reduced to absolute fluxes using Okes (74) observations of white dwarves, thereby providing a catalogue of absolute energy distributions, within a certain waveband, of a magnitude limited sample of galaxies. The spectra could also (in principle) have been used to provide information on the internal velocity dispersion of the galaxies which provide velocity independence distance indicators for early type galaxies, as has been done for the CfA by Tonry and Davis (81).

With other data available there are further possibilities.

One project underway at present is the measurement of infrared magnitudes for the northern galaxies at the U.K.Infrared Telescope on Hawaii for colour magnitude and infrared luminosity studies. It is also hoped to obtain photographic magnitudes in other passbands with the Epping PDS for similar purposes. Finally the sample, as well as providing information on 'ordinary galaxies' has revealed several unusual objects including strong emission line galaxies, abnormally bright field galaxies and so on that may be of interest for further individual study.

3.4 THE PHOTOMETRY

This section on the photometry is split into two parts, the first giving details of the photometric measurements for the AARS and the second comparing with other magnitude systems.

3.4.1 The AARS Photometry

Since the final photometry for the AARS was done by B.A.Peterson and Z, L, Zou and as full details are given in Peterson et al (83), we consider only a brief description now.

Provisional lists for the survey for three of the chosen fields were prepared from an eye examination of U.K.S.T. plates while in two of the southern fields provisional photometry was prepared from automated scans of long exposure U.K.S.T. plates using the COSMOS measuring machine (see Pratt et al, 75). Working down to a surface brightness of about 25.7 mag/(arcsec)^2, isophotal magnitudes here were measured for all objects to around seventeenth magnitude which were later examined by eye to separate galaxies from stars. Photographic saturation on these plates made magnitudes brighter than 16.0 unreliable.

To avoid saturation effects in the final photometry short exposure plates (10 mins) hypersensitized plates of all five fields were taken in good seeing at the Schmidt which were subsequently photometered by the Epping PDS. The magnitudes were measured by scanning an area around each galaxy on a PDS microdensitometer using a 10 x 10 micron scanning aperture, the final data sets being 120 x 120 arrays. A background sky intensity map was produced from local frequency histograms of pixel transmissions and the isophotal image of a galaxy was taken to be all pixels that were above the local sky density by a set density threshold which was set to correspond to a surface brightness of about 24 mag/(arcsec)^2.

The calibration of the transmission measurements into intensity was done by measuring spot wedges on each phogograph, the wedge steps in Baker density against $\log_{10}$ (intensity) being fitted by a polynomial.

The magnitude of each galaxy was then computed according to the definition (e.g. Shanks et al, 83a)

$$m = -2.5 \log_{10} \Sigma \frac{(I_j - I_{sky})}{I_{sky}} A_{pix} + m_{sky} \qquad (3.1)$$

Here A_{pix} is the pixel size in square arcseconds, I_i the relative intensity of each pixel above the isophotal threshold, I_{sky} the fitted background intensity and m_{sky} the sky intensity still to be found. The I_{sky} in the

denominator is intended to allow for sensitivity variations over the plate due to variations in emulsion sensitivity.

In order to determine m_{sky} and hence put the magnitude on an absolute scale, photoelectric sequences were used. While in some fields standard stars were available, for others sequences were measured on a small 40" telescope or Siding Spring Observatory. When the photographic images of bright standard stars were saturated secondary images, produced by a Pickering (Subbeam) prism, were measured and the magnitudes of the primaries then calculated.

To estimate the random errors, 24 galaxies were photometered on three separate plates of the same field with each plate reduced using the same calibration curve to connect relative intensity to density. The mean rms error between three plates was found to be 0.06.

The magnitudes for all the redshift galaxies to the field limits in Table 3.1 are in the catalogue in Appendix B. Galaxy images that were contaminated by stars and have corrected magnitudes are marked by the symbol '*'.

3.4.2 Comparisons with Other Systems

It is naturally of importance to compare the B_J magnitudes with other systems both to compare results of the later analysis and as a test of the PDS measurements.

Table 3.2 gives a summary of the expected theoretical transforms between the B_J system and several other systems, the calculations of which are given in the first part of the appendix to this thesis. However some data is also available for a direct comparison of the PDS magnitudes with the provisional cosmos magnitudes and with total J system of the KOS survey.

The first of these comparisons is plotted in Fig 3.2 which shows J_{PDS} against J_{COSMOS} with an 'eye' fit line corresponding to $J_{PDS} = J_{COSMOS} + 0.15$. We see the line is a reasonable fit to the data suggesting little evidence for either saturation in the cosmos magnitudes at bright magnitudes or

TABLE 3.2: Transforms of B_J Magnitudes to Other Systems

			References
$B_J^{24.1}$ (JPDS)	= $B_J^{25.7}$ (J_{COSMOS}) + 0.27	(1)	Fong et al (83)
	= $B_J^{25.7}$ + 0.15	(2)	fig 3.2
	= J_{KOS} + 0.49	(3)	Kirshner et al (78)
	= J_{KOS} + 0.45	(4)	fig 3.3
	= B_z - 0.21	(5)	Zwicky et al (61-68)
	= B(O) - 0.21	(6)	de Vaucouleurs et al (64)
	= B_T + 0.07	(7)	de Vaucouleurs et al (76)
	= B_J^{TOTAL} + 0.25	(8)	Appendix A.

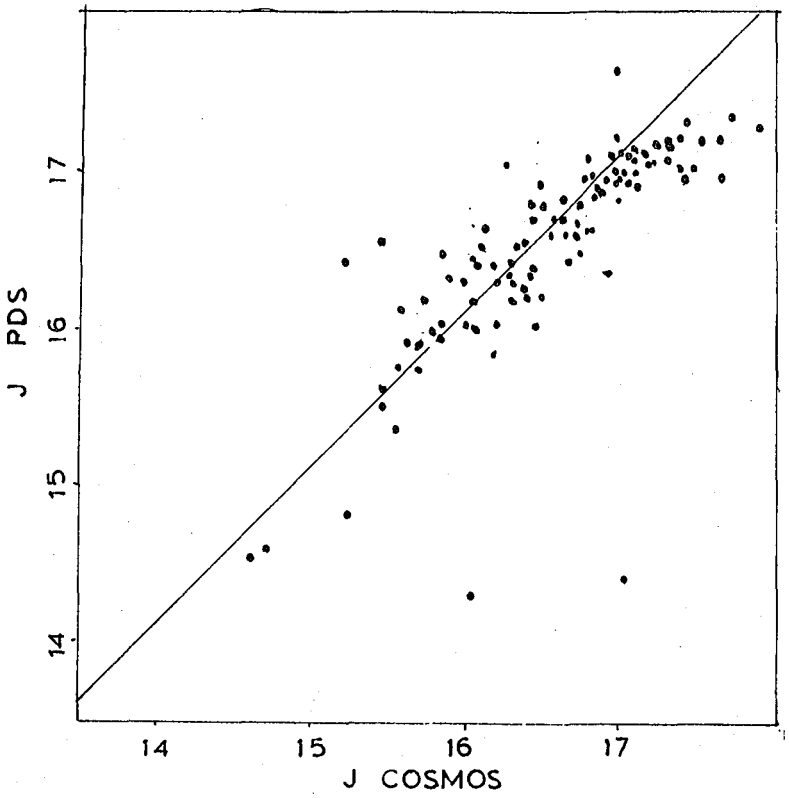

FIGURE 3.2: Comparison of Cosmos and PDS magnitudes for field GSA. The line corresponds to $J_{PDS} = J_{COSMOS} + 0.15$

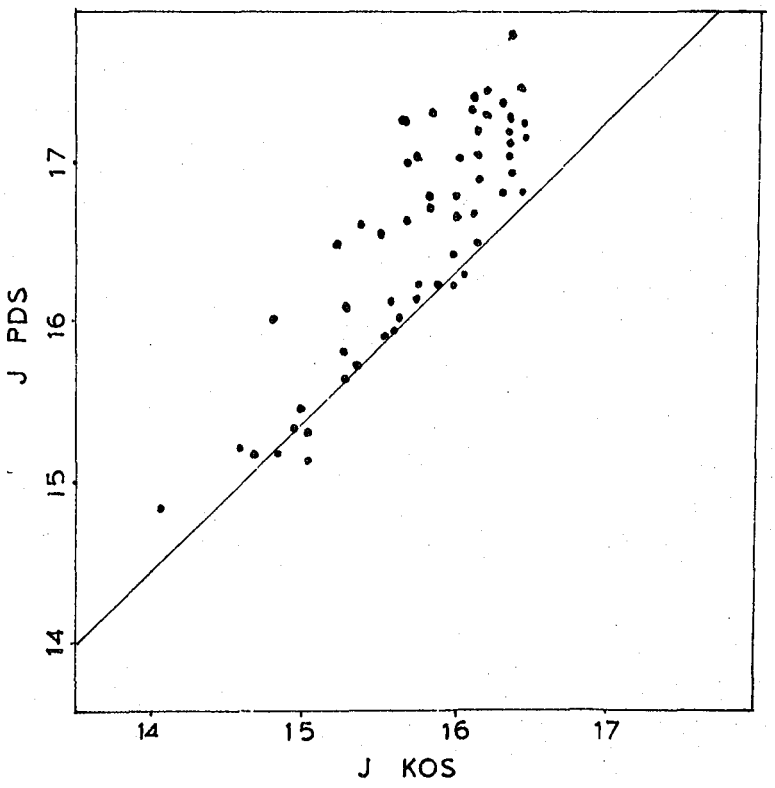

FIGURE 3.3: Comparison of KOS and PDS magnitudes for KOS field SP6. The line corresponds to $J_{PDS} = J_{KOS} + 0.45$.

possible systematic effects due to the high isophote used for the J_{PDS} measurements. However the offset is slightly smaller than expected theoretically (eqn. 1, table 3.2) when the different isophotes and slightly different passbands are corrected for.

In order to compare with the different J system used by KOS several plates of the KOS fields have been taken to scan with the PDS, although at the time of writing only J_{PDS} magnitudes were available for one field, SP6. The results of J_{PDS} against J_{KOS} for this field are shown in Fig 3.3. The line here corresponds to $J_{PDS} = J_{KOS} + 0.45$ which we see describes the transform reasonably to $J_{PDS} = 16.5$.

The large offset here (which agrees reasonably with eqn.3, Table 3.2) comes from the considerably redder passband used by KOS and because these authors attempted to measure total rather than isophotal magnitudes.

At fainter than $J_{PDS} = 16.5$, Fig 3.3 shows considerable deviations from a 45^{o} slope suggesting a systematic error in one or either system. Although the direction of the deviation could be consistent with an effect due to the high isophote used in the PDS measurements, the agreement with the cosmos magnitudes taken at lower isophote in Fig 3.2 suggests this is not happening and errors in the KOS magnitudes may be to blame. However further data for comparison is needed for firmer conclusions to be drawn.

These two empirical transforms are given in Table 3.2 along with the theoretical ones. We see both comparisons differ by a small amount, the same sense suggesting either a small systematic error in the B_J magnitues or perhaps an error in the uncertain transformation between isophotes of eqn. 3 in Appendix A.

Eqns (6) and (7) in Table 3.2 also suggest an inconsistency since together they imply $B_T \simeq B(O) - 0.27$; rather smaller than usually accepted. However eqn (6) is calculated in the appendix via the KOS and Zwicky systems and the latter is known to suffer from systematic errors,

especially at faint magnitudes (Huchra, 76) where comparison with the KOS magnitudes was made.

The two empirical transforms along with others in Table 3.2 are used in the next chapter to compare the results of the luminosity function studies and in Chapter 5 to compare number magnitude counts from several surveys. The transform of B_J to total magnitudes (eqn. 8 .) is required in Chapter 4 to estimate the total luminosity density for the AARS in the total B_J^T band.

3.5 THE REDSHIFT MEASUREMENTS

To give details of the redshift measurements this section is split into three parts. The first gives brief information on the observations and the basic data reduction and the second how the spectra are used to estimate the final velocities, including a brief mention of how the errors are calculated. The final part gives a more detailed description of the error analysis needed for a full understanding of the relative velocity studies for the Cosmic Virial Theorem.

A further account of the measurements is given in Peterson et al (83).

3.5.1 Observations and Preliminary Data Analysis

The galaxy spectra were all measured in nine observing 'quarters' spaced over around two years at the 3.8m AAT using the RGO spectrograph and normally the image photon counting system (IPCS: Boksenberg, 72).

A summary of these observations is given in Table 3.3. Although the total number of spectra quoted here is 350, of these 28 were either duplicated for one reason or other or the galaxy was later found to lie beyond the magnitude limit for the field. The spectra were normally measured at 33 Å/mm apart from two observing runs. In quarter 80:4 the dispersion was lowered to 66 Å/mm to allow a rapid completion of fields GSA and GSD between 16.5 and the limit 16.75. In 81:1 the same dispersion was also

TABLE 3.3: Summary of Redshift Observations

Year	Quarter	Nos of Nights	Starting λ_o (Å)	Detector	Nos at dispersion 33 Å/mm	Nos at dispersion 66 Å/mm
79 :	2	3	3600	IPCS	23	-
79 :	3	3	3700	IPCS	44	-
79 :	4	3	3700	IPCS	26	-
80 :	1	1	3700	IPCS	36	-
80 :	2	2	3700	IPCS	5	-
80 :	3	3	3700	IPCS	53	-
80 :	4	3	3700	IPCS	22	46
81 :	1	2	3700	IDS	-	21
81 :	2	2	3700	IPCS	74	-

TABLE 3.4: Typical Observing Set Up (High Dispersion)

Wavelength range 3700 - 4724 Å	
RGO Spectrograph	25 cm camera
	Grating 1200 B
	Blaze to collimator gives 33 Å /mm
	Slit width 600 μm = 4 arc seconds
IPCS x gain of 5" per increment (high gain)	
	Slit length 2 arc minutes
	Scan Format 34 x 2048
	Data window 24 x 2044.

used when the IPCS was unavailable. These 'low dispersion' velocities and their errors are discussed more specifically in section 5.3.

Table 3.4 gives further details of a typical observing setup for the usual high dispersion measurements.

In this wavelength range the IPCS was very efficient and in this region were many strong absorption features, including the two Ca II lines, H and K, needed to obtain high accuracy absorption redshifts. In addition many galaxies showed the oxygen 3727 Å emission doublet with provided a straightforward but lower accuracy redshift with error around 100 km/sec.

To achieve the desired 50 km/sec for the absorption velocities the galaxies were exposed for between 15-30 minutes depending on the magnitude and surface brightness of the object. The twilight time was used to take several stars and nearby 21 cm galaxies to be used as templates, the latter also providing a 'zero point' for the velocities.

Most of the preliminary data reduction was done at the Anglo Australian Observatory in Sydney on standard packages although some of the latter stages were completed at Durham with corresponding programmes. The reduction involved flat fielding and wavelength calibrating the full two dimensional data, the outer specta in each scan being then used to subtract the mean skies. At this point the centre of any emission lines present were located and used to provide an emission line velocity for nearly half the galaxies. After removing the emission lines the spectra were subsequently rebinned onto a logarithmic scale, sky subtracted and zero meaned.

Fig 3.4a shows the wavelength calibrated spectrum (consisting of 2048 channels) of a typical survey galaxy with absorption lines H and K marked. Fig 3.4b shows the same galaxy after the reduction above, with Fig 3.4c showing the equivalent spectrum for a template Kϕ star. The spectra in both cases have been moved above their means of zero for display purposes.

FIGURE 3.4

a)

Wavelength calibrated

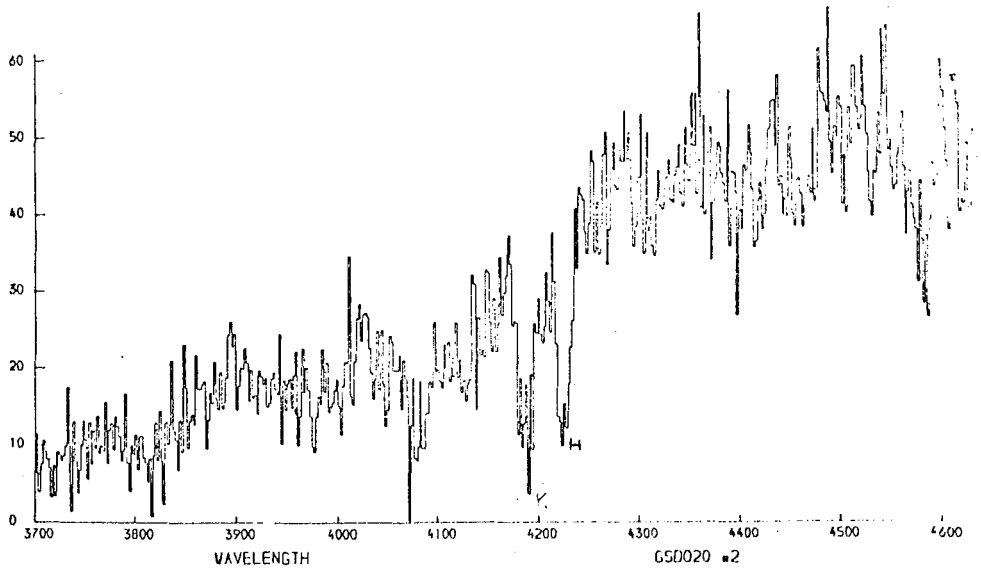

b)

Continuum subtracted, logarithmic wavelength scale

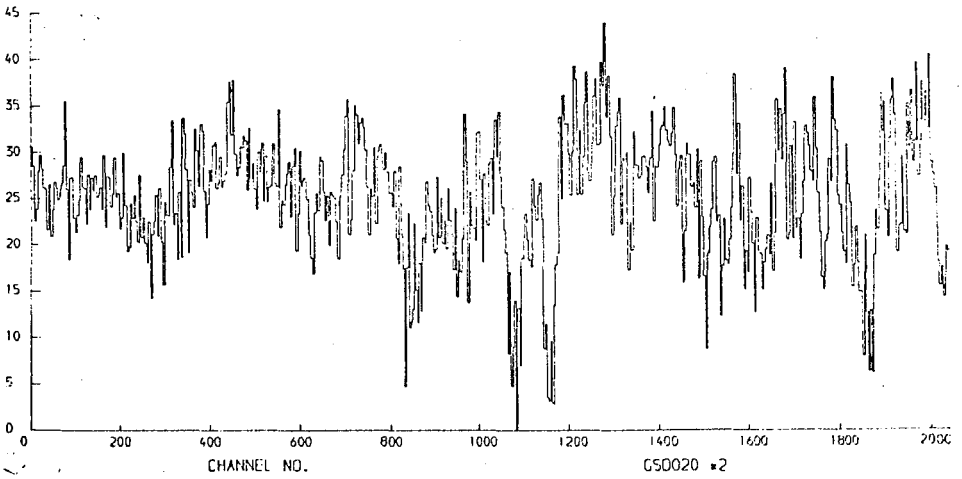

c)

KØ Stellar template

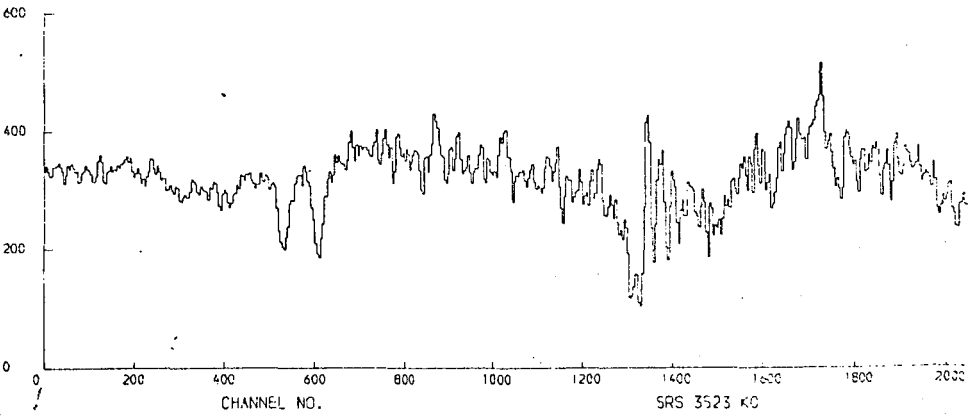

d)

Cross correlation function of (b) & (c)

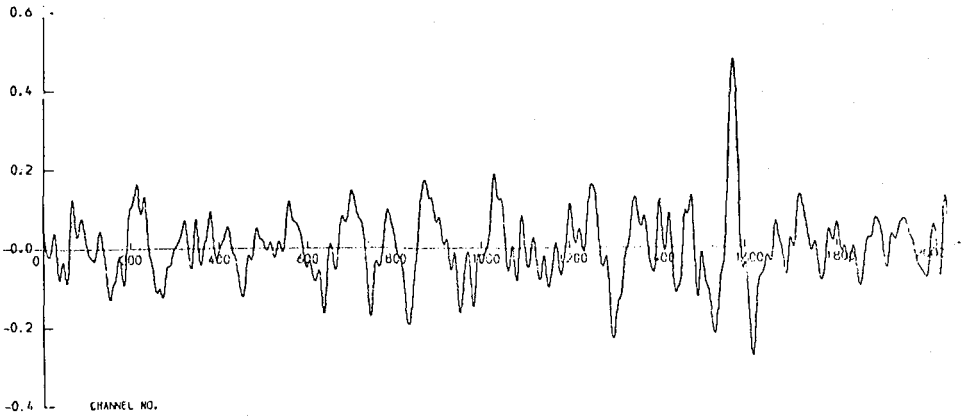

Further details of the reduction stages discussed above are given in Efsthathiou (79).

3.5.2 Estimation of Velocities

To estimate absorption velocities from the galaxy spectra, the fourier cross correlation method of Tonry and Davis (79) (TD) was adopted which was straightforward and allowed an elegant determination of the measurement errors. Since the technique is fully described in TD and also in Efsthathiou (79) the technique is described only briefly now.

Before cross correlating a galaxy and template spectrum to obtain a relative velocity, both spectra were fourier transformed to allow the removal (via a linear filter) of unwanted large and small frequency components associated with noise and residual continuum trends. The cross correlation function was then rapidly computed from the transformed galaxy and template spectra and the maximum peak of the function located and fitted by a low order polynomial to give a position of its centre and height. The relative shift of the centre then gave the relative velocity between the galaxy and template, with the ratio 'R' of the height of the main peak relative to a typical noise peak giving a measure of the velocity error through the expression

$$\Delta V = \frac{C}{1 + R} \qquad (3.2)$$

where C is a constant.

Fig 3.4d shows the cross correlation function of the galaxy and star spectra shown in Figs 3.4b and 3.4c. The relative velocity in this case is 19540 km/sec and the R ratio is 6.1 which, with C calibrated to be around 170 km/sec/channel (see Part 3), implies an error of 24 km/sec.

In order to turn the velocities calculated in this way to absolute velocities relative to the sun, two corrections had to be made. First each relative velocity had to be corrected for the helocentric motion of the

object and template at the time of observation and then, this in turn, had to be corrected for the absolute motion of the template with respect to the sun. Unless the latter had a published velocity, the relative velocities of the templates and 21 cm galaxies were compared and the absolute velocity of each template inferred consistently using the published accurate 21 cm velocities.

To decide the 'best' velocity for a given galaxy, after each observing run the galaxies observed were cross correlated with all the templates, each relative velocity corrected for the two effects above. The table of corrected velocities were subsequently examined and the template with the highest average R ratio adopted as 'standard'. The velocity from this template was then normally adopted for each galaxy although, if in a particular case it was unrepresentative of the other template velocities, one of the other velocities would be chosen.

The final absorption velocities and available emission velocities for the sample galaxies are given in the Appendix B along with the R ratios, adopted templates, observing quarters and photon counts per spectrum. It should be noted the velocities are 'representative' velocities in km/sec ($V = cz$) and have not been corrected for motion in the galaxy or local supercluster which should,by comparison, be small at these depths.

3.5.3 Velocity Error Analysis

Although errors in the velociites will arise from uncertainties in the velocity of the templates (zero point error) and intrinsic differences between the template and object spectra (template mismatch error), consistency studies suggested these errors are generally less than 20 km/sec. The biggest source of error, instead appears to come from noise in the galaxy spectra. This can lead to spurious peaks in the cross correlation function that can sit under the true peak and distort the position of its centre. As discussed in part 2, this 'random' error can be estimated from the relative heights of

the true and noise peaks if the constant C in eqn 3.2 is known. For the AARS this quantity could have been calibrated externally if sufficient sample galaxies had 21 cm velocities published. However, since few have any alternative redshifts the following experiment was conducted.

White noise was added to a high quality galaxy spectrum which was then cross correlated with the original, undergraded spectrum of the same galaxy. This was repeated for varying amounts of noise on several galaxies and the relative velocities were plotted against R ratios for each measurement, as shown in Fig 3.5. Since the relative velocity in each case was due to the noise added, C was calibrated by fitting eqn 3.2 to these points.

We see that this curve with

$$C = 170 \text{ km/sec/channel} \qquad (3.3)$$

gives a reasonable fit to the results from the experiment which also suggests that the theoretical form of eqn 3.2 is indeed a reliable representation of the errors due to noise.

Adopting this calibration, fig 3.6 shows the distribution of random redshift errors for all galaxies measured at high dispersion. The total rms error is 37 km/sec in agreement with that found by TD for the CfA catalogue where the errors were calibrated from both internal and external measurements.

Fig 3.7 shows a scatter plot of random redshift error against spectrum photon counts for the same sample of galaxies.

We see a fairly strong trend of increasing error with decreasing counts, which is to be expected if random noise dominates the value of R. Similar plots early in the project allowed the exposure times for redshift quality to be optimised. While there is little apparent correlation between redshift error and velocity or apparent magnitude we may expect a correlation with surface brightness since for low surface brightness objects the signal-to-noise will be low despite high photon counts.

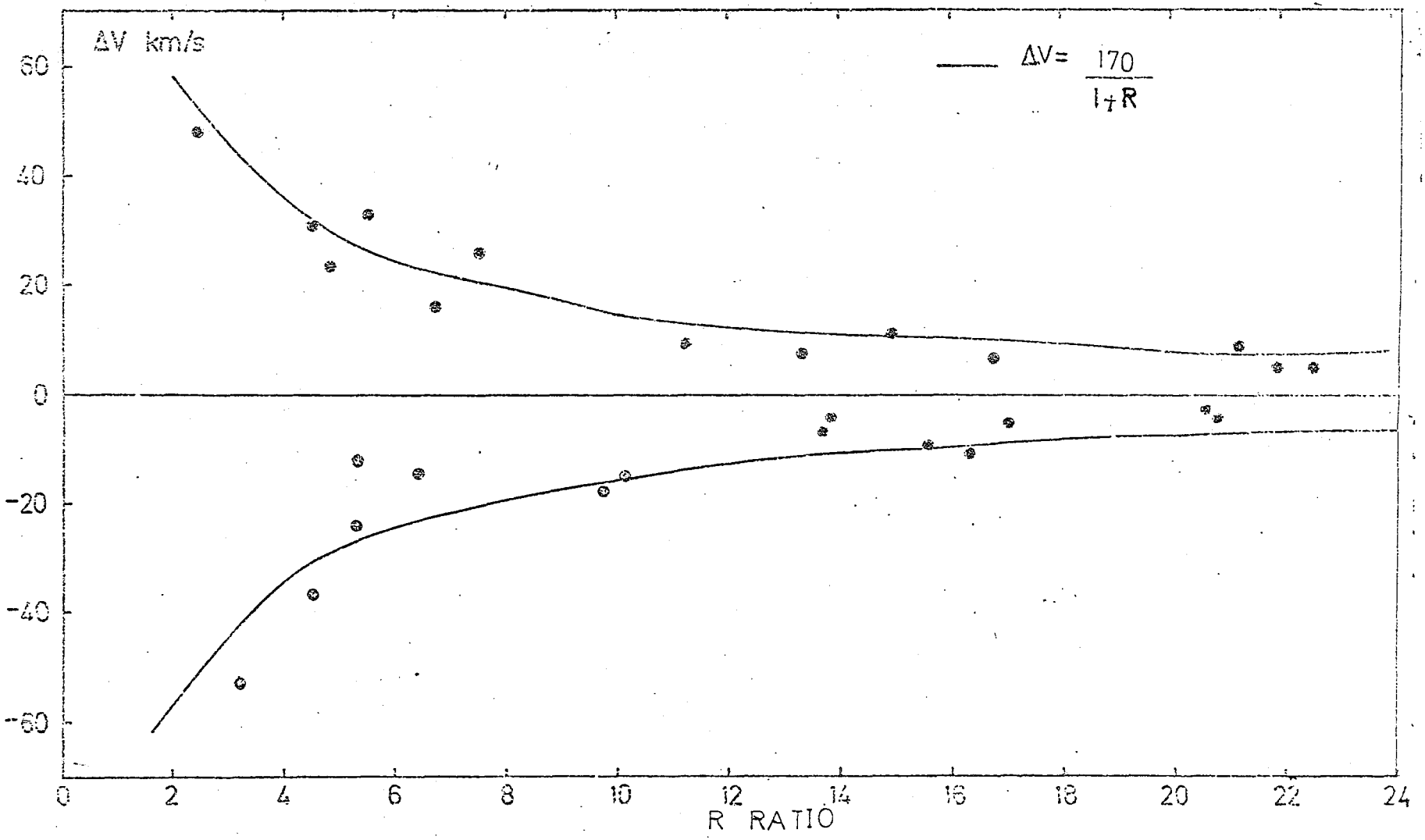

FIGURE 3.5: Results of noise degradation experiment to calibrate the random velocity error for the high dispersion sample

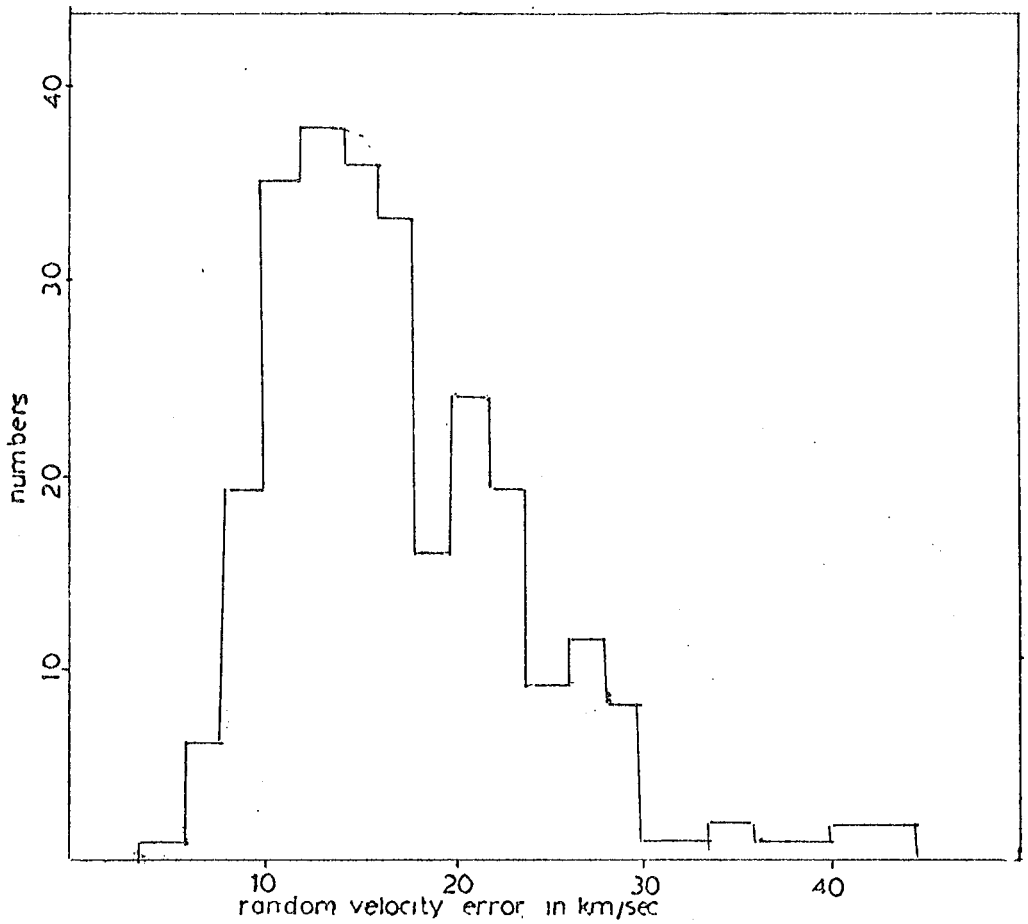

FIGURE 3.6: Distribution of random velocity errors for the high dispersion sample using the calibration in Figure 3.5.

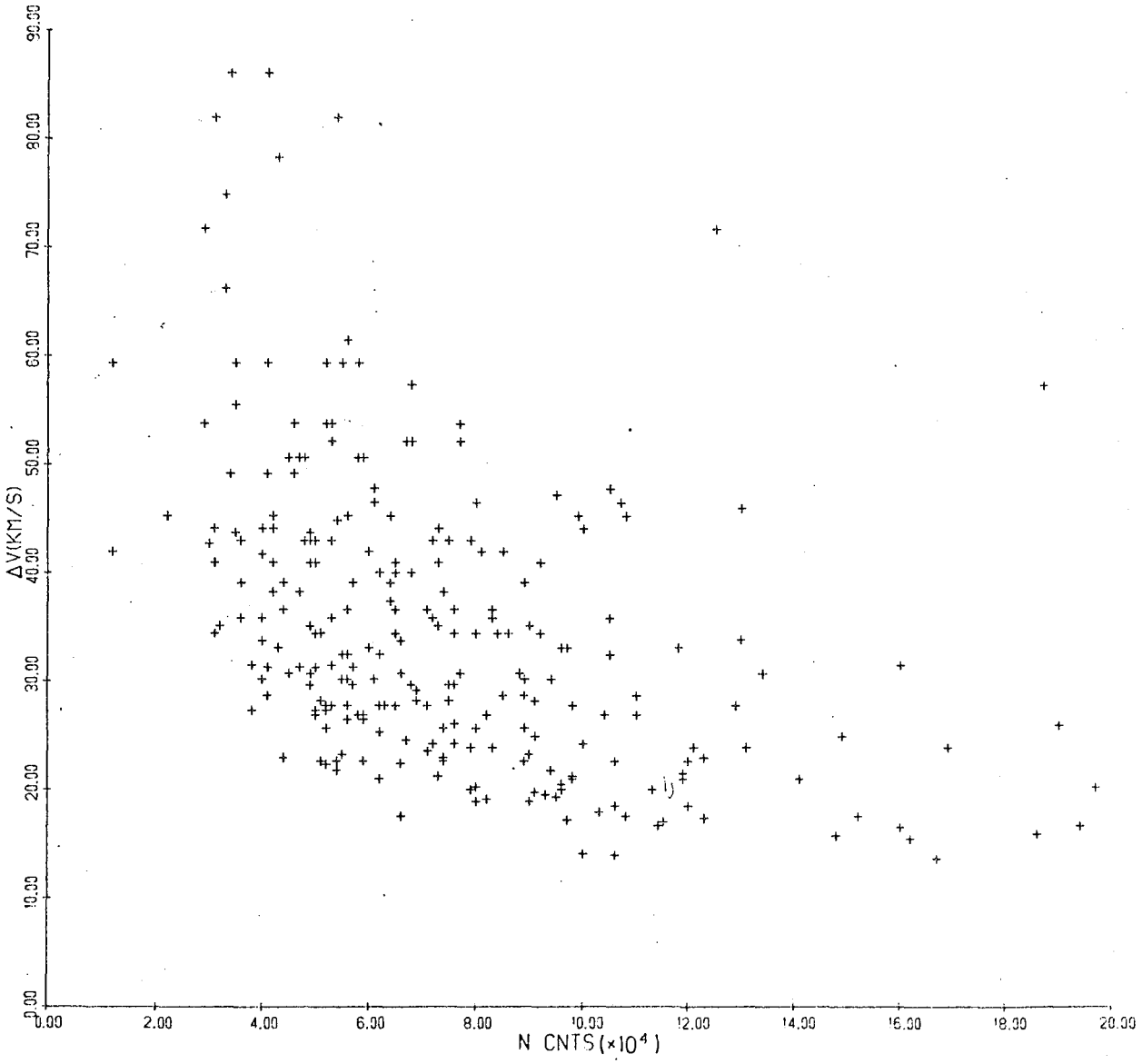

FIGURE 3.7: Scatter plot of random velocity error against spectra photon counts for the high dispersion sample.

Although the overall rms error for the high dispersion sample estimated from eqn 3.2 appears comfortably small, there is some indication that for the occasional poor velocity spectra, the error estimates are too low. In field GNA, for example, there are twelve galaxies (see Table 3.5) that were accidentally measured twice in different observing quarters that can be used to provide a rough alternative estimate of C. Ignoring firstly the three of the galaxies in Table 3.5 which have one or either R ratio $r < 2.5$, we get $\bar{C}$ = 210 km/sec/channel (using eqn 3.2) , in reasonable agreement with eqn 3.3. However, if these three poorer measurements are included, the value of $\bar{C}$ rises to 360 km/sec/channel.

Since even a small proportion of poor velocities could strongly affect the final rms error and compromise the dynamical studies, it is important to consider such galaxies in more detail.

Going through the table of high dispersion redshifts estimated with different templates, 3 6 galaxies were picked out that had general poor agreement between templates. The R ratios for these objects were found to be generally lower than average and in many cases the galaxies were low surface brightness spirals. A clue to the absorption redshift accuracy of these galaxies comes from comparison of the redshifts with the emission line redshifts which (from the high quality data) have rms errors around 100 km/sec. The rms difference between the two redshifts (corrected for the emission line error), for 25 of these galaxies was found to be 250 km/sec. However removing the five most discrepant absorption line objects this was reduced to 130 km/sec ; suggesting in most cases the errors here are comparable to those from the emission line measurements.

In the catalogue at the end of this thesis these galaxies are marked, along with the low dispersion objects, as having errors > 50 km/sec. In the worst cases, where the true correlation peak has obviously been lost by noise peaks, the R ratio has been set to zero and the emission line adopted as the best velocity.

TABLE 3.5: Double Velocity Measurements

Galaxy	Adopted Velocity (V_1)	R Ratio (R_1)	Quarter	Second Velocity (V_2)	R Ratio (R_2)	Quarter	$C\left(\frac{\lvert V_1 - V_2 \rvert \times R_2}{\sqrt{2}}\right)$
GNA002	6793	9.9	80:1	6823	4.7	79:2	120
GNA001	6869	6.5	80:1	6816	3.6	79:2	171
GNA003	3782	9.3	80:1	3740	7.0	79:2	235
GNA005	6752	9.3	80:1	6823	8.4	79:2	467
GNA004	12106	2.8	79:2	12315	2.2	80:1	470
GNA006	14237	4.6	80:1	14122	3.8	79:2	386
GNA008	4454	3.3	79:2	4374	2.8	80:1	213
GNA009	14380	8.3	80:1	14376	5.7	79:2	19
GNA007	14195	3.2	79:2	14469	1.9	80:1	556
GNA010	17859	3.1	80:1	17229	2.2	79:2	1410
GNA011	14411	4.7	79:2	14394	4.3	80:1	75
GNA013	6589	5.1	80:1	6517	3.7	79:2	204

Before leaving this section we still need to consider the errors associated with the galaxies whose spectra were measured at low dispersion in the quarters 80:4 and 81:1. Although working at lower dispersion allowed a larger range of spectral features to be included, the poorer resolution generally led to poorer velocities. For example, repeating the noise experiment on several galaxies measured in 80:4 indicated errors of around 100 km/sec for R ratios in the range $4> R > 3$; these being quite typical R values for galaxies measured in this quarter. Similar values came from comparing redshifts between the two best templates (chosen individually from galaxy to galaxy) in this quarter, the rms difference being 130 km/sec.

Although these absorption velocities are poorer than for the high dispersion sample, the larger wavelength range often allowed additional emission line velocities to be measured. Out of the 46 galaxies taken in 80:4, 9 had multiple emission lines giving several redshift estimates for each galaxy; the overall rms error between the lines being 70 km/sec.

As mentioned in Part 1, in 81:1 21 galaxies were measured at low dispersion using the IDS. Since this detector (unlike the IPCS) had no facility for removing cosmic rays from the spectra, in some cases the latter were severely degraded. Since the noise experiment gave poor results on these galaxies, the only clue to the errors of these velocities came from comparison of the velocities between different templates. For all but four of the worst spectra the rms difference gave 138 km/sec, similar to that found in 80:4 above, using the IPCS.

From the analyses discussed above we can conclude that, for all but around one hundred or so galaxies, the rms error is $\sigma_{err} \sim$ 50 km/sec (including zero point and mismatch error). For the remaining galaxies the figure is larger and more uncertain but apparently lies in the range 100-150 km/sec. This makes the total rms for the whole sample between 70 and 100 km/sec with perhaps the lower figure preferred.

In Chapter 6 we analyse the velocity dispersions between pairs using both the full sample and the smaller sample with $\sigma_{err} \lesssim$ 50 km/sec. Although smaller for statistical studies, the latter allows a welcome check with the results from the full sample.

3.6 SOME PRELIMINARY FEATURES OF THE CATALOGUE

The redshift catalogue in Appendix B gives the velocities, magnitudes and morphological types for the sample galaxies down to the limiting magnitudes for the fields given in Table 3.1. Complete magnitude information also exists to B_J = 17.0 in fields GSA, GSD and GNB, which is to be published in Peterson et al (83) ; however as this data is used only briefly in Chapter 5, it has not been included in the catalogue in this thesis. As noted in Section 5, the velocities quoted refer to representative velocities (V = Cz km/sec) with respect to the sun and which, in the remainder of the thesis, are divided by the assumed Hubble constant of 100 km/sec/MPC to give representative distances in MPCS.

To give a brief 'feel' for the sample before the detailed analyses later, the number magnitude, distance and morphological type distributions are presented in Figs 3.8, 3.9, 3.10.

Figs 3.8 (a-e) shows all the magnitude data to B_J = 17.0 in all five fields separately. The arrow in each case shows the adopted limit for the redshift survey with galaxies without redshifts shown as shaded squares. The histograms for GSF and GNA clearly show the magnitude data is incomplete in these fields beyond the adopted limit.

Although these counts give limited information on the distribution of galaxies in the fields, a much clearer view comes from the redshift counts for the five fields in Figs 3.9 (a-e). Here all galaxies in the survey with distances less than 280 MPCS are shown with the shaded squares corresponding to the galaxies discussed in section 3.5 with velocity errors > 50 km/sec.

The clustering of the sample galaxies on scales of $\sim$ 10 MPC is quite clear from these counts with clusters typically separated by 20 or 30 MPC voids.

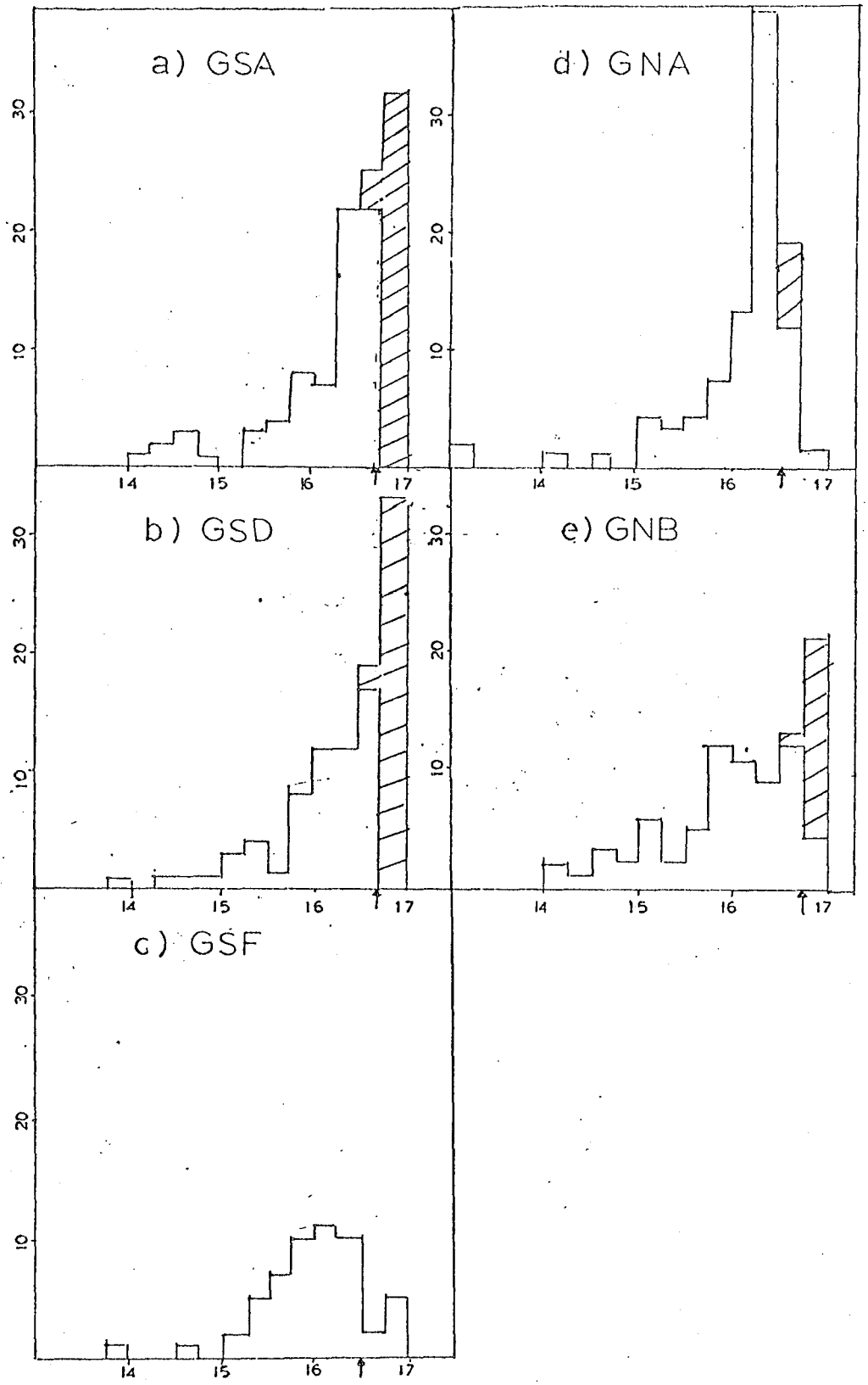

FIGURE 3.8 (a)-(e) : Number magnitude counts for the five AARS fields. The arrow indicates the assumed limit for the redshift data with the hashed boxes corresponding to galaxies without measured velocities

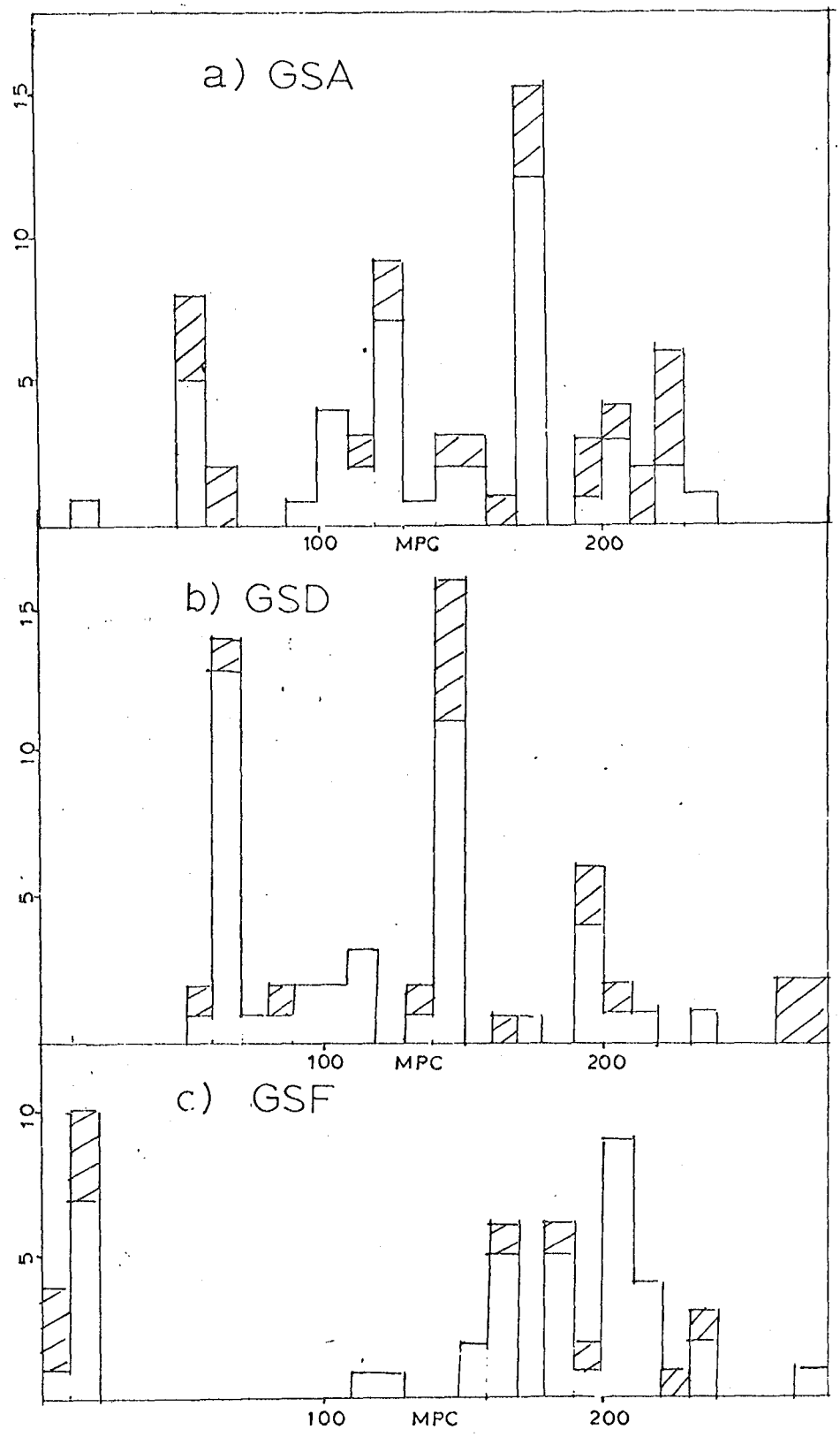

FIGURE 3.9 (a)-(c): Number distance counts for the three southern AARS fields. The hashed boxes refer to velocities with errors greater than 50 km/sec.

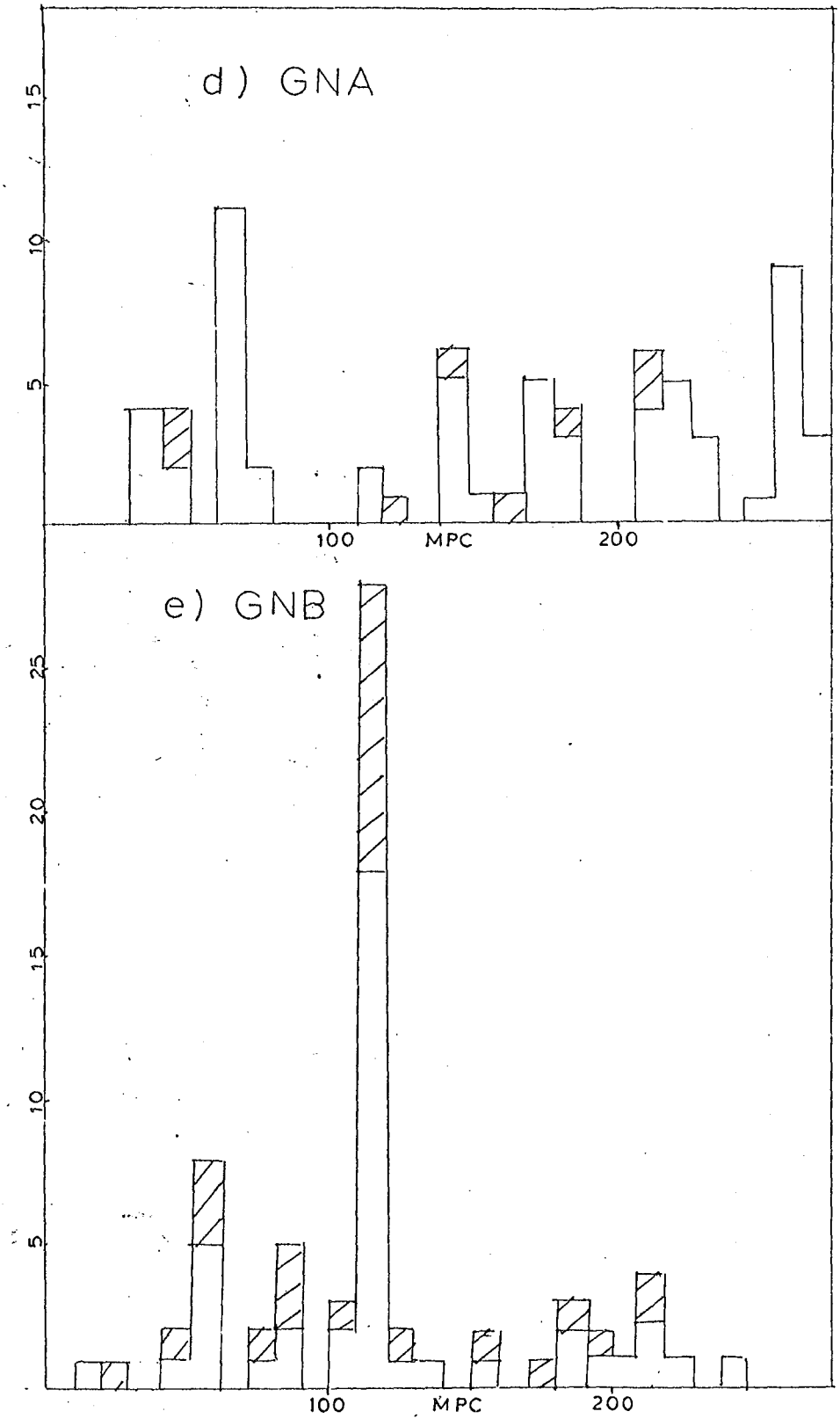

FIGURE 3.9 (d)- (e) Number distance counts for the two norhtern AARS fields. The hashed boxes refer to velocities with errors greater than 50 km/sec.

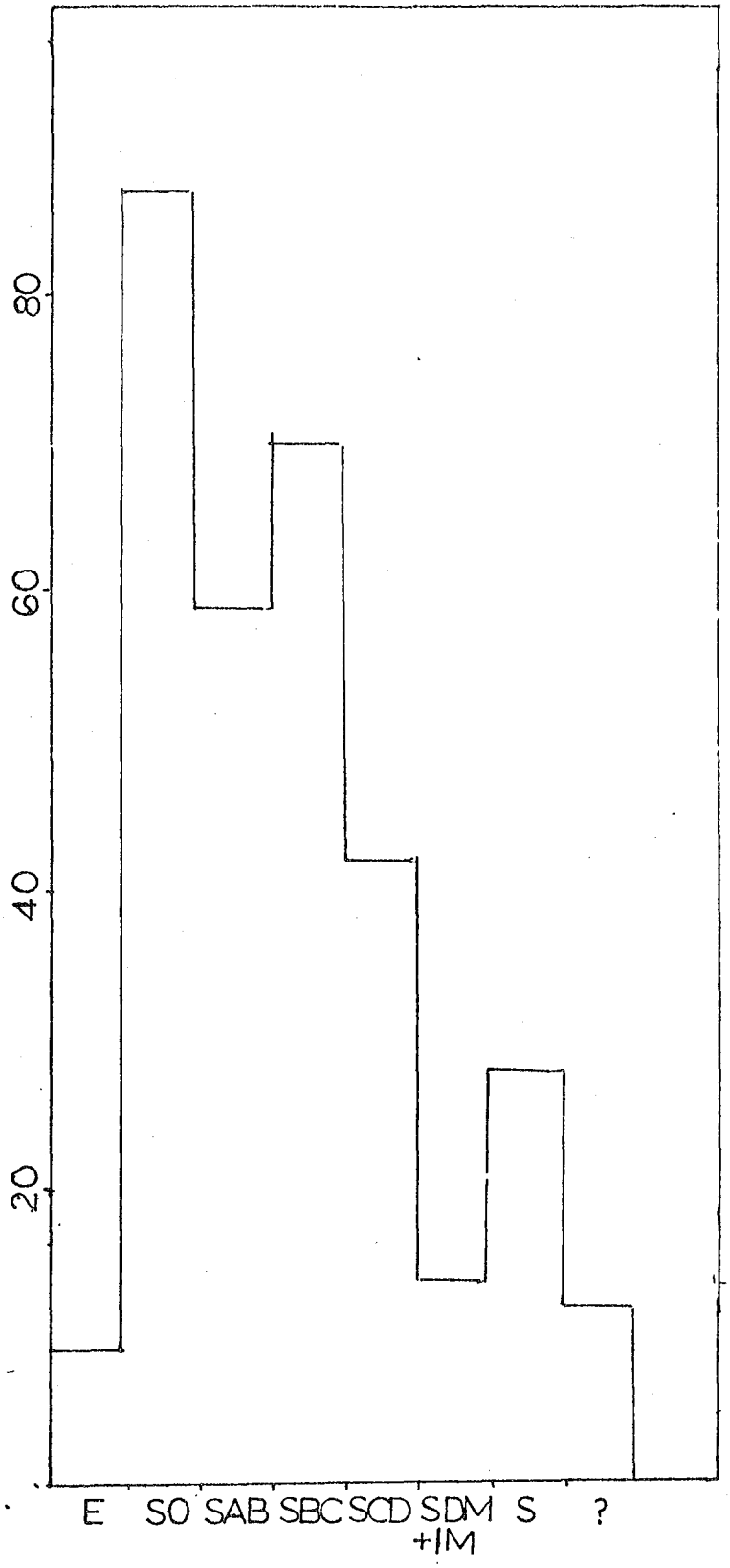

FIGURE 3.10: The distribution of morphological types for the total AARS sample. Column 7 refers to unclassified spirals and peculiar galaxies with column 8 referring to galaxies whose type is uncertain.

In field GSF a prominent void is visible between 20 and 180 MPC which is not seen in any of the two other southern fields. Indeed there is no obvious tendency for inhomogeneities in different fields to appear at the same distance as has recently been found to occur in the north for the KOSS redshift fields in fig 3.1. Finally, it may be noticed that there is some tendency for the apparent richness of clusters to fall off with increasing distance despite the larger volumes sampled. This effect is due to the selection of galaxies by apparent magnitude and vividly demonstrates the extensive range of galaxy luminosities.

Finally, Fig 3.10 shows the distribution of morphological types for the whole survey together. The histogram is split into six basic galaxy types with column seven referring to unclassified spirals or peculiar galaxies and column eight referring to galaxies whose type is uncertain. The general proportion of types in the figure is in reasonable agreement with the proportions found in the KOS survey and by Pence (76) in the Reference catalogue.

Further, more detailed discussion of the number magnitude and redshift counts are given in Chapter 5 where they are, amongst other things, used to judge the fairness of the AARS. The morphological information is used in the next chapter to correct galaxy absolute magnitudes for K dimming in the luminosity function estimates.

3.7 SIMULATIONS OF THE CATALOGUE

In order to test the methods used on the data in the luminosity function and correlation studies in Chapters 4 and 6, it was useful to repeat the analyses on simulated catalogues designed to match the observed sample as closely as possible.

For this purpose the numerical N body simulations of Efsthathiou and Eastwood (81) could have been used, which are both dynamically consistent and have sufficient particles per typical cluster to allow the

compilation of catalogues that appear to roughly match the real universe. While such catalogues have been produced to simulate the CfA survey (Davis et al, 82), to match the finer details of the observed clustering that were needed to test the correlation analysis in Chapter 6 thoroughly, it seemed preferable to set up static simulations.

To compile such a redshift catalogue with spatial two and three point correlation functions similar to observed in the AARS, a clustering hierarchy was laid down in a manner similar to that described in Soneira and Peebles (78) (SP) for projected skies, to which the reader is referred for full details. Briefly, clump centres were first placed randomly in fields of similar dimensions to the AARS and around each was constructed a nine level hierarchy with two sub-clusters per level and a maximum clump radius of 6 MPC. To match the amplitude of the observed clustering, points were removed at random from each clump until only thirty remained in each and to those that lay within the fields an absolute magnitude drawn from a Schecter luminosity function (with $M^{*} = -20.0$ and $\alpha = -1.0$) was assigned. Apparent magnitudes were then estimated assuming a K correction of 3z and particles beyond the limiting magnitude of 16.75 were removed. Finally to those that still remained, a line of sight peculiar velocity was assigned, which was added to the cosmological redshift estimated from the particle's spatial position in the field.

Following this prescription two sets of 36 simulated catalogues were produced, each with five fields and an average of sixty galaxies per field and with number redshift distributions similar to those discussed in Part 6 for the AARS. Although cruder than the simulations of SP, as discussed in Chapter 6, they do reasonably match the amplitudes of both the observed two and three point correlation functions.

To test the methods used to estimate $\langle V^2 \rangle$ in Chapter 6, the peculiar velocities were adjusted so that the catalogues in the first set had on average, $\langle V^2 \rangle^{\frac{1}{2}} = 200$ km/sec and the second set $\langle V^2 \rangle^{\frac{1}{2}} = 500$ km/sec, the

peculiar velocities in each case drawn at random from a velocity distribution function discussed in Chapter 6.5.

Although the discussion above refers specifically to simulations used in Chapter 6, (and discussed further in Chapter 5), forty other catalogues for use in Chapter 4, were compiled in a similar fashion. Since for luminosity function tests less detailed simulations were adequate, no peculiar velocities were assigned in these cases and the number of levels per clump was reduced from nine to six to reduce computational time. Also for these luminosity studies, an 'unclustered' set of forty catalogues was produced, in which 'galaxies' rather than clumps were placed at random in the volumes and an apparent magnitude limited sample formed in a similar fashion.

As noted above, more details of the clustering model is given in SP and in Chapter 5 redshift plots of some of the simulated catalogues are presented, for comparison with the observed fields.

CHAPTER FOUR

THE LUMINOSITY FUNCTION OF GALAXIES

4.1 INTRODUCTION

Fundamental in any attempt to understand the origin of galaxies is the study of the distribution of their luminosities and how this luminosity function (LF) may differ for isolated 'field' galaxies, small groups and rich clusters. Naturally, much attention has been focused on the latter where all that is required for a simple study is the distribution of magnitudes of member galaxies and the mean distance to the cluster. However, as the typical galaxy types here are significantly different from those in more normal environments, there is no reason to suppose that these LFs are representative of the general distribution. Since to measure the LF for the latter one requires a complete redshift sample, naturally most work in this area has come from nearby catalogues that are based on the same data. As we discussed in Chapter 1.4 though, the analyses here is complicated by the presence of large inhomogeneities, non-Hubble velocities, galactic obscuration and possible uncertainties in the magnitude scale. Although the deeper CfA will provide more consistent data these difficulties still apply so other studies from deeper samples are still needed for more definite conclusions to be drawn.

In the next section the LF is estimated for the AARS using three different methods, two of which do not require spatial homogeneity, and which are tested on simulated catalogues. In section 3 the same analyses is applied to the KOS catalogue, the fitted forms from these two surveys compared with other estimates in section 4. The luminosity density is determined in section 5 and the results for the chapter are summarised in the final section where a few applications of the LF are briefly mentioned.

4.2 ANALYSES OF THE AARS

To estimate the luminosity function for the AARS this sample is split into seven parts. In the first we consider a 'basic estimator' in which it is assumed galaxies are distributed homogeneously in the field volumes. A '$\frac{V}{V_{max}}$' test for the sample provides a test for this, which leads on quite naturally in Part 3 to discuss a new 'maximum likelihood estimator' that does not require spatial homogeneity. These results are then fitted to a standard Schecter function and in Part 5 another maximum likelihood method is applied, which can fit the data directly to an analytic form without any binning necessary. Conclusions of the analyses are discussed in the final part after tests on the simulated catalogues are presented.

4.2.1 Basic Estimator (B.E)

The differential luminosity function (LF) is defined as $\phi(M)dM$; the average number of galaxies of absolute magnitude in the range M to M + dM per MPC^{-3}. In principle this is easy to estimate for a fair magnitude limited sample with complete redshift information. Assuming spatial homogeneity one estimates absolute magnitudes for each object using redshifts as distance indicators and then, binning the data in M, one calculates the average distance for each bin that galaxies can be seen to at the limiting magnitude of the survey. Dividing through the number absolute magnitude distribution $dN_0(M)$ by the respective volumes of space V(M) gives the differential luminosity function for the sample. In practice though, apart from the problem of inhomogeneities, there are a number of complications in applying this 'basic' estimator (BE) to the AARS.

(1) The sample is deep enough for K dimming and curvature to be significant.

(2) Since the magnitudes are binned finitely, the volume at which a galaxy can be seen varies considerably over the width of the magnitude bin.

(3) The limiting magnitude m_{lim} varies slightly between fields.

Problem (1) is complicated by the fact that K corrections vary for different galaxy types and the volume corrections in (2) also depends on the morphology of galaxies through the K correction.

To deal with (1) and (2) we may proceed as follows :

We first calculate the absolute magnitude for a given galaxy of apparent magnitude M by the formula

$$M = m - 5.0 \log_{10} \left(\frac{Cz}{H} \right) - 25 - (K + 1.086(1-q_o))z \qquad (4.1)$$

which includes first order K and curvature corrections. This equation is then inverted by a simple iterative procedure to estimate, for this particular galaxy, the redshift z_{max} to which it is visible at m_{lim}.

The corresponding volume V_{max} is given to first order in q_o as

$$V_{max} = \frac{\Omega}{3} \left(C \frac{z_{max}}{H} \right)^3 \left(1 - \frac{3}{2} (1 + q_o) z_{max} \right) \qquad (4.2)$$

where Ω is the solid angle of the field.

The quantity $\frac{1}{V_{max}}$ is then taken as the contribution from that galaxy to the total differential luminosity function in the bin M, M + dM. Since the galaxies in the fields with brighter magnitude limits (point 3) would contribute proportionately more to the luminosity function, because the volumes are smaller, each contribution is weighted by the factor $10^{0.6 m_{lim}}$.

To estimate eqn 4.1 and eqn 4.2 for each galaxy, the following K corrections are adopted from Pence (76) - E/Sϕ : 4.3 and from Ellis (81) - SAB: 3.5 SBC: 2.35 SCD: 1.95 SDM/IM: 1.2. For any remaining galaxies a mean of 3.0 is adopted. The deceleration parameter q_o is highly uncertain but a figure of $q_o = 0.05$ is adopted, which with $\Lambda = 0$ corresponds to $\Omega = 0.1$; perhaps the most popular value in recent years, (e.g. Gott and Turner, 76).

Fig. 4.1 shows the estimates of $\phi(M)$ (in bins of 0.2 in M) as filled circles. The histogram at the foot of the figure shows the observed counts $dN_o(M)$ that contribute to $\phi(M)$. Galaxies fainter than around -17.0 are not shown because both $dN_o(M)$ and V_{max} are small here making $\phi(M)$ unstable. At bright magnitudes $\phi(M)$ falls off sharply apart from two very bright objects (not shown) with $M < -22.0$. Schecter (76) has noted in rich clusters that such discrepant objects are often massive CD galaxies that may deviate from the general distribution because of dynamical processes acting in clusters (Ostriker and Tremaine, 76). In our case one of the galaxies (GSF$\phi\phi$5 with M = -22.5) is an SC with a peculiar arm and the other (GSA$\phi\phi$4 with M = -23.7) is an Sϕ which, from visual examination, looks suspiciously small for its apparent magnitude of 14.41. Both are ignored in the subsequent analyses in this section.

Finally, Fig 4.2 shows $\phi(M)$ estimated separately from the two fields in the north and three fields in the south (shown as filled squares and circles respectively). We see the agreement between the two subsamples is surprisingly good, especially at bright magnitudes.

The other estimates on this figure and Figure 4.1 are discussed in part 3.

4.2.2 The $\frac{V}{V_{max}}$ Test

The $\frac{V}{V_{max}}$ test has been discussed by several authors (e.g. Schmidt,68) and provides an elegant alternative to the number magnitude counts to test a redshift sample for sampling fluctuations due to inhomogeneities or test for possible observational errors in the catalogue.

Defining V as the volume enclosed by a given galaxy at redshift z and z_{max} as before (eqns. 4.1 and 4.2), the mean $\frac{V}{V_{max}}$ can be estimated for the AARS and compared to the value of 0.5 expected if galaxies are homogeneously distributed.

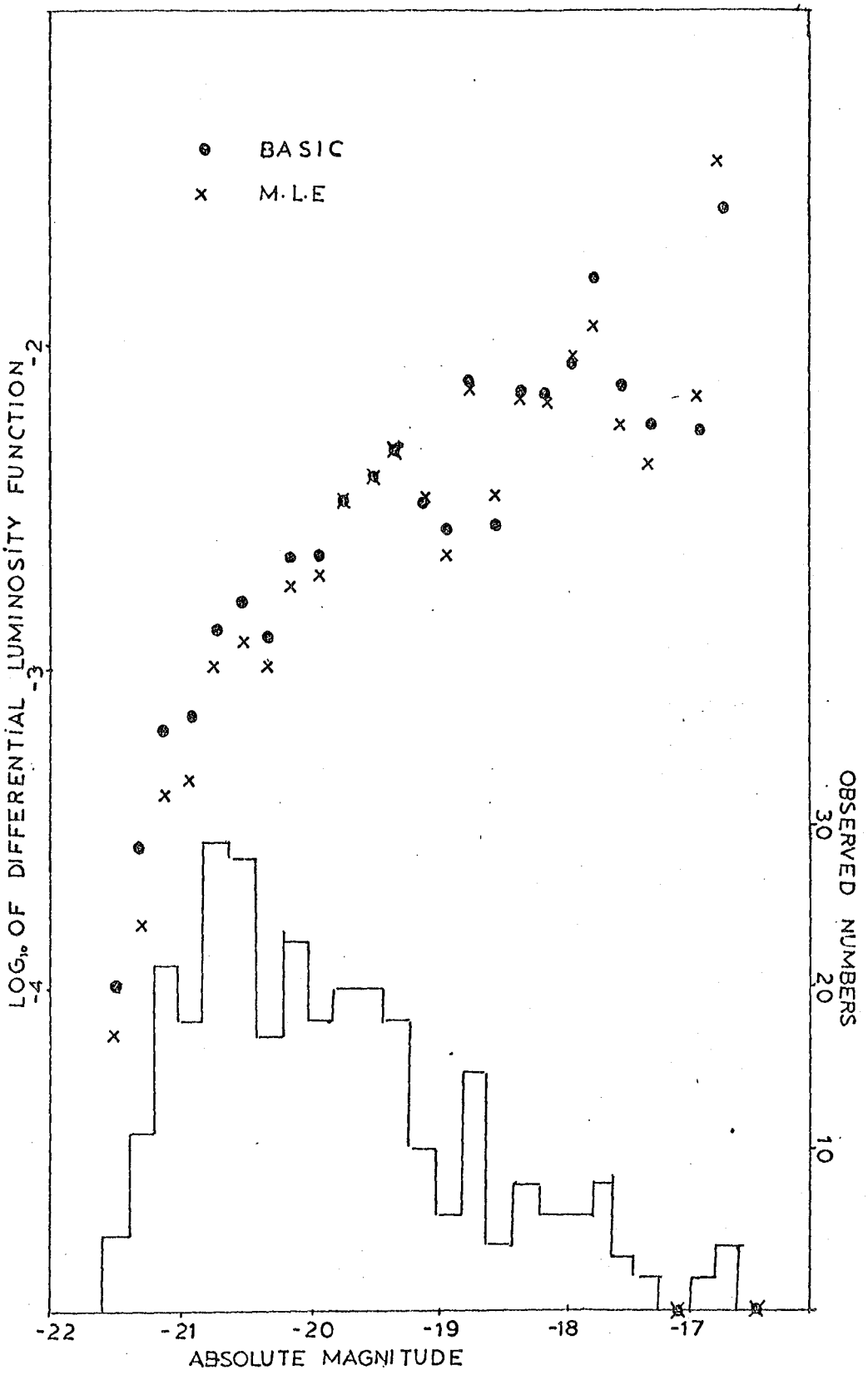

FIGURE 4.1: The two binned estimates of the luminosity function for the AARS. The solid histogram (with the scale to the right) refers to the observed numbers contributing to the estimates as a function of absolute magnitude.

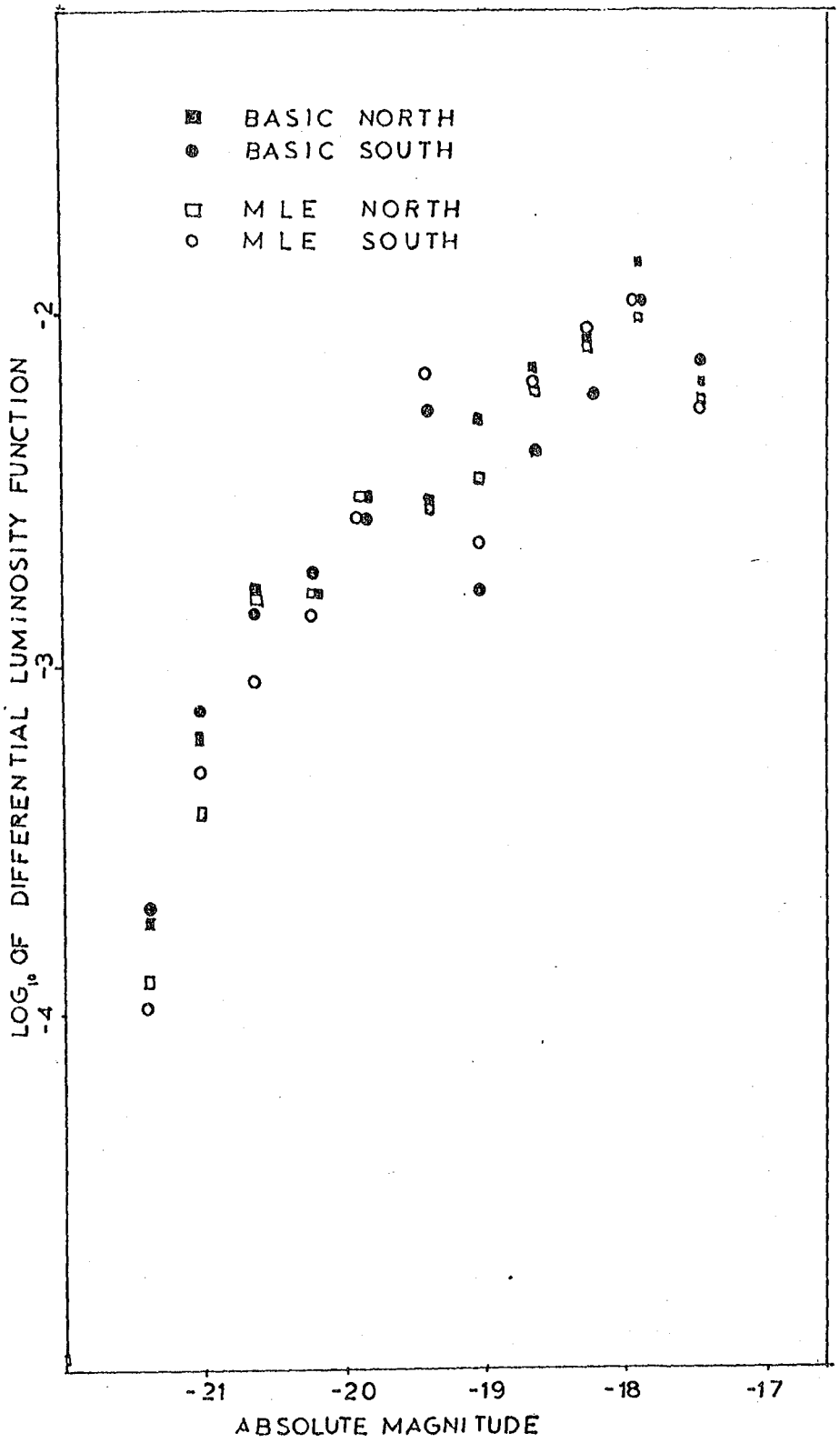

FIGURE 4.2: The luminosity function for the northern and southern AARS subsamples using the two estimators used for the total sample in Figure 4.1.

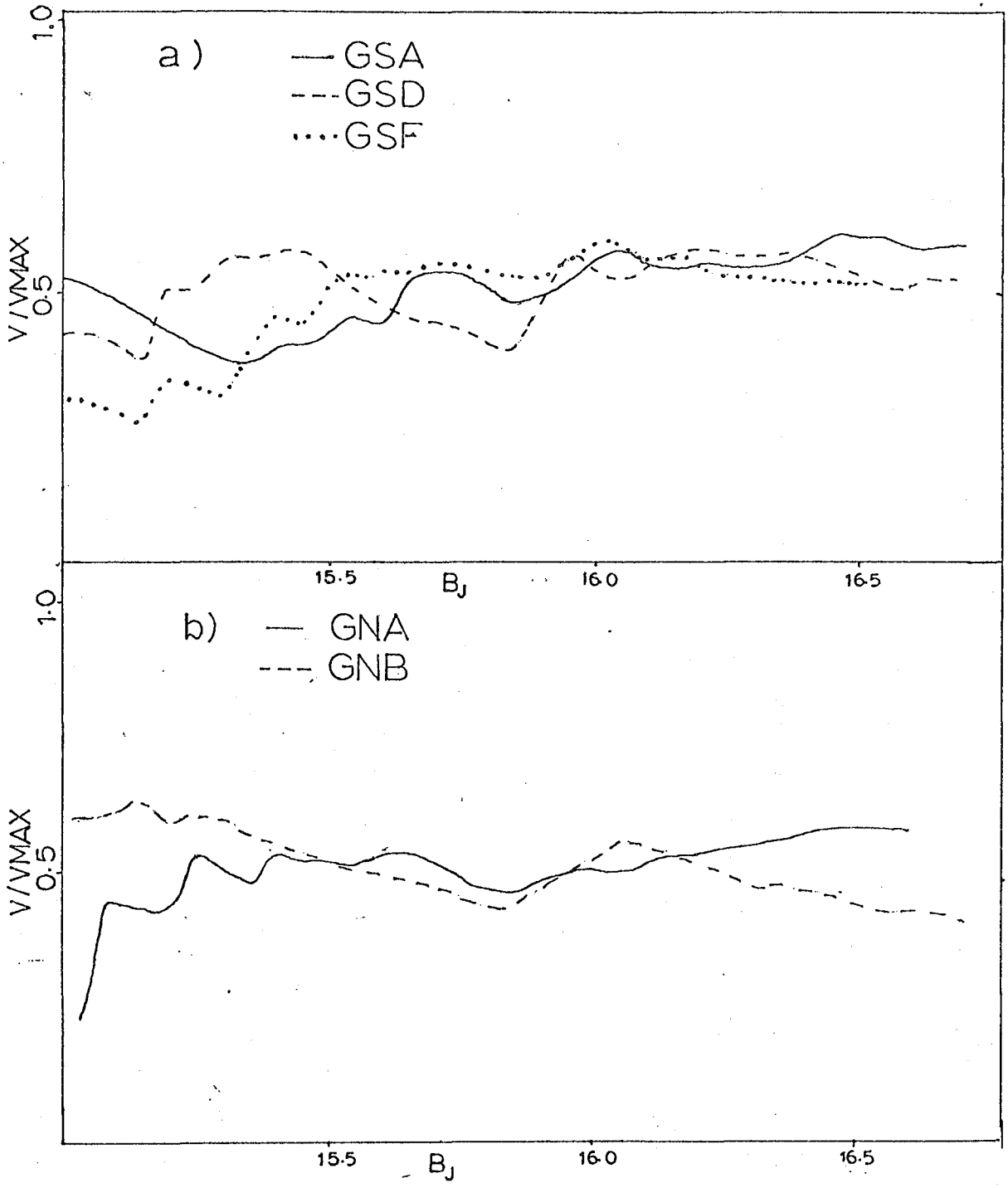

FIGURE 4.3: Figure (a) shows the mean $\frac{V}{VMAX}$ as a function of limiting magnitude for the three southern AARS fields separately. Figure (b) shows the corresponding estimates for the two northern fields.

Figures 4.3a, and b show the mean $\frac{V}{V_{max}}$ for each of the three southern and two northern fields separately as a function of limiting magnitude.

We see that four of the five fields at $B_J > 16.0$ have $\frac{V}{V_{max}}$, systematically > 0.5, the total for the sample being 0.53 at the limiting magnitude ; all rather larger than the expected value of 0.5. However, similar deviations have recently been found in the larger CfA catalogue where Davis and Huchra (82) find $\frac{V}{V_{max}} \simeq 0.55$ from galaxies in the north and $\frac{V}{V_{max}}$ in the south.

As a test for the expected fluctuations due to clustering, the set of 40 clustered simulated catalogues discussed in Chapter 3.7 were analysed in the same manner as the data, the mean and standard deviations being $\frac{\bar{V}}{V_{max}} = 0.5 \pm 0.05$.

Although the simulations suggest the observed $\frac{V}{V_{max}}$ results from the AARS is not unreasonable, we still need to consider the possibility that observational errors in the catalogue are responsible for the systematically high values of $\frac{V}{V_{max}}$ seen in four of the fields. One possibility is that random errors in the magnitudes at the limiting magnitude tend to bring in faint galaxies into the survey, these objects having high $\frac{V}{V_{max}}$. However, for this to be responsible for the observed effect the random errors would have to be much larger than implied from the discussion in Chapter 3.4. Similarly, the most plausible systematic errors such as incompleteness at the limit or an isophotal effect at faint magnitudes would tend to lower $\frac{V}{V_{max}}$, since the fainter galaxies with high $\frac{V}{V_{max}}$ would tend to be missed.

The remaining possibility is that the K corrections have been substantially over-estimated or else are partly cancelled by luminosity evolution. Some evidence for this may come from the $\frac{V}{V_{max}}$ estimates for around the hundred E and Sϕ galaxies whose mean is 0.57, suggesting these galaxies were brighter in the past. However, larger samples are necessary

to test whether this result is significant or not.

Some evidence, though, that such effects are not significantly responsible for the high $\frac{V}{V_{max}}$ estimates for the total sample comes from the fact that the values of $\frac{V}{V_{max}}$ in Figs 4.3a and 4.3b are high at $B_J = 16.0$ where K corrections etc. have much less influence. Also the effect of raising q_o (as might be the case if $\Omega \sim 1$) would tend to cancel an over-estimate of K corrections or under-estimate of evolutionary effects.

Thus, for the present, we may conclude the $\frac{V}{V_{max}}$ test probably indicates some evidence for slight departures from overall homogeneity in the AARS that may affect the LF estimate in Part 1 above.

4.2.3 Maximum Likelihood Estimator (MLE)

The redshift histograms presented in Chapter 3.6 for the AARS fields provide strong evidence for the clustering of galaxies at small scales. Evidence for slight departures from homogeneity at larger scales come from the systematically high estimates of $\frac{V}{V_{max}}$ found for the sample in Part 2. As KOS (79) point out, if homogeneity is assumed in the estimate of the luminosity function, the presence of clustering will distort its true shape, especially at the faint end, because faint galaxies are only visible in small volumes where the fluctuations from homogeneity are larger. To allow for this and dropping the absolute normalisation of the luminosity function, these authors considered a method that can still determine the overall shape of the function in the presence of inhomogeneities.

Below is discussed a variant of this method suggested to the author by P.J.E.Peebles.

Galaxies in the sample are binned into a fine two dimensional mesh n_{ij} in absolute magnitude i and redshift J. The mean number of galaxies $\bar{n}$ expected in a given bin is $\langle n_{ij} \rangle = \phi_i \rho_j$, where ϕ_i is the differential LF and ρ_j is the absolute number density of galaxies at that redshift bin multiplied by the appropriate volume element across the field.

From poisson statistics we get the probability of seeing the observed number n_{ij} in a bin as $P_n^{\bar{n}} = \bar{n}^{\,n} \frac{e^{-\bar{n}}}{n!}$.

Multiplying the probabilities from all the bins together one can form a likelihood function

$$\mathcal{L} = \prod_{iJ} (\bar{n}_{iJ})^{n_{iJ}} \frac{e^{-\bar{n}_{iJ}}}{n_{iJ}!}$$

Taking the natural logarithm $L = \ln \mathcal{L}$ and maximising $: 0 = \frac{1}{\mathcal{L}} \frac{\partial L}{\partial \phi} = \frac{1}{\mathcal{L}} \frac{\partial L}{\partial \rho_s}$

gives two equations

$$\rho_J = \sum_{i}^{n_i} \left(\frac{n_{iJ}}{\sum_{i}^{n_i} \phi_i} \right) \tag{4.3}$$

and

$$\phi_i = \sum_{J}^{n_J} \left(\frac{n_{iJ}}{\sum_{j}^{n_J} \rho_J} \right) \tag{4.4}$$

where the sums n_i and n_J (because of the selection of galaxies by apparent magnitude) are functions of J and i respectively.

To solve for ϕ_i one puts in a trial function ϕ_{io} in eqn. 4.3 and estimates ρ_{JO}, which is then inserted in eqn. 4.4 to get the first solution ϕ_{il} ; the iteration continuing until a stable solution is found.

This method can be understood by thinking of ρ_{JO} as the first estimate of the absolute mass within a redshift bin which tries to allow for inhomogeneities in the next estimate of ϕ_i, the procedure continuing until a consistent balance is reached. Alternatively for a given redshift bin J, n_{iJ} can be considered as the LF of a group at that redshift which is

then ensembled with all the other LFs in an optimal way (Turner and Gott, 76) ; taking into account the variation in magnitude range at different redshifts.

To estimate ϕ_i for the AARS by eqns. 4.3 and 4.4 we still have problems 1-3 discussed in Part 1.

To reduce the effect of (2), small 0.1 bins in M are considered with the redshift bins chosen to correspond to the distances at which the various magnitude bins are complete to (i.e. a one to one correspondence). To estimate the magnitudes and completeness distances eqn. 4.1 is used, however as the volumes are not specifically calculated eqn. 4.2 is not required.

Since the K corrections vary from type to type and the field limits also vary one ends up with different arrays in i and J for different morphological types and fields. Although the J bins in the respective arrays correspond to different distances, provided the limits n_i and n_J are chosen to agree, one can combine them to solve for ϕ_i for the total sample. The only assumptions here are that the forms of the LF and clustering properties are identical for different galaxy types (both of which are not true in detail).

Once the total matrix n_{iJ} is calculated, the estimate ϕ_{iO} from the basic method in Part 1 is used to start the iteration in eqns. 4.3 and 4.4, which converges to give ϕ_i in four or five cycles. Putting in very different starting forms ϕ_{iO} give exactly the same results suggesting the iteration procedure is quite stable.

The results for ϕ_i binned in 0.2 magnitude intervals are plotted as crosses in Fig 4.1. For comparison with the basic method, the normalisation (which is arbitrary here) has been adjusted so the results agree around -19.5, where the LF is probably best defined.

We see that, although both agree fairly well, there is some systematic disagreement especially at the bright end where it may be expected the agree-

ment should be at its best. One possible reason for the discrepancy is that, although the iteration itself is stable when ϕ_i is small, ρ_J at large distances may become unstable, making the bright end of ϕ_i uncertain. On the otherhand the $\frac{V}{V_{max}}$ studies in Part 2 suggest that at small redshifts the sample might be slightly underdense relative to the deeper volumes* so that we might expect the basic estimator would overestimate the proportion of bright galaxies to faint, as appears to be the case here. This suggests the MLE gives a more reliable estimate of the LF than the BE.

The results for the north and south subsamples (open squares and circles respectively) are shown in Fig 4.2. As with the full sample we see some systematic deviations between the estimators at bright magnitudes. Comparison with the two MLE estimates, though are in good agreement at these magnitudes.

Finally, before going on to fit the two estimates in Fig 4.1 with functional forms, it is interesting to compare this MLE with the algorithm discussed by KOS (79). These authors compared the ratio of the number of galaxies dN in an interval dM with the total number of galaxies brighter than M ($N \lesssim M$) within the volume that M is visible to. The ratio is

$$\frac{dN}{(N \lesssim M)} = d\ (\ell n\ \Psi\ (M)\ )\ ;\ \text{i.e. the derivative of the logarithm}$$

of the integral LF. Since at faint M the volumes are small and at bright M the numbers brighter become small, the results are likely to be more unstable at either end than the MLE which makes better use of the data, using all galaxies within all volumes to provide information on the shape of the LF at a given M.

---

* In the next chapter we discuss the density fluctuations ρ_J in the sample together with the number redshift distributions in more detail.

4.2.4 Fitting to the Binned Estimates

It has been customary to represent observed LFs by analytic forms both for comparison purposes and applications in various branches of cosmology. Abell (62) considered fitting cluster integral LFs by a two powerlaw model that joined at M_A^*, the differential form thus having a sharp 'spike' at M_A^* that may actually be a real feature in $\phi(M)$ in some clusters. More recently Schecter (76) has fitted a smoother form both in clusters and the 'field' that he claims give a fairly good representation to both.

The usual differential Schecter form is given in terms of luminosities

$$\phi_s\left(\frac{L}{L^*}\right) d\left(\frac{L}{L^*}\right) = \phi^* e^{-\frac{L}{L^*}} \left(\frac{L}{L^*}\right)^{\alpha} d\left(\frac{L}{L^*}\right) \qquad (4.5)$$

In terms of magnitudes this is

$$\phi_s(M)dM = \phi^*(0.4\ \ln 10)\left(\frac{L}{L^*}\right)^{\alpha+1} e^{-\frac{L}{L^*}} dM \qquad (4.6)$$

where $\frac{L}{L^*} = 10^{0.4(M^* - M)}$.

As with the Abell form this function involves a characteristic magnitude M^* and at faint magnitudes corresponds to a powerlaw slope, however at bright magnitudes the fall off is exponential rather than powerlaw. Also the two slopes, unlike the Abell function, cannot be fixed separately but are adjusted to fit through ϕ^*, M^* and α. As these parameters are highly correlated it is important to understand the errors associated with any best fit.

Since in an apparent magnitude limited sample the observed numbers contributing to $\phi(M)$ are the number magnitude counts $dN_o(M)$ it seems

reasonable to fit these rather than the volume corrected function $\phi(M)$. This procedure was followed by Schecter (76) to fit a nearby survey of field galaxies. Calculating $dN_o(M)$ for the sample he fitted

$$dN_F(M) = \phi_s(M)\, V_F(M)\, dM \qquad (4.7)$$

where $\phi_s(M)$ is eqn.4.5 and $V_F(M)$ is the analytic form of the mean volume correction for a given M. Since Schecter was using large bin sizes (dM = 1) he then corrected $V_F(M)$ by a factor calculated from its second derivative with M. As discussed in Part 1, the problem here is that V(M) itself varies over a finite bin in M and in the AARS this depends on q_o and K corrections that depend on galaxy morphology. Since the correction to $V_F(M)$ involves a second derivative of $V(M, q_o, K)$, an easier approach is adopted.

The two estimates of ϕ (M) in Fig 4.1 are divided through by the observed solid histogram $dN_o(M)$, to give what is a smooth estimate of V(M) for each in which is contained the mix of types etc. The functions are then used in eqn. 4.7 with eqn. 4.6 (ignoring the correction for bin size), the best fitting α and M^* (and ϕ^*), for each estimate of ϕ (M) being then calculated by minimising the quantity

$$\psi^2 = \sum_i \frac{(dN_{oi} - dN_{Fi})^2}{\sigma_i^2} \qquad (4.8)$$

The errors here are assumed to be poisson so that $\sigma_i^2 = dN_{Fi}$, which seems reasonable under the assumption of spatial homogeneity. While in the case of the MLE the points in the estimate of $\phi(M)$ arenot independent, since most of the noise probably comes from the observed counts $dN_o(M)$ (which should be independent), this weighting scheme may not be a bad approximation.

The results are shown in Fig 4.4 which shows the two estimates and fits with the filled circles and solid line corresponding to the BE and the crosses and dashed curve to the MLE. The bins in M here are 0.4 to ensure sufficient counts ($n \gtrsim 5$) for the ψ^2_{min} fits, which have been calculated between $-22 < M < -17.2$.

Changing the bin size makes little difference to the best fits which are $M^* = -20.34$, $\alpha = -1.26$ for the basic and -20.02, $\alpha = -1.18$ for the MLE.

In order to calculate the errors and illustrate the interdependence of parameter estimates, the quantity $\Delta S^2 = \psi^2 - \psi^2_{min}$ has been calculated in α and M^* space around the best fitting values above. As Lampton et al (76) discuss, ΔS^2 can be used to estimate errors for nonlinear fits with highly correlated parameters. In this case if we perturb one of the parameters α, M^* and ϕ^* away from its ψ^2_{min} value, ΔS^2 is distributed like a ψ^2 with three degrees of freedom.

Taking $\Delta S^2 = \psi^2_3 (1\sigma) = 3.5$, Fig 4.5 shows what should be a reasonable approximation to the one sigma error contour in M^*, α space for both the BE (solid contour) and the MLE (dashed contour). The best fitting values are shown as a filled circle and a cross respectively. The 1σ errors $d M^*_{int}$ and $d\alpha_{int}$ for M^* and α from Fig 4.5 are in Table 4.1 along with the best fitting parameters above for the two estimators. Also shown are the best fitting values of M^* for the north and south subsamples in Fig. 4.2 with α constrained to be -1.0.

In Part 6 we check these error estimates are reasonable using simulated catalogues. Discussion of Fig 4.5 and Table 4.1 is postponed until after discussing the final estimator, plotted as the dotted contour on Fig. 4.5.

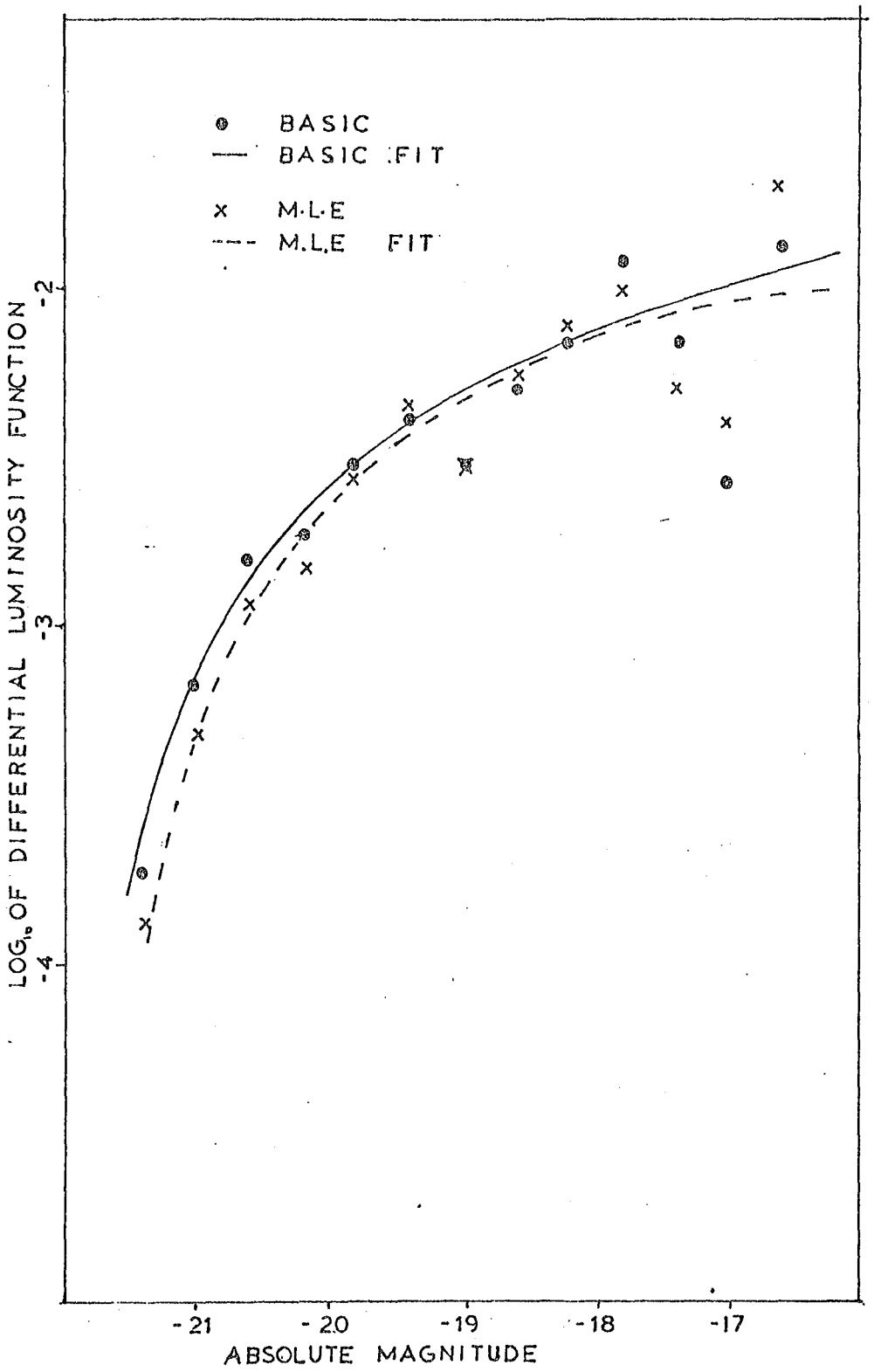

FIGURE 4.4: The two binned estimates of the luminosity function for the AARS along with corresponding Schecter fits.

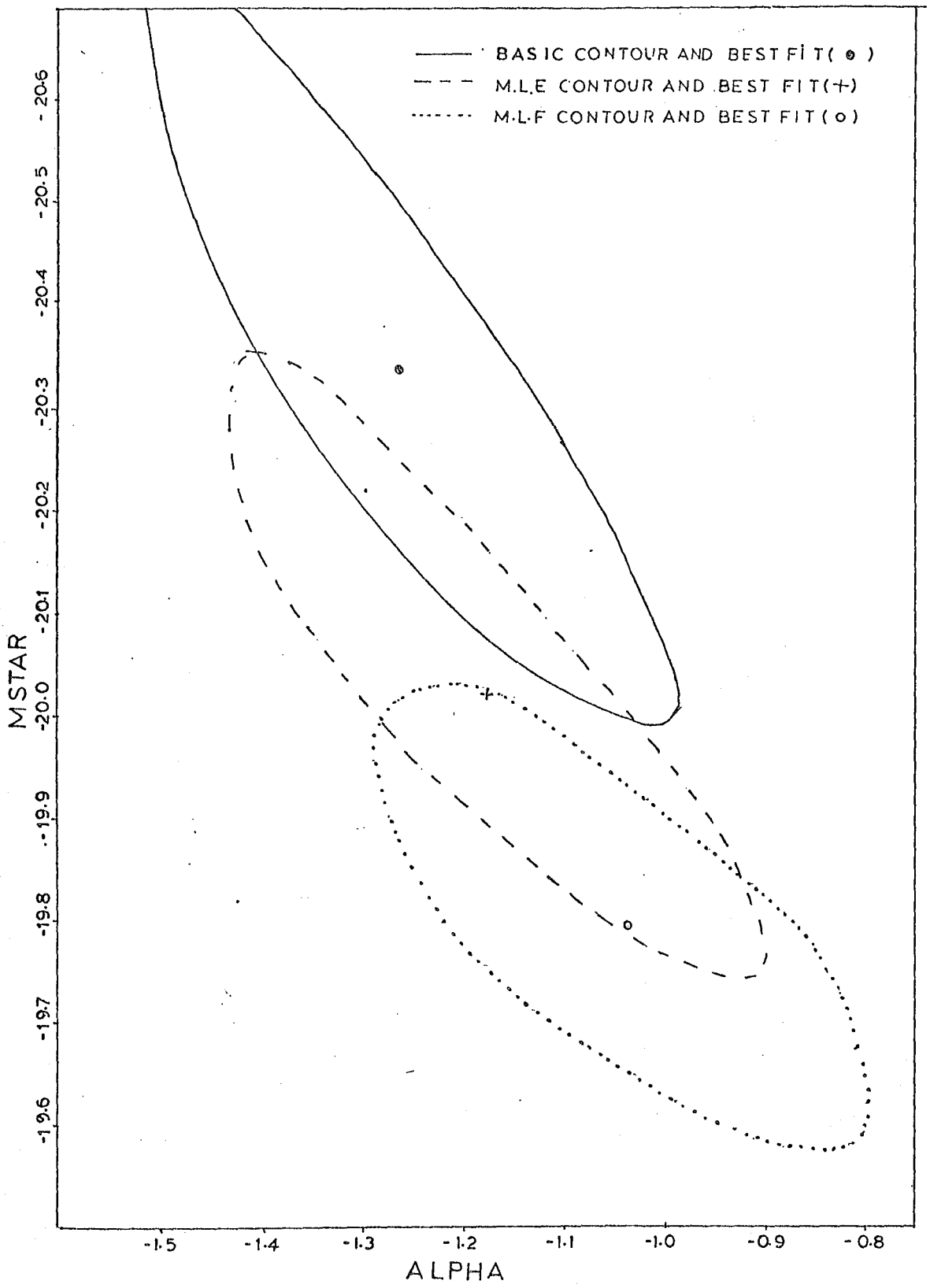

FIGURE 4.5: One sigma contours for the three Schecter fits of the total AARS luminosity function estimates.

TABLE 4.1: AARS Schecter Fits

Method	$-M^*$	$-\alpha$	dM^*_{int}	$d\alpha_{int}$	$-M^*(\alpha=-1.0)$	P(%)	$-M^*$ North $\alpha=-1.0$	$-M^*$ South $\alpha=-1.0$
BE	20.34	1.26	0.18	0.12	20.03	40	19.94	20.08
MLE	20.02	1.18	0.13	0.12	19.86	80	19.90	19.78
MLF	19.78	1.04	0.14	0.17	19.74	96	19.76	19.76

4.2.5 Maximum Likelihood Fitting Method (MLF)

At this point we consider another maximum likelihood method discussed by Sandage et al (79) that can be used to provide a further estimate of M^* and α for the sample without the need for binning the data or the requirement of spatial homogeneity. Like the MLE, though it does assume the LF, clustering and morphology of galaxies are uncorrelated.

Assuming galaxies are drawn from a Schecter LF, $\phi_s(M)$ one can ask what is the probability P_i that a particular galaxy i at redshift z_i has on absolute magnitude M. One can write this probability as

$$P_i \propto \frac{\phi_s(M_i)}{\int_{-\infty}^{M_i(z_i)} \phi_s(M)\, dM}$$

where M_i is the observed absolute magnitude and $M(z_i)$ is the faintest absolute magnitude visible at z_i at m_{lim}. Multiplying the probabilities, as in the MLE in Part 3, but over all galaxies, we can construct a likelihood function $\mathcal{L} = \prod_i P_i$.

Taking the natural log we get $\ln \mathcal{L} = \sum_i \ln (P_i)$

$$= \sum_i (\alpha + 1) \ln L_i - \sum_i L_i - \sum_i \ln \Gamma(\alpha + 1, 10^{0.4(M^* - M(z_i))})$$

where $L_i = 10^{0.4(M^* - M_i)}$

The objective here is to find the value for α and M^* for which $\ln \mathcal{L}$ is a maximum.

To apply to the AARS M_i and $M(z_i)$ have been calculated from eqn.4.1 which, maximising for galaxies between $-22 < M < -17$ gives the best Schecter parameters $M^* = -19.78$, $\alpha = -1.04$.

Following Lampton et al (76) again, the quantity $\Delta L = \ln \mathcal{L}_{max} - \ln \mathcal{L}$ for n free parameters should be distributed like a ψ^2 with n degrees of

freedom such that $\Delta L = \frac{1}{2}\psi^2_n(\beta)$, where β is the confidence level. Since in this case there are two degrees of freedom the one sigma error is given by $\Delta L = \frac{1}{2}\psi^2_2(1\sigma) = 1.15$. The errors from this are in Table 4.1 (along with α and M^*) and plotted as the remaining contour (dotted) in Fig 4.5 with the best fits shown as an open circle. Also in Table 4.1 are the results of M^* with $\alpha = -1.0$ for the northern and southern subsamples using the MLF method.

4.2.6 Numerical Simulation Tests

In order to test the three estimators and to test the internal errors from each, the analyses have been repeated on simulated catalogues in which the real input parameters are known. To do this two sets of simulations described in Chapter 3.7 were used, each set consisting of 40 catalogues. In the first set the galaxies were homogeneously distributed. and in the second, clustered about as strongly as seen in the data. The first set were designed to test the effects of poisson noise on the methods and the second to test if the MLE and MLF really have any advantages for samples with clustering properties like the AARS.

Table 4.2 shows the mean and standard deviations of M^* and α for the basic and MLE for the two sets of simulations. Bins in 0.4 M were used and like the data the results were not sensitive to this choice. Also shown are the mean errors $d M^*_{int}$ and $d\alpha_{int}$ calculated individually from each simulation in the same way as the internal error estimates for the data.

We see from this table that these latter errors are roughly half that from the standard deviations dM^* and $d\alpha$ suggesting the internal errors are underestimates of the true errors. We also see for the first set, the basic estimator gives an unbiased estimate of M^* and α with smaller errors than the MLE. For the clustered set the MLE gives smaller errors, however, in both sets this estimator seems to give slightly bright values of M^*.

TABLE 4.2: Simulation Schecter Fits

Set	Method	$-\bar{M}^*$	$-\bar{\alpha}$	$d\bar{M}^*$	$d\bar{\alpha}$	$\overline{d\bar{M}^*}_{int}$	$\overline{d\bar{\alpha}}_{int}$
Unclustered Simulations	BE	20.02	1.01	0.18	0.18	0.08	0.14
	MLE	20.10	0.97	0.25	0.22	0.09	0.14
	MLF(M^*_{input}=-19.9)	19.91	1.01	0.16	0.16	-	-
Clustered Simulations	BE	20.05	0.99	0.27	0.30	0.08	0.13
	MLE	20.15	1.01	0.26	0.23	0.09	0.13
	MLF(M^*_{input}=-19.9)	19.89	0.98	0.14	0.17	-	-

Efsthathiou (see Efsthathiou et al, 83) has also used similar simulations to test the MLF. From 40 clustered catalogues he finds the method gives an unbiased estimate of M^* and α with $dM^* = 0.14$ and $d\alpha = 0.17$, smaller than those from the BE and MLE and in agreement with the internal error estimates from the data. We may expect the method to give low errors since the data does not require binning and the form fitted is known to have the functional form assigned to the simulations.

4.2.7 Discussion of the Results

Having considered the three different estimators of the LF for the AARS and tested the methods on simulated catalogues we are now in the position to compare the estimates more fully and decide which is the most reliable.

Turning back to examine fig 4.5 we see that each of the three contours from the three estimators are elongated at roughly 45^o in the M^*, α plane showing that M^* and α are highly correlated. Although the MLE and MLF best fits just lie within each other 1σ contour, both differ considerably from the BE. To compare the estimators more closely and because M^* and are so correlated, α has been constrained to be $\alpha = -1.0$ and the best fitting M^* found from the M^*, α array of ψ^2 values for each method. These are in Table 4.1 under the column $M^* \alpha = -1.0$, along with the confidence level (P) on the transformed M^* away from the best fit for each method.

It might be noted at this point that the slope of the contours in fig 4.5 means the change in $M^*_{\alpha = -1.0}$ from the best fitting M^* is almost identical to the change in α suggesting a simple rule of thumb transform ;

$$M^*_{\alpha = -1.0} = M^* - (\alpha + 1) \qquad (4.9)$$

Although this is used in section 4 to compare the LFs between samples, for transforms in α as large as for the BE, it appears to work only moderately well.

From Table 4.1 we see the MLE gives an $M^*_{\alpha=-1.0}$ some 0.1 magnitudes brighter than for the MLF whereas for the BE the difference rises to 0.3. As noted in Part 3 this discrepancy with the BE can apparently be explained quite naturally by the slight relative abundance of (bright) galaxies in the AARS fields at large redshifts.

Turning to the results in Part 6 we saw that of the three methods, the MLF gives the most reliable estimate of M^* and α (with the smallest errors) in simulated catalogues clustered about as strongly as the AARS. One potential source of worry in this method though for the real data is its sensitivity to the steep bright end slope of the LF. If the bright galaxies in the AARS do not fit a schecter function the whole fit may be upset even though it overall fits the data well. While the goodness of fit cannot be tested for this method, the MLE allows an examination of the binned form, unbiased by inhomogeneities, and we see from fig 4.4 the fit to a schecter form is good at both bright and faint magnitudes. Thus, in this way, the MLE and MLF are a good compliment to each other.

From this discussion it seems reasonable to take the MLF as the most reliable estimate of M^* and α for the AARS which for simplicity is taken to be

$$\alpha = 1.0 \quad M^* = -19.75 \pm 0.17 \tag{4.10}$$

Although this M^* is fainter than the MLE by 0.1 the simulations suggest the fit to the latter estimator is biased to bright magnitudes by about this factor. Similarly the 0.3 difference between the MLF and BE is about the same as the 1 σ error calculated from the simulations for the latter. As concluded in Part 2, this suggests the deviations from overall homogeneity seen in the AARS are not an unlikely fluctuation.

Finally it may be noted the estimates of M^* and α for the North and South subsamples given in Table 4.1 lie within the errors for each method, the agreement for the MLF between the two subsamples being remarkable.

4.3 ANALYSES OF THE KOS CATALOGUE

This section briefly reports on some of the techniques of the last section applied to the KOS catalogue. This was reanalysed to compare the results from the two samples using consistent methods and to compare with the previous analysis by KOS (79).

Although these authors used their data complete to 14.9 for the luminosity studies, since redshift data exists to fainter magnitudes the limits used later in their analysis were adopted. These are given in Table 4.3. Using these deeper limits includes another twenty redshift galaxies at the expense of including another three without redshifts. As before obscuration was ignored and q_o = 0.05 assumed, however the following K corrections were adopted as more suitable for the KOS J band -

E1Sϕ : 3.3 SA - SC : 2.2 SCD - 1M : 1.1 and any others 2.2.

Since the sample is shallower than the AARS, the results are less dependent on these corrections.

Fig 4.6 shows the mean $\frac{V}{V_{max}}$ for the northern and southern fields taken together up to 14.9, the total mean for the whole sample being 0.55. Particularly striking is the curve for the north with $0.7 > \frac{V}{V_{max}} > 0.6$, showing evidence for considerable inhomogeneities at large depth in these fields.

Fig 4.7 shows the BE (filled circles) and MLE (crosses) fitted with Schecter forms (solid and dashed curves respectively) between $-17.6 < M < -21.6$.

Although at bright magnitudes the estimates agree well, at fainter than -19.0 the MLE is considerably enhanced, consistent with the method compensating for the relative underdensity of galaxies at small redshifts suggested by the $\frac{V}{V_{max}}$ study. However it should be noted from the $dN_o(M)$ histogram at the foot of the figure that relatively few galaxies contribute to the LF at these magnitudes so it is not clear how well the faint end slope is determined from this sample.

TABLE 4.3: The KOS Survey

Field	Field Centres			Adopted limit	Numbers to limit		Area
	α	δ	B_{II}	J_{KOS}	Total	With Redshifts	$(deg)^2$
NP4	12 6	26 47	81	14.9	35	35	14.90
NP5	13 37	26 56	79	15.2	26	23	13.79
NP6	8 27	65 40	35	15.1	30	29	19.58
NP7	16 00	41 56	49	14.9	22	19	13.93
SP3	0 31	-29 56	-85	15.0	14	14	13.93
SP4	0 45	-22 00	-84	14.9	15	14	15.76
SP5	22 32	-20 58	-32	14.8	12	12	15.88
SP6	2 59	-10 9	-55	14.95	25	25	15.50

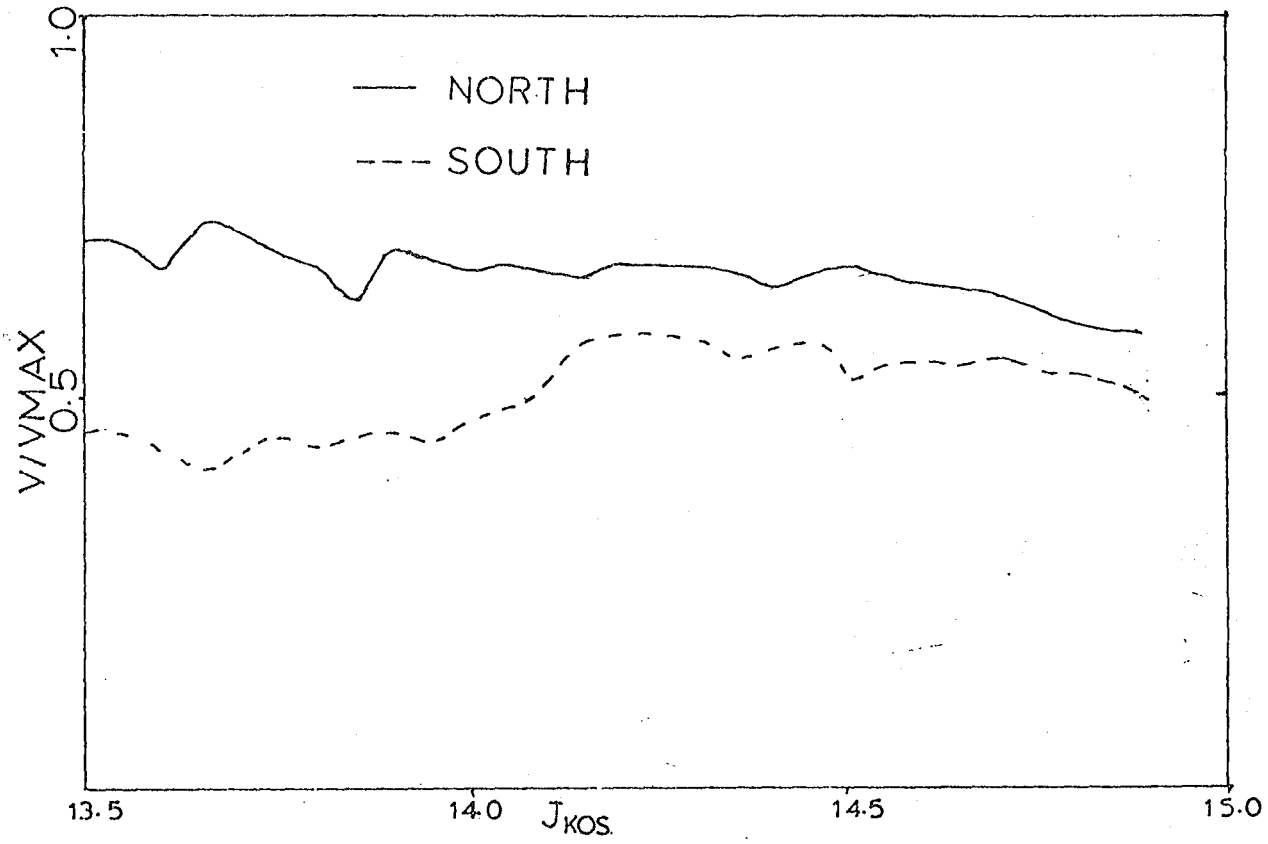

FIGURE 4.6: The mean V/VMAX as a function of limiting magnitude for the four northern and southern KOS fields taken together.

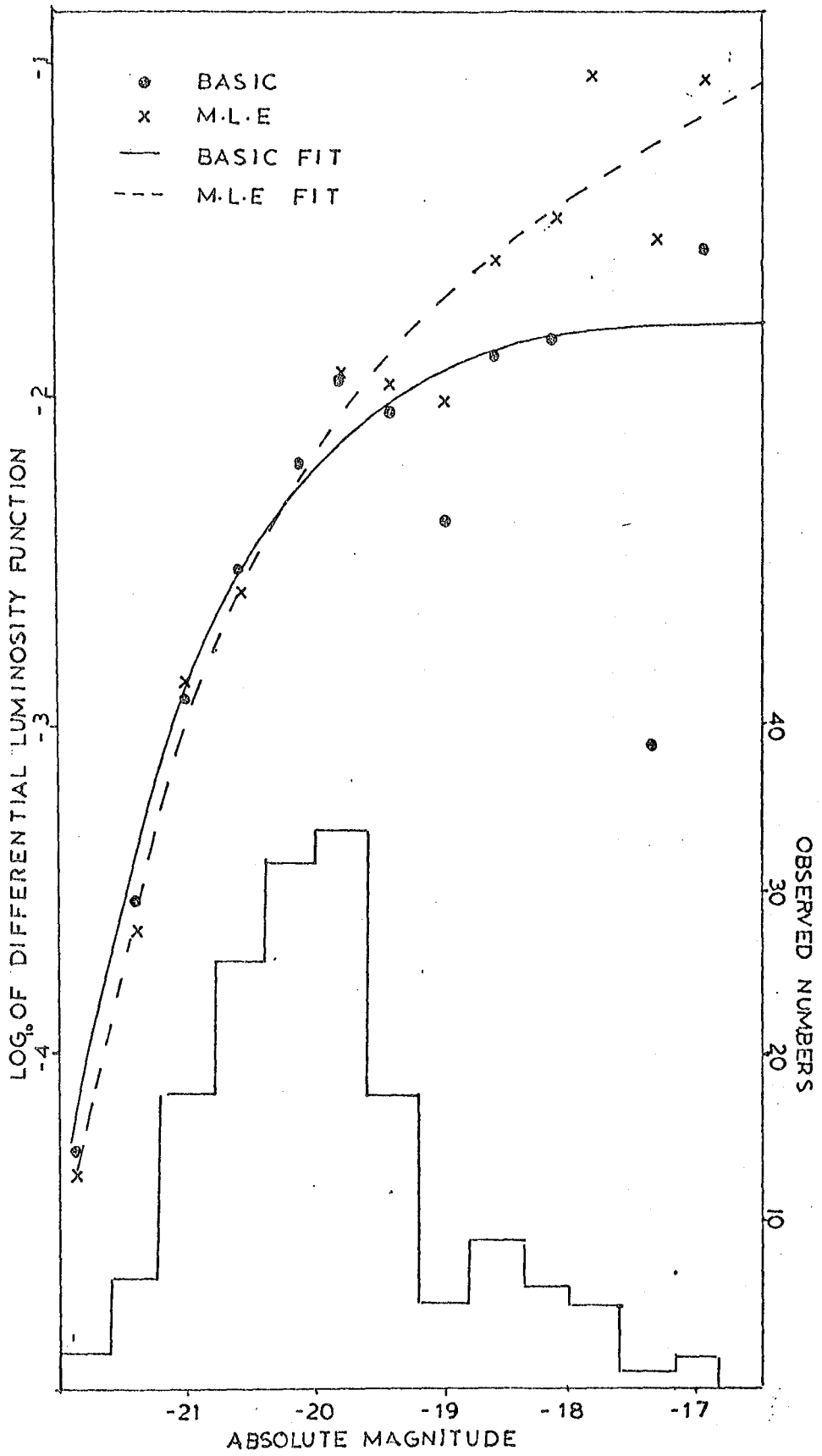

FIGURE 4.7: The two binned estimates and corresponding Schecter fits of the luminosity function for the KOS survey. The solid histogram (with the scale to the right) refers to the observed numbers contributing to the observed estimates as a function of absolute magnitude.

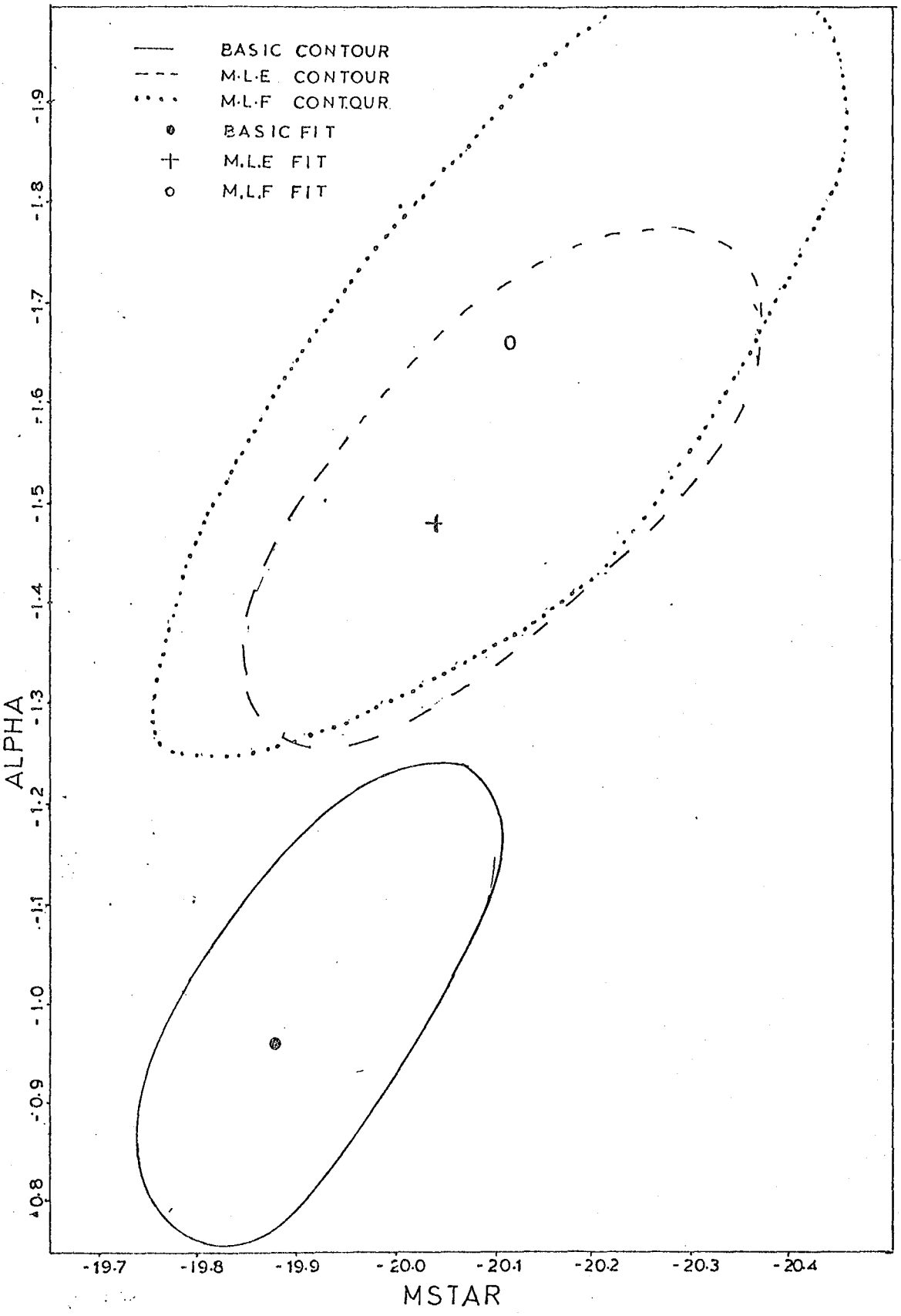

FIGURE 4.3: One sigma contours for the three Schecter fits of the total KOS survey.

TABLE 4.4: KOS Schecter Fits

Method	$-M^*$	$-\alpha$	dM^*_{int}	$d\alpha_{int}$	$-M^*(\alpha=-1.66)$	P(%)
BE	19.88	0.96	0.13	0.19	20.30	<< 1
MLE	20.04	1.48	0.22	0.20	20.22	90
MLF	20.12	1.66	0.26	0.28	20.12	-
KOS(79)	-19.85	1.34	0.2	0.29	20.17	-

Fig 4.8 corresponds to Fig 4.5 of the AARS with the best fits and error estimates in Table 4.4 corresponding to the results in Table 4.1.

In this case though, for comparison, the results have been fixed with $\alpha = -1.66$ which corresponds to the MLF best estimate of α . We see that, as for the AARS, M^* for the MLE and MLF vary by about 0.1 while the BE appears to be within 0.2 of M^*_{MLF}. However, a glance at Fig 4.8 shows the BE lies well outside the 1 σ contour for the MLF and the significance levels in Table 4.4 shows the fit is a very poor approximation to the original basic estimate fit. Transforming M^*_{BE} instead by eqn. 4.9 increases the difference to 0.43.

Also shown in Table 4.4 is the KOS (79) estimate and quoted errors transformed by eqn. 4.9 to $\alpha = -1.66$. Although the transformation agrees well with M^*_{MLF}, when the obscuration correction factor of 0.17 cosec b assumed by KOS is allowed for, the difference amounts to 0.2. However, allowing for the K corrections assumed in the MLF will reduce this to about 0.1, bringing the two estimates in reasonable agreement.

In the remainder of this thesis it will be normally assumed, like the AARS, the best estimate of the LF for the KOS survey comes from the MLF Schecter parameters

$$\alpha = -1.66 \quad M^* = -20.12 \qquad (4.11)$$

in the J_{KOS} system.

4.4 COMPARISON OF LUMINOSITY FUNCTIONS

It is of interest to compare the Schecter representations fitted to the AAT and KOS data in this chapter with Schecter fits to galaxy luminosity functions estimated from other samples.

The resultant fits from several such estimates are given in Table 4.5 along with appropriate references and brief information on the catalogue.

TABLE 4.5: Comparison of Schecter Fits

Survey	Comments	$-\alpha$	$-M^*_{PUB}$	$-M^*_{PDS}$	$-M^*_{CORR}$	OBSC	Survey Size	References
1 AARS	INHOM CORR	1.0	19.75	19.75	19.75	-	300	Chapter 4.2
2 KOS	INHOM CORR	1.66	20.12	19.67[4]	19.01	-	170	Chapter 4.3
3 HUCHRA	SOUTHERN	1.0	19.0	19.21[6]	19.21	-	190	Davis et al (78)
4 RSA	INHOM CORR	1.03	19.2	19.13[7]	19.10	-	1200	Tammann et al (79)
5 SRC	INHOM CORR	1.02	19.5	19.47[7]	19.25	0.2	400	KOS (79)
6 RC	$B(0) \leq 11.75$	1.25	19.1	19.31[6]	18.94	0.12	185	Schecter (76)
7 CfA	NO INFALL	1.5	19.5	19.71[5]	19.21	-	2400	Davis & Huchra (82)
8 CfA	INFALL	1.3	19.4	19.61[5]	19.31	-	2400	Davis & Huchra (82)
9 CfA	INHOM CORR	0.9	19.2	19.41[5]	19.51	-	1846	Davis & Huchra (82)
10 GROUPS		1.0	19.35	19.56[5]	19.56	-	63 groups	Turner & Gott (76)
11 CLUSTERS	OEMLER (74)	1.25	19.1	19.31[6]	18.94	0.12	13 clusters	Schecter (76)

The published α and M^*_{PUB} (for H = 100 km/sec/MPC) for each are given with M^*_{PDS} referring to M^* transformed into the JPDS (B_J) system by the corresponding transforms in Table 3.2, the numbers alongside referring to the corresponding transforms in that table. More details of the transforms are given in Appendix A. Since α and M^* are highly correlated M^*_{PDS} has been converted to M^*_{corr} by the simple transform of eqn. 4.9, in each case α being fixed to =-1. Also included in M^*_{corr} is a transform to zero obscuration that subtracts the observers assumed obscuration (if any) at the galactic poles. Since a cosec b law is normally assumed this will be a slight underestimate of the true correction.

Comparing M^*_{corr} for the eleven estimates in Table 4.5 one quickly sees that the value M^*_{corr} found for the AARS in Section 2 is the brightest of all the estimates and in all but two cases the difference amounts to a factor of 0.4 magnitudes or larger.

The most obvious explanation for this discrepancy is that the AARS result is due to a statistical fluctuation in the sample or else some bias has occurred in the estimation or fitting procedure. However, the thorough discussion in section 2 has shown that, although the estimate does depend on the technique used, the two most sophisticated methods that do not require the assumption of spatial homogeneity give very similar Schecter forms despite different weighting schemes in the fitting procedure. Also the results from the simulations show the adopted method should give an unbiased estimate of the LF in the presence of inhomogeneities with the expected errors in M^* and α, much lower than the half magnitude or so needed to account for the discrepancy with other samples. This is borne out by the good agreement in $M^*_{\alpha=-1.0}$ for the northern and southern subsamples studied separately.

The remaining possible reasons for uncertainties in the AARS estimate are serious errors in the magnitudes (or transforms) or at the large depth of the sample luminosity evolution or some other effect may 'brighten' galaxies at large redshifts, cancelling the effect of K dimming. The first possibility

may be suggested by the comparison of the AAT and KOS systems in Chapter 3.4 where a systematic error appears to be occurring at magnitudes fainter than $J_{PDS} = 16.5$ in the sense of the J_{PDS} magnitudes being too faint. However, as well as this effect being in the wrong sense to account for the discrepancy, as discussed in Section 4 support for the J_{PDS} measurements at these magnitudes come from the reasonable agreement with the cosmos magnitudes. In this case and the KOS comparison the observed offset between the systems are also in reasonable agreement with that expected theoretically suggesting the transforms used between the systems are consistent.

The second possibility of luminosity evolution was discussed in Section 2 as a possible explanation for the high $\frac{V}{V_{max}}$ for the sample. Although this may be suggested by the particularly high $\frac{V}{V_{max}}$ for the early type galaxies, to make M^* even 0.3 fainter would require that the luminosity evolution cancel the K correction of 3Z for all galaxies, which seems unreasonable.

Although these latter two possibilities discussed above appear an unlikely explanation for the discrepancy, as a test the magnitude limit for the sample was cut to 16.0. At this limit the J_{PDS} magnitudes agree (within a constant) with the comparison with the KOS system and at these magnitudes the effect of K corrections is much reduced. Repeating the LF estimates in Section 2 it is found the Schecter fits are essentially unchanged although the fluctuations are larger in the much reduced sample.

Having discussed the possible sources of error in the AARS studies it seems reasonable now to discuss the other entries in Table 4.5 one by one.

Starting at entry 2 we see that almost the largest discrepancy with the AARS comes from the most comparable sample, the KOS survey. The difference (0.74 magnitudes) is all the more surprising since the Schecter fit here was estimated in Section 3 in the same way as the AARS and also because the transform between the magnitude systems was calculated empirically in Chapter 3.4. As noted in Section 3 though, the comparisons between the

samples is not simple because the value of α for the KOS sample is so negative and transforming to $\alpha = -1$ gives a poor fit to the data. Indeed from Table 4.5 we see α for this sample is lower than all the other entries and is responsible for the particularly faint M^*_{corr} here. As discussed in Section 3, the faint end slope is determined by very few galaxies and it may take only a modest increase in sample size to dramatically change α. Ignoring the effects of inhomogeneities and using M^* from the basic method in Section 3 (which gives a similar fit at bright magnitudes to the MLF) we find the fitted slope α quite close to -1. and $M^*_{corr} = -19.47$; in much better agreement with the AARS.

Turning to magnitudes, we saw in Chapter 3.4 that at $J_{KOS} < 15.5$ the available magnitudes are in reasonable agreement with the expected transformed J_{PDS} measurements. However, not discussed by KOS (78) is the possibility that the brighter magnitudes are saturated, leading to magnitudes that are too faint.

Entries 3-6 are several estimates of the LF from local catalogues using often incomplete velocity information. Since the catalogues are based on similar data the estimates cannot be considered independent.

Although these studies have normally removed the area around the Virgo centre, local inhomogeneities may still tend to enhance the faint end of the LF, relative to the bright end, making α too low and M^*_{corr} too faint. While the estimates from the RSA and SRC do allow for this, none of the studies have used a correction for Virgocentric flow which may considerably 'brighten' the galaxies around Virgo by increasing the calculated distances. Indeed recent work by Efsthathiou (private communication) suggest an infall velocity of 300 km/sec towards Virgo will brighten M^*_{corr} by about 0.2 for $B < 12.5$.

Entries 7-9 refer to preliminary estimates of α and M^* from the deeper and better controlled CfA that goes to $B_z = 14.5$. The first two entries here were estimated assuming spatial homogeneity but with a Virgo infall

velocity of 0 and 300 km/sec respectively. We see the latter correction at this depth brightens M^*_{corr} by about 0.1. The small values of α from these two estimates indicate the effect of local inhomogeneities on the faint end of the LF which can also be seen in North/South variations in their data. The effect of inhomogeneities was allowed for in entry 9 and, although no infall was included, this is perhaps the most representative value of M^*_{corr} for this sample. We see that this estimate is just 0.24 magnitudes fainter than for the AARS and if an infall of 300 km/sec were included the discrepancy would probably be reduced to~0.15. If the infall was higher still or obscuration was significantly affecting the CfA at low galactic latitudes, the entire difference could be removed between the CfA and AARS estimates. Although this appears good support for the bright values of M^* for the AARS it should be remembered that at the fainter magnitudes the CfA rests on the Zwicky system that may contain large random or systematic errors (Huchra, 76).

The final two entries in Table 4.5 come from studies of groups and clusters. The first is based on a group detection study using incomplete redshift information which, as the authors discuss, may suffer from unknown biases. In particular, as Felten (77) discusses, the selection process may tend to pick up groups with the brightest galaxy considerably brighter than the fainter members. Thus the reasonable agreement of M^*_{corr} here with that from the AARS should not be given much weight.

The other sample comes from a composite luminosity distribution constructed from 13 of Oemler's cluster distributions, transformed by Schecter from the J_{OEM} system to B(O) magnitudes, and fitted by a Schecter function. We see that M^*_{corr} for the clusters is in good agreement with the results from the local samples which Schecter (76) argues is good evidence for both being drawn from the same distribution. However, 'by eye' comparisons of the LFS from Godwin's clusters (Godwin, 76) with the AARS estimates in Section 2, suggest this data at least (although not fitted with Schecter forms)

is consistent with the 'field' estimates from the AARS. In any case, it should be remembered that any differences implied by the present observations may just reflect differences in the mix of morphological types found in and outside rich clusters.

Despite the large amount of data from clusters there are still uncertainties associated with these studies where, unless redshifts are available, the faint end slope can be enhanced by background galaxies. Although their contribution is normally subtracted statistically, for clusters at faint magnitudes the correction factor is large. While the faint end slope for field samples may also be uncertain because of the small volumes sampled and the cluster studies do not require such a volume correction, the cluster distributions still need to be ensembled in a way that allows for the different magnitude range sampled at different redshifts. Having to ensemble the data taking this into account tends to reduce the advantage gained by the large numbers of individual galaxies contributing to these studies.

4.5 THE MEAN LUMINOSITY DENSITY

One further luminosity study is to estimate the mean luminosity density ρ_L of the universe. As Felten (77) discusses the calculation of total spectral luminosities is a non-trivial problem that requires total magnitudes, the absolute normalisation and shape of the LF as well as allowance for other corrections. Thus a sample like the AARS based on an isophotal magnitude system is not ideal for such studies. Nevertheless, it is still instructive to estimate $\rho_{L,PDS}$ and examine the relative contributions to it from galaxies of different luminosities.

Assuming spatial homogeneity in the AARS one can follow a method similar to that in Section 2.1 and calculate $\rho_{L,PDS} = \sum_i \frac{L_i}{V_{max}}$ over all galaxies where $L_i = 10^{0.4(J_\odot - M)}$ and M and V_{max} are calculated from eqns. 4.1 and 4.2. Here $J_\odot$ is the absolute magnitude of the sun in the B_J band which, from eqn. 1 in Appendix A and $\langle B-V \rangle = 0.6$ and $B_\odot = 5.48$, Allen(73), is $J_\odot = 5.34$.

Fig 4.9 shows the contribution to ρ_L from different magnitude bins for galaxies brighter than -16.4. We see the function is bellshaped with $\sim$ 80% of the light coming from galaxies with M< -18.5 that have a space density of $\sim$ 0.01 MPC^{-3}.

Table 4.6 shows the estimates of $\rho_{L,PDS}$ for individual fields with M< -16.4, the total for the sample being $1.06 \pm 0.1 \times 10^8 L_\odot MPC^{-3}$. Also in the table are estimates that include the fainter galaxies, the larger total : $1.38 \pm 0.25 \times 10^8 L_\odot MPC^{-3}$ suggesting these galaxies may make a non-negligible contribution to the luminosity density. However the larger error here reflects the uncertain behaviour of the LF at faint magnitudes discussed in Section 2.1.

Dropping the assumption of spatial homogeneity one can estimate $\rho_{L,PDS}$ using the LF parameters α and M^* adopted in Section 2.7. The luminosity density of galaxies, integrating to infinitely faint galaxies, is then given by the integral over the LF

$$\rho_{L,PDS} = \phi^* \int_0^\infty e^{-\frac{L}{L^*}} \left(\frac{L}{L^*}\right)^{\alpha+1} d\left(\frac{L}{L^*}\right) = \phi^* L^* \Gamma(\alpha+2) \qquad (4.12)$$

In the next chapter from the deep counts to $B_J = 17.0$ we find $\phi^* = 0.012$ which with $M^* = -19.75$ and $\alpha = -1.0$ gives $\rho_{L,PDS} = \phi^* L^* = 1.3 \times 10^8 L_\odot MPC^{-3}$. Since these figures refer to the luminosity density from sources within the isophotes they are likely to be underestimates of the total ρ_L in the B_J band. Transforming to total B_J by eqn. 8, Table 3.2 we find,

$$\rho_{L,B_J}^T = 1.65 \times 10^8 L_\odot MPC^{-3} \qquad (4.13)$$

This value is rather lower than the figure $1.9 \times 10^8 L_\odot MPC^{-3}$ found by KOS (79) for their sample but considerably larger than $L_B = 1.1 \times 10^8$ found recently from the CfA catalogue (Davis and Huchra, 82). However, since the latter is not based on a total magnitude system, the difference is not unexpected.

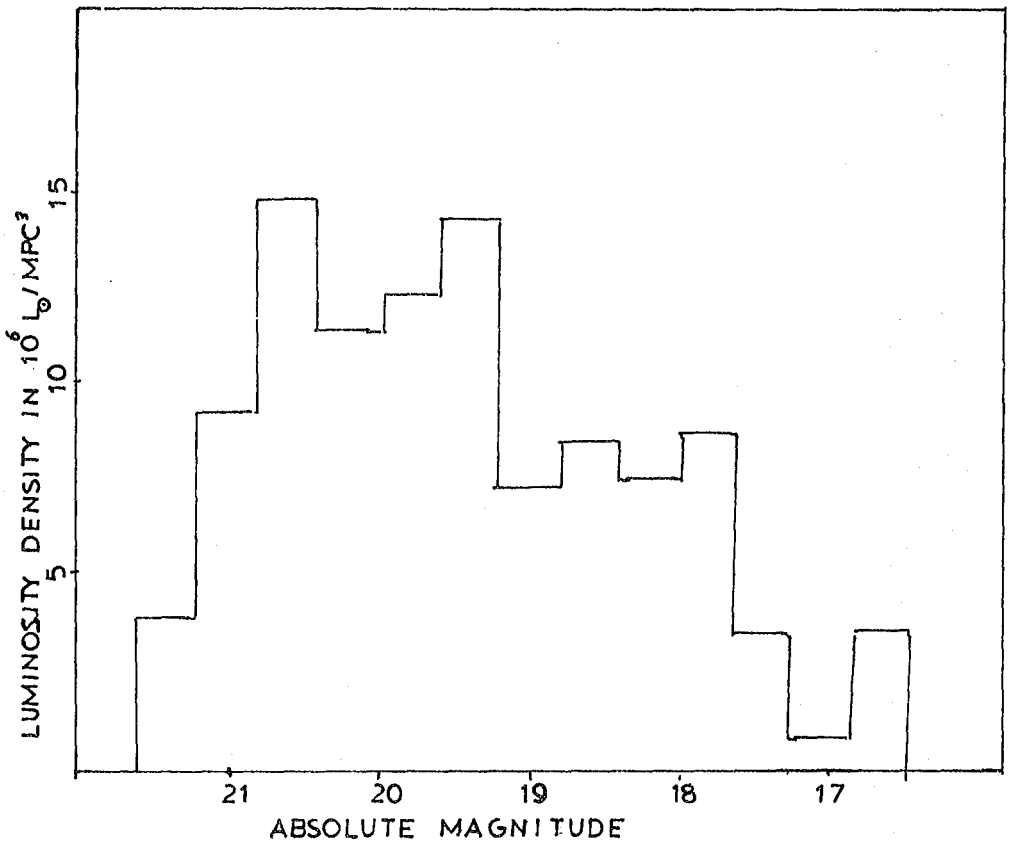

FIGURE 4.9: Contributions to the luminosity density from galaxies brighter than -16.4 in the total AARS.

TABLE 4.6: Luminosity Density for the AARS

Field	For M < - 16.4		All Magnitudes	
	$\rho_L (10^8 L_\odot / MPC^3)$	Numbers	$\rho_L (10^8 L_\odot / MPC^3)$	Numbers
GSA	1.10	72	1.20	74
GSD	1.04	62	1.04	62
GSF	0.70	40	2.49	50
GNA	1.36	68	1.36	68
GNB	1.12	67	1.18	68

In addition to correction for the isophote, corrections should also be made for internal absorption and inclination in spirals (Tinsley and Donly, 80) and absorption in our own galaxy. As discussed later in Chapter 5, there is also some indication that ϕ^* (even to $B_J = 17.0$) in the AARS fields is rather lower than for the universe as a whole.

Finally it should be noted that if α were to be $\lesssim -2$ the integral in eqn. 4.12 diverges. Although the discussion in the Section 4 suggests $\alpha = -1.0$ fits most of the data including the AARS, we still need to consider the possibility that much of the light comes from the very faintest galaxies that are poorly represented in magnitude limited samples and hard to distinguish from background galaxies in normal cluster studies.

A clue to the behaviour at the faint end of the LF comes from the work of Jones and Jones (80) who measured redshifts of faint galaxies in the nearby Fornax cluster to determine the distribution in absolute magnitude of member galaxies. They found that down to magnitudes of about -15.0 a slope of $\alpha > -1.0$, the numbers of galaxies per bin at the faintest limits actually falling with increasing magnitude. Similar conclusions have come from the studies of Tammann and Kran (77) who have shown that the large numbers of detectable faint galaxies in the local group and other nearby groups contribute little to their total luminosity. Thus it seems likely that most of the light is contained in bright galaxies selected in apparent magnitude limited samples and fig 4.9 is a reasonable representation of the total contribution to ρ_L for the AARS.

4.6 SUMMARY AND CONCLUSIONS

The analyses in this chapter has indicated that considerable care is needed with the estimate of the LF from redshift samples and in the fitting of the rather inflexible Schecter function.

The poor agreement of M^* from the AARS with previous studies of shallow catalogues may be partly due to the fact that these studies have often ignored the effects of inhomogeneities that can strongly distort the shape of the

luminosity function, as demonstrated by the analysis of the KOS sample in Section 3. Indeed comparison with the preliminary estimates from the large CfA, when inhomogeneities and Virgo infall is accounted for, indicate better agreement with the AARS than with other samples.

Although not touched on in this thesis, the AARS is nearly large enough to make reliable estimates of the LF for galaxies of different morphological types. The larger CfA will be more useful here, the estimates perhaps allowing a fairer comparison of the LF found in rich clusters with field samples containing early type galaxies.

As indicated in the next chapter, and Chapter 8, the shape of the LF has important applications forthe interpretation of deep number counters that can be used to put constraints on models for galaxy evolution and estimates of q_o. Knowledge of its form can also provide non-redshift distance indicators in clusters and groups (e.g. Schecter and Press,76) for cosmological studies and to map out the large scale distribution (Cf Kiang and Saslaw, 69). Nearby the LF for the general distribution with redshift information can provide constraints on local non Hubble velocities and the local group infall velocity towards Virgo (Yahil et al, 80).

In Chapter 7 we also consider how the number density of bright galaxies may affect the interpretation of the cosmic virial theorem studies and how the form of the LF can provide insight into theories of galaxy and cluster formation.

* In this context, the difference between M^* from the local catalogues and that found from the AARS and CFA may, by the arguments in section 4, imply a considerable infall velocity (> 300 km/sec) of the galaxy towards Virgo.

CHAPTER FIVE

THE DISTRIBUTION OF GALAXIES

5.1 INTRODUCTION

As well as providing information on the peculiar velocities of galaxies, redshift samples provide a much more detailed picture of the distribution of galaxies than from projected catalogues, both in the projected and radial directions.

At scales of around 10 MPC and smaller we have already been from the number distance counts for each field in Chapter 3.6, clear evidence for the existence of galaxy clusters. The $\frac{V}{V_{max}}$ and luminosity studies in the last chapter also suggest slight deviations from homogeneity on scales comparable to the sample depth. In the next chapter we look at the clustering of galaxies at small and large scales by means of correlation functions estimated using the redshift and angular coordinates. However, before doing so, in this chapter we discuss other available data on the distribution of galaxies in the redshift volumes with particular attention focussed on how representative they may be of the universe.

The first of the two main sections in this chapter looks at the large scale radial density distributions of galaxies from the observed number magnitude and redshift counts for the AARS and other catalogues compared with models. The first of these counts provide a test of the homogeneity of the sample and comparisons with deeper observations allow a test of the fairness of the redshift volumes and an absolute normalisation of the LF. More details of the density gradients come from model number redshift counts based on the LF estimates in the last chapter. These model counts also provide a measure of the background density of galaxies needed to estimate the correlation functions in the next chapter.

In the second half of this chapter are presented plots of the galaxy distributions in projection and redshift space that allow a clearer view

of the details of the clustering at small scales and also provide a qualitative impression of the magnitudes of the typical peculiar velocities of galaxies.

Finally, the results for the chapter are summarised in section 4.

5.2 THE MAGNITUDE AND REDSHIFT DISTRIBUTIONS

To discuss the binned data this section is split into four parts. In the first two are presented and discussed models for the number magnitude and redshift data, the results of which are further discussed in part 3 where conclusions are presented on how representative the AARS fields may be of the universe as a whole. In the final part we look at an alternative model for the number redshift distributions that can be used as an alternative measure of the background number density of galaxies needed to estimate the correlation functions in the next chapter.

5.2.1 The Number Magnitude Counts

Galaxy counts have long been used to provide information on the radial density distribution of galaxies and test the overall homogeneity of the universe (Hubble, 34) without the need for measuring redshifts. More recently very deep counts (Kron, 78, Tyson and Jarvis, 79) have been used to constrain models of galaxy evolution for galaxies of different morphological type. For our purposes the counts provide a test of how representative the AARS volumes are compared with deeper surveys and allow a normalisation of the LF.

As is well known, if galaxies are homogeneously distributed in a euclidean universe both the differential and integral magnitude counts are expected to scale as $10^{0.6m}$, independent of the form of the LF if K corrections and evolution are ignored.

Fig 5.1 shows the differential counts per square degree for galaxies brighter than B_J = 15.0 with the AARS counts shown (with field to field errors) as crosses. The data beyond 16.5 here comes from the three fields mentioned in Chapter 3.6 that have complete photometry to B_J = 17.0. The

model curve (solid line) on the figure, described more fully later, has been normalised to the integral counts at the limit of the data at 17.0 and has a slope slightly flatter than the scaling discussed above due mainly to the allowance made for K corrections at these magnitudes. The filled circles and dashed line on the figure refer to the recent UKST counts and associated models discussed in Shanks et al (83a) that have been transformed into the JPDS system by the empirical transform of eqn 2, table 3.2.

We see from figure 5.1 that the agreement between the model and observations for the AARS is quite reasonable apart from the data being slightly under the model at bright magnitudes. This suggests that the galaxies are reasonably homogeneously distributed in the sampled volumes. Turning to the UKST counts we see the first two points join on well to the model for the AARS. However, it is probable that photographic saturation here makes the data lie below the dashed line which fits the counts beyond $B_J = 18.0$ and also fits deeper AAT data presented in Shanks et al (83a).

If these deep counts (which appear to be in reasonable agreement with other data) are representative of the universe the implication from fig 5.1 is that the AARS volumes are underdense by a factor of 30% if the two models are compared at around $B_J = 17.0$. However the discrepancy is reduced slightly if we use the expected theoretical transform between the two magnitude systems of eqn 1 in table 3.2.

A further indication that the galaxy density in the AARS volumes is lower than average appears to come from the KOS counts, shown on fig 5.1 as open circles, that have been transformed to B_J by the empirical transform eqn 4, table 3.2. However, as KOS (79) discuss, considerable enhancements in the four northern fields compared to the four southern are visible in their survey that are also seen at B_T ($\sim$ B_J) $\lesssim 16.0$ in the Zwicky counts, suggesting there may be a large overdensity of galaxies extending over a large solid angle in the north.

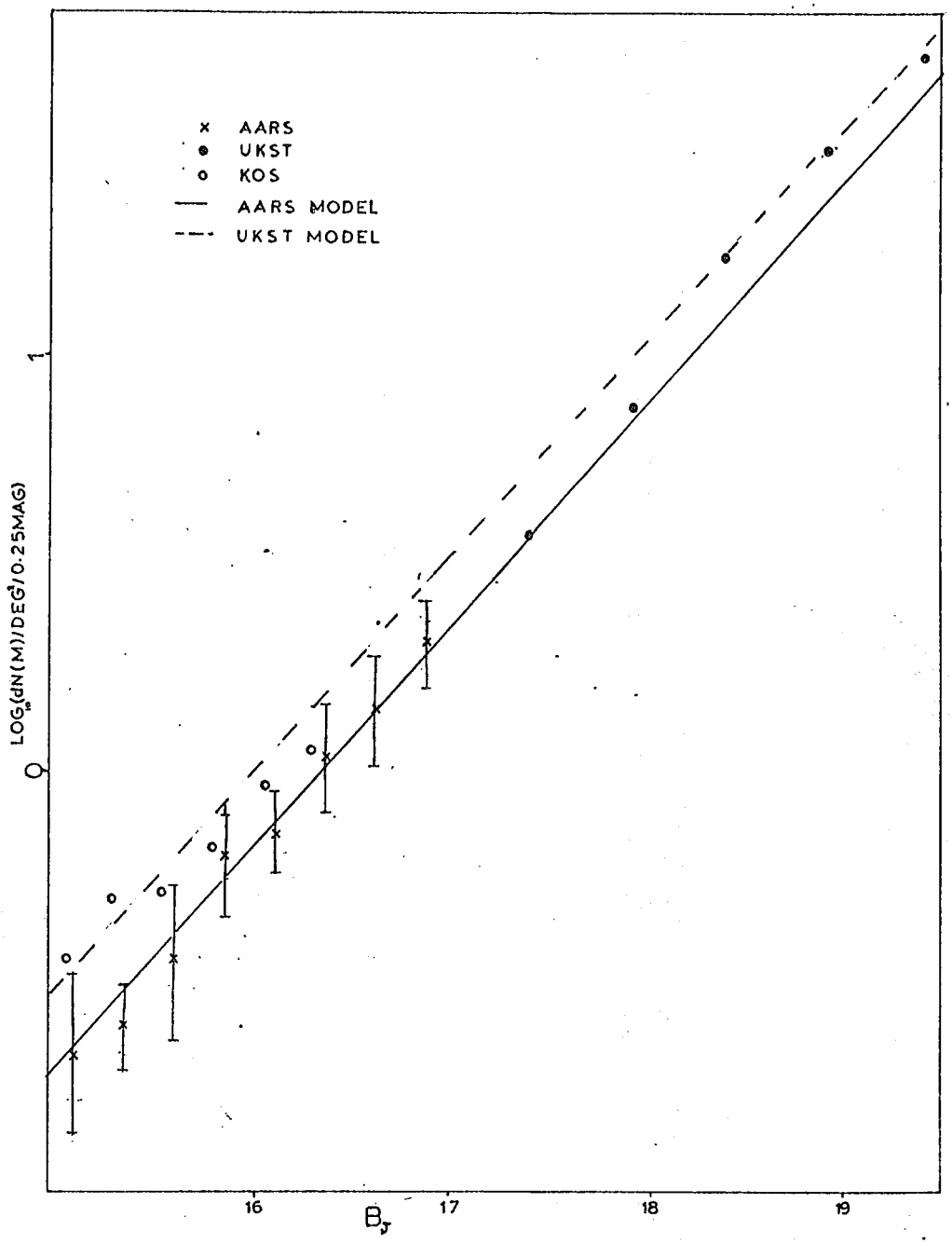

FIGURE 5.1: Differential number magnitude counts and model for the AARS and other surveys. The errors on the AARS counts come from field to field fluctuations.

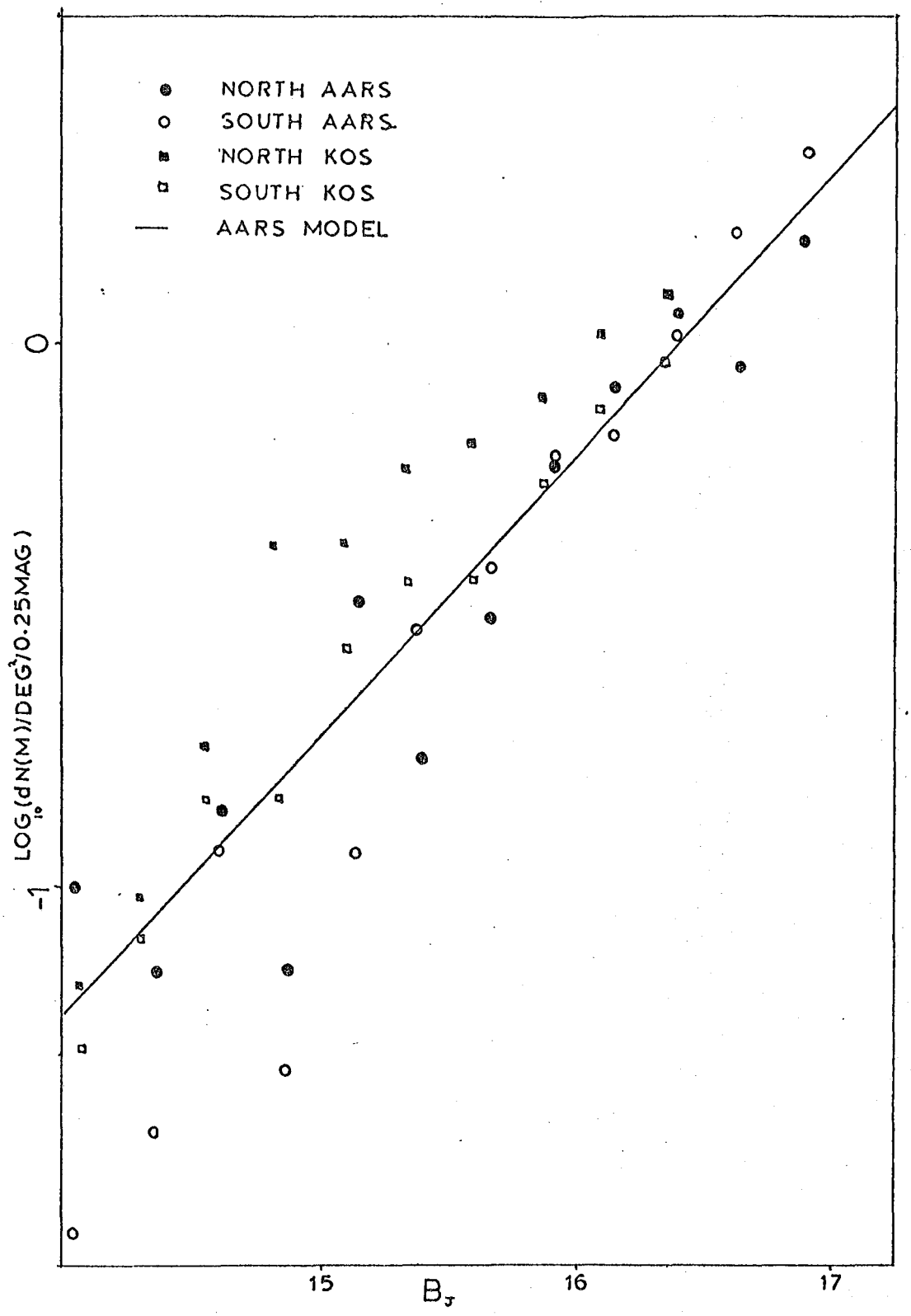

FIGURE 5.2: Differential number magnitude counts and model for the northern and southern AARS and KOS survey.

This can be seen in fig 5.2 which shows the same solid line model as fig 5.1 along with the AARS and KOS counts (circles and squares), the filled and open symbols referring to north and south subsamples respectively.

We see from this figure that the north/south difference is particularly prominent at around $B_J = 15.0$ in the KOS counts suggesting a supercluster spanning the northern fields at this depth. Taking M* from eqn. 4.10 the characteristic distance corresponds to D* = 90 MPC, well beyond the Virgo supercluster. Despite considerable fluctuations in the AARS counts between north and south at these magnitudes, there is no obvious overdensity in the north suggesting this feature, if real, is not included in the AARS. In the next part of this section we discuss how the number redshift counts with models can give us a considerably clearer view of the radial density fluctuations in the AARS and KOS volumes.

Before doing so we still need to discuss details of the solid line model in figs 5.1 and 5.2 that, as well as providing a test for the homogeneity of the sample, also allows a normalisation of the LF.

The relation between the integral number counts and galaxy number density is given by an integral over the LF.

$$N(\leq m) = \Omega \int \phi(M)\ V(M)\ dM \qquad (5.1)$$

where V(M) is the volume of space sampled by galaxies brighter than M and Ω is the solid angle of the survey area. Ignoring K corrections and curvature and using the Schecter function (eqn 4.5) this becomes (e.g. KOS (79))

$$N(\leq m) = \frac{1}{3}\ \Omega\ D^{*3}\ \phi^*\ \ \Gamma(\frac{5}{2} + \alpha) \qquad (5.2)$$

where $D^* = 10^{0.2(M-M + 25)}$.

Since K corrections are important at $B_J = 17.0$, a mean K correction of 3z was adopted along with $q_o = 0.05$ and V(M) calculated using eqns 4.1 and 4.2. Taking the Schecter function with M* and α from 4.10, eqn. 5.1

was numerically integrated in 0.2 magnitude intervals in order to provide a model for the differential counts.

Normalising the observed integral counts at $B_J = 17.0$ to the model gave

$$\phi^* = 0.012 \pm 0.00057 \qquad (5.3)$$

the error coming from field to field fluctuations. This value for ϕ^* was used to normalise the corresponding model curves for the differential counts per deg^{-2} in figs 5.1 and 5.2, and was also used in Chapter 4.5 to estimate the mean luminosity density.

5.2.2 The Number Redshift Counts

A much clearer view of the galaxy distributions in the AARS fields comes from the number redshift counts rather than the magnitude counts because redshift is a much better distance indicator than apparent magnitude. However, to examine the actual density gradients, and in the next chapter the clustering and velocity statistics, we need an estimate of $\psi_i(r)$; that is the number density of galaxies visible in a particular volume element at a particular distance in a particular field.

As KOS (79) and Davis and Huchra (82) discuss, in a sample with large inhomogeneities a measure of $\psi_i(r)$ comes from the luminosity function $\phi(M)$ if, like two of the estimates in Chapter 4, it is calculated by a method unbiased by clustering.

Following KOS (79), $\psi_i(r)$ can be estimated by introducing a faint magnitude cutoff MLOW to the integral .LF to allow for the selection of galaxies by apparent magnitude. This gives

$$\psi_i(r) = \int_{-\infty}^{MLOW} \phi(M)\, dM$$

To compute this for each field of AARS, M^* and α from eqn 4.10 were assumed, with MLIM calculated from eqn 4.1. As with the eqn 5.1

in Part 1, a mean K correction of 3.0 z and q_o = 0.05 were adopted in eqn 4.1 but the estimate was restricted to the distance range 20-280 MPC. This is because at small and large redshifts . $\psi_i(r)$ depends on the uncertain behaviour of $\phi(M)$ at the faint and bright ends respectively.

Like the model curves for dN(m) in Part 1, we still require an estimate of ϕ^* to normalise $\psi_i(r)$. One possibility is to use the value in eqn 5.3 from the integral magnitude counts to B_J = 17.0. However, as discussed later in Chapter 6.3, to reduce statistical fluctuations in the correlation functions it is preferable to assume the sampled volumes under analysis are representative and calculate ϕ^* accordingly. As Davis and Huchra (82) discuss though, in an apparent magnitude limited sample there are several ways to estimate ϕ^* within a given volume that should all give equivalent results in a perfectly fair sample but, in practice after varying degrees of bias versus stability. As these authors discuss, in theory the most consistent approach is to give equal volumes of space equal weight when calculating ϕ^*, rather than weighting to the observed numbers in a volume. However in practice this gives much more weight to information from galaxies in distant clusters whose density contrasts are sensitive to the bright end of the LF. Instead, the more stable approach adopted here, is to equate the total observed number of redshift galaxies N_T with that expected in an homogeneous universe assuming a given shape for $\psi_i(r)$. If homogeneity is assumed the expected number of galaxies visible in a volume dV(r) in a given field i is given by

$$dN_{iH}(r) = \Omega_i \ \psi_i(r) \ dV(r) \qquad (5.4)$$

where Ω_i is the solid angle of the field and the volume segments dV(r) are calculated from eqn. 4.2 with q_o = 0.05.

Adding up the contributions in 10 MPC bins between 20 and 280 MPC

from all fields and equating to N_T we get

$$\phi^* = 0.01057 \pm 0.00074 \qquad (5.5)$$

The slight difference between this value for ϕ^* and eqn 5.3 is due to the slightly different volumes sampled by the counts at $B_J = 17.0$ and those considered here.

Although this normalisation procedure is not really consistent with the estimation of the shape of $\phi(M)$ (since homogeneity is assumed for the former) and could be biased by the presence of nearby inhomogeneities (where faint galaxies dominate), the general agreement between the observed counts and the model suggest the procedure is reasonably self consistent .

This can be seen from fig 5.3a which shows the observed ensemble number distance histogram $dN_o(r)$ binned in 20 MPC intervals together with the ensemble model curves $dN_H(r)$ (eqn 5.4) normalised with ϕ^* from eqn 5.5. The dashed histogram on the same figure refers to the quantity $\delta(r) = \frac{dN_o(r)}{dN_H(r)}^*$, which is the absolute density in that volume compared with the mean for the sample (scale to the right).

We see from this figure that at distances < 200 MPC the data and model agree well, consistent with overall homogeneity on scales of around 20 MPC. At distances > 200 MPC there appears to be a systematic rise of density with distance that is also seen in $\delta(r)$ for both the north and south subsamples shown in figs 5.3b and 5.3c.

This effect was noted in Chapter 4.2.3 as an explanation of the slightly different estimates of $\phi(M)$ from the basic and MLE methods and suggest either a real density gradient in the sample (as assumed there) or a systematic error in the selection function. Some evidence for the former explanation (for fig c at least) comes from the contributory number counts

* This could also be estimated from the analysis in Chapter 4.2.3 using the ρ_J estimates at the appropriate distances divided by the appropriate volume segments $dV(r)$.

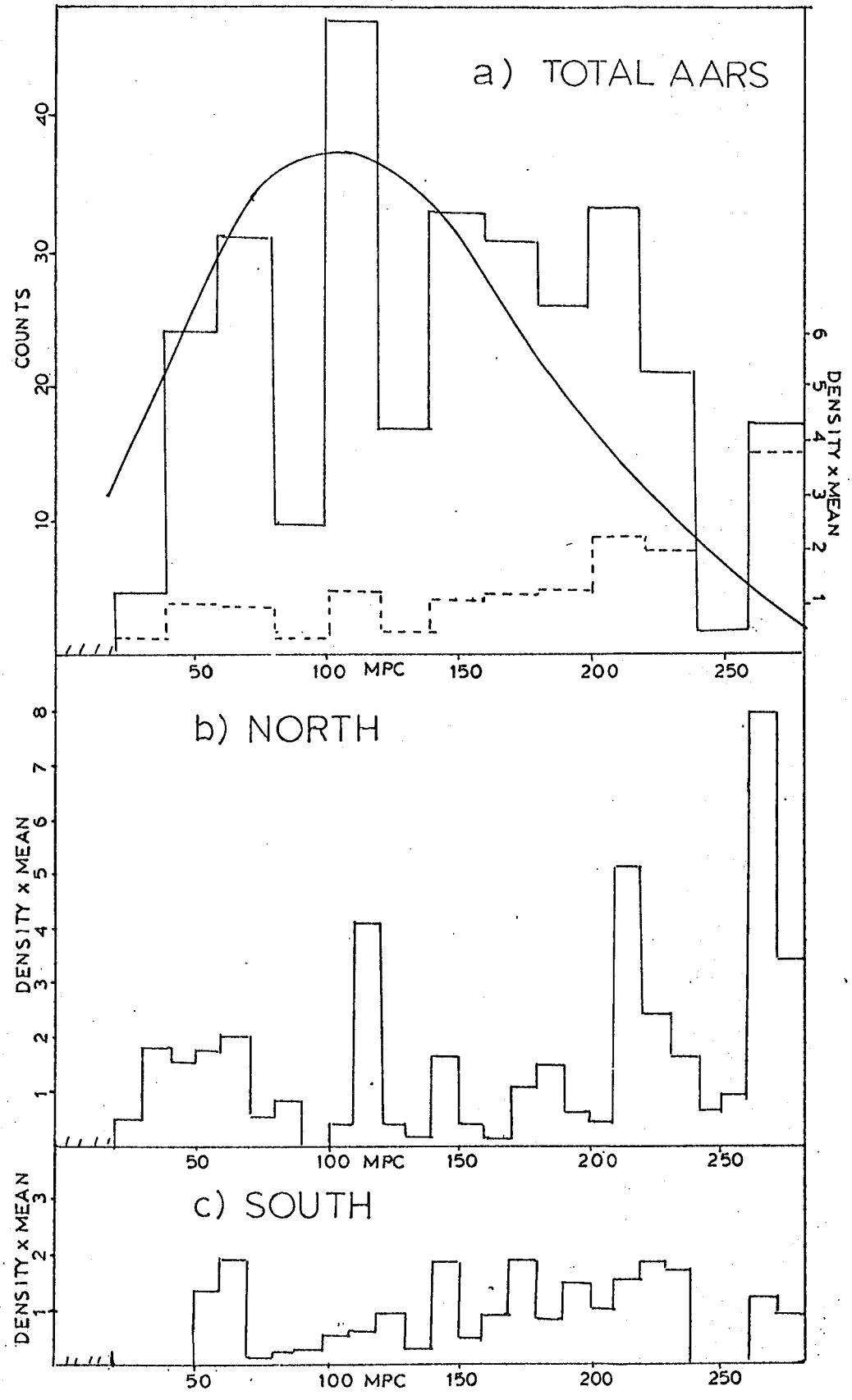

FIGURE 5.3: Figure (a) shows the observed number distance counts (solid histogram) for the AARS along with a model based on the integral luminosity function. The dashed histogram (with scale to the right) is the density compared to the mean calculated from the model. The corresponding densities for the northern and southern subsamples are in Figs (b) and (c).

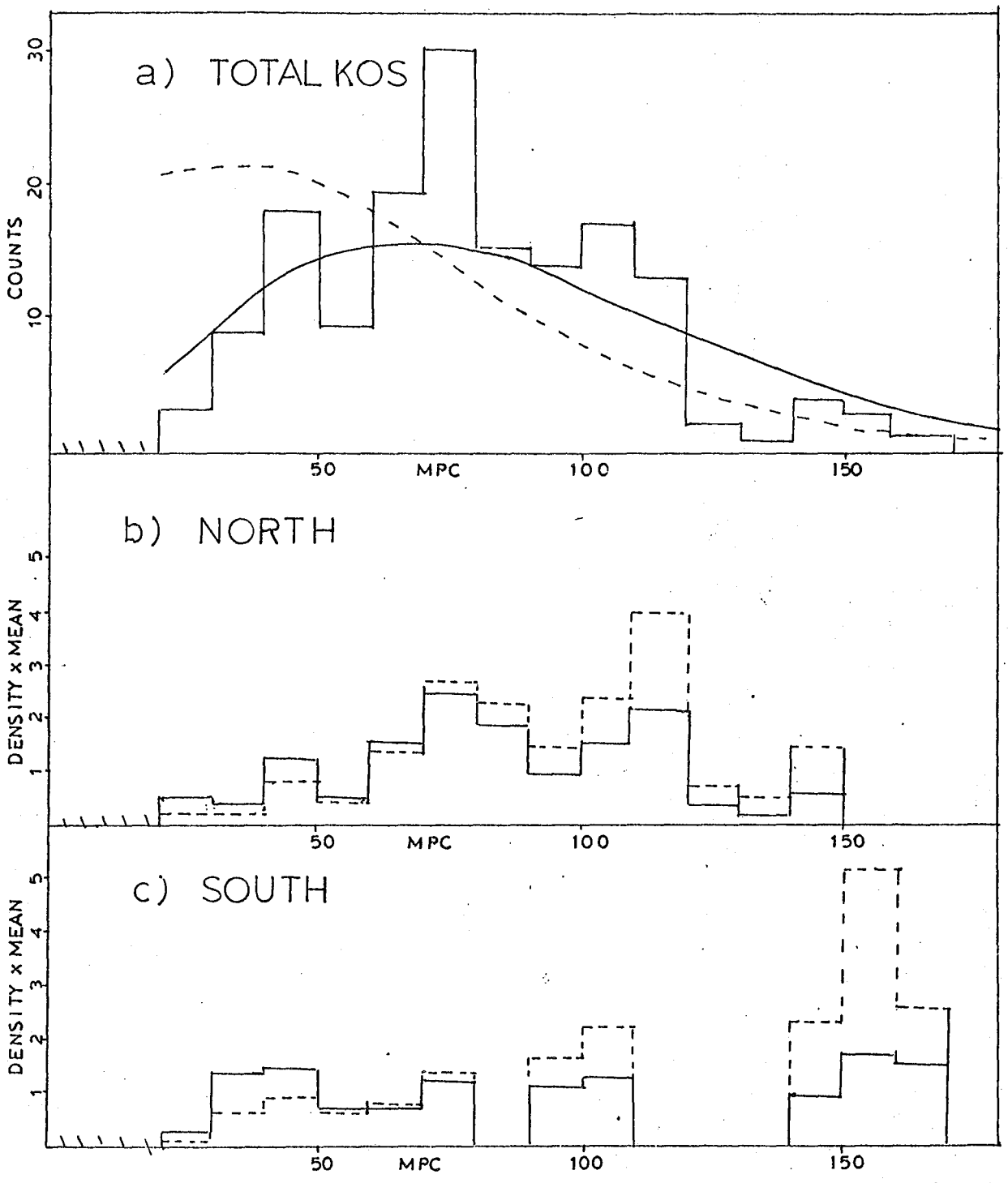

FIGURE 5.4: Fig (a) shows the observed number distance counts for the KOS survey along with models based on the integral luminosity function from the AARS Schecter fits (solid curve) and the KOS fits (dashed curve). The corresponding densities from these two models (solid and dashed) compared to the mean for the northern and southern subsamples are in Figs (b) and (c).

for field GSF shown in fig 3.9c where a large void is quite apparent at < 180 MPC. The same effect is implied in the $\frac{V}{V_{MAX}}$ study in Chapter 4.2.2 which does not depend on an assumed LF but only requires that the photometry and K corrections etc. be reliable. It might be noted here that this slight density gradient would be much enhanced if a more conventional, fainter M^* were were used in the calculation of $\psi_i(r)$ since it would lead to the model $dN_H(r)$ curve peaking at smaller redshifts.

In this context it is interesting to consider corresponding models for the KOS sample and study the effect on the density distributions of changes in the assumed LF. Fig 5.4a shows the results of calculating $dN_H(z)$ (solid curve) in the same way as for the AARS but using M^* and α from eqn. 4.10 transformed into the J_{PDS} system by eqn. 4 of table 3.2 and assuming a mean K correction of 2.2 z. The dashed curve uses the LF parameters from the MLF (eqn 4.11) estimated consistently from the sample in Chapter 4.3. Figs 5.4b and c show estimates of $\delta(r)$ for the northern and southern subsamples respectively with the solid and dashed curves corresponding the selection functions in fig a.

We see the dashed line in fig a implies large scale inhomogeneities on scales of the depth of the sample, particularly in the north (fig b) where the results for $\delta(r)$ agree well with the corresponding quantity $\phi^*(R)$ shown in fig 3 of KOS (79). In the south (fig c) too there is evidence for a considerable density gradient that rises with increasing distance. However, we see that using $\psi_i(r)$ calculated from the AARS LF (solid curve) the fit to the data in fig a is much better and gives rise to a much more even density field in the south. In the north a considerable overdensity is still present between 60 and 120 MPC (as implied by the magnitude counts in fig 5.2) but is considerably reduced from the dashed histogram and the supercluster here discussed by KOS (79).

Although this discussion does not imply the solid curve in fig a is necessarily nearer the truth, the dashed histograms in figs b and c do suggest the MLF method discussed in Chapter 4.3 for the KOS sample may, in certain cases, give unstable results.

5.2.3 The Homogeneity of the AARS

Having presented and discussed models for the number magnitude and redshift distributions for the AARS and other catalogues, we can ask what they tell us about the typical scale of density fluctuations in the universe and,in turn how representative the AARS may be of a fair sample. As indicated below though, with the present fairly small samples we can only attempt to argue from consistency arguments.

Obviously on scales less than 10 MPC prominent galaxy clusters make the distribution inhomogeneous, however averaged over larger scales and all fields the number magnitude counts in fig 5.1 for the AARS suggest galaxies are fairly homogeneously distributed in these volumes. Indeed from the number of redshift models in figs 5.3 a-c the scale at which the distribution is homogeneous may be as low as 20 or 30 MPC. Although here we see some systematic deviations from homogeneity at distances > 200 MPC, even if the sample does allow a reliable estimate of $\psi(r)$, we might expect statistical fluctuations to cause the observed counts to deviate from the model at some level.

As well as sampling fluctuations causing deviations away from the shape of the expected number redshift distributions we may also expect the overall normalisation ϕ^* to vary from that of a completely representative sample. Since galaxies are clustered, the uncertainties in ϕ^* in the sample will be greater than the square root of the number of galaxies and will depend more closely on the number of independent clusters in the sample. The expected fluctuations in the normalisation $\frac{dN}{N}$ can be calculated theoretically (Davis and Huchra, 82) but this involves a complicated integral

over the selection function and the two point correlation function. A simpler way is to calculate deviations in N from the simulated catalogues that were designed to approximately match the observed selection function and clustering statistics for the sample.

Using the first set of simulations described in Chapter 3.7 we find $\frac{dN}{N} \sim 0.15$ (5.6), considerably larger than the interfield errors in eqn 5.5 but probably a more realistic figure.

Similar values ($\frac{dN}{N} \sim 0.1$ to 0.2) have recently been proposed for the northern CfA sample by Davis and Peebles (82) (DP). However, as this sample has some four times the galaxies and volumes of the AARS it may be wondered why the expected fluctuations are so similar. One reason is that DP assumed the clustering of galaxies extends to 20 MPC whereas in the simulations of the AARS at scales $\gtrsim$ 10MPC the distributions are close to poisson. Another contributing factor is the roughly spherical and relatively shallow limits of the CfA . will tend to increase the statistical fluctuations in the number of clusters present especially if coherent structures exists on scales comparable to the sample depth (as DP assumed in their calculation). Indeed, as noted in Chapter 1.4, considerable large scale structure is evident in the projected Zwicky catalogue at these magnitudes and in the observed number redshifts distributions for the CfA that are poorer fits to the model counts (Davis and Huchra, 82) than seen in fig 5.3 for the AARS. In turn this may mean at large scales the deep AARS fields are more representative of the universe than the larger but shallower CfA.

Of course if real structure does exist on scales >> 10 MPC the estimates of $\frac{dN}{N}$ in (5.6) for the AARS may be gross underestimates, in which case we come back to the problem of how representative the sample is. Indeed we might even expect to see parts of the same coherent structure appearing in different well separated fields.

Some evidence for this appears to come from the number magnitude and redshift counts for the KOS survey that show evidence for a huge inhomogeneity (of which the Coma supercluster seen in the CfA is just a part) that extends over much of the northern galactic cap. As discussed in Part 2 though, the density field is very sensitive to the assumed selection function and we might expect considerable chance fluctuations in such a small sample.

Further evidence for large correlations between widely spaced fields has been claimed by KOSS(81) from their extension of the original survey in three northern fields in smaller but deeper patches. Finding that each field exhibits a prominent void between 120 and 180 MPC and since each field is separated by 35^{o} from each other field, these authors have suggested that this may indicate a real hole in the galaxy distribution in Böotes of the order 10^{6} MPC^{3} in volume. While some support for considerable overdensities surrounding this proposed void come from the work of Bahcall and Soneira (82), recent studies of chosen areas between the fields by several observers (e.g. Sanduleak and Pesch, 82) suggest the void contains significant numbers of galaxies. Also the effect may at least be partly caused by the very narrow fields considered by KOSS that have widths at their characteristic depth similar to the correlation length ($r_{o} \sim$ 5 MPC)of galaxies. In this way one tends, in a given distance range, to either sample a cluster or not, creating the apparent large voids and sharp clusters seen in each field. Since there are only three fields there is then a fairly high probability by chance of these voids appearing at the same place in each field.

Turning back to the AARS counts, we see from fig 3.1 that the two northern AARS fields are as near NP4 and NP5 of the KOS sample as these are to the two other KOS fields, and yet the redshift counts in fig 5.3b show no evidence for the large density excess between 60 and 120 MPC seen

in the KOS data (fig 5.4b). Similarly, there is no evidence for the void between 120 and 180 MPC seen in the KOSS fields that are quite close to the field GNA. Although in the southern fields, GSF shows a large void between 20 and 180 MPC, as noted in Chapter 3.6, there is no evidence for it in the other two southern fields, so that it is evidently not as wide in angular extent as it is along the redshift direction.

We see from the data discussed above, the evidence regarding inhomogeneities on scales of tens of MPCS is still uncertain. Indeed there may even exist deviations from homogeneity on still larger scales that would be hard to detect by comparing small samples as done here. One might argue that fig 5.1 provides evidence that the nearer volumes of space may be underdense relative to deeper volumes. However, as discussed in Part 1, systematic errors in the transforms may be responsible and, as noted above, we may expect considerable fluctuations in ϕ^* for the AARS due to its small size.

In Chapter 6.3 we discuss how correlation functions for the AARS can provide more objective information on the clustering of galaxies on scales of tens of MPCS but discuss how fluctuations in small samples could lead to small systematic effects at larger scales.

5.2.4 An Alternative Selection Function

In the last part of this section it was argued that the galaxy distribution in the AARS averaged over scales of tens of MPCS appears homogeneous and the survey might be reasonably representative of the universe. Although real structure may exist on these scales and the sample is relatively small, by going deep in well separated fields one has the maximum chance of fair sampling. While the CfA has the advantage of sampling larger volumes, the relative shallowness can increase the chance of statistical fluctuations as suggested by the poor fit of the model to the observed number redshift counts. A similar poor fit is found for the deep KOSS sample where the narrowness of the fields increase the chance of statistical fluctuations in the redshift counts.

If the AARS is a good approximation to a fair sample, as suggested by fig 5.3a, a straightforward estimate of $\psi_i(r)$ comes from the observed counts binned up and fitted by a low order polynomial to reduce fluctuations from individual clusters.

Since the magnitude limits vary slightly from field to field to calculate this estimate of $\psi_i(r)$ one should strictly fit all the data complete to a given magnitude limit separately, combining the results to give smooth polynomial fits for each field separately. However, an adequate simplification is to fit the total AARS counts in 30 MPC bins to a fourth order polynomial, accommodating the changes in background number density expected in the different fields by weighting the normalisation of the polynomial by the factor $10^{0.6\, m_{lim}}$, where m_{lim} is the limiting magnitude of a given field.

The results of this procedure are in fig 5.5 which shows the observed counts are reasonably smooth when averaged over 30 MPC scales and the polynomial gives a reasonable and stable fit.

This type of estimator of $\psi_i(r)$ has the possible advantage over that based on the LF in Part 2 that it would not be affected by errors in the magnitudes (such as saturation at bright magnitudes) or K corrections provided selection is consistent from field to field and spatial homogeneity applies. The obvious disadvantage is that it throws away information on any large scale inhomogeneities that the LF provides, so that by fitting the observed counts one may be eliminating large scale clustering.

In the statistical analyses reported in the next chapter correlation functions have been estimated from selection functions based on the curves in fig 5.3a and fig 5.5 between 20 and 280 MPC, divided by the appropriate volume elements across each field. Since a full relativistic study there was too complicated to be worthwhile, the actual $\psi_i(r)$ corresponding to the curve in fig 5.3 a was re-estimated ignoring curvature in the calculation of M_{LOW} and the volume elements. Although this is not quite consistent and

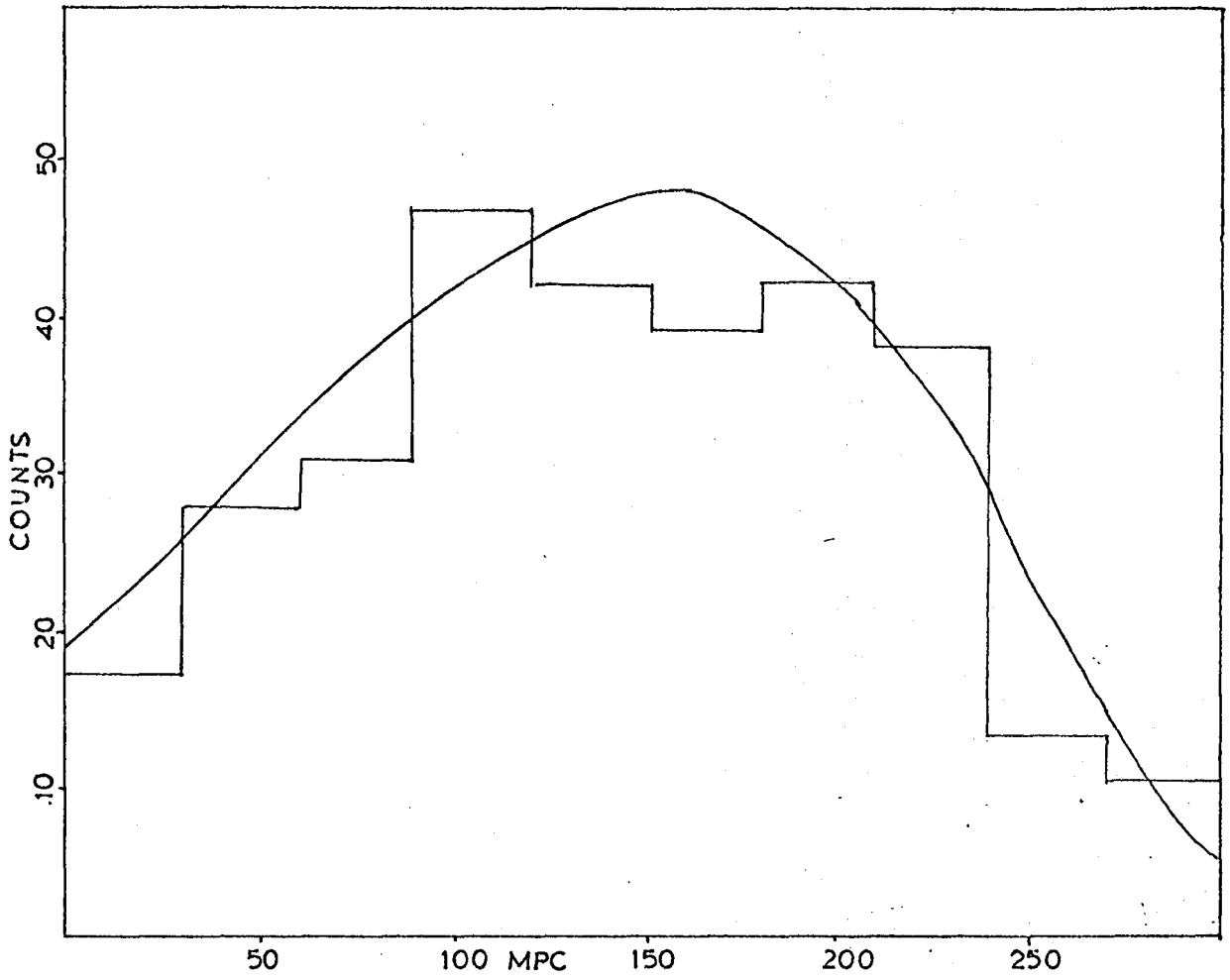

FIGURE 5.5: The total observed number distance counts for the AARS fitted with a fourth order polynomial.

the resulting selection function is slightly different at large distances, since the resultant correlation functions are virtually indistinguishable from those calculated from fig 5.5 this does not seem to be a worry. Also discussed in Chapter 6 is a selection function used for a statistical study of the Huchra catalogue where inhomogeneities on the scale of the catalogue can strongly affect and possibly invalidate the estimation of correlation functions.

5.3 PLOTS OF THE GALAXY DISTRIBUTIONS

Although the correlation studies in the next chapter provide objective measures of the clustering and peculiar velocities of galaxies, since they are not sensitive to all features that may be present in the data it is instructive to examine the visual appearance of the distribution. In Part 1 are presented plots of the redshift fields with prominent clusters picked out by redshift with particular attention devoted to the typical peculiar velocities in these regions. In Part 2 plots in redshift space are discussed and compared with several fields taken from the simulated catalogues.

5.3.1 Plots in Projection

As with the apparent magnitude counts in each field presented in fig 3.8, the positions on the sky at fixed apparent magnitude for the AARS provide little information on the distribution of galaxies in the fields, this time because the depth means that clusters at different distances are superimposed on each other. However, with the redshift information we can eliminate obvious projection effects if we assume at large redshift separations peculiar velocities are negligible.

Figs 5.6(a-f) show the five AARS fields and the richest KOS field NP4 seen on the sky with the redshift distances to the galaxies marked (those nearer than 280 MPC) and the most prominent clusters marked with different symbols. The velocities judged in Chapter 3.5 to have errors > 50 km/sec are enclosed with circles and the angular scale is in radians

a) GSA

b) GSD

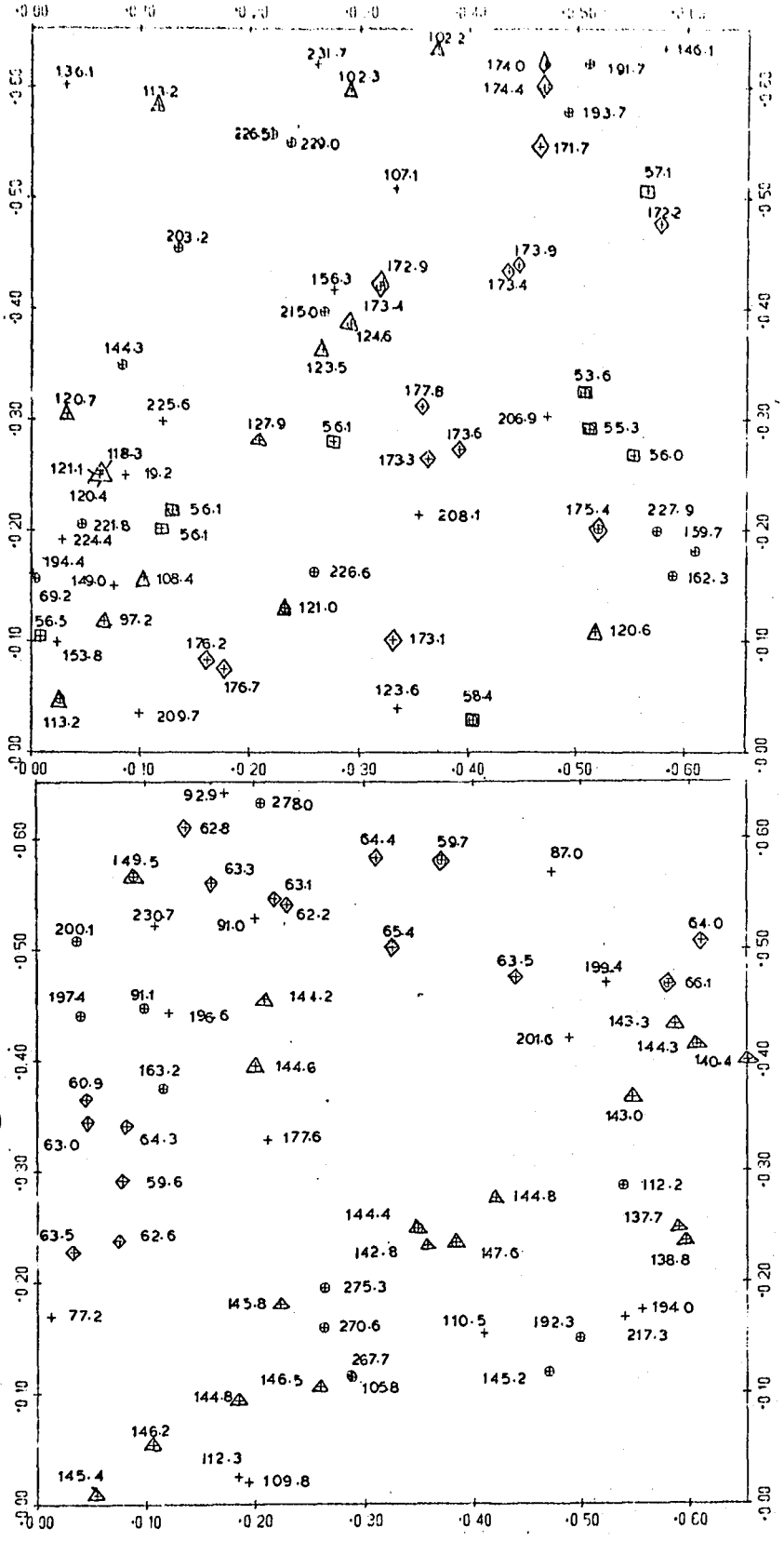

FIGURE 5.6 (a)-(b): Projected plots for two of the southern AAPS fields with distances to the galaxies given and the galaxies in the most prominent groups picked out and marked with common symbols. Circles surrounding the crosses indicate galaxies have velocity errors greater than 50 km/sec.

c) GSF

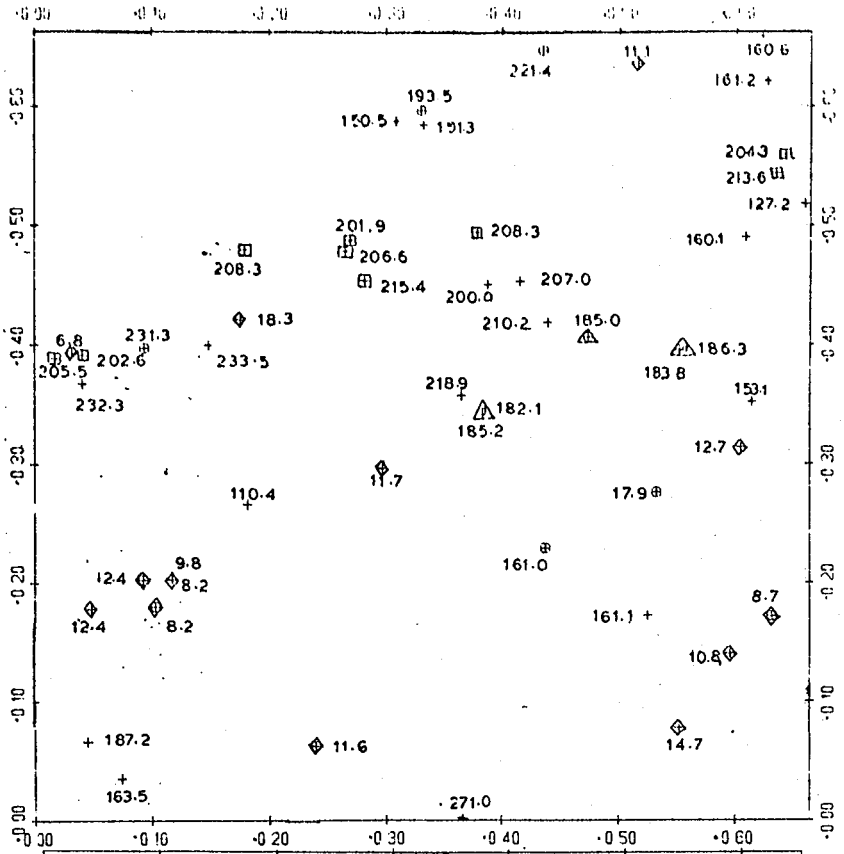

d) GNA

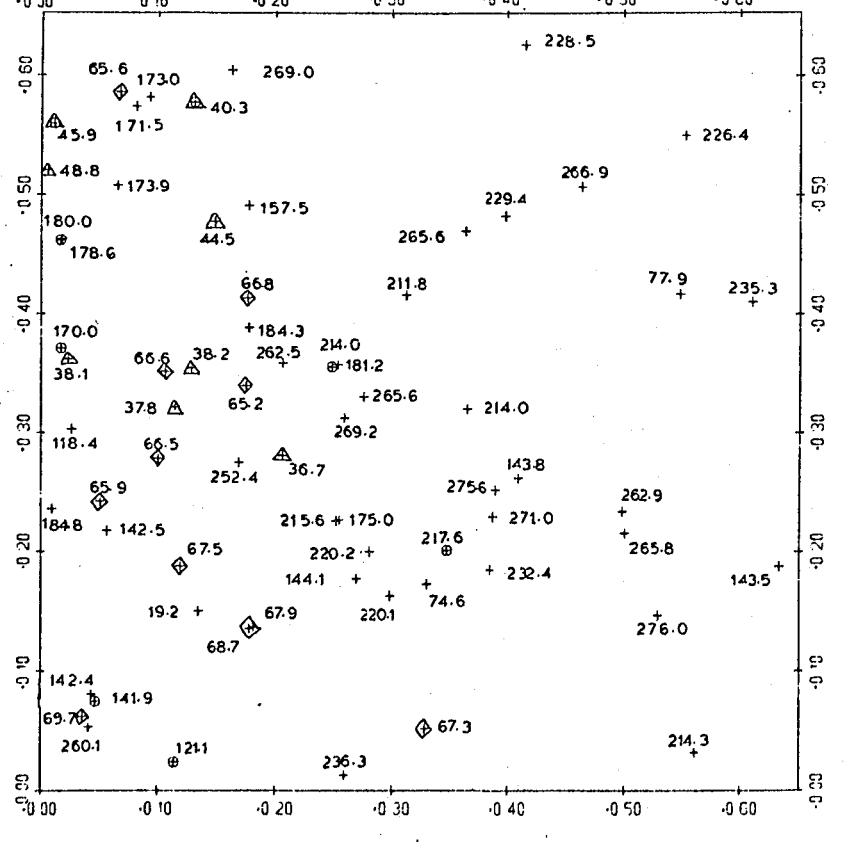

FIGURE 5.6 (c) - (d): As for Fig (a) and (b) for the remaining southern and one of the northern fields.

e) GNB

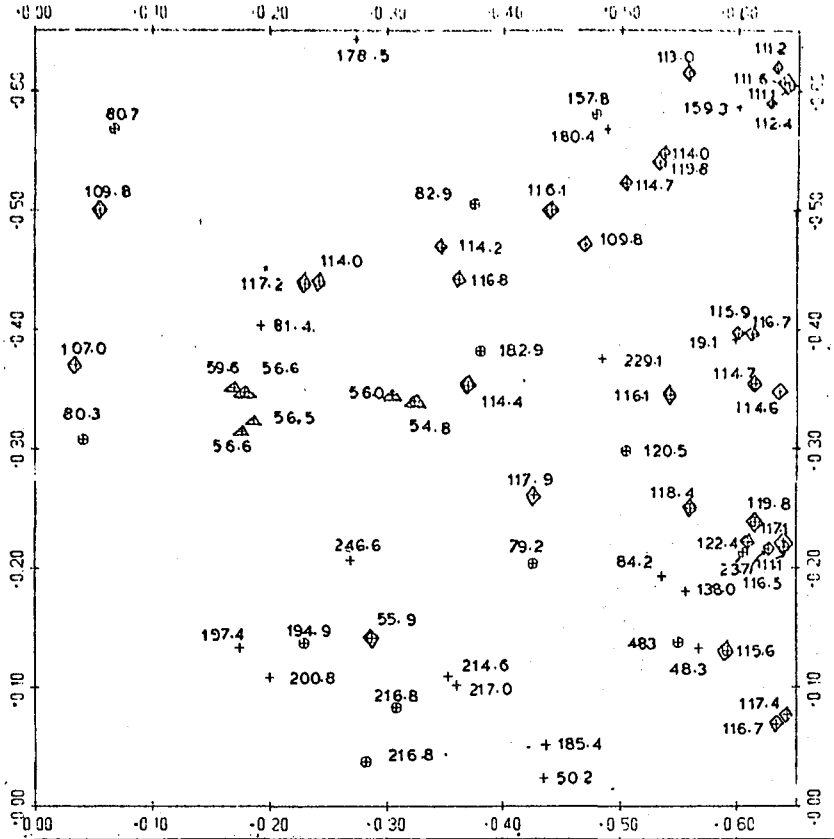

f) NP4

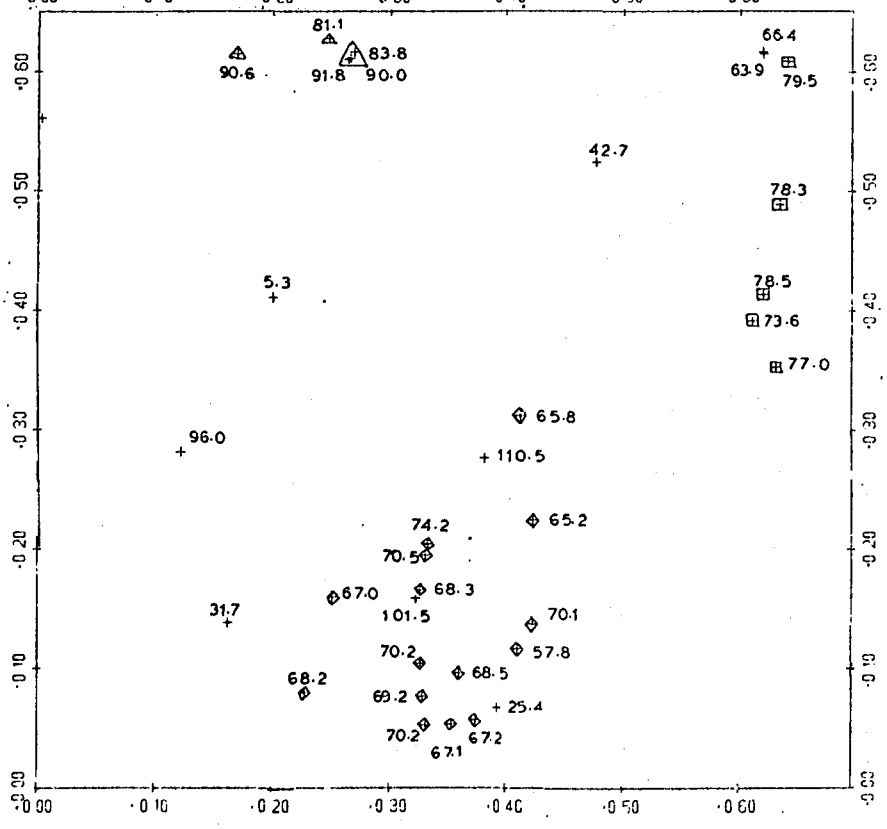

FIGURE 5.6 (e) - (f): As for Fig (a) and (b) with the remaining northern field and field NP4 of the KOS survey.

for easy conversion to projected distances.

The general impression looking at these plots is that the redshift galaxies are mainly situated in loose groups that themselves are clustered, sometimes forming 'stringlike' structures such as seen in GSD in the cluster at 140 MPC. Even taking into account the selection of galaxies by apparent magnitude we see very few well defined and condensed groups with several bright members of the type detected by Gott and Turner (77b), suitable for individual virial analysis. In GNB we see a cluster of 30 or so galaxies in a radius of $\sim$ 3 MPC which in turn could be split into three or so sub-groups of four or five galaxies that are surrounded by the remaining galaxies. Although this is the richest association in the sample it is much less prominent on the sky than even a poor Abell cluster would appear at a similar distance in the fields.

This can be crudely seen by using the Abell galaxy cross correlation statistics considered by Seldner and Peebles (77a) and the selection function estimated for the AARS in section 2.2. In this way one finds that if a typical Abell cluster lay at a distance of~100 MPC in one of the fields one would expect to see thirty* or so galaxies within a radius of 1 MPC, well above that seen in the cluster in GNB. Taking the mean number density of such clusters to be $n_c = 4.8 \times 10^{-6}$ MPC^{-3} (Peebles, 80a p.300) we find that the average number of such clusters expected in the volumes is around one.

While the plots provide some information on the projected appearance of the clusters, the redshift difference between close galaxies is likely to reflect the typical peculiar velocities. Calculating the velocity dispersion for the cluster in GNB discussed above we find $\langle v^2 \rangle^{\frac{1}{2}} \sim$ 400 km/sec, however as the crossing time ($t_c \sim \frac{\text{Radius}}{\langle v^2 \rangle^{\frac{1}{2}}}$) is around the age of the universe this

* Due to uncertainties in the assumptions this figure may be uncertain by a factor of two or more.

figure is likely to include Hubble expansion velocities. Splitting the cluster into the three subgroups mentioned above, we find two have $\langle V^2 \rangle^{\frac{1}{2}} \sim$ 100 km/sec while the third has $\langle V^2 \rangle^{\frac{1}{2}} \sim$ 540 km/sec. In GSD one can split the cluster at 60 MPC into three groups with four or so members that have an average relative velocity dispersion $\langle V^2 \rangle^{\frac{1}{2}} \sim$ 220 km/sec, a similar figure to that found from the dozen or so isolated close pairs of galaxies seen in the five fields.

In this context is also of interest finally to discuss field NP4 of the KOS sample (Fig 5.6 f) since this field is mainly responsible for the high velocity dispersion $\langle V^2 \rangle^{\frac{1}{2}} \sim$ 500 km/sec found statistically for the sample by Peebles (79). As KOS (78) discuss, this field includes galaxies in the Coma/A1367 supercluster and contains three or so groups of galaxies at the supercluster velocity. Particularly prominent in fig f is a fairly isolated cluster of early type galaxies at ∿70 MPC that contains 15 possible members within a projected radius of 1 MPC and within 1000 km/sec of the mean cluster velocity. From the same analysis applied to this cluster as the one in GNB, we would expect a typical Abell cluster at this position in the KOS fields to show around 25 members within a radius of 1 MPC, comparable to that seen.

Since the cluster is well isolated on the sky it is interesting to apply the virial theorem to estimate its mass. Using its observed velocity dispersion $\sigma_c \tilde{\sim}$ 360 km/sec a crude analysis yields a total mass of $\sim 1.5 \times 10^{14} M_\odot$. Correcting for fainter members by assuming the usual LF, this yields a $\frac{M}{L} \sim 500$ in the B_J total system, typical to that found in rich clusters. However the estimate is very sensitive to the inclusion of the two most deviant velocities which, if removed as interlopers, reduces the mass by a factor of 4 or so. A similar membership ambiguity comes from the group in NP4 marked on the sky with triangles which appears a tight group on the sky but which may consist of two well separated groups seen in

chance projection. This vividly illustrates the membership problem associated with these studies discussed in Chapter 2.2 and points the need for statistical methods which add all the data from groups together and deal with projection problems statistically.

5.3.2 Plots in Redshift Space

A more vivid picture of the clustering of galaxies comes from plots of the galaxy distributions in redshift space and indeed several observers (e.g. Einasto et al, 80) have obtained large numbers of redshifts mainly for this purpose. Like the plots in projection though, when examining the distributions one has to bear in mind the ability of the eye to pick out certain structures when none may exist. Therefore, to test objectively for any features that appear significant statistics of some sort are necessary.

Figs 5.7(a-f) show 'cone' plots of the five fields along the redshift direction for distances <280 MPC. Here I and II in each field refer to projections on to right ascension and declination respectively with the subtending angles calculated using the small angle approximation $\theta << 1$. As before the velocities with probable errors >50 km/sec are marked with circles and field NP4 of the KOS survey is shown, but at twice the scale of the AARS.

Looking at these plots we see the clustering is very prominent in each field and of various degrees of richness and compactness although comparison at different redshifts is complicated by selection by apparent magnitudes. Apart from field GSF being devoid of galaxies at intermediate redshifts, in general galaxies are clustered strongly on scales 5 to 10 MPC with voids often immediately adjacent, the clusters typically separated by 20 to 40 MPC gaps. In some cases the clusters appear non-spherical and particularly striking here are two clusters in GSA and GSD that appear to be flattened along the line of sight. Similarly orientated bands have been noticed by Tifft and Gregory (77) in the Coma and Perseus superclusters, the

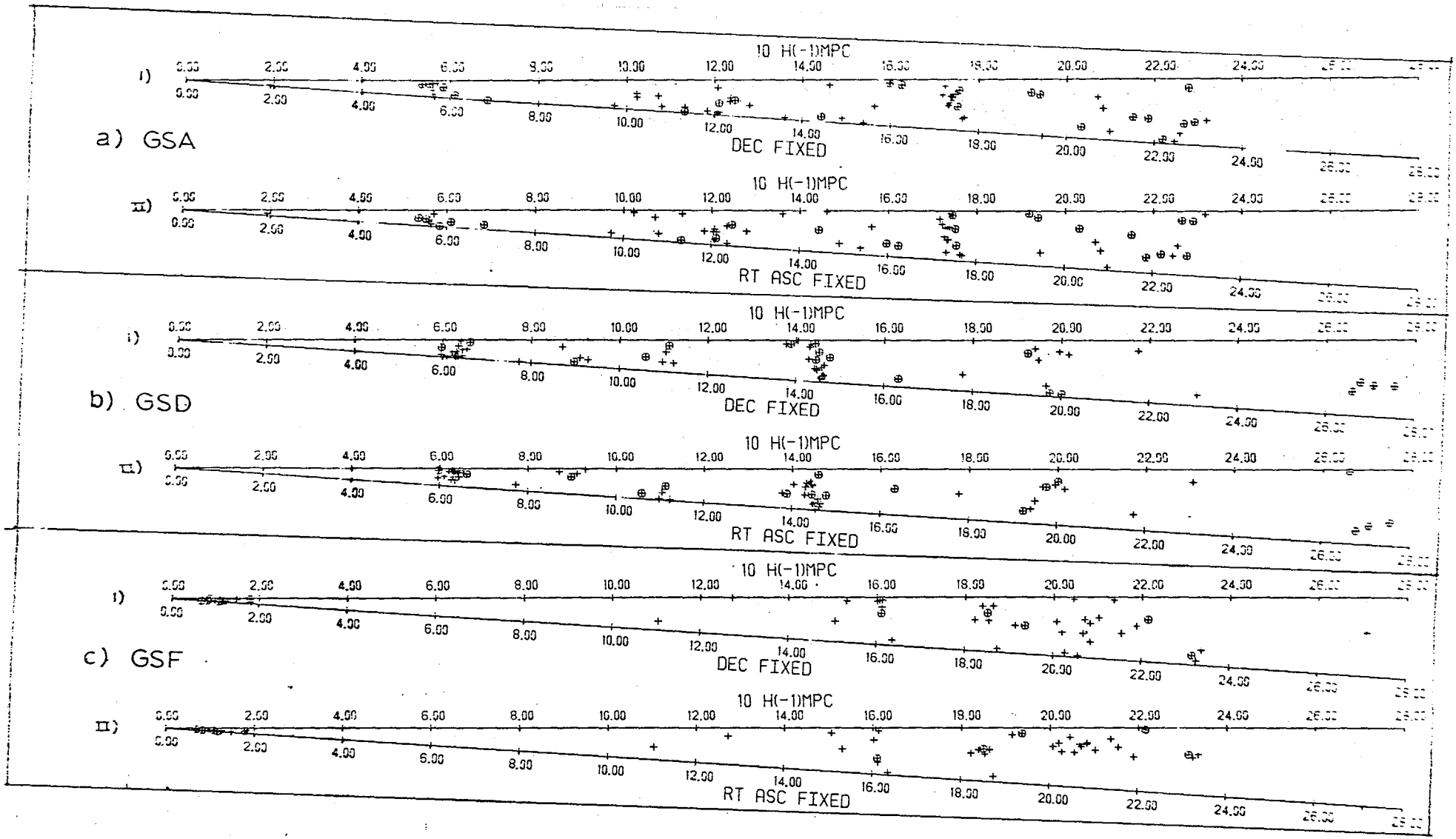

FIGURE 5.7 (a) - (c): Redshift plots for the three southern AARS fields with I and II in each case corresponding to projections onto the right ascension and declination respectively. Circles surrounding the crosses indicate galaxies have velocity errors greater than 50 km/sec.

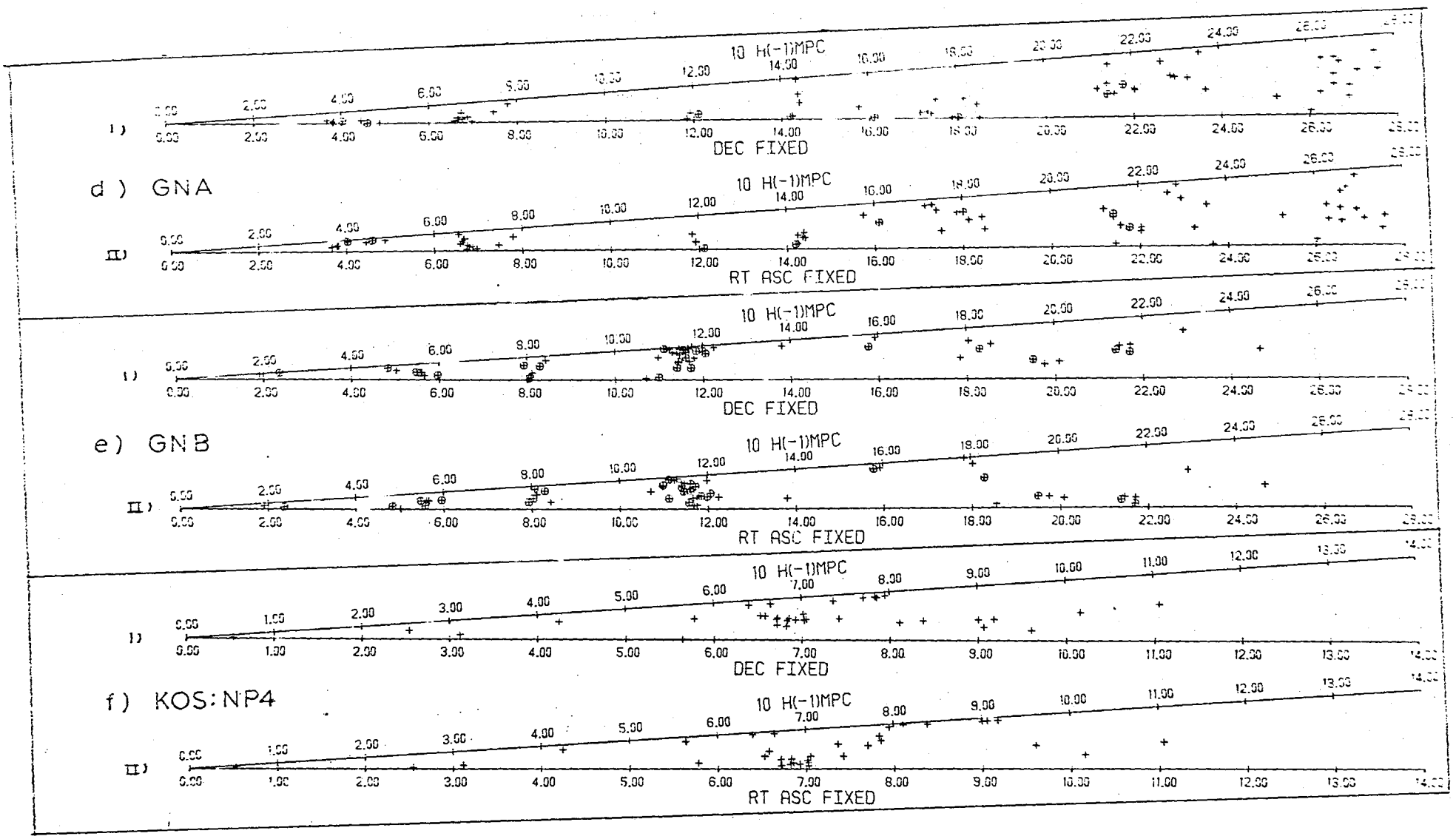

FIGURE 5.7 (d) - (f): As for Figs (a)-(c) but for the two northern AARS fields and field NP4 of the KOS survey. The latter is shown at twice the scale of the AARS.

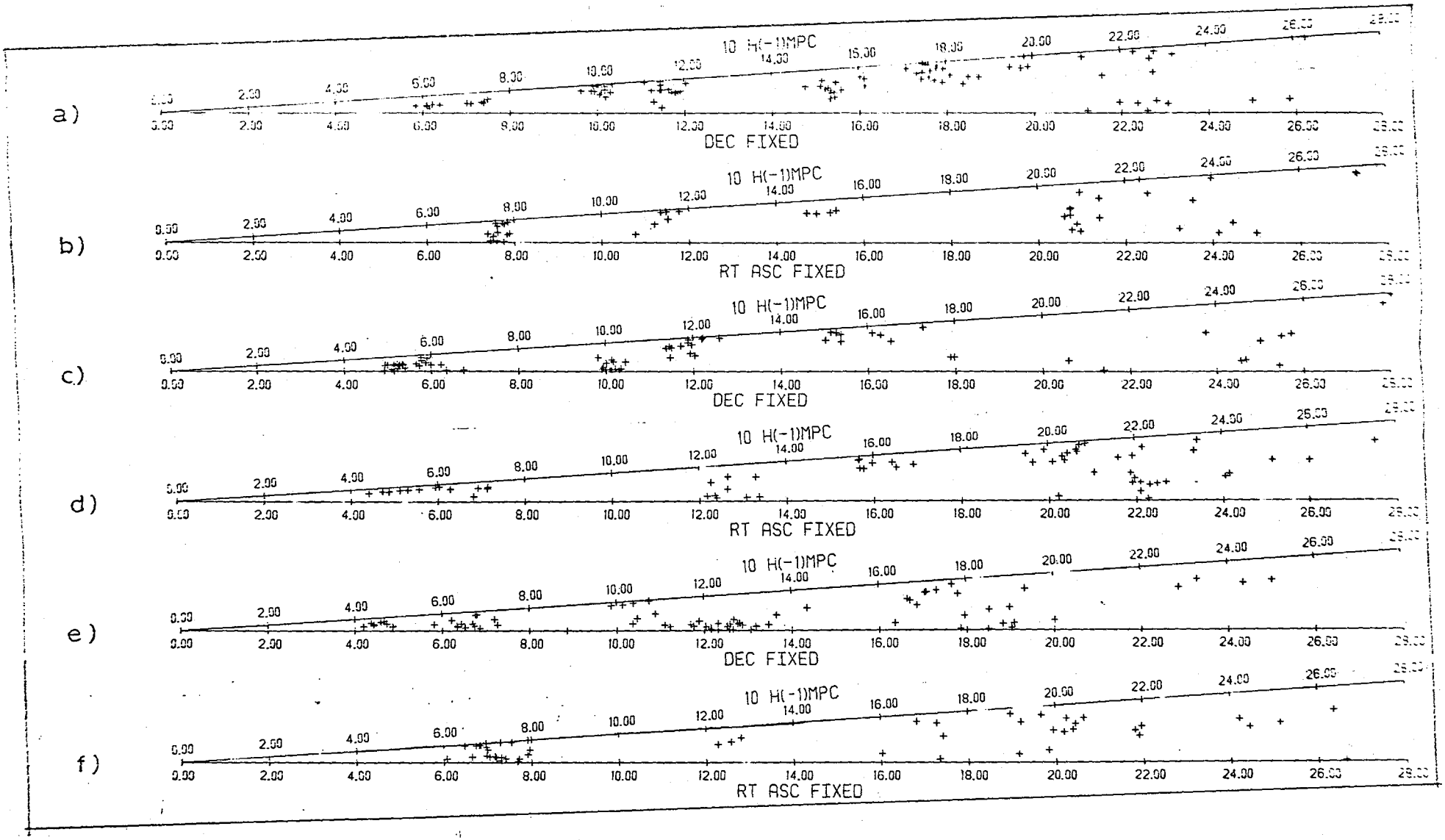

FIGURE 5.8 (a) - (f): Redshift plots for six separate fields of the simulated catalogues. Figs (a)-(c) come from catalogues with input $\langle v^2 \rangle^{\frac{1}{2}}$ = 200 km/sec with Figs (d) - (f) having $\langle v^2 \rangle^{\frac{1}{2}}$ = 500 km/sec.

classical interpretation being that the clusters are collapsing so that the redshift difference along the line of sight is reduced from pure Hubble flow (Jackson, 72).

Of more interest for our later purposes is the existence of structure preferentially elongated along the line of sight due to small scale motion in virialised groups. No such effect is very apparent in the AARS fields although some elongation is seen in the rich NP4 field of the KOS sample discussed in Part 1. The cluster in GNB, also discussed there, shows slight fingering but since this is the richest association in the sample, higher velocity dispersions may be expected. However, it should be noted that many of the galaxies in this cluster have poor velocities so the effect may be at least partly spurious.

This lack of fingering could be used as further evidence that the sample does not contain any prominent clusters where the velocity dispersions are known to be large. It may be noted too, that in a given instance, we do not know if the fingers (or flattening) are due to peculiar velocities or structure physically cigar-shaped and expanding along the line of sight. The correlation functions discussed in the next chapter allow for this by averaging overall orientations of clusters to give an estimate of $\langle V^2 \rangle$ averaged over all galaxy pairs.

Turning from the real data, Figs 5.8 (a-f) shows plots of six independent fields from the hierarchy simulations described in Chapter 3.7 that are primarily intended to test the statistical estimators used in the next chapter. The first three fields have included on the Hubble velocities random peculiar velocities of $\langle V^2 \rangle^{\frac{1}{2}} = 200$ km/sec the second three having a higher dispersion $\langle V^2 \rangle^{\frac{1}{2}} = 500$ km/sec.

Naturally the simulations do bear some resemblance to the observations since the three dimensional correlation functions are similar. Some sharp holes similar to the real data are seen, however this effect is probably

due to the discrete way that very similar model clusters were placed in the field volumes. Indeed it is doubtful such crude models are a fair match to the expected distribution from the gravitational clustering process that they are normally assumed to represent. Catalogues prepared from N body simulations may be a fairer representation (see below) but as noted in Chapter 3.7 these give a poorer match to the overall correlation statistics.

Perhaps the most useful comment that can be made from Fig 5.8 is that clusters in the last three plots look much more elongated in the redshift direction than either the first three plots or the observations, suggesting $\langle V^2 \rangle^{\frac{1}{2}}$ is, in reality, closer to 200 km/sec then 500 km/sec. In the next chapter correlation functions are used to test for such elongation in the data and simulations.

As noted above, the discussion in this section should be taken in a qualitative spirit, especially in a sample so small. In the larger CfA catalogue there are more independent clusters to examine and the large angle allows much of the large scale structure to be followed for its entire extent. Also the sample is large enough to partially volume limit the catalogue to dilute the affect of apparent magnitude selection.

As Davis et al (82) discuss, the general appearance of the clustering distribution in the CfA is 'frothy' and filamentary with prominent voids around clusters. Only a few large scale clusters appear significantly flattened along the line of sight and only in the three richest clusters are there strong fingers pointing away from the observer suggesting, like the AARS, the peculiar velocities are generally quite low.

These authors have also compared plots of the observations with catalogues prepared from the large N body simulations of Efsthathiou and Eastwood (81) that were evolved by gravity from poisson initial conditions. Although the overall amplitude of the clustering was made to match the CfA

as closely as possible, neither in the details of the clustering statistics or the overall 'texture' did the simulations resemble the CfA suggesting the initial conditions were different in the real universe or some 'secret ingredient' is missing in the simulations. One possibility here are processes included in the 'pancake' theory discussed in Chapter 2.1.2 in which large scale dissipative forces play an important role in forming large scale structure. Although harder to simulate than the gravitational clustering scenario simulations of the adiabatic picture (Melott, 83) suggest pancakes should collapse and form a cellular network structure with voids between, the cells expanding along one axis but collapsing along another. While these simulations are crude they do appear to match the visual distribution as well as or better than N body simulations perhaps suggesting these processes are involved in the real universe.

In Chapter 7 the theories are discussed again in the light of the clustering and velocity studies in the next chapter.

5.4 SUMMARY AND CONCLUSIONS

Although there is some evidence from the number magnitude and redshift counts of several catalogues for significant inhomogeneities on scales of tens of MPCS or larger, consistency studies on the AARS suggest the galaxy distribution in this sample, averaged over these scales, is close to homogeneity. This feature of the AARS, despite its relatively small volumes, may be due to the choice of fields whose depth and separation have certain advantages over the shallower surveys such as the KOS sample and even the much larger CfA. The width of the AARS fields compared to the depth is also large enough to reduce fluctuations that could occur in narrower but deep fields like those of the KOSS (81) sample.

While the sample may be reasonably representative of the universe as far as the overall homogeneity of the sample is concerned, examination of plots of the distributions in projection and redshift space suggest

occasional rich clusters present in large volumes of the universe have not been sampled in the AARS. Nevertheless the clustering at scales less than 10 MPC is very prominent, galaxies often situated in non-spherical clusters immediately surrounded by quite prominent voids. Rough estimates of $\langle V^2 \rangle$ from small groups picked out in projection and from comparison of redshift plots of the observations with simulated catalogues suggest $\langle V^2 \rangle^{\frac{1}{2}}$ is closer to 200 km/sec than the figure of 500 km/sec found statistically by Peebles from several redshift samples (Chapter 2.2.5).

We now turn to more objective studies of the clustering and relative velocities of galaxies by means of such statistical techniques applied to the newly compiled AARS.

CHAPTER SIX

CORRELATION FUNCTIONS IN POSITION AND VELOCITY

6.1 INTRODUCTION

One of the main motivations for the AARS was to measure reliably, perhaps for the first time, $\langle v^2 \rangle$, the relative peculiar velocity between galaxy pairs at small separations. With this, along with the amplitudes of the two and three point spatial correlation functions for the sample, we can use the Cosmic Virial Theorem to make an estimate of Ω. Deep samples, such as the AARS, are also ideal for examining the actual form of the three dimensional correlation function $\xi(r)$, especially at scales > 10 MPC where there has been much uncertainty.

As we discussed in Chapter 2, information on these statistics come from correlation functions estimated from the angular and velocity information in complete redshift samples. Although previous catalogues have been unrepresentative, the overall homogeneity of the AARS demonstrated in the last chapter suggests it should be meaningful to estimate correlation functions for this sample.

In the next section we define and discuss the estimation of the two point correlation functions $\xi_v(\sigma,\pi)$ and $\xi_s(s)$ mentioned in Chapter 2. The results of the estimates for both the AARS and simulated catalogues are presented and briefly discussed, indicating how they are to be used in the spatial and velocity studies.

Sections 3 and 4 are devoted to an estimate of $\xi(r)$. The first of these concentrates on the behaviour of $\xi_s(s)$ at scales > 10 MPC, the discussion involving a reanalysis of the KOS survey and comparison with the recently published CfA results. Section 4 examines the small scale

form and amplitude of $\xi(r)$ in considerable detail, on which $\xi_s(s)$ and $\xi_v(\sigma,\pi)$ provide complimentary information. Comparison is made again with the CfA results and with the well established projected studies.

The peculiar velocity dispersions are studied in Section 5, where $\xi_v(\sigma,\pi)$ is used to determine $\langle V^2 \rangle$ at several projected scales. A similar analyses of the KOS and Huchra catalogues is reported on and the results from the CfA discussed. Section 6 moves from the two to the three point correlation function and describes the estimation of Q for the AARS and KOS samples, which are compared with other results. Finally in Chapter 7, we briefly discuss aspects of the analysis that have been left out of section 4 and which rely, to some extent, on the results of sections 5.

6.2 ESTIMATION OF $\xi_s(s)$ AND $\xi_v(\sigma,\pi)$

After defining the correlation functions in Part 1, the estimation of $\xi_v(\sigma,\pi)$ and $\xi_s(s)$ for the observations and simulations are described together since the computation of both follows similar lines. Some of the results are presented in the final part which are briefly discussed before the more detailed analyses in the subsequent sections.

6.2.1 Definitions

To estimate the two point correlation function with the redshifts and angular coordinates of galaxies we consider a coordinate system in which σ and π are distances in redshift separation perpendicular and parallel to the line of sight between a galaxy i and a neighbour j. If these have an angular separation Θ in radians and $\Theta \ll 1$, these can simply be defined as $\sigma = V_i \Theta$ and $\pi = V_i - V_J$.

Following the discussion in Chapter 2.1, $\xi_v(\sigma,\pi)$ is defined through the probability dp of finding a neighbouring galaxy in volume element $dV_{\sigma',\pi'}$ at separation (σ,π) from a random galaxy

$$dp = \phi(r) \left(1 + \xi_v(\sigma,\pi) \right) d V_{\sigma,\pi} \qquad (6.1)$$

where $\phi(r)$ is the number density of galaxies at distance r in the sample.

Since at large scales the direct redshift separation between pairs is likely to be a good measure of distance one can estimate $\xi(r)$ directly as a function of redshift separation, $S = (\sigma^2 + \pi^2)^{\frac{1}{2}}$. This estimator, denoted as $\xi_s(s)$, can be given by an expression similar to eqn (6.1), involving the probability of finding a neighbour at distance s in any direction in a shell dV_s

$$dp = \phi(r) \left(1 + \xi_s(s) \right) dV_s \qquad (6.2)$$

6.2.2 Computation

As in the projected studies of $\xi(r)$ from $\omega(\theta)$, one can think of several alternative methods of estimating correlation functions with redshift information which would all give equivalent results in a perfectly fair sample of the universe but which in a finite sample may be expected to give slightly differing results. In $\omega(\theta)$, for example, as well as having to allow for edge effects in some way, one has the choice of counting unclustered pair counts from around real galaxies in the sample or from around points randomly distributed in the survey area. One also has to decide if to normalise these counts to the observed background surface density of galaxies or take the normalisation from a larger sample. To estimate correlation functions with complete redshift information we also require an estimate of $\phi(r)$, the selection function as a function of distance for the sample. As discussed in Chapter 5.2 even with the shape assumed, the selection of galaxies by apparent magnitude allows several ways to normalise it within the sampled volumes. The same arguments in Chapter 5 that applied to the normalisation also applies to the weighting of pairs ; to weight volumes of space equally one should weight each pair by the quantity $\frac{1}{\phi_i \phi_J}$ rather than equally.

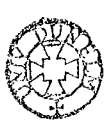

Taking these and other points into consideration the following estimates of the correlation functions was adopted, the choice of procedure being justified as the techniques is described now.

The sum of all observed pairs DD in a given interval $(d\sigma, d\pi)$ or dS were formed by counting the observed neighbours around each galaxy in the sample at separation (σ,π) or S and summing the counts from all galaxies. For $\xi_v(\sigma,\pi)$ the bin sizes were $d\sigma = d\pi = 0.5$ MPC with pairs around each galaxy calculated for $\sigma < 8.0$ MPC and $\pi < 20$ MPC. For $\xi_s(s)$ bin sizes of $\Delta\log(S$ MPC) = 0.1 were taken with only separations less than 200 MPC included. In neither $\xi_v(\sigma,\pi)$ or $\xi_s(s)$ were pairs counted between different fields and in both only galaxies with distances from 20 to 280 MPC were included, over which range the selection function is well defined.

Since the latter, estimated from Fig 5.3a of Chapter 5, varies by a large factor over this distance range, each pair was weighted equally since the weighting scheme $\frac{1}{\phi_i \phi_J}$ would cause relatively few distant pairs to dominate the counts. Although this means that an unfair excess or deficit of nearby clusters could bias the results, the agreement in Fig 5.3a between the data and the model suggest the sample is fair enough for this not to be a problem.

To calculate the pairs expected if galaxies were not clustered, 'background counts' were estimated around each observed galaxy by the relations $DR(\sigma,\pi) = \phi(r)\ dV_{\sigma,\pi}$ and $DR(s) = \phi(r)\ dV_s$, which were summed over all galaxies in the sample. The selective function was taken from Fig 5.3a which is normalised to the observed numbers in the sample. Although departures from the true number density will be present, as we discuss in the next section, normalising in this manner one can reduce associated fluctuations in the correlation functions.

Since the details of the estimate of DR differs between $\xi_v(\sigma,\pi)$ and $\xi_s(s)$ at this stage they are discussed separately now.

To estimate DR(σ,π) the prescription in Peeble (79) was followed and the volume $dV_{\sigma,\pi} = d\pi \times dA\ (\sigma)$ estimated by a Monte Carlo integration in which points were placed at random in σ around each galaxy and the fraction that fell in the AARS fields counted. To calculate $\phi(r)$ at (σ,π) around each galaxy Peebles used the observed galaxy counts at distance $r = V_i + \pi$ in all the fields apart from the one containing the galaxy. Although this gave a straightforward estimate of $\phi(V_i + \pi)$, it introduces unnecessary noise into DR(σ,π). Instead, to obtain smooth background counts, the form of $\phi(r)$ from Fig 5.3a was calculated in 0.5 MPC bins which were stored in a look up table during the computation.

Finally combining the counts DD and DR at $+\pi$ and $-\pi$, (since ξ_v should be even in π) $\xi_v(\sigma,\pi)$ was estimated from

$$\xi_v\ (\sigma,\pi) \quad = \quad \frac{DD\ (\sigma,\pi)}{DR\ (\ \sigma,\pi)} \quad - 1 \qquad (6.3)$$

To estimate DR(s), Nr points were placed at random in the redshift volumes with density at distance V_i proportional to $\phi(r)$ from Fig 5.3a. Counts of these random points were then made around each observed galaxy, this procedure dealing automatically with substantial and awkward edge effects and the selection of galaxies by apparent magnitude. To reduce the noise a factor of one hundred more points were placed down in each field than the numbers n expected to be visible in that field and $\xi_s(s)$ calculated from

$$\xi_s(s) \quad = \quad \frac{Nr}{n} \quad \frac{DD(s)}{DR(s)} - 1 \qquad (6.4)$$

As a test of this method for $\xi_s(s)$, a 'cells' estimator was considered by Shanks et al (83b) for the AARS. This involved dividing each field volume into 8 $(MPC)^3$ cubic cells and then forming the pair counts in bins of separation s. The advantage here is that random numbers are not needed because no awkward edge effects are involved and $\phi(r)$ can be

calculated analytically in the same manner as for $\xi_v(\sigma,\pi)$. The disadvantage is that the method loses (10%) pairs from bins that overlap the edge of the volumes and at small scales the binning in cells causes resolution to be lost.

Apart from estimating the correlation functions for the complete sample, they were also estimated for individual fields and for the sample split into north and south subsamples. In these cases, $\phi(r)$ was normalised as usual, to the numbers in the sample under consideration. Although individual field estimates do provide some insight into the errors on the total sample, a better understanding of these can be obtained by repeating the analysis on the first two sets of simulated catalogues described in Chapter 3.7. In this case one logically uses the input luminosity function and mean K correction to obtain $\phi(r)$, but with the normalisation estimated, as usual, from the total observed numbers in each catalogue. The only difference with the observations in the estimates of the correlation functions came in $\xi_s(s)$, where the ratio $\frac{Nr}{n}$ was reduced to 50 for computational speed.

Before discussing the results from the data and simulations it should be noted that all estimates of the correlation function were very insensitive to reasonable changes in the shape used for $\phi(r)$. For example the counts $DR(\sigma,\pi)$ changed only by two or three per cent if the selection function from the polynomial fits in Fig 5.5 was adopted rather than taken from the luminosity function in Fig 5.3a. Similarly on scales much larger than the cell size in the 'cell' estimator of $\xi_s(s)$ the results were in good agreement with the adopted method above despite the different weighting used in the estimation of the random pairs. This lack of sensitivity to the procedures adopted may be further evidence that the sample has no large biases and is fairly representative.

6.2.3. Presentation of the Results

The results for $\xi_v(\sigma,\pi)$ and $\xi_s(s)$ for the data are presented and discussed in (a) and (b) below. The ensemble estimates of $\xi_s(s)$ for the

simulations are presented in (c) along with models described later in this chapter.

(a) $\xi_v(\sigma,\pi)$

The results for $\xi_v(\sigma,\pi)$ are plotted in Figs 6.1 (a-c) which have been binned up in σ and π. The dashed lines correspond to fixed σ and π varying and the solid to fixed π and σ varying. The fixed variable in (a-c) corresponds to separations 0-0.5, 0.5-1.0 and 1.0-2.0 MPC, respectively.

Since the projected separation σ between pairs corresponds to a characteristic separation in space, comparison of the dashed and solid histograms in Fig 6.1 gives some idea of the peculiar velocities at different spatial scales. Although not apparent in the cone plots discussed in Chapter 5.3, the expected elongation along the π direction is very prominent in Fig (a) at $\sigma < 0.5$ MPC and considerably larger than the same effect expected due to measuring error. In Figs (b-c) the 'anisotropy' is hardly detectable, though at these scales we do expect it to appear less as the Hubble expansion velocities will be more dominant here. In fact in these two figs the solid histograms cross the dashed at scales > 4.0 MPC suggesting the clustering is actually flattened along the line of sight. A hint of this is visible in the redshift plots, at least those for fields GSA and GSD, and could be due to clusters forming at these scales. However, the sample is too small to tell whether the flattening is statistically significant.

The curves drawn on Figs 6.1 come from models of $\xi_v(\sigma,\pi)$ calculated by convolving the model spatial function with a velocity distribution with $\langle v^2 \rangle^{\frac{1}{2}} = 200$ km/sec, details of which are given in Section 5.

At scales larger than those shown in Figs 6.1, $\xi_v(\sigma,\pi)$ becomes significantly anticorrelated out to scales of 20 or 30 MPC. At these scales though a clearer view of the spatial function comes from $\xi_s(s)$.

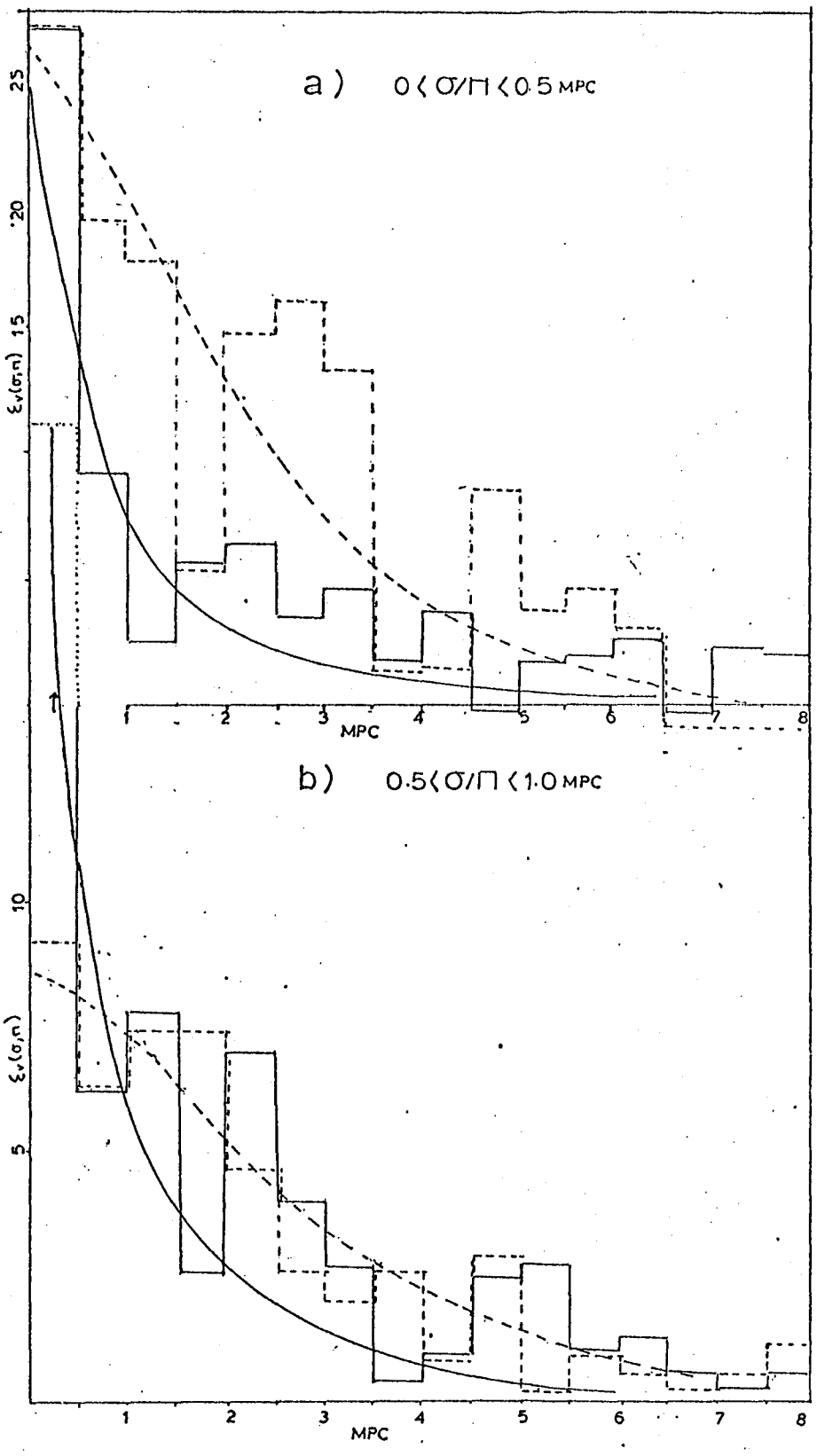

FIGURE 6.1 (a) - (b): Estimated $\xi_v(\sigma,\pi)$ and models for two separations with the dashed and solid histograms corresponding to σ and π fixed, respectively. The corresponding dashed and solid model curves assume $\langle V^2 \rangle^{\frac{1}{2}} = 200$ km/sec and $B = 1.3$.

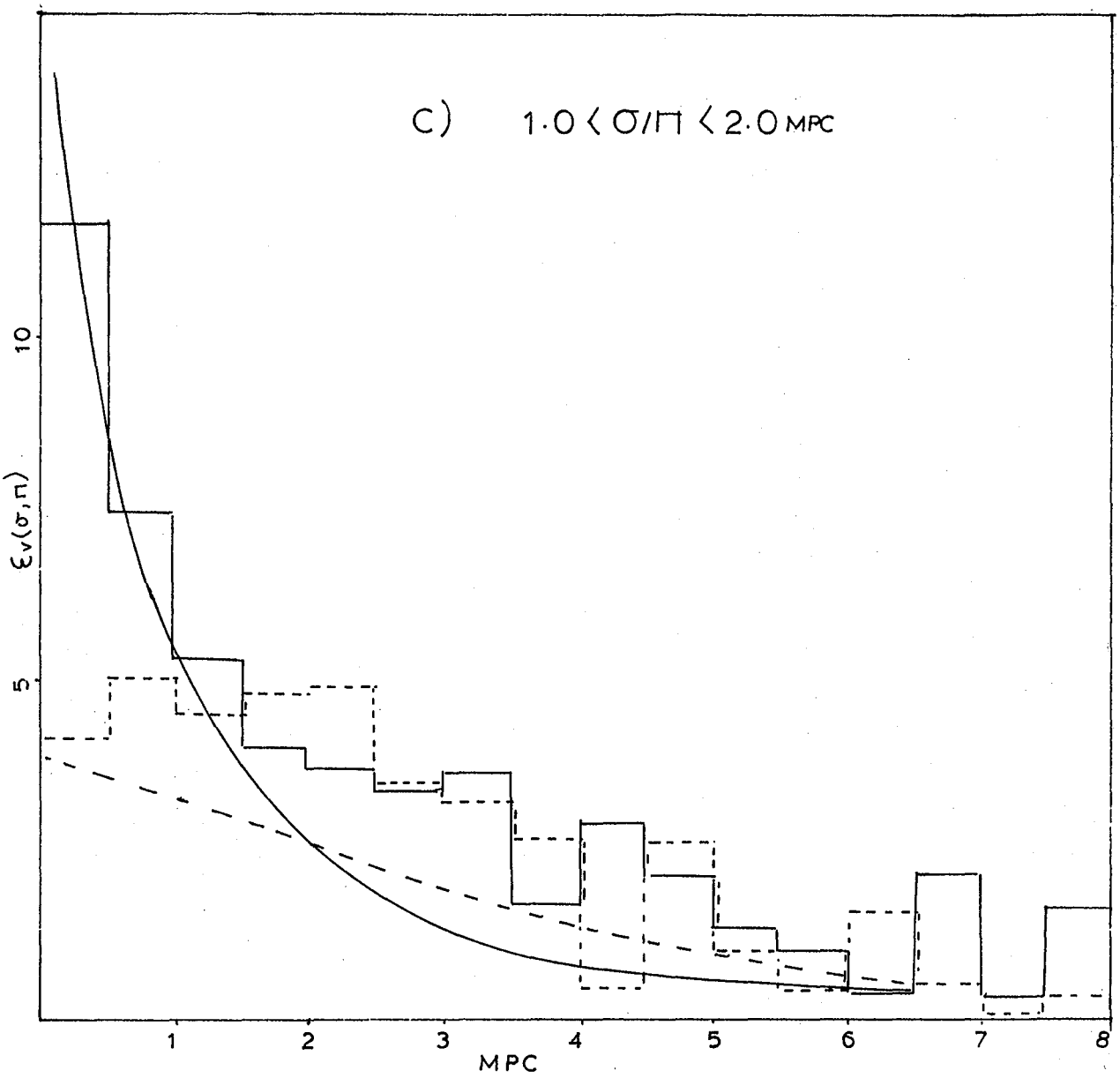

FIGURE 6.1 (c): As for Figs (a) and (b) for the final separation.

(b) $\xi_s(s)$

Fig 6.2 shows $\xi_s(s)$ against log s for scales 200>S> 1 MPC. The errors are taken from the analysis of the simulated catalogues, which are presented shortly, and agree well with fluctuations calculated from field to field estimates (not shown).

We see at scales > 20 MPC that $\xi_s(s)$ is mildly negative with $\xi_s \sim -0.1$, while in the range 10 <S <20 MPC it is significantly anti-correlated ($\xi_{mim} = -0.35$). The latter result and the strong clustering at smaller scales is suggested by examination of the redshift plots of Chapter 5, where we see prominent clusters immediately surrounded by quite empty regions. As discussed in Chapter 5.3, similar voids have been noted visually by other observers and $\xi_s(s)$ plotted here may be the first convincing statistical evidence for their reality.

One other prominent feature in Fig 6.2 is the 'bump' at 55 MPC which also appears statistically significant. This may indicate a lattice network of structure on these scales which is perhaps consistent with the findings of KOSS (81). Although obviously such a real feature could have vast implications for our understanding of the large scale structure of the universe and galaxy formation, further samples are necessary before any further discussion of it seems worthwhile.

In the next section we discuss Fig 6.2 more fully after comparing the results with those from other redshift samples.

A clearer view of the small scale clustering is given in Fig 6.3 where log ($\xi_s(s)$) is plotted against log s to test the powerlaw behaviour of the two point correlation function. The crosses refer to the total sample with the filled and open circles on the end of the error bars referring to estimates from the northern and southern subsamples respectively. The solid and dashed lines both represent -1.8 powerlaw models for $\xi(r)$ with amplitudes that vary by a factor of two and which are discussed in detail in Section 4.

For the present we can note that over the range 2-6 MPC the dashed line gives a reasonable representation of the behaviour of $\xi_s(s)$ (in both subsamples), but at smaller scales the solid line is more representative. Although peculiar velocities can reduce the clustering at these scales, the effect of convolving the solid line with a peculiar velocity dispersion $\langle V^2 \rangle^{\frac{1}{2}} = 200$ km/sec (dotted curve), shows the effect to be slight.

At scales greater than 6.0 MPC where $\xi_s(s) \lesssim 1$, $\xi_s(s)$ steepens away from the dashed line to a slope that, between 6 and 10 MPC, is closer to -4.0. As discussed in Chapter 2.1, the angular catalogues show a similar shoulder or 'break', the scale of which varies between 3 and 9 MPC.

Full details of the shape of $\xi(r)$ at these scales are given in Section 4, with $\xi_v(\sigma,\pi)$ providing information on the shape of $\xi(r)$ at the smallest scales, independent of peculiar velocities.

(c) $\xi_s(s)$ for the simulations

Fig 6.4 shows the ensemble $\xi_s(s)$ from the first and second set of simulations which are marked as filled circles and crosses respectively. The assumed spatial correlation function in both cases (dotted lines) is represented crudely by two powerlaw sections with slopes -1.8 and -4.0 joining at 6 MPC, the amplitude, slope and break of the small scale slope having been adjusted by the procedure in Chapter 3.7 to agree roughly with the results of $\xi_s(s)$ for the data in Fig 6.3. The dashed and solid curves are based on models for $\xi_s(s)$ estimated using this model for the spatial correlation function convolved with a velocity distribution function with dispersion corresponding to $\langle V^2 \rangle^{\frac{1}{2}} = 200$ and 500 km/sec respectively.

We see the two model curves reasonably fit the ensemble $\xi_s(s)$ from the two sets of simulations and while the dashed curve is close to the spatial function at scales beyond one MPC, the high velocity model and

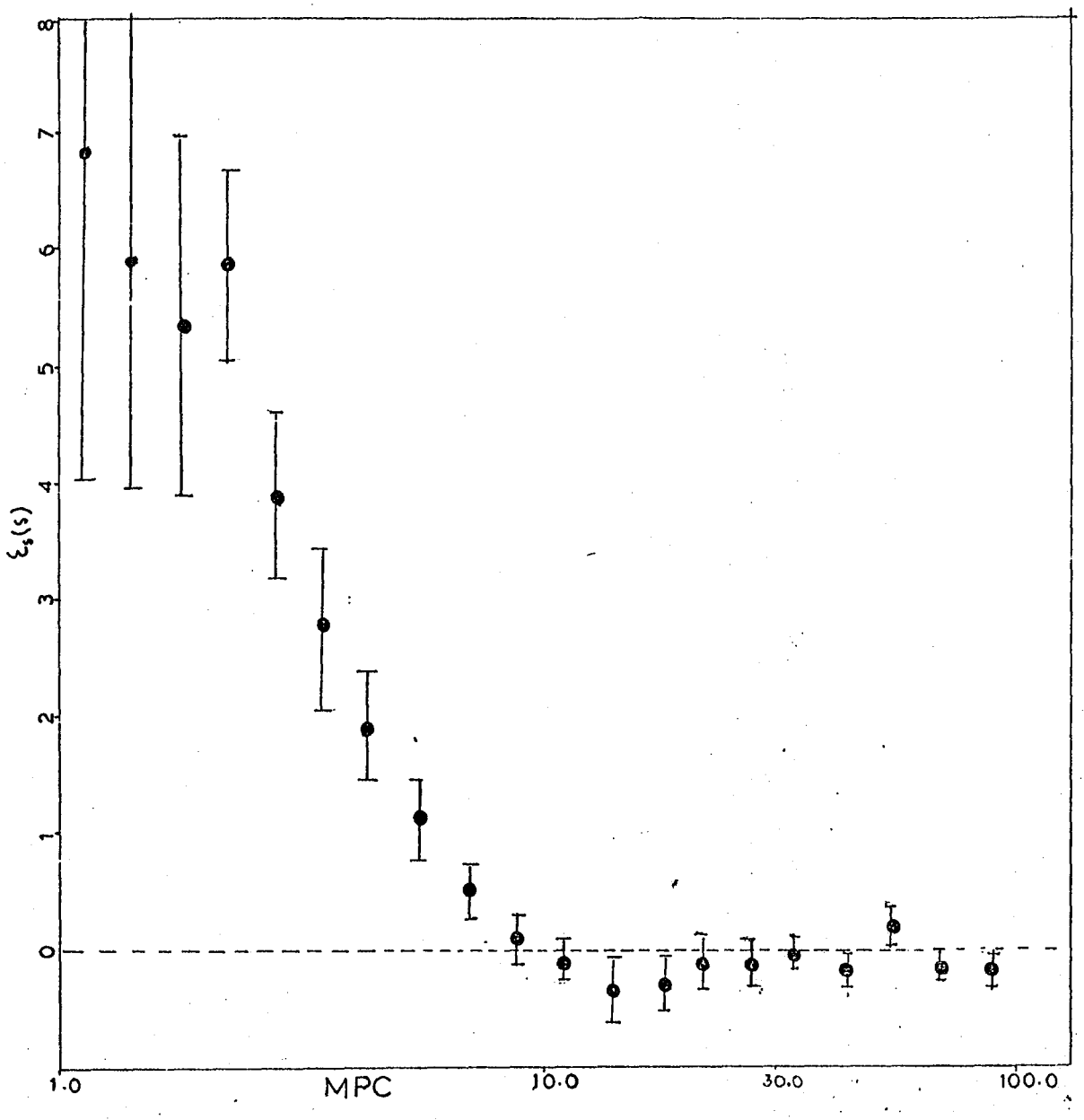

FIGURE 6.2: Estimated $\xi_s(s)$ for the AARS with errors taken from the simulated catalogues.

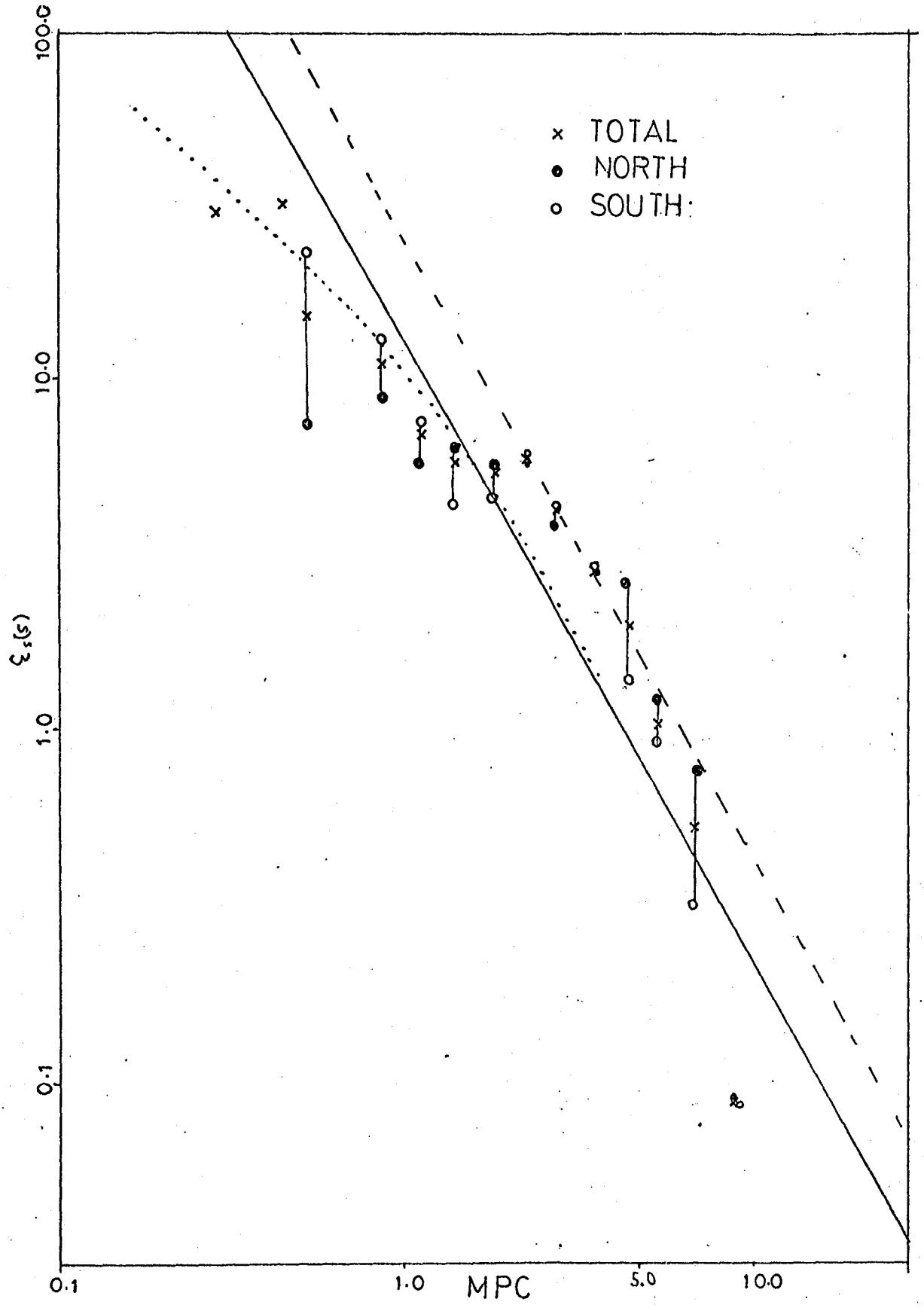

FIGURE 6.3: Estimated $\xi_s(s)$ for the AAPS along with models. The solid and dashed lines both represent -1.8 powerlaw models for $\xi(r)$ with amplitudes B = 13 and 26 respectively with the dotted curve corresponding to the solid powerlaw convolved with a velocity dispersion $\langle v^2 \rangle^{\frac{1}{2}} = 200$ km/sec.

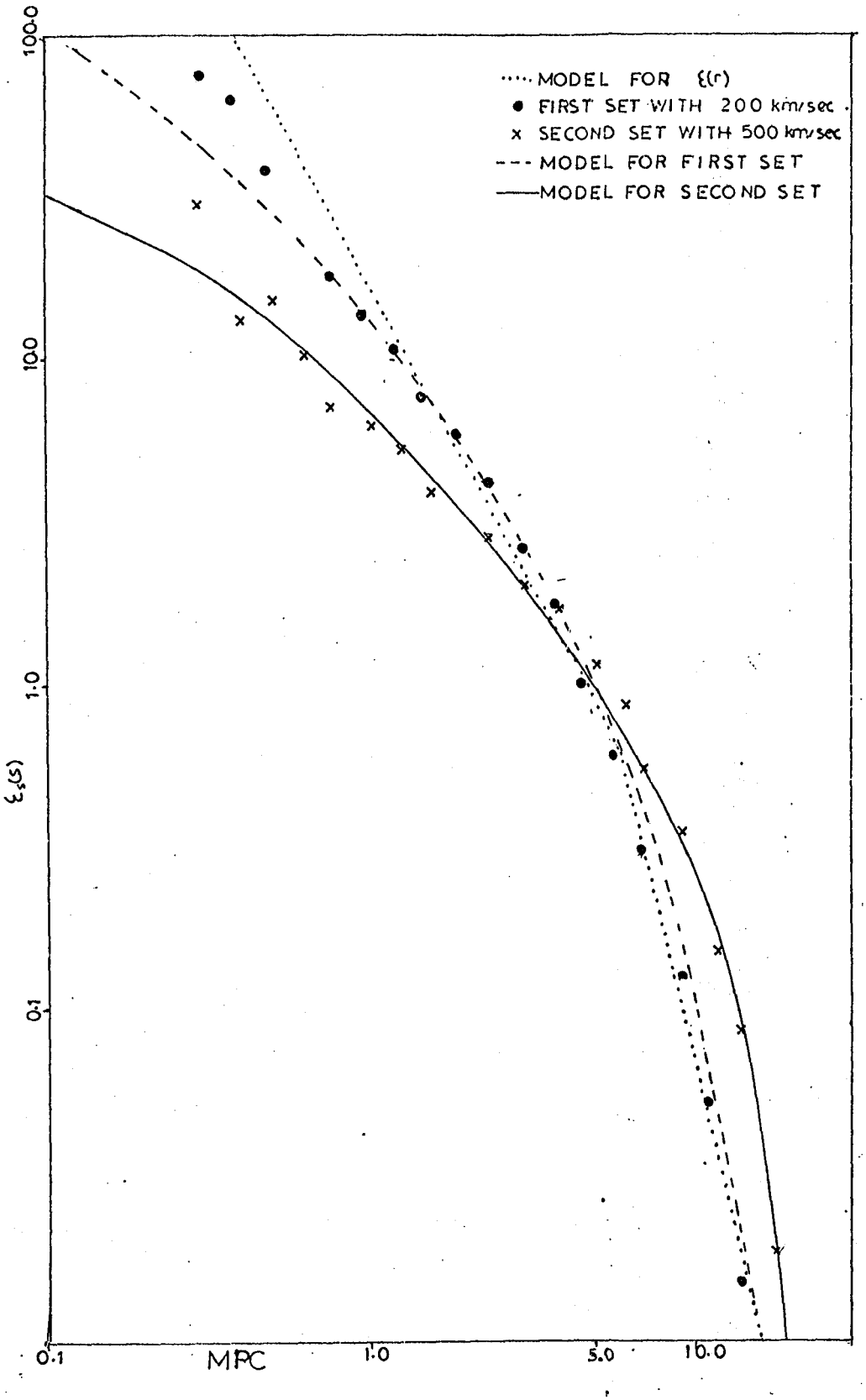

FIGURE 6.4: Ensemble $\xi_s(s)$ for the two sets of simulated catalogues. The corresponding models were both calculated assuming $\xi(r)$ is given by the two dotted powerlaw sections.

spatial function differ out to scales of 20 MPC. At larger scales though, the ensemble $\xi_s(s)$ for both sets are very close to zero, as expected.

Some of the results from the simulations are used in the following two sections to discuss $\xi(r)$ for the observations. Since the models here and in Fig 6.3 are similar to those for $\xi_v(\sigma,\pi)$ fully described in Section 5, in which the peculiar velocities for the sample are fully discussed, more detailed discussion of them is postponed until Section 7 of this chapter.

6.3 THE LARGE SCALE FORM OF $\xi(r)$

As discussed in Chapter 1, even modest redshift samples can provide considerably more information on the large scale form of $\xi(r)$ at scales greater than 10 MPC than $\omega(\theta)$ because the signal to noise is higher and because estimates are less affected by systematic errors that may occur at large angular scales. In Part 1 the results of a reanalysis of $\xi_s(s)$ for the KOS survey are described and in Part 2 the recently published estimates from the CfA are discussed. The results from the samples are discussed further in the final part where conclusions are presented.

6.3.1 $\xi_s(s)$ for the KOS Survey

The results for $\xi_s(s)$ in Fig 6.2 for the AARS are in sharp disagreement with the published results of Kirshner et al (79) (KOS) who claimed to have found correlations of order unity on scales $\sim$ 30 MPC. To check their results, $\xi_s(s)$ was re-estimated for the KOS survey by the method in Section 2.2, using galaxies between 20 and 180 MPC and with $\phi(r)$ taken from the solid curve in Fig 5.4a.

The results of the computation are shown in Fig 6.5 as crosses with the original KOS estimate marked as filled circles. We see the re-estimate is in much better agreement with $\xi_s(s)$ for the AARS than the original KOS estimate.

In an attempt to understand the different results the differences between the estimators were examined. In all there are three main points:

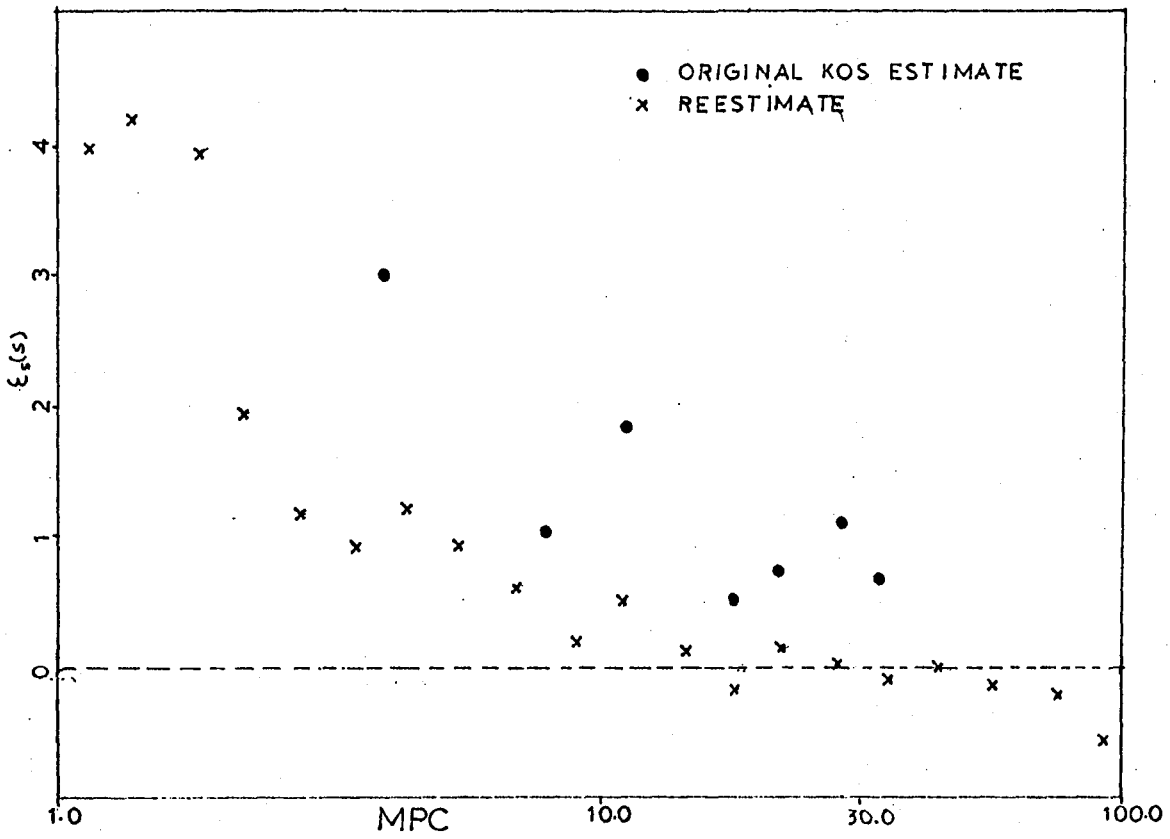

FIGURE 6.5: Estimates of $\xi_s(s)$ for the KOS survey

(a) The selection function used by KOS was closer to the dashed curve in Fig 5.4a than the solid curve.

(b) To normalise $\phi(r)$, KOS estimated ϕ^* from deeper number magnitude counts and normalised the dense northern fields with the less dense southern fields and vice versa.

(c) Rather than counting the pairs DD(s) and DR(s) cumulatively, KOS counted the factor $\left(\frac{DD}{DR} - 1\right)$ for each galaxy, weighted by $\frac{1}{\phi}$, so the outer volumes of the survey are given more weight than the estimator in Section 2.2.

Since from Fig 5.4 we see considerable inhomogeneities in the outer KOS volumes in the north compared to the rest of the sample, and, as differences (a-c) would tend to give a greater weight to these regions in $\xi_s(s)$, it might be thought these differences in the estimators may account for the seemingly larger clustering correlations found by KOS. However, adopting these changes to the estimator in Section 2.2 it was found that (a) and (b) made little difference to $\xi_s(s)$, while (c) produced results that bear no resemblance to either estimate, since $\xi_s(s)$ is then so strongly biased to pairs at larger distances in the fields.

Perhaps one of the reasons why large scale correlations were not induced by the change in (a) is that many of the pairs in the sample come from the strong clustering in field NP4 at around 60 MPC where the two selection functions in Fig 5.4a agree, the overdensity at large distances implied by the dashed curve being mainly cancelled by the underdensity in the nearer volumes.

Although the re-analysis is unsatisfactory in that it was unable to reproduce the original KOS results, Efstathiou (private communication) has found very similar results to the re-analysis estimates in Fig 6.5 with an independent program using a similar estimator to that used in Section 2.2. While this does not help account for the discrepancy it does indicate that

the results from the re-analysis of the sample are not due to an error in the computation. From this we can only conclude that the estimate of $\xi_s(s)$ given by the crosses in Fig.6.5 is the more reasonable one, as every care was taken to choose an unbiased an estimator as possible, considering the particular sampling problems of the KOS catalogue.

6.3.2 $\xi_s(s)$ for the CFA

It is also of interest to compare Fig 6.2 for the AARS with the newly published results of $\xi_s(s)$ from the CFA catalogue at large scales. This correlation function has been estimated for this sample by Davis and Peebles (83) (DP) who used galaxies with $B'' > 40^{\circ}$, $\delta > 0$ and $b_z \leq 14.5$. Eliminating the intrinsically faint galaxies to judiciously dilute the affect of Virgo and removing the galaxies at distances greater than 100 MPC, the remaining sample had some 1200 galaxies.

The computation used was similar to that in Section 2.2 but in this case the counts DD(s) and DR(s) were weighted by the factor $\frac{1}{\phi_i \phi_J}$. As DP discuss, since the sample is so large and partially volume limited the weighting should not bring in too much noise at the larger scales.

Although the results (DP, Fig 1) from the northern sample (and from 270 galaxies in the south) agree with the results in Fig 6.2 in that no large correlations are seen on tens of MPCS, in detail the estimates of $\xi_s(s)$ differ between the two samples. DP find for the CFA positive clustering between 10 and 20 MPC with $\xi_s(s)$ steadily falling from 0.5 to zero in contrast to the quite strong anticorrelation found in the AARS at these scales. Over the range $30 < s < 50$ MPC the agreement is better with $\xi_s(s)$ averaging -0.05 for the CFA, similar to the AARS.

Since the northern CFA sample contains roughly four times the galaxies and volumes sampled as the AARS it might be supposed that the results from this sample are considerably more reliable. However, as discussed in Chapter 5.2, this need not be the case for several reasons.

Although the CFA volumes are large the characteristic depth $\sim$ 60 MPC is quite shallow so we only expect a few spatial groupings on the scales discussed above. Another related problem is that the model number redshifts relation used to estimate $\phi(r)$ is a poor fit to the observed data (Davis and Huchra, 82) and clearly shows clustering on scales comparable to the depth of the survey. While DP used a selection function estimated in a manner unbiased by inhomogeneities, $\phi(r)$ still depends on the accuracy of the Zwicky magnitude system and on the assumed model for Virgo infall. Also systematic effects such as galactic obscuration could make $\phi(r)$ depend on projected position as well as redshift. Since these could all affect $\phi(r)$, the estimate of $\xi_s(s)$ could also be systematically altered at large scale through systematic effects both in the background counts and weighting of the observed counts. Unfortunately, these authors have not discussed the dependence of their results on reasonable changes in $\phi(r)$.

Of course similar effects may occur in the AARS but here the depth of $\sim$ 200 MPC reduces the effect of such coherence problems and makes $\xi_s(s)$ insensitive to reasonable changes in $\phi(r)$ so long as it is a reasonable fit to the observed number redshift counts, as we have seen in Fig 5.3.

6.3.3 Discussion of the Results

Perhaps the most important results from the discussion in this section is that the AARS, CFA and KOS samples all appear to be consistent with $\xi(r)$ close to zero on scales > 20 MPC. Although $\xi_s(s)$ is slightly negative at these scales, small systematic effects are likely to occur on the maximum scales of the samples due to errors in the model for $\phi(r)$, the integral constraint discussed by Groth and Peeble (77) and the relatively few independent clusters that contribute to the pair counts.

As discussed in Chapter 5.2, the small numbers of independent clusters means there can also be considerable errors in the normalisation, which from the simulations of the AARS amount to $\frac{dN}{N} \sim 0.15$. However as DP

discuss, this need not imply $\xi_s(s)$ is uncertain by this factor, since if the normalisation is taken from the sample itself, fluctuations in DD(s) and DR(s) due to errors in the normalisation will tend to cancel leaving $\xi(r)$ unaffected. While there is the possibility that the behaviour of $\xi(r) > 20$ MPC reflects real anticlustering, it is equally likely that for the present samples systematic errors are responsible for the effects.

However, much harder to explain in this way is the strong anti-correlation at scales 10-20 MPC seen in the AARS. While this is not seen in either of the two other samples, since the AARS is larger than the KOS survey and deeper than the CFA it may as yet be the most reliable estimate of $\xi(r)$ at these scales, providing the first convincing statistical evidence for the holes noted by many observers recently.

Some external evidence for anticlustering over some range of scales comes from the recent, very low estimates of the quadrapole anisotropy of the microwave background (Lubin,82) that provides constraints on the clustering of the matter distribution. In particular a vanishing quadrapole moment, similar to observed, implies the integral $J_3(r_c) = \int_o^{r_c} \xi(r) r^2 \, dr$ (Peebles, 82) goes to zero if integrated to infinite scale, requiring that $\xi(r)$ must become negative over some of its range. Taking $\xi(r)$ from Fig 6.2 and adding a constant 0.1 to bring $\xi_s(s)$ close to zero beyong > 20 MPC, we find the positive and negative contributions to J_3 on scales less than 20 MPC agree to within 70%, not inconsistent with $J_3 \sim 0$.

While this appears attractive support for the observed anticorrelation seen in the AARS, it should be remembered the statistical significance of the feature is still quite low and it would take only a slight anti-correlation at larger values of r to produce the result $J_3 \sim 0$.

At present, taking the redshift samples together, it is probably fair to say that at scales greater than 10 MPC galaxies are roughly homogeneously

distributed. Of course this does not exclude occasional structure occurring at larger scales ; indeed, as DP discuss, it takes only weak clustering in $\xi(r)$ at $r > 10$ MPC to produce considerable fluctuations in density on much larger scales that are so evident in plots of the galaxy distribution in the CFA.

As discussed in Chapter 1.2, there is some strong statistical evidence for structure present on scales > 10 MPC, with clustering correlations of order unity existing between Abell clusters on scales of 30 MPC (Hauser and Peebles, 73) and the envelopes of these clusters existing to 40 MPC (Seldner and Peebles, 77a). However, as Peebles (80a, p.299) notes, the Abell clusters need not be good tracers of the general galaxy distribution and their contribution to $\xi(r)$ on the scales of interest may be quite small.

In Chapter 7 we consider how knowledge of the large scale form of $\xi(r)$ can, with dynamical information, provide constraints on the large scale distribution of matter and Ω, and insight into the processes involved in galaxy formation.

6.4 THE SMALL SCALE FORM OF $\xi(r)$

In order to investigate the unusual form of $\xi(r)$ at scales less than 10 MPC found for the AARS, this section is split into four parts. The first gives details of the shape of $\xi(r)$ derived from $\xi_v(\sigma,\pi)$ and $\xi_s(s)$ for the AARS, the second using similar estimates of these functions from the CFA and simulated catalogues to test the findings of the AARS. The third part compares the AARS results with $\omega(\theta)$ from projected catalogues, the analyses being summarised and concluded in the final part.

6.4.1 Analyses of $\xi_v(\sigma,\pi)$ and $\xi_s(s)$

As outlined in Chapter 2.1, the redshift correlation functions can be used to examine the shape and amplitude of $\xi(r)$ at small scales, independent of the effects of peculiar velocities.

This can be done by means of an integral of $\xi_v(\sigma,\pi)$ defined as

$$W_v(\sigma) = \int_0^{\pi cut} \xi_v(\sigma,\pi)\, d\pi \qquad (6.5)$$

By conservation of pairs along the line of sight it can be seen that (Peebles, 79)

$$W_v(\sigma) = \int_0^{\pi cut} \xi((\sigma^2 + \pi^2)^{\frac{1}{2}})\, d\pi \qquad (6.6)$$

provided that we choose $\pi cut >> \frac{\langle v^2 \rangle^{\frac{1}{2}}}{H}$ (6.7)

at which scale we expect $\xi_v \sim \xi$.

If we model $\xi(r)$ by a powerlaw out to large scales (eqn. 2.3) then eqn. (6.6) gives

$$W_{PL}(\sigma) = \frac{B}{\sigma^{\gamma-1}} \quad \frac{\Gamma(0.5)\,\Gamma(\gamma-1)}{\Gamma\,(\frac{\gamma}{2})} \qquad (6.8)$$

provided eqn (6.7) holds and $\pi cut >> \sigma$, so as to include all correlated pairs and peculiar velocities.

Fig 6.6 shows the result of plotting log $(W_v(\sigma))$ as a function of log σ (crosses) with $\xi_v(\sigma,\pi)$ from the data calculated at six values of σ and with πcut = 20.0 MPC in eqn 6.5. The solid line comes from the powerlaw model in eqn 6.8 fitted by eye with $B \simeq 11.5$ and $\gamma = 1.8$.

We see that the data is in remarkable agreement with the powerlaw slope of -0.8 found for $\omega(\theta)$ at small angular scales from several projected catalogues (see Chapter 2.1). However, as shown below, this need not imply that $\xi(r)$ is well approximated by a simple -1.8 powerlaw over the corresponding spatial scales.

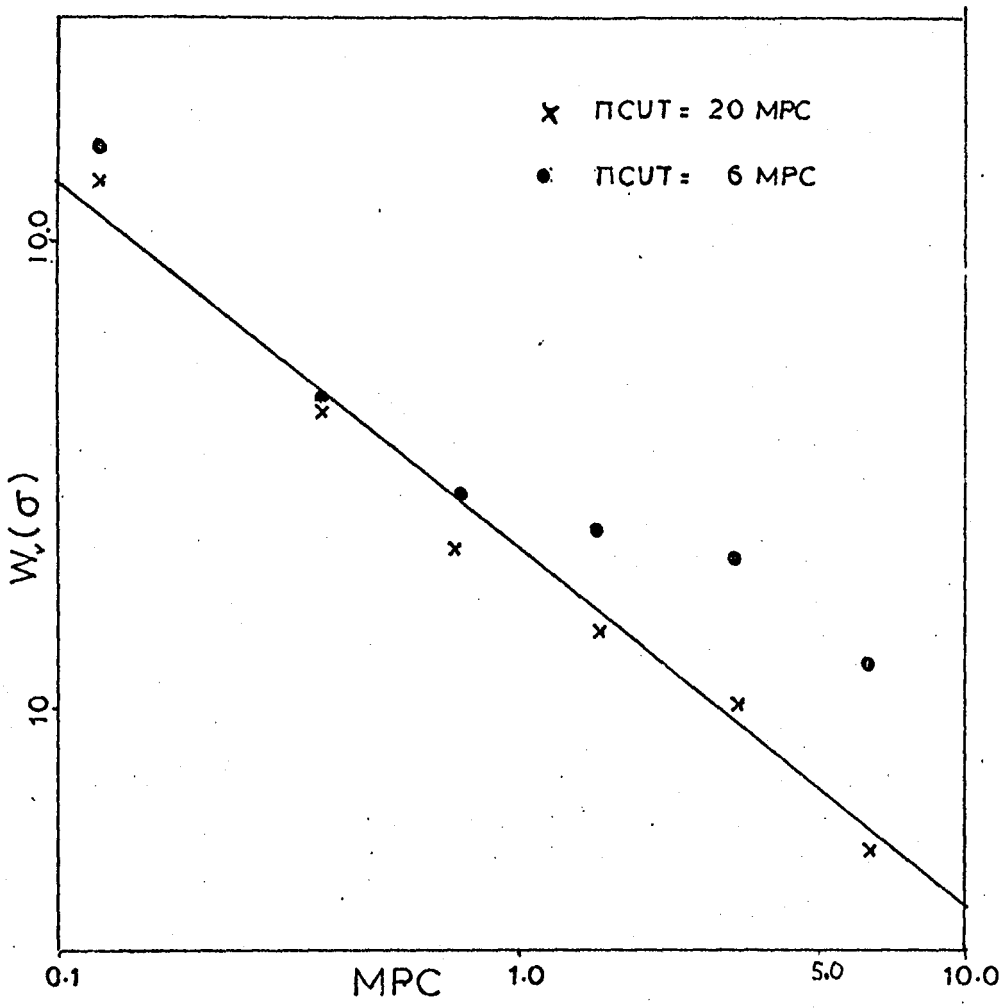

FIGURE 6.6: Estimated $\omega_v(\sigma)$ (crosses) from the integral of $\xi_v(\sigma,\pi)$ for the AARS along with expected powerlaw model (solid line). Filled circles show behaviour expected when integral is confined to $\pi cut \leq 6.0$ MPC.

TABLE 6.1: B as a Function of Separation for the AARS

$\bar{\sigma}$ (MPC)	B	B(NORTH)	B(SOUTH)
0.125	15.8	20.0	10.7
0.375	10.9	9.2	14.9
0.75	12.2	13.5	10.1
1.5	16.9	22.3	13.9
3.0	25.8	36.6	19.4
6.0	25.9	29.0	18.0

From Fig 6.2 we see at 20 > r >6 MPC $\xi_s(s)$ appears to exhibit strong non-powerlaw behaviour and, as this is not allowed for in the model in eqn 6.8, this can significantly affect the estimates of B and γ. To check the consistency of the model with data, πcut was reduced to 6.0 MPC and the right-hand side of eqn 6.6 with the powerlaw model for $\xi(r)$ in eqn 2.3 was numerically integrated to obtain B at different values of σ(Peebles, 79). Although πcut is now considerably reduced, the models for $\xi_v(\sigma,\pi)$ in the next section suggest the requirement in eqn 6.7 still holds so most peculiar velocities are included.

The results are in Table 6.1, along with estimates from the sample split into north and south subsamples. To show the effect of this correction in Fig 6.6, the filled circles refer to points calculated from eqn 6.6 with amplitudes B corresponding to those given in Table 6.1.

Although the estimates on Fig 6.6 are little changed at the smallest scales, at σ > 1 MPC there is a steady rise above the solid line out to 6 MPC that is also seen in the subsamples in Table 6.1.

It might be thought that this behaviour is due to fluctuations from the relatively few distant clusters that contribute to $W_v(\sigma)$ at these scales. However similar behaviour is seen in $\xi_s(s)$* in Fig 6.3, where pairs preferentially come from the π rather than the σ directions. In this figure we see the solid line (which corresponds to a -1.8 powerlaw with B = 13 which fits $W_v(\sigma)$ at σ < 1.0 MPC) is a poor fit to $\xi_s(s)$ at scales > 2.0 MPC. At this and larger scales the dashed line with B = 26 fits reasonably and agrees with B found at these scales from Table 6.1.

* It should be noted that large streaming motion could be partly responsible for the overall flatter slope in $\xi_s(s)$ than expected, since close pairs would be drawn together more in the redshift direction at small than large scales. However it seems unlikely that this could significantly affect the conclusions from $W_v(\sigma)$.

The most obvious explanation for the behaviour in $\xi_s(s)$ is that peculiar velocities move pairs from smaller to larger scales raising the apparent clustering there. However, as noted in Section 2.3, the dotted curve in Fig 6.3 is a model for $\xi_s(s)$ based on $\xi(r)$ from the solid line convolved with a peculiar velocity distribution function with $\langle V^2 \rangle^{\frac{1}{2}} = 200$ km/sec. Although this fits the observed $\xi_s(s)$ at $s < 2.0$ MPC, at larger scales we see peculiar velocities are not able to account for the rise above the solid line. This can also be seen in the models and ensemble estimates of $\xi_s(s)$ for both sets of simulated catalogues in Fig 6.4.

That this should be the case can also easily be seen from a conservation of pairs condition for $\xi_s(s)$ similar to that used for $W_V(\sigma)$ above. The relation involves $J_3(r)$ (mentioned in Section 3.3.) so that

$$J_3(\text{Scut}) = \int_0^{\text{Scut}} r^2 \, \xi(r) \, dr = \int_0^{\text{Scut}} s^2 \, \xi_s(s) \, ds \qquad (6.9)$$

which holds for $\text{Scut} >> \frac{\langle V^2 \rangle^{\frac{1}{2}}}{H}$.

Taking Scut = 6.0 MPC we find the right-hand side of eqn 6.9 from the data gives J_3 (6.0 MPC) = 186, which equating to the left-hand side model implies that if $\xi(r)$ is a -1.8 powerlaw it must have an amplitude B = 26. This corresponds to the dashed rather than the solid line in Fig 6.3.

From this discussion we must conclude that the rise of $\xi(r)$ above a-1.8 powerlaw at separations greater than 1 MPC is a real feature of the spatial clustering correlation function for the AARS. Whether it is a true feature of the universal $\xi(r)$ is a topic we discuss in the next two parts of this section.

For the present though,we have to decide what is the most characteristic amplitude of B to use in the CVT. Since the latter can only be applied reliably at small scales and as $\xi(r)$ (through $W_V(\sigma)$) appears to

converge quite well to a - 1.8 powerlaw at scales smaller than 1 MPC, it seems appropriate to use B at these scales.

Taking the mean of the first three values of B in Table 6.1 we find

$$B = 13.0 \pm 4.0 \qquad (6.10)$$

which is adopted as characteristic for the sample in most future discussions. The error here comes from $W_v(\sigma)$ calculated from the simulations at these scales which is discussed in the next part. If, instead we were to take the standard error of the six values from the north and south subsamples in Table 6.1 we get a lower error for B of $\pm$ 1.4.

Finally, it is interesting to note the value in eqn 6.10 is close to the amplitude B = 12.8 $\pm$ 1.4 found by Peebles (79) for the KOS sample using the same method but averaged over scales σ < 4.0 MPC. Although it is considerably lower than B = 21.5 quoted for the CFA at σ < 2.0 MPC (Davis and Peebles, 82) it is quite close to B = 16.0 found from W (θ) for the Zwicky and Lick catalogues estimated using an assumed luminosity function (see Chapter 2.1). These latter two values are discussed in the two subsections that follow now.

6.4.2 Comparison with the Simulations and the CFA

In order to test the significance of the non-powerlaw behaviour found in $\xi(r)$ in Part 1 the results from $W_v(\sigma)$ and $\xi_s(s)$ for the AARS have been compared with estimates from simulated catalogues and the CFA.

The quantity $W_v(\sigma)$ given by eqn 6.5 was calculated with πcut = 6.0 MPC for the CFA using the published diagrams of $\xi_v(\sigma,\pi)$ given in Davis and Peebles (82) (DP), the latter having been estimated by a procedure similar to that described in Section 2.2. for the AARS. The corresponding estimate of $W_v(\sigma)$ for the simulations was computed from $\xi_v(\sigma,\pi)$ with πcut = 6.0 from each simulation, from which an ensemble $W_v(\sigma)$ and standard deviations were estimated. Assuming a powerlaw model for $\xi(r)$ with γ = 1.8 in eqn 6.6, these estimates of $W_v(\sigma)$ were used to provide an amplitude B as function of

separation σ in the same way as for the AARS in Table 6.1.

The amplitude B as a function of separation is shown in Fig 6.7 for the AARS, CFA and simulations which are represented as circles, triangles and squares respectively. The open symbols in each case refer to B from $W_v(\sigma)$ while the filled symbols come from binned up estimates of $\xi_s(s)$ taken from Fig 6.3 for the AARS, Fig 6.4 (filled circles) for the simulations, with the CFA results coming from Fig 1 of DP. For these filled symbols the value B refers to the amplitude a -1.8 powerlaw would need to have to pass through $\xi_s(s)$ at the separation concerned which, to avoid the effects of peculiar velocities, are taken at scales $S \gtrsim 2.0$ MPC. The errors on the AARS results come from fluctuations in B from $W_v(\sigma)$ and $\xi_s(s)$ estimated from the simulated catalogues at the corresponding separations.

We see from this figure that, while the AARS shows a strong rise of B with scale, the simulations are roughly consistent with a -1.8 power law out to $\sim$ 5 MPC ; although there is some indication that the slope assumed in the estimate of B is somewhat steeper than -1.8 probably due to the finite nature of the hierarchy put down in Chapter 3.7. It might be expected that increasing statistical fluctuations at scales > 1 MPC can account for the behaviour seen for the AARS. However, the errors from the simulations show that the rise between 1 and 5 MPC is significant at over the two sigma level and the effect is seen in both subsamples in Fig 6.3. Furthermore, a similar, although weaker, trend is seen in the CFA where B from $W_v(\sigma)$ rises by 50% over the same scale range, the triangles in most cases lying within the error bounds for the AARS.

Since the CFA is considerably larger than the AARS we would expect, at least at scales < 5 MPC, that the fluctuations in B for this sample should be smaller than given by the simulations. This gives strong support for a real rise above a -1.8 powerlaw in $\xi(r)$, at the scales of interest in Fig 6.7.

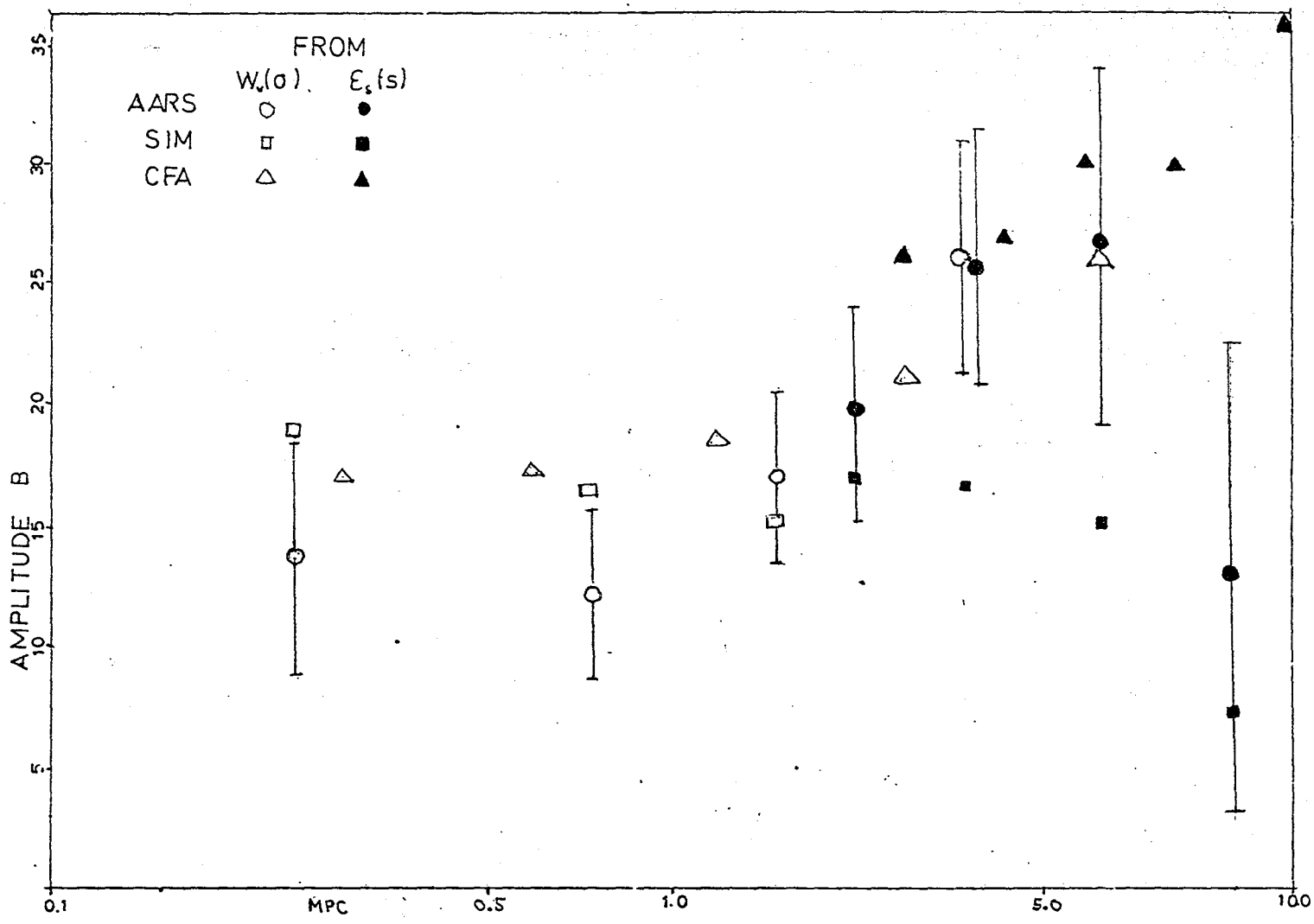

FIGURE 6.7: The amplitude B of $\xi(r)$ as a function of separation from two redshift samples and the simulated catalogues. The errors on the AARS results come from corresponding estimates from the simulated catalogues.

Although the data from the velocity smoothed $W_v(\sigma)$ in Fig 6.7 for the AARS and CFA indicate a fairly continuous rise above a powerlaw beyond 1 MPC (the data for the CFA fitting a -1.5 slope reasonably), Fig 6.3 shows that the direct estimate of $\xi_s(s)$ for the AARS has a quite prominent feature at 2 MPC (that is seen in both subsamples) that is unlikely to be due to peculiar velocities. While no corresponding 'hump' is seen in $\xi_s(s)$ for the CFA, as DP discuss, weighting the pairs by the selection function, as was done forthe CFA, will tend to increase the noise at small scales which may cause features to be missed. Naturally larger redshift samples are necessary both to test the general non-powerlaw behaviour further and search for any particular features that may be present.

It may be wondered at this stage, why the non-powerlaw behaviour found for $\xi(r)$ in the CFA here, was not noted by Davis and Peebles (82)*. The reason for this can be seen as follows :

To calculate B for the CFA, DP estimated $W_v(\sigma)$ for $\sigma < 16.0$ MPC with πcut = 25 MPC. The resultant curve (Fig 2 of DP), like Fig 6.5 for the AARS, is well approximated by a -0.8 powerlaw slope over the range 1 to 6 MPC in σ, the fit to $W_v(\sigma)$ at $\sigma <$ 2.0 MPC giving B = 19.5, with a similar value being found by inverting $W_v(\sigma)$ to give $\xi(r)$ directly. However, as discussed in Part 1 of this section, the assumption here is that the simple powerlaw holds out to 25 MPC in the integral over $\xi_v(\sigma,\pi)$ (eqn 6.5). As DP discuss, at scales s > 10 MPC $\xi_s(s)$ falls quite rapidly, while at s = 6.5 (where ξ= 1) we see from Fig 6.7 that B = 30 ; hardly consistent

* The present discussion is based on an early preprint in which the authors claimed that models for $\xi_v(\sigma,\pi)$ were well fitted at $\sigma < 6.4$ MPC by a -1.8 powerlaw for $\xi(r)$ with B = 18. However a private communication established that this claim was in error, as can be seen by models of $\xi_v(\sigma,\pi)$ for the CFA sample presented in Section 5.6.

with simple powerlaw behaviour. Although this latter behaviour is significantly different from that seen in Fig 6.3 for the AARS, apparently the smoothing in velocity over large scales in each sample makes $W_v(\sigma)$ approximate a powerlaw at $\sigma < 6.0$ MPC.

We now turn to discuss the behaviour of $\xi(r)$ at scales > 6.0 MPC and projections of $\xi(r)$ in more detail.

6.4.3 Comparison with Projected Catalogues

In Part 1 we saw that $W_v(\sigma)$, when smoothed over large separations, gave rise to a simple powerlaw, close to the observed form seen in $\omega(\theta)$ from several projected catalogues. Since the latter are considerably larger than the AARS and generally regarded as fair samples, it is important to test if $\omega(\theta)$ for the AARS is consistent, both in form and overall amplitude, with these observations.

Although the AARS is too small for a direct estimate, by projecting $\xi(r)$ for the sample through limbers eqn (Limber, 54) one can predict the form of $\omega(\theta)$ one would expect to see. The transformation is given by

$$\omega_M(\theta) = \frac{\int_0^\infty x^2 \phi^2(x)\,dx \int_{-\infty}^{\infty} dy\ \xi\left((y^2 + (\theta x)^2)^{\frac{1}{2}}\right)}{\left[\int_0^\infty x^2 dx \phi(x)\right]^2} \qquad (6.11)$$

where $\phi(x)$ is the selection function. Although this particular form assumes $\theta \ll 1$ and $(y^2 + (\theta x)^2)^{\frac{1}{2}} \ll x$ it should give a reasonable approximation to the behaviour of $\omega(\theta)$ at small angular scales.

To apply to the AARS, $\xi(r)$ was modelled with the two powerlaw sections shown in Fig 6.3 (solid at $s \lesssim 2$ MPC, dashed at $s > 2$ MPC) with a powerlaw slope of -4.0 between 6.0 and 10.0 MPC. To model the observed behaviour at > 10 MPC, $\xi(r) = -0.11$ was set for $r < 20$ MPC, with $\xi(r) = 0.0$ beyond. This value was chosen to roughly model the anticorrelation seen in Fig 6.2, but give $J_3 = 0$, consistent with the discussion in Section 3.3.

Using the selection function based on the curve for the AARS in Fig 5.3a transformed into Zwicky magnitudes by eqn 5 in Table 3.2, eqn. 6.11 was numerically integrated to estimate how $\omega(\theta)$ would appear at $B_2 = 15.0$. At these depths one degree corresponds to a characteristic projected distance of slightly over 1 MPC.

The results of log ($\omega_\mu(\theta)$) against log (θ degrees) are shown in Fig 6.8 as a solid line, along with the observed Zwicky (crosses) and scaled Lick (circles) estimates, discussed in Chapter 2.1. The filled squares are a mean of the two scaled estimates given in Fig 12.b of Shanks et al (80), where $\omega(\theta)$ was estimated from deep machine measured catalogues taken from U.K. Schmidt plates. Also shown are the model results (dashed line) of extending the first (solid) powerlaw in Fig 6.3 to 6.0 MPC, steepening the slope to -4.0 out to 10 MPC with $\xi(r) = 0.0$ beyond.

Considering first $\omega_\mu(\theta)$ at small scales, we see from Fig 6.8 that, like the estimates of $\omega_v(\theta)$ in part 1, the smoothing of $\xi(r)$ along the line of sight for the AARS gives a slope and amplitude that is in reasonable agreement with the scaled observations of $\omega(\theta)$. This suggests that the AARS may be a reasonable approximation ot a fair sample. Conversely one might say that the agreement of the observations of $\omega(\theta)$ with $\xi(r)$ projected from the AARS, suggest that the observed slope and amplitude of $\omega(\theta)$ from projected catalogues is not significantly affected by patchy obscuration, as has recently been proposed by Seldner and Uson (83).

Although the details of the model for $\xi(r)$ used in the solid curve is not intended to be a realistic representation of the real behaviour of $\xi(r)$ at $r < 6.0$ MPC, it does demonstrate that for a powerlaw to persist in $\omega(\theta)$ in the presence of a break in $\xi(r)$ at larger scales, $\xi(r)$ must rise above the corresponding spatial powerlaw at smaller scales ; otherwise $\omega(\theta)$ will start to 'droop' away from a powerlaw at small angular scales(as seen in the dashed curve). This requirement has been noted by Soneira and Peebles (77) in their clustering simulations of the Lick catalogue and is demonstrated

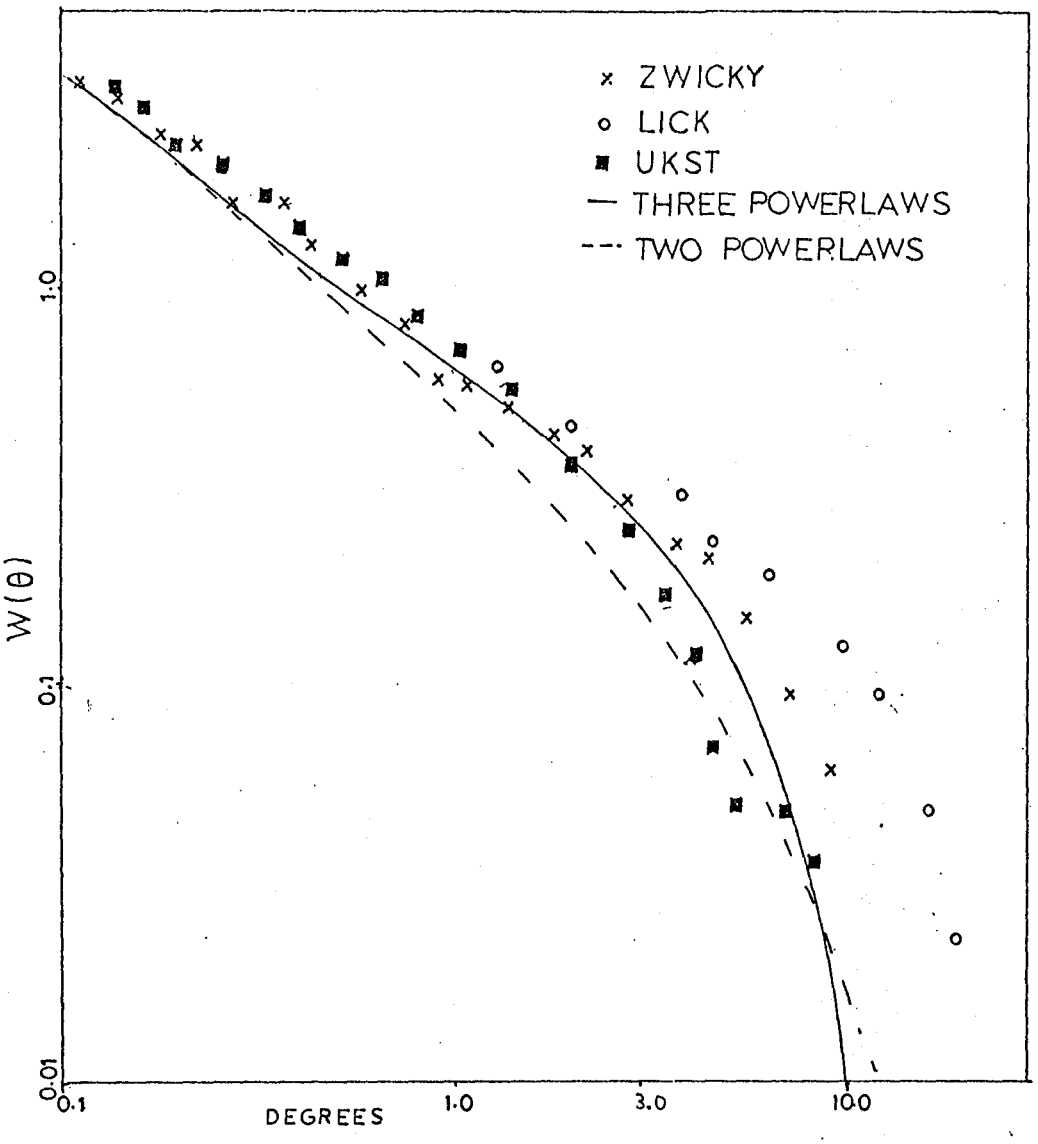

FIGURE 6.8: Observed scaled estimates of $\omega(\theta)$ from several projected catalogues along with models discussed in section 4.3.

by the instability of eqn 6.11 to inversion (Fall and Tremaine, 77). It might be argued in this case that such a large rise above a powerlaw at < 6 MPC can be mainly hidden in $\omega(\theta)$, only by the presence of the sharp break in $\xi(r)$ at relatively high density contrast and the anticorrelation at larger scales, neither of which may be real features of the galaxy distribution. While this might be the case, (although, as discussed in Section 3 and below, there are reasons to believe both may be real) from the discussion in Part 2, we saw that, despite the very different behaviour in $\xi(r)$ for the CFA at scales > 6.0 MPC, non-powerlaw behaviour at smaller scales was still hidden in $\omega_v(\theta)$ by velocity smoothing at large separations.

Turning to more of the details of the models and data in Fig 6.8, we see some evidence of the non powerlaw rise in $\xi(r)$ is still visible in projection in the solid curve. However this could be eliminated by lowering the rise in $\xi(r)$ in the model to match the results from the CFA in Fig 6.7. Another possibility is that the clustering at the smallest scales could be filled in by pair counts from rich regions that are poorly sampled in the AARS. This would bring the amplitude and shape of the model and observations into closer agreement. Alternatively, the slightly lower amplitude of the model at the smaller scales ($\theta < 1^{\circ}$), may just reflect uncertainties in the selection function used to project $\xi(r)$. For example, making M^* in $\phi(x)$ fainter by 0.3 magnitudes would bring the model and observations into agreement. By the discussion in Chapter 4.4 this would also make M^* from the AARS agree better with conventional estimates from other samples.

While the angular correlation functions agree at small scales in Fig. 6.8, the observations vary beyond $\sim 3^{\circ}$. As discussed in Chapter 1.2, the shape of $\omega(\theta)$ (and hence $\xi(r)$) here is of great interest for theories of galaxy formation, however the main problem is that the signal to noise at these scales in projection is so low.

From Fig 6.8 we see that, although the projected curve for the AARS differs strongly from the Lick results at $\theta > 3^{o}$, it lies between and reasonably close to the Zwicky and Schmidt* observations. Furthermore, recent estimates of $\omega(\theta)$ at several different depths by Shanks et al (83c), have shown evidence for a break at a similar angular scale to the original estimate (squares) in Fig 6.8 ; the break scaling in the expected way with depth. This is strong support that the feature at this scale is neither due to systematic errors in the catalogue preparation or the estimator, or due to galactic obscuration.

Although these machine measured catalogues are better controlled than the Lick survey and the scaled estimates of $\omega(\theta)$ perhaps more believable, some support for the break at larger scales seen in the Lick, comes from $\xi_s(s)$ for the CFA. As noted in Part 2, the results of Davis and Peebles (82) differ strongly from the AARS at scales > 6.0 MPC, $\xi_s(s)$ only eventually exhibiting a steepening at scales of 10 MPC. Despite being much larger than the AARS, by the arguments in Section 3.3, it is not clear that at these and larger scales these results are more reliable than those for the AARS, where the break occurs at $\sim$ 6.0 MPC in both subsamples (Fig 6.3). Indeed plots of $\xi_v(\sigma,\pi)$ at between $6.4 < \sigma < 12.8$ MPC given in Fig 5.9 of DP, suggest that large statistical fluctuations are affecting $\xi(r)$ in the CFA at these scales.

* In a re-estimate using a similarly prepared catalogue to that used by Shanks et al (80a), Hewett (82) has claimed that the shoulder in $\omega(\theta)$ occurs at an angular scale closer to that seen in the Lick catalogue. However, as Shanks (1983) notes, if plotted logarithmically, Hewett's estimates agree with the squares in Fig 6.8.

From this discussion we must conclude that the uncertainties, discussed in Chapter 1.2, of the position of the break in $\xi(r)$ remain, and larger redshift samples are needed to provide a more reliable estimate.

6.4.4 Summary and Conclusions

Initially the main interest in studying $\xi(r)$ for the AARS at small scales was to determine the overall amplitude and true position of the break away from powerlaw behaviour, suggested in studies of the projected catalogues. However, as the extensive analyses discussed in this section has shown, there may be evidence for considerable non-powerlaw behaviour apart from the break.

Although at the smallest scales $\xi(r)$ for the AARS appears to approximate a -1.8 powerlaw with amplitude similar to projected estimates of $\omega(\Theta)$, both the analyses of $\xi_v(\sigma,\pi)$ and $\xi_s(s)$ over the range 1 to 6 MPC show $\xi(r)$ exhibits a strong rise above a -1.8 powerlaw. Models show the effect is unlikely to be due to peculiar velocities and the analysis of the simulated catalogues suggest the rise is statistically significant.

External support for the behaviour comes from an examination of the correlation functions for the CFA where a smaller but still strong effect is evident over the same scale range where the statistics in each sample should be good. Furthermore, projection of $\xi(r)$ from the AARS in both $W_v(\Theta)$ and $\omega(\Theta)$ show the strong rise above powerlaw behaviour is essentially compensated for by smoothing over the fall away from powerlaw at large scales. In the CFA a similar smoothing over the line of sight occurs in $W_v(\Theta)$, which also shows the expected powerlaw behaviour, although in this case the behaviour of $\xi(r)$ at larger scales is different.

From these arguments one must conclude that either $\xi(r)$ from the two samples are unrepresentative at scales < 5 MPC and the agreement with projected catalogues fortuitous or, that at scales 1 - 5 MPC $\xi(r)$ is considerably flatter than a - 1.8 powerlaw.

At scales larger than 6.0 MPC, $\xi_s(s)$ in the two catalogues differ strongly. In the CFA a break occurs at a scale similar to that seen in $\omega(\theta)$ for the Lick catalogue whereas the break in $\xi_s(s)$ for the AARS is closer to that found in the Zwicky and Schmidt catalogues. Thus, at these and smaller scales, larger redshift samples are needed for a fuller understanding of the galaxy distribution, as measured by $\xi(r)$.

For the present though, it is interesting to note that analyses of projected catalogues by Shanks (79) and Hewett et al (81) using the statistic 'meads analysis', have shown evidence for a feature in the clustering distribution at scales 2-3 MPC. This would contradict the claim by Groth and Peebles (77) that $\xi(r)$ exhibits pure powerlaw behaviour to scales of 9 MPC. A similar 'hump' at 2 MPC, as seen in $\xi_s(s)$ for the AARS in Fig 6.3, has been seen in the radial counts of several clusters studied by Oemler (74). While no such rich clusters are present in the AARS, if both features are real they may be connected and correspond to some preferred scale that exists both in compact clusters and in the general galaxy distribution.

In Chapter 7 we discuss possible implications of the shape of $\xi(r)$ and such features for theories of cluster and galaxy formation.

Although there does appear to be good evidence for some sort of departure from a -1.8 powerlaw slope in $\xi(r)$, even at quite small scales, in the remainder of this chapter it is generally assumed a conventional pure powerlaw applies. Where appropriate though, the affect on the results of using a different model are discussed.

6.5 ESTIMATES OF $\langle V^2 \rangle$ FROM $\xi_v(\sigma,\pi)$

In order to discuss fully the estimates of $\langle V^2 \rangle$ from $\xi_v(\sigma,\pi)$, this section is split into seven parts. The first gives details of a model for $\xi_v(\sigma,\pi)$ and the two that follow use this to provide two alternative estimates of $\langle V^2 \rangle$ which are tested in each case on the simulated catalogues. Possible uncertainties in the model are discussed in the fourth part and the

results for the AARS are summarised in the fifth. The sixth gives results from a reanalysis of several other redshift surveys and a summary of the conclusions for the section are presented in the last part.

6.5.1 A Model for $\xi_v(\sigma,\pi)$

In Fig 6.2 a model for $\xi_s(s)$ was presented which, assuming a model for $\xi(r)$ and the distribution function of peculiar velocities, can provide some information on $\langle V^2 \rangle$, averaged over all spatial scales. A much more sensitive estimate of the velocity dispersions at different spatial scales comes from considering a similar model for $\xi_v(\sigma,\pi)$ at different values of σ.

To do this we can follow Peebles (79) and assume the redshift difference π between galaxy pairs at separation σ is the sum of a cosmological part Hy and a line of sight peculiar part W. If W is drawn from a distribution function $F(W, \langle W^2 \rangle^{\frac{1}{2}})$ such that $\langle W^2(\sigma) \rangle = \int F\, W^2\, d\, W$ (6.12) we can get a model for $\xi_v(\sigma,\pi)$:

$$\xi_v(\sigma,\pi) = \int_{-\infty}^{\infty} F\,(W \langle W^2 \rangle^{\frac{1}{2}})\quad \xi(\,(\sigma^2 + y^2)^{\frac{1}{2}}\, dW \qquad (6.13)$$

where $y = \pi - W$

One approach using this model is to assume a form for F and $\xi(r)$ and adjust $\langle W^2 \rangle$ to give the best fit to the observed $\xi_v(\sigma,\pi)$ histograms at different σ. An alternative numerical estimate based on eqn 6.12 and eqn 6.13 is

$$\langle W^2 \rangle = \frac{\int_0^{\pi\ \mathrm{cut}} (\xi_v(\sigma,\pi) - \xi(\,(\sigma^2 + \pi^2)^{\frac{1}{2}}\,)\ \pi^2\, d\pi}{\int_0^{\pi \mathrm{cut}} \xi_v(\sigma,\pi)\ d\pi} \qquad (6.14)$$

Although this does not require a form for F it is sensitive to noise in $\xi_v(\sigma,\pi)$ and the assumed form of $\xi(r)$ at large scales.

Like the theory of the CVT discussed in Chapter 2.2, estimates of $\langle V^2 \rangle$ based on eqn 6.13 are based on a number of assumptions concerning the peculiar velocities and clustering of galaxies. Firstly they assume that both $\langle W^2 \rangle$ and the form for F are roughly independent of separation and are isotropic in the three dimensional relative velocity $\underline{W}$. This is consistent with the stability assumptions in Chapter 2.2.3 where $\langle V^2 \rangle$ is isotropic and a slowly varying function of separation.

The second assumption is that the clustering is expanding with Hubble velocities at all scales. Although this says that the clusters are not bound at any scale, this should not affect estimates much at small σ where, by the stability assumption, we expect $\langle W^2 \rangle^{\frac{1}{2}} >> (H\sigma)^2$. At larger scales though, where $\langle W^2 \rangle^{\frac{1}{2}} \sim H\sigma$, estimates based on eqn 6.13 will cause $\langle W^2 \rangle$ to be underestimated if the clustering on these scales is stable or the expansion is significantly slowed by streaming motions.

The model in eqn 6.13 also requires a form for $\xi(r)$ which, from the discussion in the last section, at present appears uncertain. Assuming a -1.8 powerlaw in the next two subsections at scales < 6.0 MPC will tend to overestimate $\langle W^2 \rangle$, especially at large σ , if $\xi(r)$ rises significantly above this powerlaw. However this effect may be cancelled at large scales by the possibility of streaming motions, mentioned above. These possible uncertainties in the model for $\xi_v(\sigma,\pi)$ and hence systematic errors in the estimates of $\langle W^2 \rangle$ are discussed in Section 4.

Finally it should be noted that the model in eqn 6.13 is consistent with the assumptions used in setting up the simulated catalogues in Chapter 3.7 where the clustering was assumed to be in free expansion and

the peculiar velocities were randomly drawn from the same* distribution function to be used in eqn 6.13 in Part 3. Thus the analysis of these catalogues, where $\langle V^2 \rangle$ is known, should be a fair test of the statistical uncertainties in $\langle W^2 \rangle$ from the methods used on the data.

6.5.2 A Second Moments Estimate of $\langle V^2 \rangle$

Estimates from the data and simulations are in (a) and (b) below.

(a) For the AARS

The first term on the right-handside of eqn 6.14, which we will denote as $\langle w_o^2(\sigma) \rangle$, corresponds to the full relative velocity dispersion of all pairs at separation σ. As in the traditional group studies this second moment integral is very sensitive to the choice at which true peculiar velocities are distinguished from line of sight Hubble velocities. However, in this case we can statistically subtract out this latter contribution by the integral over $\xi(r)$, denoted as $\langle H^2 Y^2 \rangle$. Taking the usual powerlaw model for $\xi(r)$ with slope -1.8 and equating the denominator of eqn. 6.14 with eqn. 6.6 of section 4.1, we find that for $\pi_{cut} >> \sigma$, $\langle H^2 Y^2 \rangle \sim \sigma^{0.8} \pi_{cut}^{1.2}$. Although this is a divergent integral, if we choose π_{cut} so that $\xi_v \sim \xi$ (as with $\omega_v(\sigma)$), eqn 6.14 should converge to give $\langle W^2(\sigma) \rangle$.

Figs 6.9(a-c) shows $\langle W_o^2(\sigma) \rangle^{\frac{1}{2}}$ (crosses) and $\langle W^2(\sigma) \rangle^{\frac{1}{2}}$ (filled circles) as a function of π_{cut} for the three separations in Figs 6.1(a-c). To model the sharp fall in $\xi(r)$ seen in the data, the powerlaw slope beyond

---

* Since the form of the distribution function to be used in the model for $\xi_v(\sigma,\pi)$ and used to assign individual peculiar velocities in the simulations differs slightly from a gaussian, the relative peculiar velocity distribution for the simulations has a slightly different form. However, it is unlikely this at all affects the overall conclusions from the results of the simulations presented after the data in the next two subsections.

TABLE 6.2: Second Moments Estimates of $\langle W^2 \rangle^{\frac{1}{2}}$ (in km/sec)

$\bar{\sigma}$ (MPC)	$\langle W_o^2 \rangle^{\frac{1}{2}}_{max}$	$\langle W^2 \rangle^{\frac{1}{2}}$	$\langle W^2 \rangle^{\frac{1}{2}}_{\gamma = 1.4}$
0.25	260	220	195
0.75	270	160	125
1.5	280	120	65

TABLE 6.3: Fitted Estimates of $\langle W^2 \rangle^{\frac{1}{2}}$ (in km/sec) with ψ^2_{min} (in brackets)

$\bar{\sigma}$ (MPC)	$\langle W^2 \rangle^{\frac{1}{2}}$	$\langle W^2 \rangle^{\frac{1}{2}}_{exp}$	$\langle W^2 \rangle^{\frac{1}{2}}_{gauss}$	$\langle W^2 \rangle^{\frac{1}{2}}_{\gamma = 1.4}$	$\langle W^2 \rangle^{\frac{1}{2}}_{infall}$
0.25	260 (9.1)	310 (10.6)	250 (9.9)	230 (9.2)	280
0.75	180 (2.8)	210 (4.0)	170 (2.6)	145 (4.0)	240
1.5	195 (20.4)	205 (23.6)	170 (17.6)	155 (22.8)	285

TABLE 6.4: Fitted Estimates of $\langle W^2 \rangle^{\frac{1}{2}}$ (in km/sec) from the Simulations

$\bar{\sigma}$ (MPC)	1st Set (200 km/sec)	2nd Set (500 km/sec)
0.25	220 $\pm$ 50	575 $\pm$ 100
0.75	230 $\pm$ 73	600 $\pm$ 160
1.5	200 $\pm$ 80	540 $\pm$ 200
All Three	215 $\pm$ 60	570 $\pm$ 135

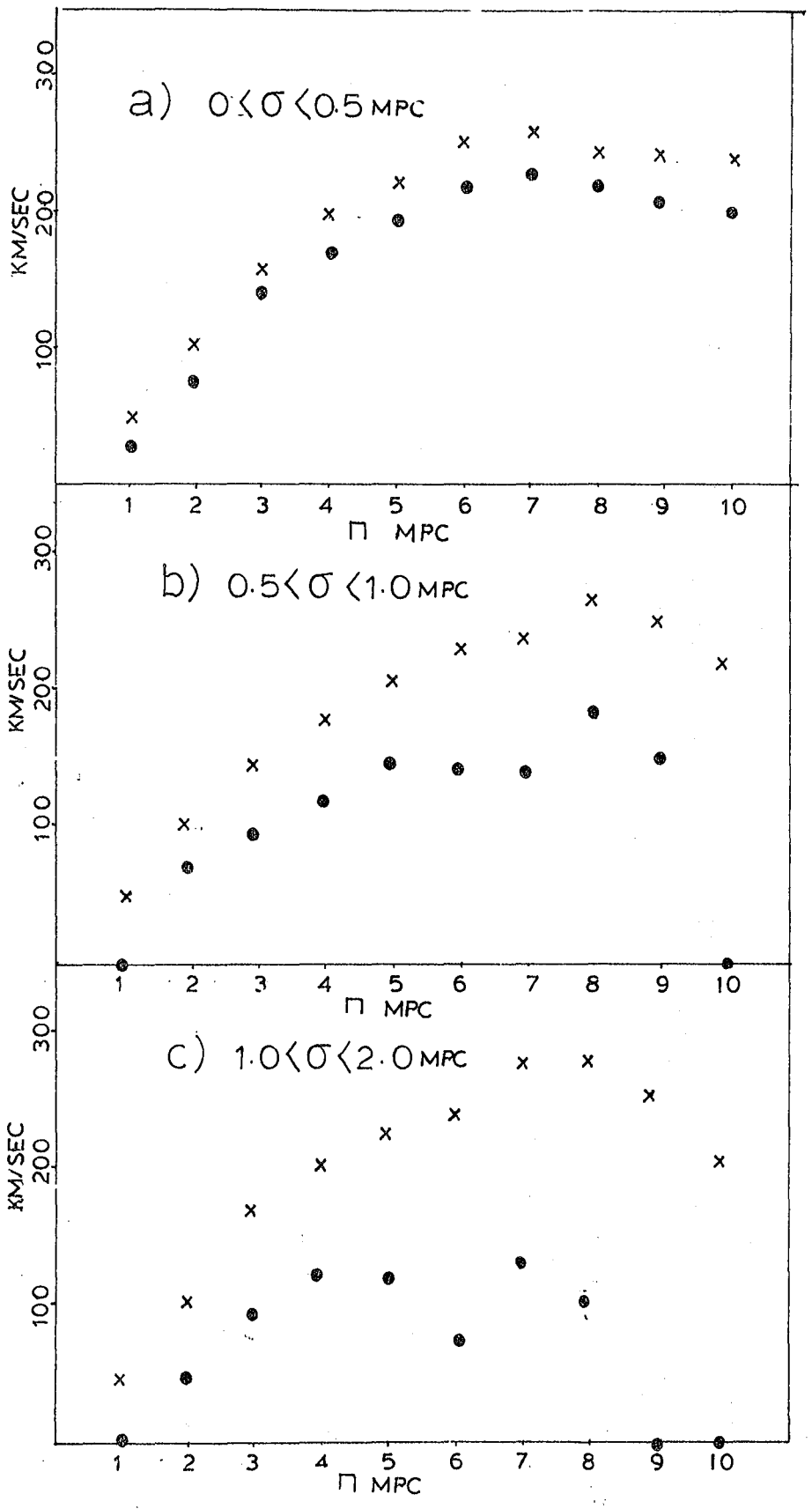

FIGURE 6.9: Estimates of $\langle W_o^2 \rangle^{\frac{1}{2}}$ (crosses) and $\langle W^2 \rangle^{\frac{1}{2}}$ (filled circles) as a function of πcut for the three separations in σ.

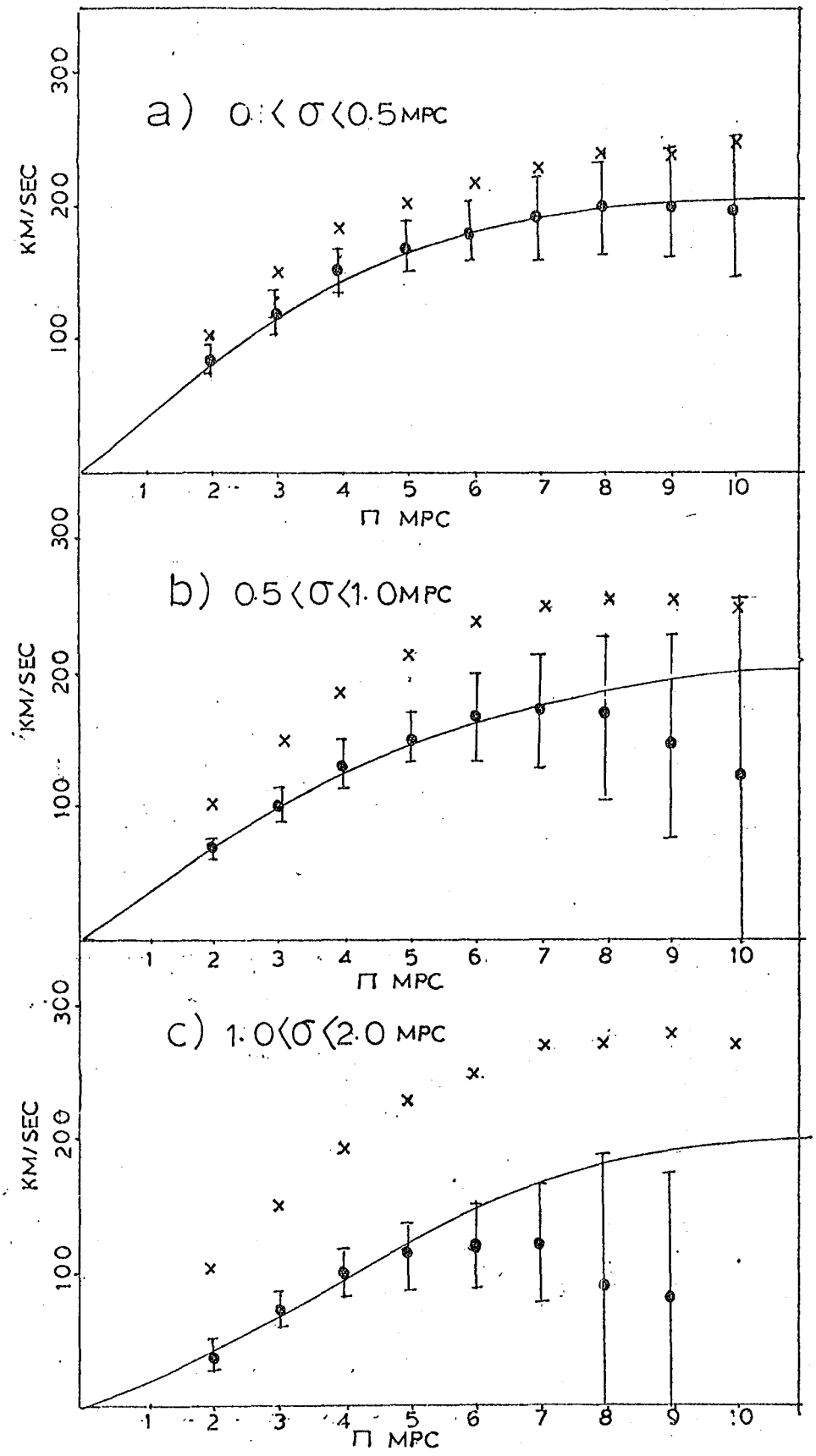

FIGURE 6.10: Ensemble estimates $\overline{\langle W_o^2 \rangle^{\frac{1}{2}}}$ (crosses) and $\langle W^2 \rangle^{\frac{1}{2}}$ (filled circles) as a function of πcut for the first set of simulated catalogues with $\langle V^2 \rangle^{\frac{1}{2}} = 200$ km/sec. The solid curve is the expected behaviour for $\langle W^2 \rangle^{\frac{1}{2}}$.

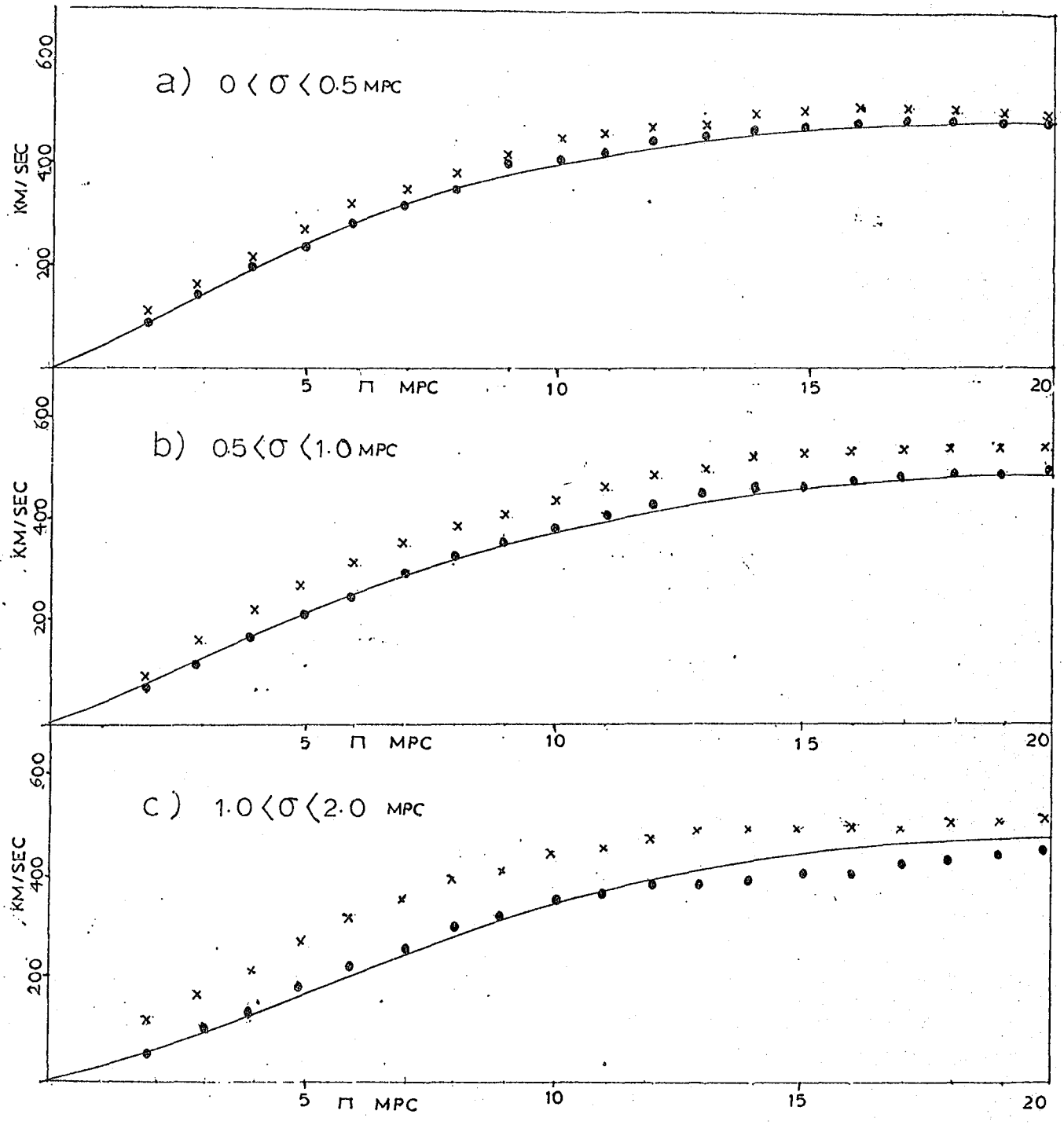

FIGURE 6.11: Ensemble estimates $(\overline{\langle W_o^2 \rangle})^{\frac{1}{2}}$ (crosses) and $(\overline{\langle W^2 \rangle})^{\frac{1}{2}}$ (filled circles) as a function of π_{cut} for the second set of simulated catalogues with $\langle V^2 \rangle^{\frac{1}{2}} = 500$ km/sec. The solid curve is the expected behaviour for $\langle W^2 \rangle^{\frac{1}{2}}$.

6.0 MPC was steepened to -4.0 in calculating $\langle H^2Y^2 \rangle$.

We see that $\langle W^2 \rangle^{\frac{1}{2}}$ converges to 220 km/sec at $\sigma < 0.5$ MPC but in Figs b and c falls to around 160 and 120 km/sec respectively. These and the maximum estimates of $\langle W_o^2 \rangle^{\frac{1}{2}}$ are recorded in Table 6.2.

In principle this method does not require a form for F and an asymptotic value of $\langle W^2 \rangle^{\frac{1}{2}}$ should be reached if the shape of $\xi(r)$ is known at large scales. In practice though, we may expect the convergence to be slow, especially at large σ, and here we may lose any long tail contribution of $\xi_v(\sigma,\pi)$ to $\langle W_o^2 \rangle$ due to background errors in $\xi_v(\sigma,\pi)$, which have a larger effect at low density contrasts. Also the estimates are increasingly sensitive to the Hubble flow models as σ and πcut rise. For example at $\bar{\sigma}$ = 1.5 MPC and πcut = 7.0 MPC, $\langle H^2Y^2 \rangle^{\frac{1}{2}} \sim 240$ km/sec so that $\langle W^2 \rangle^{\frac{1}{2}}$ becomes the small difference between two comparable numbers.

Since together these effects may be responsible for the apparent fall of $\langle W^2 \rangle^{\frac{1}{2}}$ with scale, the method has been tested on the two sets of simulated catalogues where the true $\langle W^2 \rangle$ is known and is independent of separation.

(b) Tests on the Simulations

Figures 6.10 (a-c) shows the ensemble mean of $\overline{\langle W_o^2 \rangle^{\frac{1}{2}}}$ (crosses) and $\overline{\langle W^2 \rangle^{\frac{1}{2}}}$ (filled circles) as a function of πcut for the first set of simulations in Chapter 3.7, using the same model for $\langle H^2Y^2 \rangle$ as the data. The error bars come from the standard deviations in $\langle W_o^2 \rangle^{\frac{1}{2}}$ and the smooth curves are based on eqn. 6.13 using the model for $\xi_v(\sigma,\pi)$ appropriate to the simulations.

We see at $\sigma < 0.5$ MPC the mean $\langle W^2 \rangle^{\frac{1}{2}}$ converges to 200 km/sec with quite small errors but the ensemble in Figs (b) and (c) fall below the model curve. Although this may in part be due to inadequacies in the model for $\langle H^2Y^2 \rangle$, the effect is also seen in the second set of simulations where the Hubble correction is small compared with the expected $\langle W^2 \rangle^{\frac{1}{2}}$ of 500 km/sec.

If instead of taking the mean of $\langle W_o^2 \rangle^{\frac{1}{2}}$ we take the root of the mean of $\langle W_o^2 \rangle$ for the ensemble we see from Figures 6.11 (a-c) for the second set, that $\langle W^2 \rangle^{\frac{1}{2}}$ converges quite reasonably. This suggests that most of the contribution to the ensemble $\langle W_o^2 \rangle^{\frac{1}{2}}$ at larger σ, come from a small proportion of samples, so in general a sample taken at random will underestimate the true $\langle W^2 \rangle^{\frac{1}{2}}$.

We may conclude from the simulations that at $\sigma > 0.5$ MPC, the second moments of $\xi_v(\sigma,\pi)$ will underestimate $\langle W^2 \rangle^{\frac{1}{2}}$ for small data sets like the AARS.

6.5.3 $\langle V^2 \rangle$ From Fits to $\xi_v(\sigma,\pi)$

Estimates from the data and simulations are in (a) and (b) below.

(a) For the AARS

The alternative approach using eqn. 6.13 to estimate $\langle W^2 \rangle$, is to assume a functional form for F and model the observed broadening in $\xi_v(\sigma,\pi)$.

One clue to the form of F for the real universe comes from the N body simulations of Efsthathiou and Eastwood (81) mentioned in Chapter 2.2. Using the three dimensional positions and velocities for all particles one can examine F for different pair separations and values of Ω. Analysis from both an open and closed universe for the simulations with 20,000 particles, give a smooth form, approximately independent of separation and usefully fitted by

$$F(W,\langle W^2 \rangle^{\frac{1}{2}}) = 0.476 \langle W^2 \rangle^{-\frac{1}{2}} \exp\left(-0.797 \frac{|W|^{\frac{3}{2}}}{\langle W^2 \rangle^{\frac{3}{4}}} \right) \qquad (6.15)$$

The results of using this '$W^{\frac{3}{2}}$' form in eqn. 6.13 and assuming a -1.8 powerlaw for $\xi(r)$ with B given by eqn. 6.10, are shown on Figs 6.1 (a-c). The dispersion here is $\langle W^2 \rangle^{\frac{1}{2}} = 200$ km/sec with the dashed and solid curves corresponding to the dashed and solid histograms.

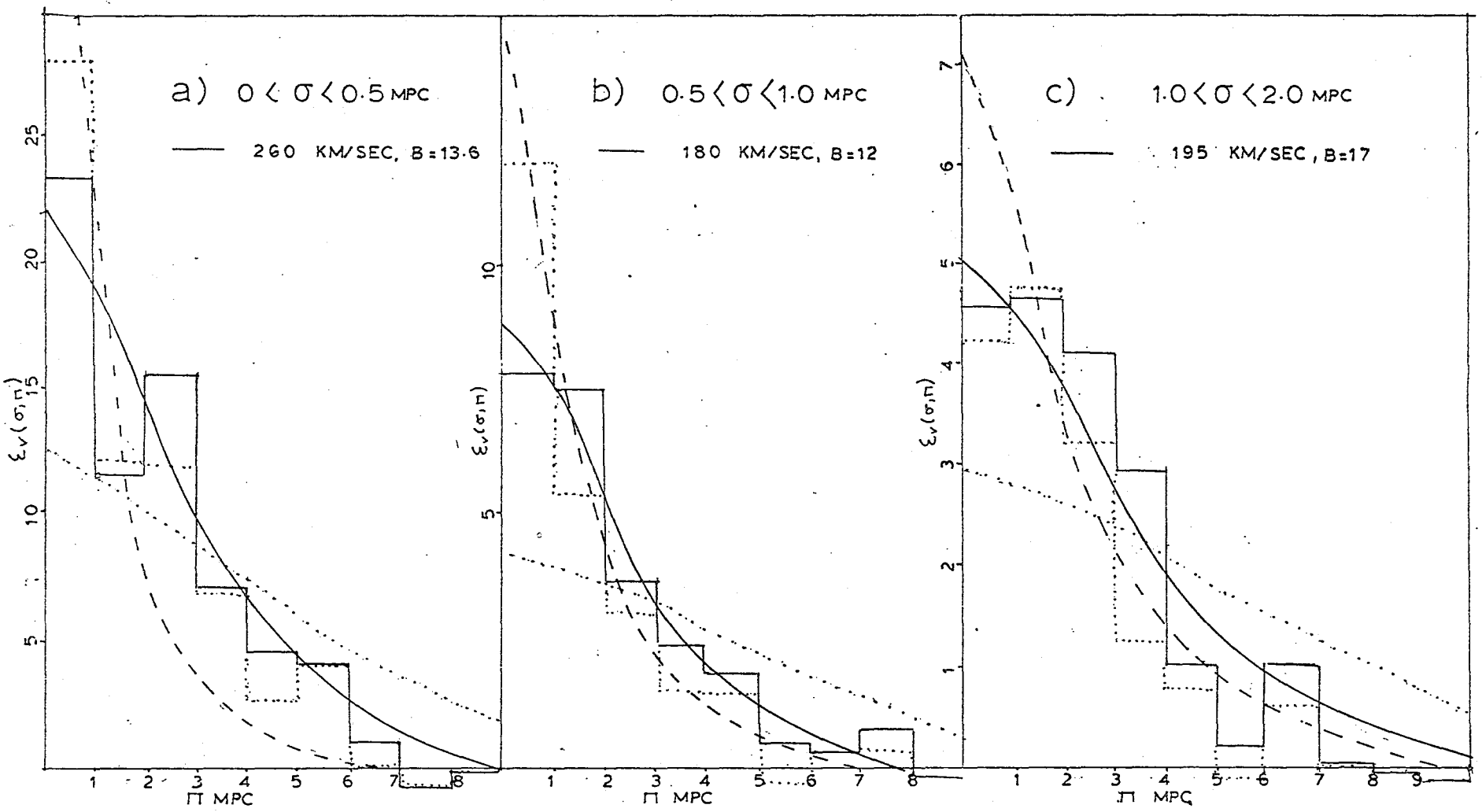

FIGURE 6.12: Estimates of $\xi_v(\sigma,\pi)$ (solid histograms) with best fitting curves (solid) along with model curves with 100 km/sec (dashed) and 500 km/sec (dotted). The dotted histogram refers to a subsample of the AARS with the best velocity data.

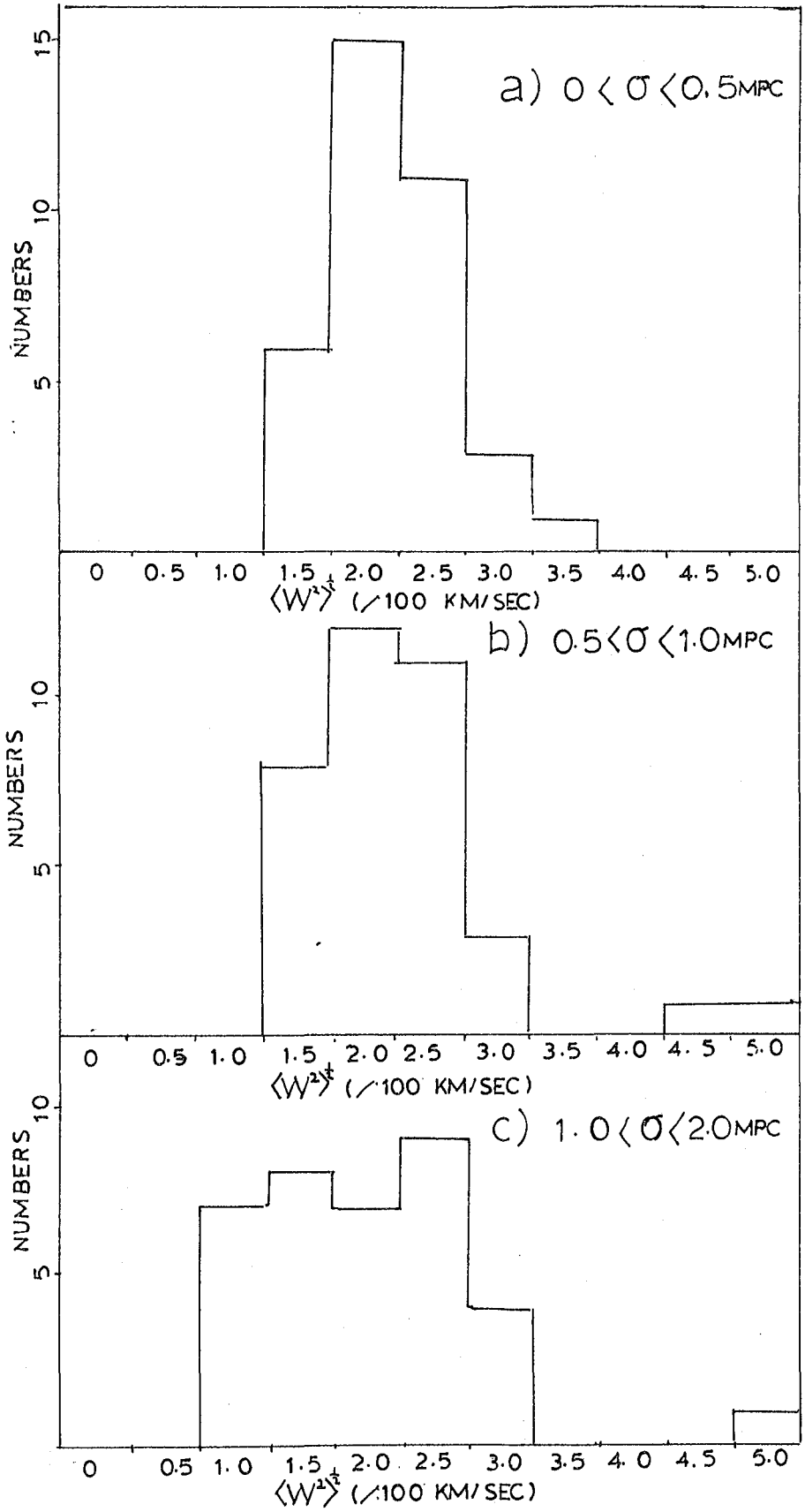

FIGURE 6.13: Numbers against best fitting velocity from fits to $\xi_v(\sigma,\pi)$ from the first set of simulations

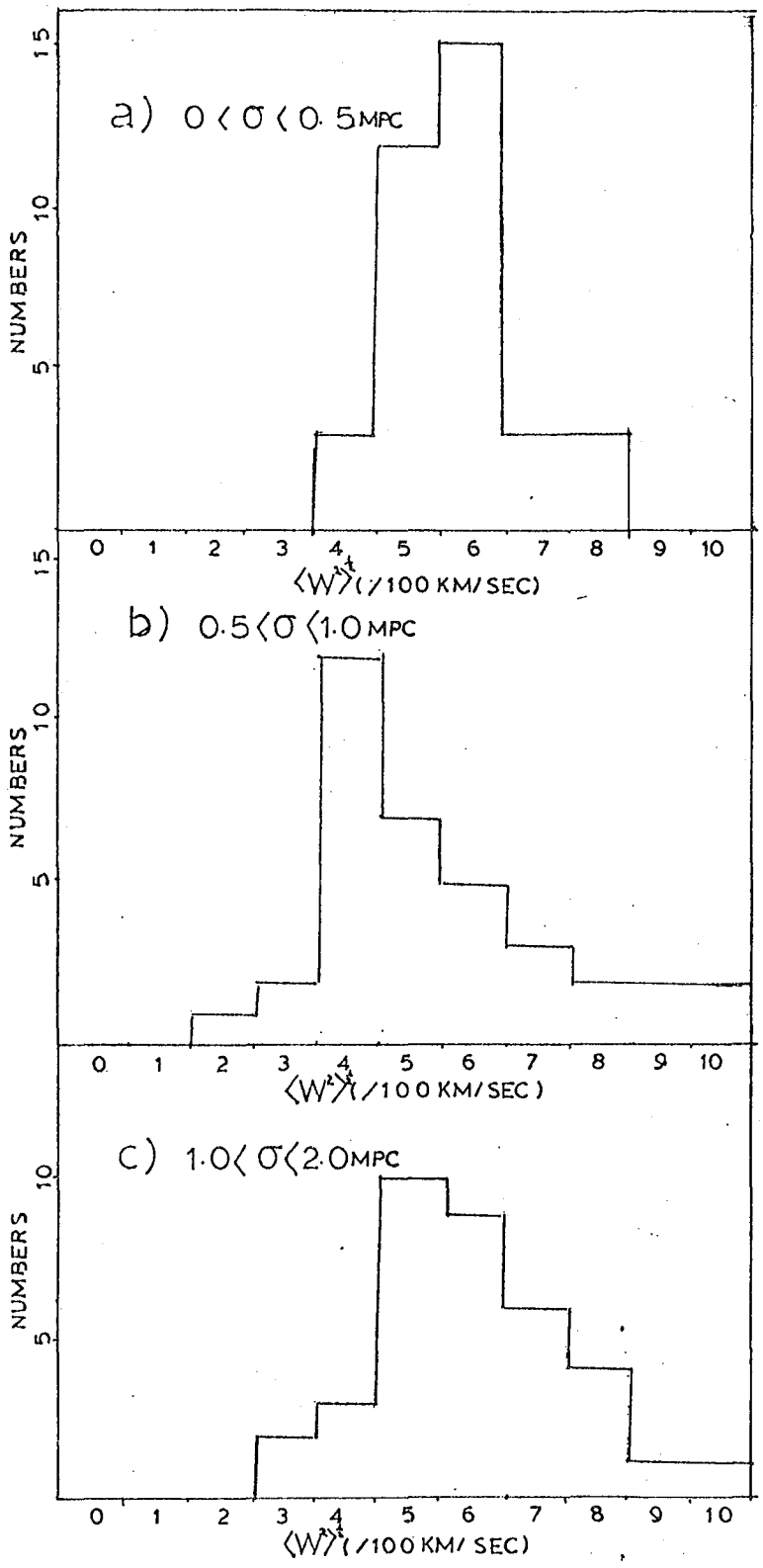

FIGURE 6.14: Numbers against best fitting velocity from fits to $\xi_v(\sigma,\pi)$ from the second set of simulations.

The models show that the observed elongation is expected to become progressively less as σ rises, as seen in the data. In Fig (a) we see the dashed curve fits the data at small π but misses the observed tail at larger scales, the reverse being true in Fig (b). In Fig (c) comparison is hard because the amplitude of the model is too low. This is also seen in the comparison of all the solid curves and histograms which give more information on the shape of $\xi(r)$ than $\langle W^2 \rangle$. We see the data here all lie well above the models at $\sigma > 1.0$ MPC, reminding us of the rise of $\xi(r)$ above a -1.8 powerlaw discussed in detail in the last section.

In order to quantify the method to give more definite estimates of $\langle W^2 \rangle$, least square fits were performed on the dashed histograms. To accommodate the observed non-powerlaw behaviour, the amplitude B was adjusted to correspond to the integral pair counts for each histogram which are given in Fig 6.7 (open circles) of section 4.2.

The best fitting $\langle W^2 \rangle^{\frac{1}{2}}$ came from minimising the quantity

$$\rho^2 = \sum_{n=o}^{n\ max} \frac{(\xi_v(\sigma,\pi) - \xi_v^{model}(\sigma,\pi))^2}{\alpha^2}$$

where $\alpha^2 \propto (\xi_v^{model}(\sigma,\pi) + 1)$; $\xi_v^{model}(\sigma,\pi)$ being estimated from eqn. 6.13 for different values of $\langle W^2 \rangle^{\frac{1}{2}}$. The weighting scheme assumes root N fluctuations in the number of pairs contributing to $\xi_v(\sigma,\pi)$ so ρ^2 corresponds to a ψ^2_{min} statistic. Although the points in each bin are not really independent, the results do not change appreciably if other weighting schemes are adopted.

The results of ψ^2_{min} estimated between $0 < \Pi < 6$ MPC are shown as solid curves in Figs 12 (a-c), where the data (solid histograms) has been binned up from the dashed histograms in Figs 6.1 (a-c). The best fits for the three separations are 260, 180 and 195 km/sec respectively, which are

recorded in Table 6.3 along with their corresponding ψ^2_{min} values. Also on the figures are curves with 100 km/sec (dashed lines) and 500 km/sec (dotted lines) dispersions and the dotted histograms refer to a subsample of the data discussed in part 5.

We see the solid curves in Figs (a) and (b) give good fits to the data while the fit in (c) is poorer. Although the difference between the curves is less at this separation the other two curves give much worse fits.

From Tables 6.2 and 6.3 we see that the results from this fitting analysis give closer values of $\langle W^2 \rangle^{\frac{1}{2}}$ at the different separations compared with the second moments estimates in part 3.

(b) Tests on the Simulations

To test the fitting method a similar ψ^2 analysis was performed on each of the two sets of simulated catalogues, and the best fitting velocity was recorded for each simulation. As for the data, the fits were insensitive to the adopted weighting scheme.

Figs 6.13 (a-c) show the resulting histograms at the three separations for the first set of simulations, the means and standard deviations being in Table 6.4.

We see the distributions are all fairly symmetric about 200 km/sec and there is only a slight bias that may just be a statistical fluctuation. As expected, the errors of $\langle W^2 \rangle^{\frac{1}{2}}$ are larger as σ rises. The results from all three separations were also combined by calculating the mean of $\langle W^2 \rangle^{\frac{1}{2}}$ for each simulation. The mean and standard deviations for the resulting distribution are

$$\overline{\langle W^2 \rangle^{\frac{1}{2}}} = 215 \pm 60 \text{ km/sec.} \qquad (6.16)$$

Figures 6.14 (a-c) shows the histograms for the second set of simulations which were fitted between $0 < \Pi < 10$ MPC. The results in Table 6.4 show the means are more biased to high velocity dispersions than the first set.

Taking the mean and standard deviations averaged over all three separations as before gives

$$\overline{\langle W^2 \rangle^{\frac{1}{2}}} = 570 \pm 135 \text{ km/sec} \qquad (6.17)$$

From the simulations we may conclude that the ψ^2_{min} analysis give reasonably unbiased estimates of $\langle W^2 \rangle^{\frac{1}{2}}$ at the scales of interest (at least for the first set of simulations that match the data best). Of course this assumes the correct model for F of the real universe has been chosen.

6.5.4 Changes in the Model for $\xi_v(\sigma,\pi)$

In the last two subsections we have discussed random and systematic errors in the estimates of $\langle W^2 \rangle$ from $\xi_v(\sigma,\pi)$ using the simulated catalogues. However, the analyses can still be criticised on the grounds that neither the model for $\xi_v(\sigma,\pi)$ or the simulations match the clustering and dynamics of the real universe.

Below we discuss the dependence of the estimates of $\langle W^2 \rangle^{\frac{1}{2}}$ on the models for F, $\xi(r)$ and the expansion velocities.

(a) Other Forms for F $(W, \langle W^2 \rangle^{\frac{1}{2}})$

Although the solid curves in Figs 6.12 (a-c) are reasonable representations of the data, and indeed at $\sigma < 0.5$ MPC we may expect $\xi_v(\sigma,\pi) \sim$ F, it is still important to test the effect on $\langle W^2 \rangle^{\frac{1}{2}}$ of considering other reasonable distribution functions in the model fits analysis in Part 3.

Peebles (79,81) has advocated an exponential form, $F \sim \exp\left(-|W|\left(\frac{2}{\langle W^2 \rangle}\right)^{\frac{1}{2}}\right)$, from several complete redshift samples whereas Yahil and Vidal (77), Rood and Dickel (78), have fitted velocity distributions from clusters and group studies with gaussians $\left(F \sim \exp\left(\frac{-|W|^2}{2\langle W^2 \rangle}\right)\right)$.

Table 6.3 shows the best fitting estimates of $\langle W^2 \rangle^{\frac{1}{2}}$ and the

ψ^2_{min} values from the analysis in part 3 using these two other functional forms.

Since the adopted '$W^{\frac{3}{2}}$' form from eqn. 6.15 lies between an exponential and a gaussian, not surprisingly, the best fits for this function lie between the latter two.

We see at small separations the ψ^2 method is quite sensitive to the model form chosen although the gaussian and $W^{\frac{3}{2}}$ forms give quite close results and generally better fits than the exponential. As the ψ^2_{min} indicate, at $\sigma < 0.5$ MPC the exponential gives about as good fits as the other two forms but is less reasonable since the model for $\xi_v(\sigma,\pi)$ has a long tail at $\pi > 6.0$ MPC that is completely lacking in the data. This demonstrates the fitting method relies on the accuracy of the chosen model for F in describing the behaviour of the real velocity distribution both at small velocities (where it may be affected by measuring error) and in any long tail ; in this sense it is as sensitive at large scales as using the second moments of $\xi_v(\sigma,\pi)$.

However the problem can be eased if the choice of F can be justified in some way. Physical justification for adopting eqn. 6.15 comes from the N body simulations which give crude agreements with the clustering properties of the observed universe. In compact, relaxed groups and clusters and in the possible extended isothermal halos around bright galaxies we may expect a gaussian to be appropriate (e.g. Yahil, 77), perhaps with a velocity truncation at the systems' escape velocity.

From this we may conclude that using the $W^{\frac{3}{2}}$ form or a gaussian give better fits to the observed $\xi_v(\sigma,\pi)$ than an exponential and are probably more realistic functions to use in eqn. 6.13.

(b) Other Models for $\xi(r)$

In view of the general poor fits to a -1.8 powerlaw discussed in section 4 and seen in the models for $\xi_v(\sigma,\pi)$ in Figs 6.1 (a-c), it seems reasonable to

test the effect on $\langle W^2 \rangle^{\frac{1}{2}}$ of using a more representative model of $\xi(r)$ for the sample.

To do this the analyses of the last two subsections has been repeated using a flatter powerlaw slope at $r < 6.0$ MPC of -1.4, which gives a more consistent fit to $W_v(\sigma)$ and $\xi_s(s)$ than using the usual slope of -1.8.

The modified results, marked as $\langle W^2 \rangle^{\frac{1}{2}}_{\gamma = 1.4}$ in tables 6.2 and 6.3, show this different model for $\xi(r)$ reduces $\langle W^2 \rangle^{\frac{1}{2}}$ by between only 20-30 km/sec at $\sigma < 0.5$ MPC but 30-60 km/sec at the outer separations.

(c) Correction for Streaming Motion

Another possibility, mentioned in part 1, is that the assumption of pure Hubble flow in eqn. 6.13 can cause $\langle W^2 \rangle$ to be underestimated. For example, in the extreme case of no Hubble velocities, $\langle W_o^2 \rangle^{\frac{1}{2}}_{max}$ in Table 6.2 should give the best estimate of $\langle V^2 \rangle^{\frac{1}{2}}$ from the second moments of $\xi_v(\sigma,\pi)$.

A more realistic correction for non-Hubble motion in the model for $\xi_v(\sigma,\pi)$ has recently been considered by Davis and Peebles (82) in their statistical study of the CFA. These authors adopted a model for the streaming velocity relative to the Hubble flow of

$$h(r) = \left[1 + \left(\frac{r_o}{r}\right)^2\right]^{-1} \qquad (6.18)$$

which was incorporated into eqn. 6.13 by replacing the right-hand side of $y = \pi - W$ with the solution to

$$W = \pi - Hy\,(1 - h\,(\,(\sigma^2 + y^2)^{\frac{1}{2}}\,)\,)$$

Efsthathiou (seen Bean and Efsthathiou et al, 83) has used the same correction to $\xi_v(\sigma,\pi)$ for the AARS, and using eqn. 6.15 for F has followed a ψ^2 analysis similar to that described in part 3 but allowing the amplitude B to be another free parameter in the fit at each separation. The result

of adding the difference of his fits, with and without this infall, to the best fits in Table 6.3 (that agree within 20 km/sec with his fits without infall) are given in column 6 of the same table. Since we see the corrections with this model are substantial at the outer separations, amounting to nearly 100 km/sec at $\bar{\sigma}$ = 1.5 MPC, it is important to discuss them in more detail.

The model h(r) in eqn. 6.18 is based on the similarity solution (Ω= 1) of the BB GKY equations (Davis and Peebles, 77) in which the clustering is only dominated by the expansion at scales $r_H > r_o$. However if $\Omega << 1$ we would expect clusters at scales smaller than r_o to have mean densities less than the critical density and so be unbound and in approximate free expansion. Taking Ω = 0.1 for example, we might expect this scale r_H to occur at roughly a mean over-density of $\frac{d\rho}{\rho} \sim 10$. Since a measure of the mean over-density at scale r around a random galaxy comes from the relation

$$\frac{d\rho}{\rho} \simeq \xi(r) \quad \frac{3}{3-\gamma} \tag{6.19}$$

(White and Rees, 78, eqn. 2.14), we find $r_H \simeq \frac{1}{2} r_o \sim 2$ MPC.

Some support for a small infall correction on scales $\sim r_o$ comes from studies of the local galaxy distribution within $\sim$ 5 MPC which suggest that beyond the local group, galaxies are expanding at a rate roughly proportional to their distance (Sandage and Tamman, 75). Although in this case the picture may be complicated by the tidal field of the Virgo cluster, it does suggest the model for h(r) used in eqn. 6.18 probably overestimates the correction to $\langle w^2 \rangle^{\frac{1}{2}}$ due to streaming motion.

It should also be noted that the streaming term h(r) is based on a particular model for cluster formation. If clusters instead collapse according to the sperical model (Gott and Rees, 75), any flattening in $\xi_v(\sigma,\pi)$ could reflect the scale at which clusters are now fragmenting out of the Hubble flow, which in turn could reflect Ω (Sargent and Turner, 77).

Taking $\Omega \sim 0.1$ again we expect clusters in this picture to turn around at $\frac{d\rho}{\rho} \sim 30$, which from eqn. 6.19 above corresponds to a scale of $\sim \frac{r_o}{4.0} \sim 1$ MPC.

Interestingly we do see $\xi_v(\sigma,\pi)$ at $\sigma < 0.5$ MPC in Fig 6.1(a) is flattened compared with Fig 6.1 (b) (as seen in fits in Table 6.3) but the sample is too small to distinguish it from sampling fluctuations. In a much larger sample one might be able to simultaneously fit $\langle W^2 \rangle^{\frac{1}{2}}$ and, with certain constraints, discriminate between models for cluster collapse through the shape of $\xi_v(\sigma,\pi)$ at different scales.

The infall correction is discussed further in part 6 in considering the results from the CFA and in Chapter 7.2 we discuss estimates of Ω based on streaming motion at scales considerably larger than r_o MPC around rich clusters.

6.5.5 Final Choice of $\langle V^2 \rangle$ for the AARS

In (a) below we discuss the most reliable estimates of $\langle V^2 \rangle$ for the AARS and in (b) the correction for measurement error is considered.

(a) $\langle V^2 \rangle$ as a Function of Separation

Fig. 6.15 shows estimates of $\langle W^2 \rangle^{\frac{1}{2}}$ as a function of σ from some of the analyses in this section. Also on the figure are some additional estimates for the AARS, which are discussed below, and the open triangles refer to estimates from the CFA that are reported in part 6.

At $\sigma < 0.5$ MPC the entries for the AARS all refer to second moments estimates, which do not require a model form for F and which the simulations suggest should give an unbiased estimate of $\langle W^2 \rangle^{\frac{1}{2}}$. The error bar at $\bar{\sigma} = 0.25$ comes from Fig 6.10 (a) of the simulations and the open and filled squares refer to estimates that were made from the northern and southern subsamples respectively. We see that both lie within the error bounds which are comparable to the upper and lower bounds (filled and open circles) that come from corrections to the Hubble flow and from changes in $\xi(r)$, discussed in part 5 and given in Table 6.2. Splitting the data from this separation into

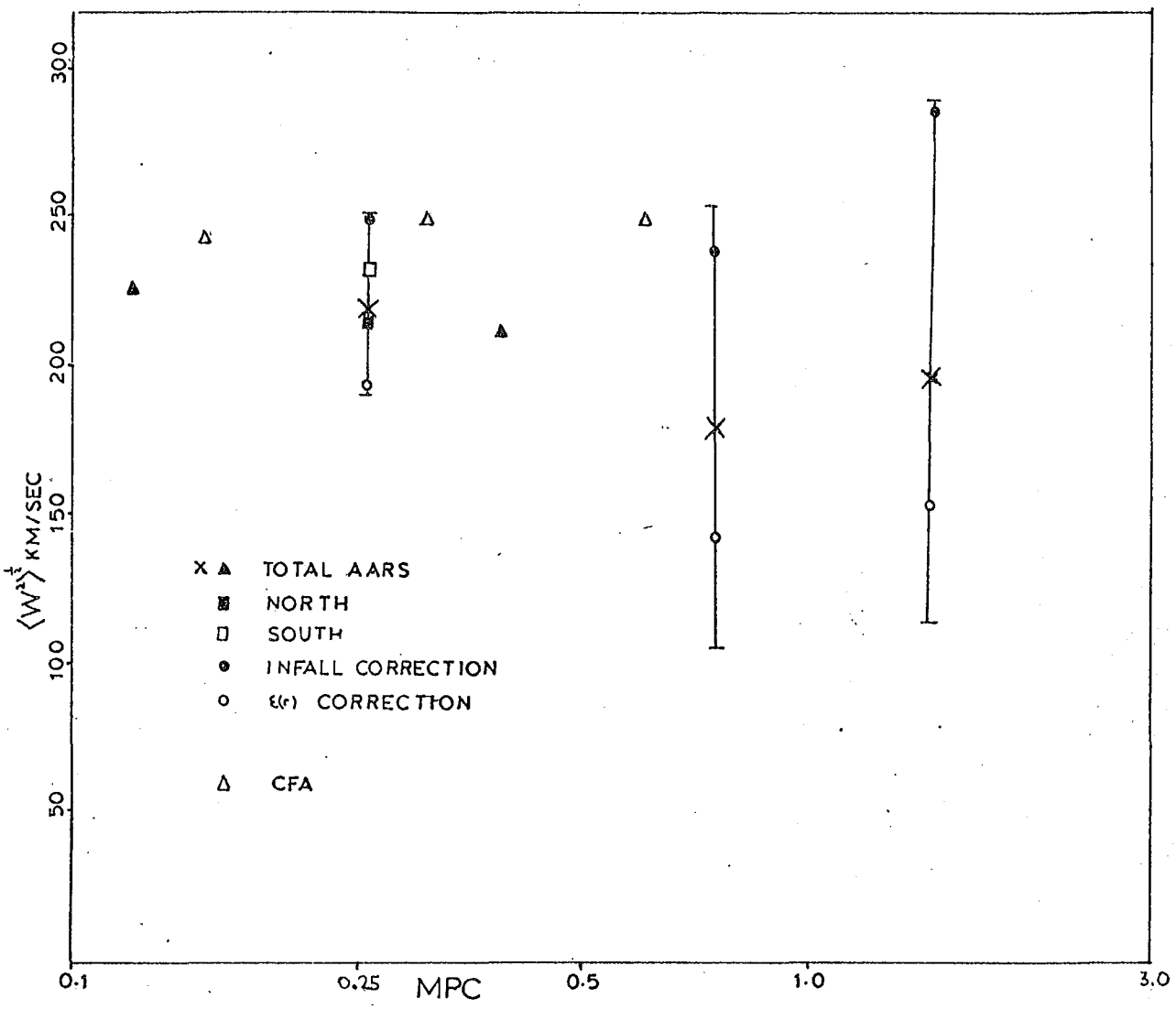

FIGURE 6.15: $\langle W^2 \rangle^{\frac{1}{2}}$ as a function of separation for the AARS and CFA (open triangles). The three main estimates (crosses) come from the analyses discussed in Parts 2 and 3 with corresponding errors from the simulations. At scales less than 0.5 MPC all estimates for the AARS come from the second moments of $\xi_v(\sigma,\pi)$.

two (solid triangles) also agrees well with the overall estimate at these scales.

At $\sigma > 0.5$ MPC the entries (crosses) come from the ψ^2 analysis in part 3 with the errors from the first set of simulations, given in Table 6.4. Although at these scales the estimates are not too sensitive to the exact form of F chosen, they do depend more sensitively on the corrections mentioned above (circles), in particular due to streaming motion (filled circles). However, as both are likely to be upper bounds to the corrections we can realistically expect in each case, the crosses may be reasonable estimates of $\langle W^2 \rangle^{\frac{1}{2}}$ at these scales (i.e. the corrections tend to cancel).

In general we see that Fig 6.15 is as we might expect with $\langle W^2 \rangle^{\frac{1}{2}}$ roughly independent of separation and with errors due to fluctuations rising at larger separations. Taking the mean of the three main estimates to be 200 km/sec, we can ask at what significance 500 km/sec is excluded. If we assume the value of 60 km/sec from eqn. 6.16 encompasses the expected statistical fluctuations averaged over the three separations, we find 500 km/sec excluded at the five sigma level. If instead we take the error of 135 km/sec from eqn. 6.17 from the second set of simulations we find 200 km/sec excluded at the two to three sigma level. Thus we can say with confidence the AARS is inconsistent with $\langle W^2 \rangle^{\frac{1}{2}} \sim 500$ km/sec.

Finally, as with B in section 4.1, we still have to decide what is the most representative value of $\langle W^2 \rangle^{\frac{1}{2}}$ for the sample. Although from the theory in Chapter 2.2 we expect $\langle W^2 \rangle^{\frac{1}{2}}$ to scale as $\sigma^{0.1}$ and the present analysis is not inconsistent with this, there seems little point in representing the variation with σ in Fig 6.15 by an analytic form.

Since the most reliable and model independent estimate in Fig 6.15 comes from $\sigma < 0.5$ MPC and the CVT can only reliably be applied at the smallest scales anyway (where $\langle W^2 \rangle >> (H\sigma)^2$), it seems appropriate to take $\langle W^2 \rangle^{\frac{1}{2}} = 220$ km/sec at $\sigma = 0.25$ MPC, a value which is also quite representative of all the other measurements in Fig 6.15.

(b) Correction for Measurement Error

One final important correction* to $\langle W^2 \rangle$ is to remove the contribution due to measurement error. Taking the rms error for the sample from Chapter 3.5 as σ_{err} = 70 km/sec and subtracting according to the relation $\langle W_c^2 \rangle = \langle W^2 \rangle - 2\,\sigma_{err}^2$, we find $\langle W_c^2 \rangle^{\frac{1}{2}}$ = 196 km/sec. However, if σ_{err} is nearer 100 km/sec, as seems possible from the analysis in Chapter 3.5, we get $\langle W_c^2 \rangle^{\frac{1}{2}}$ = 170 km/sec.

Since it would require only a modest increase in σ_{err} to make a further, more appreciable reduction in $\langle W_c^2 \rangle^{\frac{1}{2}}$, the selection function $\phi(r)$ (with appropriate magnitude limits) and then $\xi_v(\sigma,\pi)$ was re-estimated for the subsample of high quality redshifts, discussed in Chapter 3.5.

The results for $\xi_v(\sigma,\pi)$ for this subsample are shown as the dotted histograms on Figs 6.12 (a-c), along with the histograms and model curves for the total sample. Although around one hundred galaxies have been removed the two histograms at σ < 0.5 MPC are quite similar, the second moments estimate, corrected for Hubble flow and σ_{err} = 50 km/sec, giving $\langle W^2 \rangle^{\frac{1}{2}}$ = 190 km/sec. In the two outer separations the amplitudes agree but we do see some reduction in the broadening, the dashed curves with 100 km/sec fitting the dotted histograms better than the best fitting curves for the total sample. This difference may be due to statistical fluctuations in the smaller sample or indicate broadening due to redshift errors in the total sample.

We may conclude that the value $\langle W^2 \rangle^{\frac{1}{2}}$ = 220 km/sec at σ < 0.5 MPC for the full sample is probably not compromised by large measurement errors and adopt

$$\langle V^2 \rangle^{\frac{1}{2}} = 200 \text{ km/sec} \qquad (6.20)$$

* It may be noted that, since the velocities here are based on pseudo-velocities v = cz km/sec, $\langle v^2 \rangle^{\frac{1}{2}}$ will be slightly over-estimated. However, as we expect the correction to be $\langle v^2 \rangle^{\frac{1}{2}}_{corr} \simeq \frac{\langle v^2 \rangle^{\frac{1}{2}}}{(1+\bar{z})}$ (e.g. Harrison and Noonan, 79) and $\bar{z} \sim 0.05$ for the sample, it has been ignored.

as the most reliable estimate of the rms relative peculiar velocity dispersion between pairs in the AARS at an average projected separation of 0.25 MPC.

6.5.6 $\langle V^2 \rangle$ from other Redshift Catalogues

The results from the AARS seem to be in direct conflict with the estimates $\langle V^2 \rangle^{\frac{1}{2}} \sim 500$ km/sec found by Peebles (79,81) from the KOS and Huchra/Rood catalogues. This disagreement seems especially puzzling as these samples were also analysed using $\xi_v(\sigma,\pi)$ and in both cases the amplitude B of $\xi(r)$ is in quite close agreement with eqn. 6.10 for the AARS. To attempt to account for the discrepancy, $\xi_v(\sigma,\pi)$ has been re-estimated for the KOS and Huchra catalogues and the former has been combined with the AARS to form an ensemble estimate of $\langle V^2 \rangle^{\frac{1}{2}}$.

This analysis is described below and the results for $\xi_v(\sigma,\pi)$ are presented along with simple model curves calculated using the usual $W^{\frac{3}{2}}$ distribution function. The newly published diagrams of $\xi_v(\sigma,\pi)$ from the CFA catalogue are presented along with the models in part C, and the results compared with the published estimates of $\langle V^2 \rangle$.

(a) Analyses of the KOS Catalogue

To estimate $\xi_v(\sigma,\pi)$ the prescription in section 2.2 was followed with $\phi(r)$ calculated from the solid curve in Fig. 5.4 (a) of Chapter 5. As in the estimate of $\xi_s(s)$ for this sample in section 3.1, the results are not sensitive to the form of $\phi(r)$ chosen. As the sample is small and the correlation functions noisy, the pairs have been combined to form one histogram for $\sigma < 1.0$ MPC.

The results are in Fig 6.16 along with model curves with B = 12, the latter in agreement with the value found by Peebles (79). Since we see $\xi_v(\sigma,\pi)$ has a long tail and as Peebles estimate of $\langle W^2 \rangle$ came from the second moments of $\xi_v(\sigma,\pi)$ with $\pi_{cut} = 15$ MPC, the reason he found a large velocity dispersion for the sample is quite apparent. Although some elongation

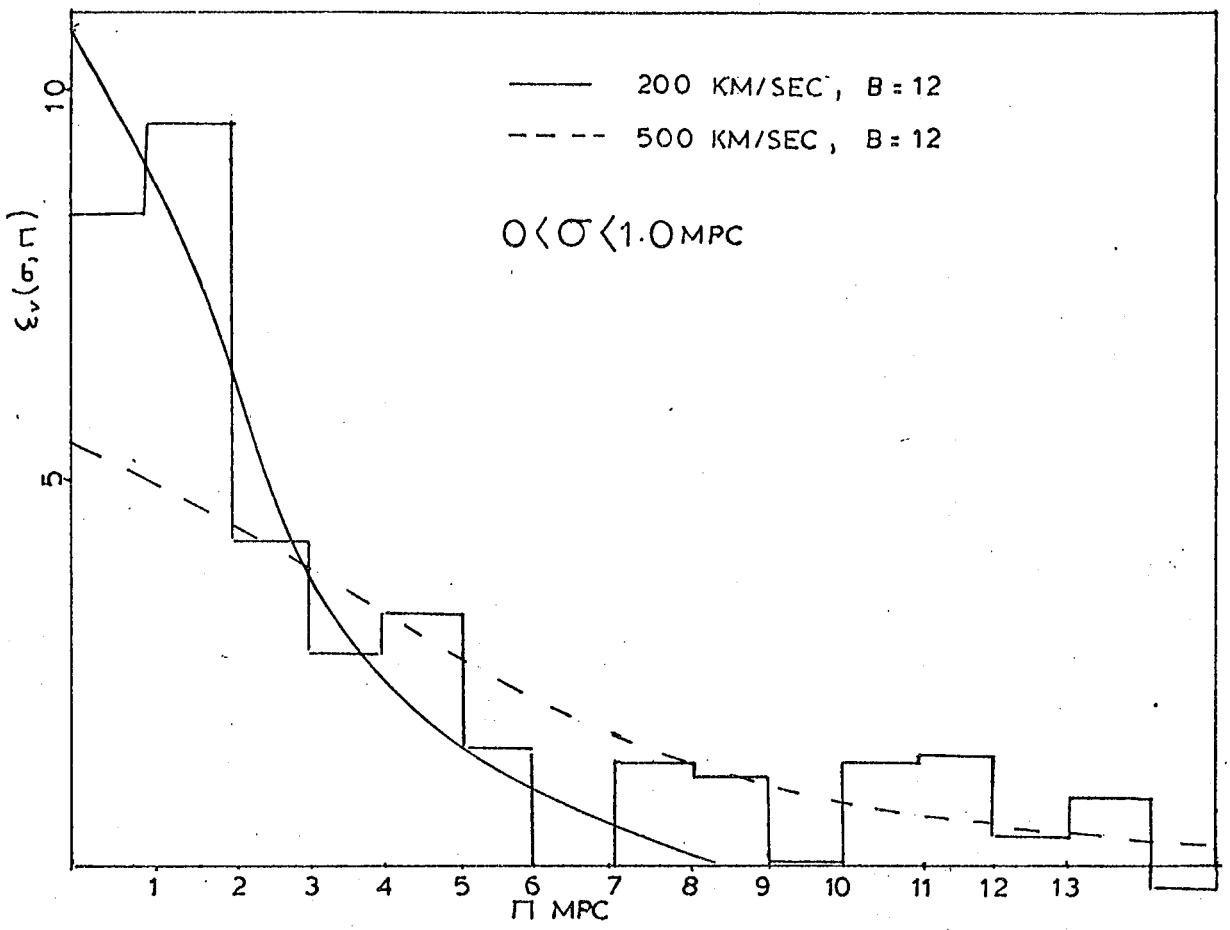

FIGURE 6.16: Estimates of $\xi_v(\sigma,\pi)$ for the KOS survey along with model curves.

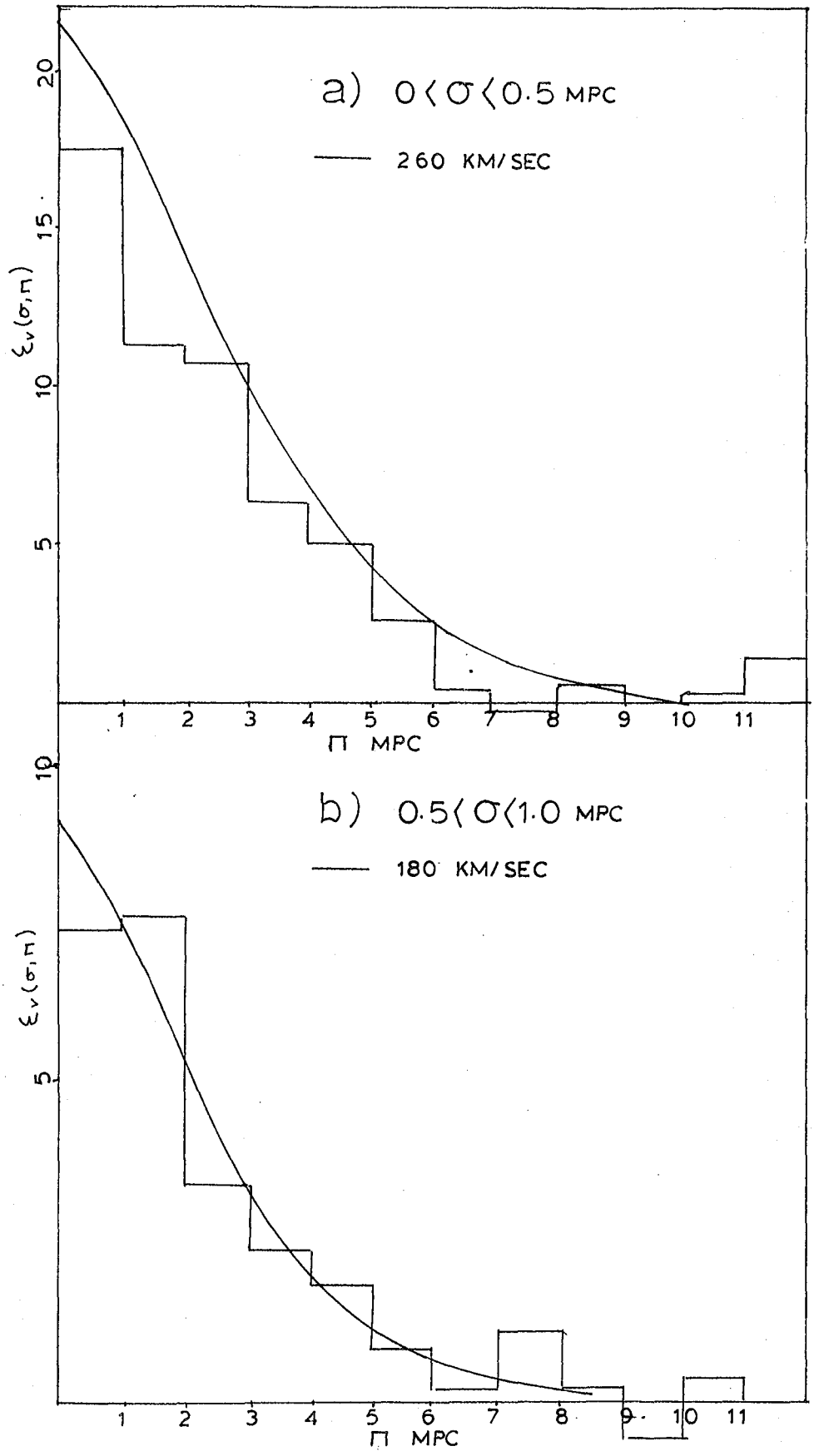

FIGURE 6.17: Estimates of $\xi_v(\sigma,\pi)$ from the combined AARS and KOS samples. The model curves are the best fitting curves for the AARS sample taken from Figs 6.12(a) & (b).

is apparent in the plots of field NP4 (Chapter 5.3) and the dashed curve with 500 km/sec approximately fits the data at $7 < \Pi < 15$ MPC, the solid curve with 200 km/sec gives a much better fit at $\Pi < 7.0$ MPC. Since at the smaller scales we expect the statistics to be best, this suggests that, unless the $W^{-\frac{3}{2}}$ form is completely unrepresentative, $\langle W^2 \rangle^{\frac{1}{2}}$ for this sample is closer to 200 than 500 km/sec and the tail in $\xi_v(\sigma,\pi)$ is merely due to statistical fluctuations in the small sample. As Peebles notes, removing the richest field NP4 from the sample reduces the second moments estimate of $\langle W^2 \rangle^{\frac{1}{2}}$ by a factor of two or so.

Since the main problem with this catalogue seems to be its small size and as it is similar in nature to the AARS, it is interesting to combine them to produce a sample of $\sim$ 500 galaxies. A crude way to do this is to merely combine the total pair counts $DD(\sigma,\pi)$ and $DR(\sigma,\pi)$ for each sample together and recalculate $\xi_v(\sigma,\pi)$ using eqn. 6.3 of section 2.2.

Figs 6.17 (a-b) show $\xi_v(\sigma,\pi)$ for the two usual separations in σ with the curves taken from the best fits in Figs 6.12 (a-b) for the AARS.

We see at $\sigma < 0.5$ MPC the histograms in both figures are quite similar while at $0.5 < \sigma < 1.0$ MPC the agreement is remarkable. It might be thought this resemblance is due to the fact that the AARS completely dominates the pair counts. Although this is true at $\sigma > 1.0$ MPC, at the separations discussed here the pair counts $DD(\sigma,\pi)$ for $\pi <$ 15 MPC are in the proportion AAT : KOS, 10 : 7.3 and 10 : 9.3 for Figs a and b respectively.

Since the measuring error for the KOS sample is quoted by Rood (82) and Kirshner et al (78) as 100 km/sec and this is little larger than for the AARS, we may conclude that the combined samples agree with the estimate of $\langle V^2 \rangle$ for the AARS in part 5.

(b) Analyses of the Huchra Catalogue

In another study, Peebles (80b) has estimated $\xi_v(\sigma,\pi)$ from the bright southern galaxies with $m_B \lesssim 13.0$ in the SRC and noted that models

with 500 km/sec fit the data reasonably well.

To test this, the method outlined in Peebles (80b) has been followed, and $\xi_v(\sigma,\pi)$ estimated in the similar Huchra catalogue (Davis et al, 78) for galaxies with $m_b \leq 13.0$, $b^{II} < -30^o$ and with measuring error quoted as less than 100 km/sec. Following Peebles, to estimate $\phi(r)$ the observed number redshift counts (solid histogram in Fig 6.18) for all galaxies between 10 and 30 MPCwas used, divided by the appropriate volume elements, as in Chapter 5.2. Since the sample only contains 170 galaxies, the pairs at $\sigma < 1$ MPC were combined to form one bin (as was done for the KOS sample), the results being in Fig 6.19.

We see the model curve shown with 500 km/sec and B = 12.5 crudely fits the data at $\pi < 7.0$ MPC, although misses the long tail at larger scales.

As Peebles notes, the high dispersion implied may in part be due to measuring error or to the possibility that redshifts have preferentially been measured in small patches of the sky, such as in rich selected groups. However, as galaxies with large redshift errors were excluded and as the catalogue is nearly complete to $m_b = 13.0$ neither seems an attractive explanation.

Another, more likely bias in the catalogue comes from clustering on the scale of the sample. Although the volumes do not include the Virgo cluster, the mean $\frac{V}{Vmax}$ (Chapter 4.2) for the sample is 0.4 to 0.45 (Davis et al, 78), suggesting considerable inhomogeneities in the nearer volumes. To allow for this $\phi(r)$ was re-estimated for the sample (ignoring Virgo infall) using the method in Chapter 5.2 with the Schecter parameters from the AARS transformed into the Huchra system by eqn. 6 of Table 3.2.

The results in Fig 6.20(a) show $\xi_v(\sigma,\pi)$ (solid histogram) is now reasonably fitted by a model with 200 km/sec and B = 18. Furthermore, the fit is improved (dashed histogram) if galaxies within 12^o of the core of the Fornax cluster are removed where the relative rms velocity dispersion

is known to be $\langle V^2 \rangle^{\frac{1}{2}} \sim 450$ km/sec (Jones and Jones, 80).

This behaviour of $\xi_v(\sigma,\pi)$ can be understood from an examination of Fig 6.18 which shows that the observed counts around the distance of the Fornax cluster (dashed histogram is Fornax core out) are considerably larger than the smooth model curve from the luminosity function. Since most of the pairs $DD(\sigma,\pi)$ come from this region, estimating $DR(\sigma,\pi)$ from the observed background density here (as in Fig 6.19) will underestimate $\xi_v(\sigma,\pi)$ at small π and overestimate it at larger π, giving rise to a low apparent amplitude of B and large estimate of $\langle W^2 \rangle^{\frac{1}{2}}$. Naturally the results in Fig 6.20a depend on the smooth model in Fig 6.18 being a reasonable estimate of $\phi(r)$ for the sample. Of course conversely one might use the agreement between $\langle W^2 \rangle^{\frac{1}{2}}$ here and that for the AARS to be evidence that this model for $\phi(r)$ is reasonable.

A similar effect to this occurs in the northern galaxies from the catalogue discussed by Peebles (80a, p.285). These galaxies, with distances between 15 and 40 MPC, have an observed number redshift histogram that peaks near 15 MPC, whereas the same LF model as used for $\phi(r)$ above, peaks at larger distances.

The results of $\xi_v(\sigma,\pi)$ using the smooth curve for $\phi(r)$ for this sample are plotted in Fig 6.20(b) as a solid histogram along with a model curve with B = 21 and $\langle W^2 \rangle^{\frac{1}{2}} = 200$ km/sec. Although the lower bound 15 MPC mostly eliminates the Virgo core there is still the possibility some high velocity pairs are included that could dominate $\langle W^2 \rangle$. Also Tully (82) has noted considerable prolate structure radiating and expanding from Virgo that could also elongate $\xi_v(\sigma,\pi)$. Excluding the region within 12° of the Virgo core, to help eliminate these possibilities, we see the dashed histogram gives a reasonable fit to the model.

It should be emphasised that the discussion here is only intended to show the local catalogues may be consistent with $\langle V^2 \rangle^{\frac{1}{2}} = 200$ km/sec found

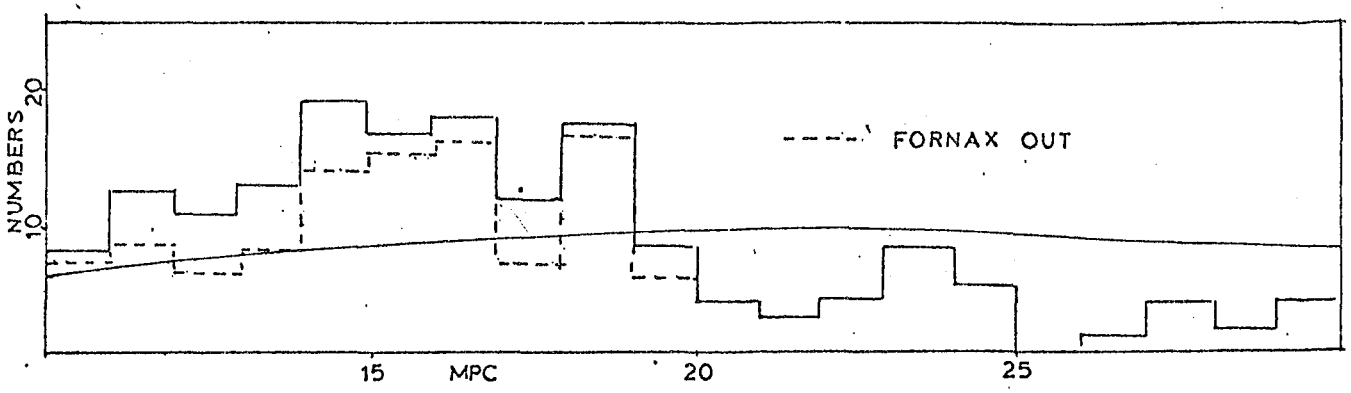

FIGURE 6.18: Number distance counts for the southern Huchra catalogue at M_B <13.0 along with a model calculated assuming the Schecter luminosity function parameters found for the AARS.

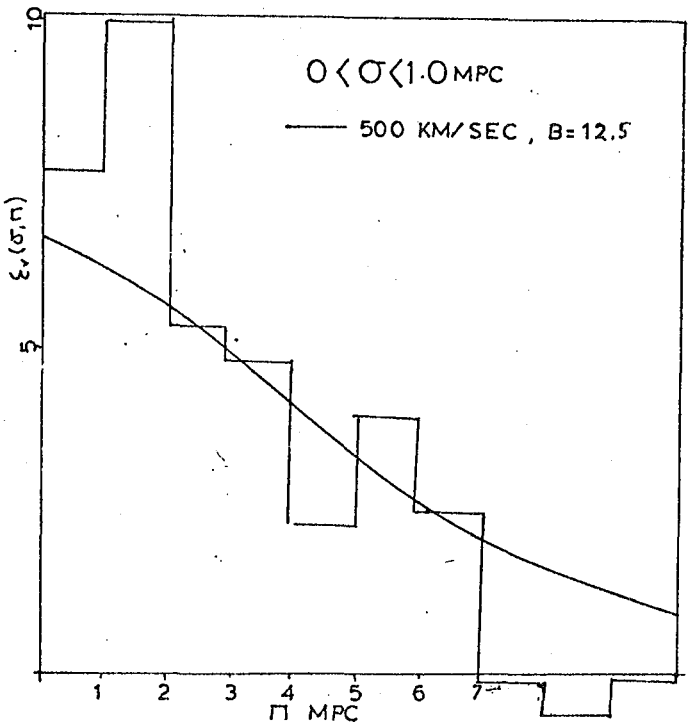

FIGURE 6.19: Estimate and model of $\xi_v(\sigma,\pi)$ for the southern Huchra catalogue using the selection function calculated from the solid histogram in Fig 6.18.

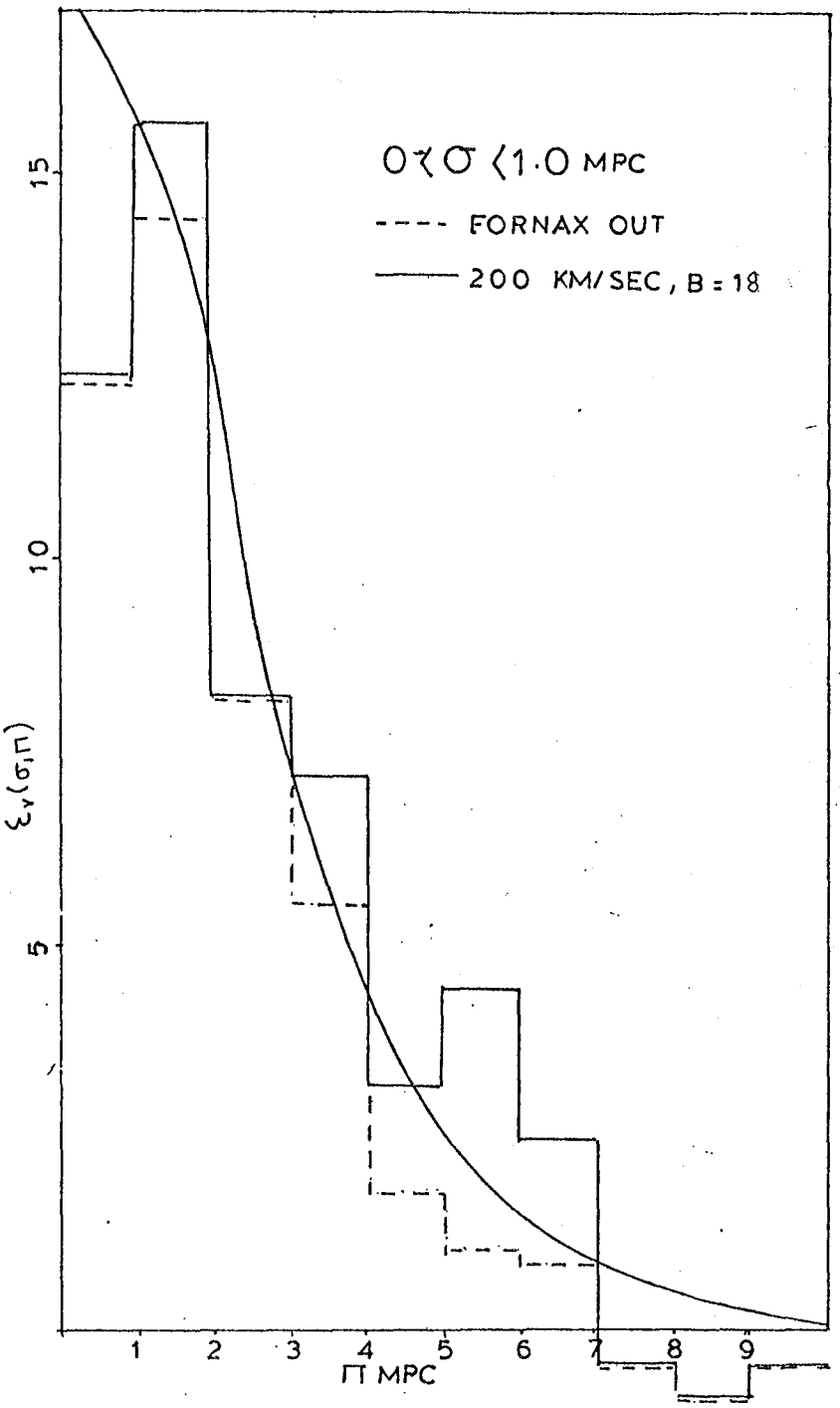

FIGURE 6.20 (a) : Estimate and model of $\xi_v(\sigma,\pi)$ for the southern Huchra catalogue using the selection function calculated from the solid curve in Fig 6.18.

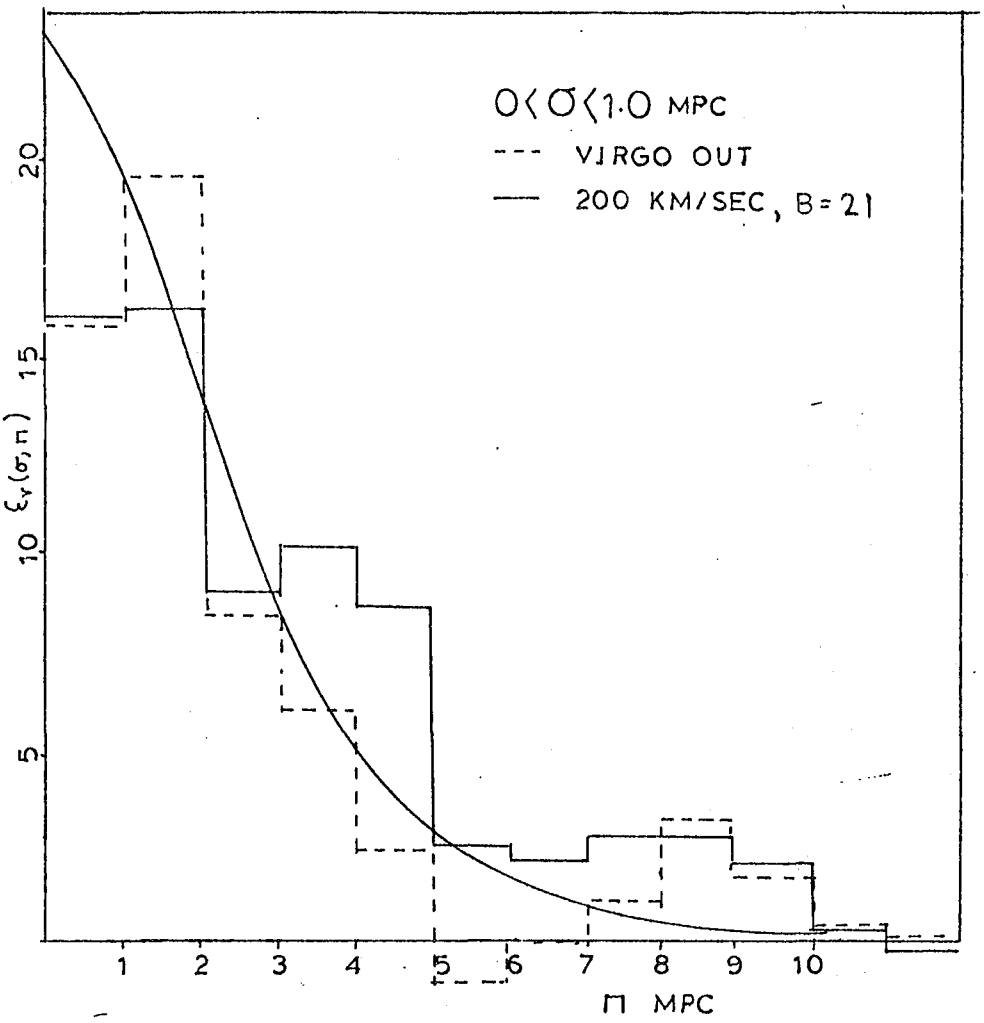

FIGURE 6.20 (b): Estimate and model of $\xi_v(\sigma,\pi)$ for the northern Huchra catalogue using a selection function based on the AARS Schecter fits.

for the AARS. Since we see the samples are strongly biased by inhomogeneities and the results are very sensitive to the form of $\phi(r)$ assumed, it may not be very meaningful even attempting to estimate correlation functions.

(c) The CfA Catalogue

The analysis in (b) above leads on quite naturally to discuss the newly published results of $\xi_v(\sigma,\pi)$ for the CfA (Davis and Peebles, 82, DP), which by its shear size should be taken more seriously than the KOS and Huchra catalogues. Although the northern sample contains nearly four times the number of galaxies as the AARS, as discussed in Section 3.2, the relatively shallow depth has certain disadvantages. While systematic errors may only affect estimates of $\xi_v(\sigma,\pi)$ on scales >> 10 MPC, since the CfA is only a factor of two or so deeper than the Huchra catalogue discussed above and the model curves used by DP are a poor fit to the observed number redshift distribution, there is still the possibility of systematic effects occurring at small scales. As with $\xi_s(s)$ though, DP do not discuss the dependence of $\xi_v(\sigma,\pi)$ on the form of the selection function.

Turning to the results from $\xi_v(\sigma,\pi)$, DP have fitted estimates of $\langle W^2\rangle^{\frac{1}{2}}$ as a function separation σ with a powerlaw over the range 10 KPC $< \sigma <$ 1.6 MPC, the data at the smallest scales coming from new accurate redshift measurements of Turner's close binary galaxies (Turner, 76). They find over this range a reasonably fit to the data is

$$\langle V^2\rangle^{\frac{1}{2}} = 340 \pm 40 \left(\frac{\sigma}{1\text{MPC}}\right)^{0.13} \text{ km/sec} \qquad (6.21)$$

the scaling in close agreement with that expected in the theory. Since the tehcniques used to estimate $\langle V^2\rangle$ from the relative velocity data often differ from those used on the AARS earlier in this section, it is important to discuss them in some detail.

At σ < 0.2 MPC five out of the seven estimates are based on second moments estimates of $\langle V^2 \rangle^{\frac{1}{2}}$, two of which come from $\xi_v(\sigma,\pi)$ for the CfA and so are fairly comparable to the AARS analysis. Taking πcut = 7.5 MPC, DP find $\langle W^2 \rangle^{\frac{1}{2}}$ = 194 km/sec at σ < 100 KPC and 265 km/sec at 100 <σ< 200 KPC. Since these refer to estimates of $\langle W_o^2 \rangle^{\frac{1}{2}}$, they have been corrected for Hubble flow according to eqn. 6.14. The corrected results are 182 and 245 km/sec, the latter figure shown as an open triangle at σ = 0.15 MPC in Fig 6.15, along with the AARS results. A similar value of 220 km/sec comes from the binary data averaged over the three separations in σ, at $\bar{\sigma}$ = 10, 30 and 90 KPC.

At σ > 0.2 MPC the estimates are all based on a fitting analysis of $\xi_v(\sigma,\pi)$ for the CfA similar to that described in part 3 but with the models using an exponential distribution function and the correction for streaming motion given in eqn. 6.18. To compare these results consistently with those of the AARS, $\xi_v(\sigma,\pi)$ has been taken from their diagrams and fitted by eye with models using the $W^{\frac{3}{2}}$ form and no streaming motion, as used on the AARS in part 3.

Figs 6.21 (a-b) show the histograms for $\xi_v(\sigma,\pi)$ (binned up to 1 MPC in π) between 0.2 < σ < 0.4 MPC and 0.4 < σ < 0.8 MPC respectively, along with curves 250 km/sec (dashed) and 300 km/sec (solid) with B in both cases taken as 17.2 from Fig 6.7 of section 4.2.

In both cases we see the $W^{\frac{3}{2}}$ form with 250 km/sec fits better than the solid curve. The corresponding best fits found by DP for Fig a and b were 317 and 358 km/sec respectively, which were reduced to 290 and 300 km/sec when the infall correction was reduced by 90%. These results and those for the AARS in Table 6.3 for the different models suggest that in Fig a the difference between the dashed curve value and the value preferred by DP is mainly due to their using an exponential rather than the $W^{\frac{3}{2}}$ form. In Fig b the difference of $\sim$ 100 km/sec comes about equally from the differences in the distribution function and the infall model.

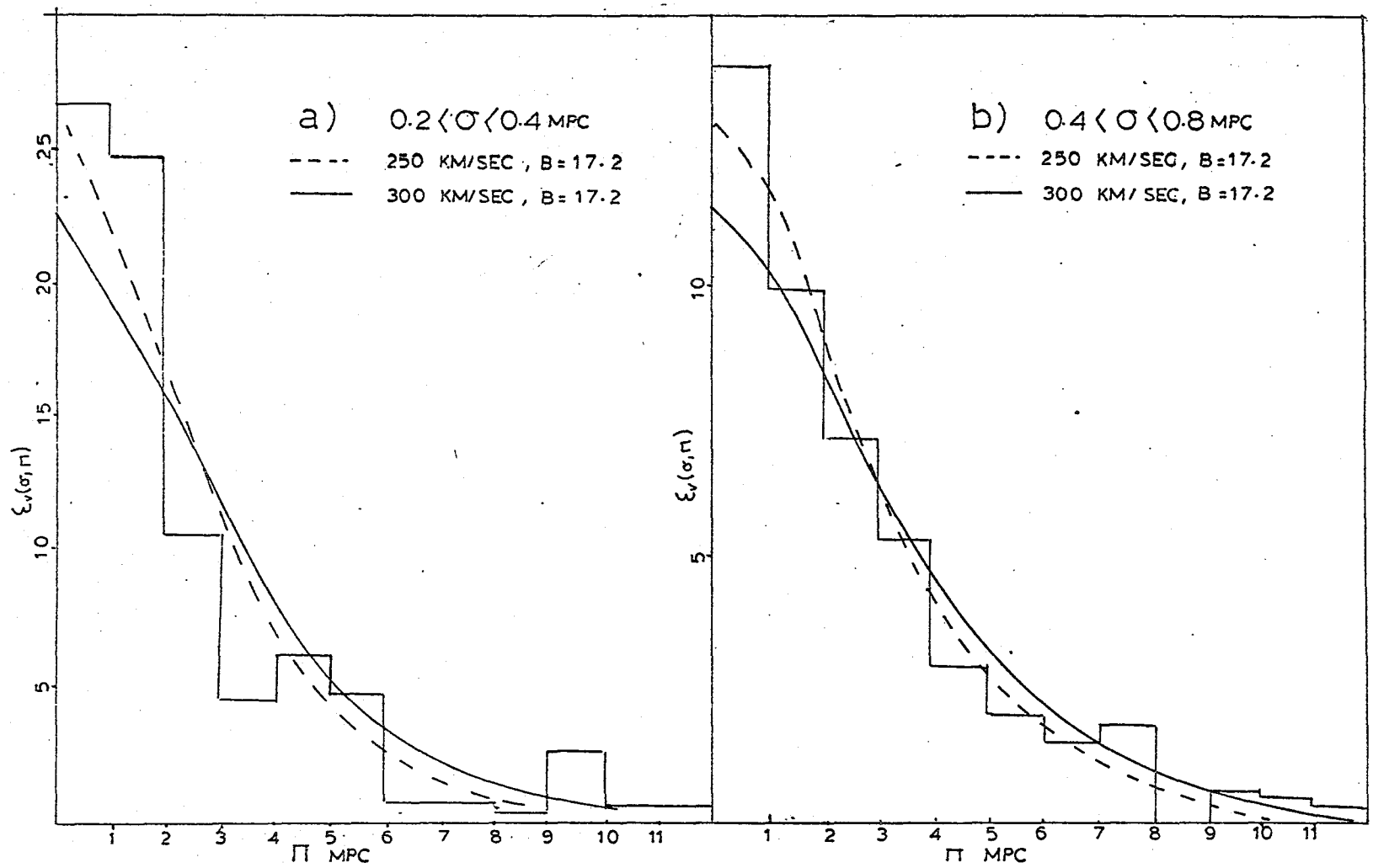

FIGURE 6.21 (a)-(b): Published estimates of $\xi_v(\sigma,\pi)$ for the CFA along with models.

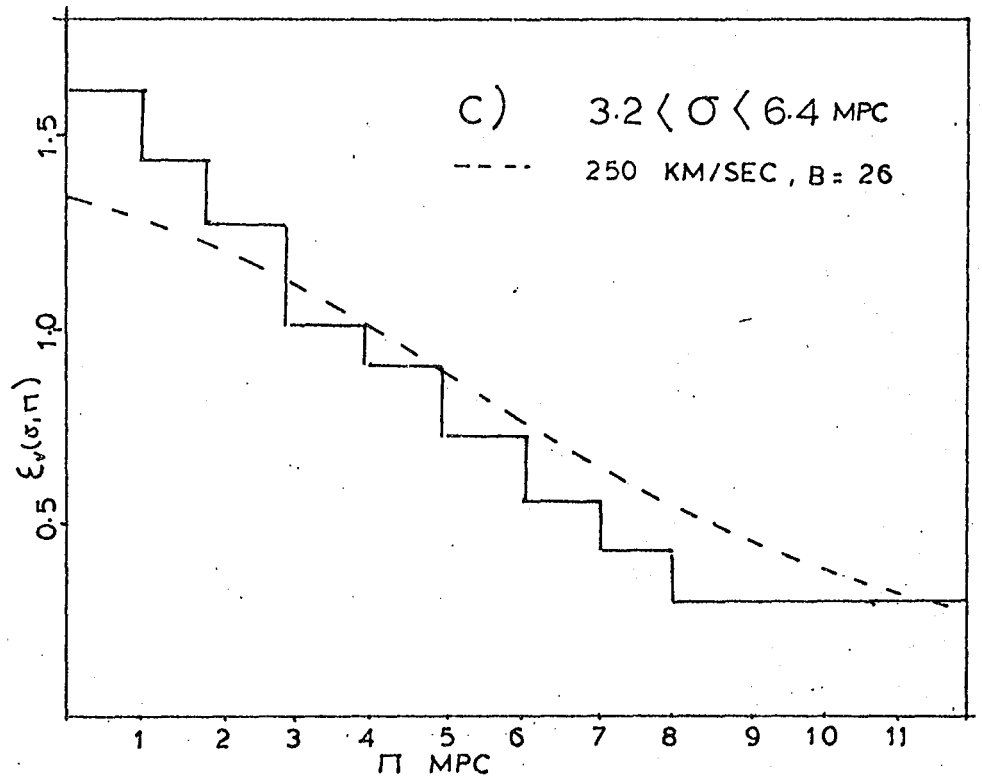

FIGURE 6.21 (c): Same as Figs (a) and (b) for an outer separation.

As discussed in part 4, the problem with the fitting method, especially at large. σ, is the uncertainty in the model for $\xi_v(\sigma,\pi)$. Although it was suggested in part 4 that a gaussian or $W^{\frac{3}{2}}$ are probably more physically reasonable than an exponential, there is the possibility that the spread in cluster richness in the CfA could make the distribution broader than a gaussian or even an exponential. For example we may expect a very long tail in $\xi_v(\sigma,\pi)$ due to the known high velocities in rich clusters, which seems to have been missed in the fits of DP because these authors found the estimates of $\langle V^2 \rangle$ (unlike Q for the Zwicky catalogue) insensitive to the removal of prominent clusters in the sample. In this general context though, some justification for using the $W^{\frac{3}{2}}$ form of eqn. 6.15 may come from the N body simulations which, like the CFA, have a considerable spread in cluster richness.

Another uncertainty in the DP model for $\xi_v(\sigma,\pi)$ comes from their unrealistically large streaming motion (Part 4) which may, in any case, be compensated by the apparent rise in $\xi(r)$ above a-1.8 powerlaw (section 4).

An insight into these last two effects comes from considering $\xi_v(\sigma,\pi)$ for $3.2 < \sigma < 6.4$ MPC, which is shown in Fig 6.21 (c). The model corresponds to 250 km/sec and B comes from Fig 6.7 of section 4.2.

We see this model with B = 26 gives the correct overall amplitude at these scales, a factor of 50% larger than in Figs (a) and (b), and demonstrates the non-powerlaw behaviour discussed for this sample in section 4.2. The sharper peak seen in the data than the model may reflect the need for infall in the latter, however using the full infall model DP find $\langle W^2 \rangle^{\frac{1}{2}}$ = 510 km/sec, which is lowered to 290 km/sec when removed. Making the reasonable physical constraint that $\langle V^2 \rangle$ is little larger at this scale than at $\sigma < 1.0$ MPC, in turn could suggest the full infall model used by DP is too high. As noted in part 4, firm constraints on the infall (and shape of $\xi(r)$) along this line will require larger redshift samples.

Putting the two values of $\langle V^2 \rangle^{\frac{1}{2}}$ from the dashed curves in Fig 5.21 (a-b) on Fig 6.15, we see the three estimates (open triangles) considered here from the CfA are in reasonable agreement with those found by a similar analysis of the AARS. Correcting these values for a measurement error of 50 km/sec*, we may take $\langle V^2 \rangle^{\frac{1}{2}}$ = 240 km/sec at σ = 1 MPC as a possible alternative to the figure 340 km/sec found by DP for the CfA at σ = 1 MPC.

6.5.7 Summary and Conclusions

The great importance of the statistical methods used for estimating velocity dispersions in this section is that they do not require subjective decisions about how galaxies should be assigned to groups. The statistic $\xi_v(\sigma,\pi)$ estimated for the AARS is insensitive to the model used for the selection function and gives a convincing demonstration at projected separations $\sigma < 0.5$ MPC of the effects of peculiar velocities in distorting the clustering along the line of sight. This effect is considerably larger than we would expect from measuring error. At these scales the simulations show the second moments of $\xi_v(\sigma,\pi)$ should give an unbiased estimate of $\langle V^2 \rangle$ with the Hubble flow contribution statistically subtracted. Although the latter correction does require a model for $\xi(r)$, at these scales the contribution is small and the value $\langle V^2 \rangle^{\frac{1}{2}} \simeq$ 200 km/sec found here is quite stable. At the larger projected scales the model fits to $\xi_v(\sigma,\pi)$ give more reliable estimates of $\langle V^2 \rangle$. Here the histograms are quite well fitted by models calculated using physically reasonable velocity distribution functions; these fitting a gaussian or $W^{\frac{3}{2}}$ form better than an exponential. While the estimates here have larger statistical fluctuations and are more dependent

* 60% of the CfA sample comes from the measurements of Tonry and Davis (79) that have $\sigma_{err} \simeq$ 35 km/sec, the remaining 40% having a mean error of 70 km/sec. If the rms value for the latter 40% of the galaxies is equal to the mean we get a total rms of $\sim$ 50 km/sec. If instead the rms is larger than the mean, the total rms error may be comparable to the figure of 70 km/sec adopted for the AARS in Chapter 3.5.

on models for $\xi(r)$ and streaming motion, at $\sigma < 2.0$ MPC the data is not inconsistent with a slow variation of $\langle v^2 \rangle$ with separation expected physically.

Although from previous analyses of the KOS and Huchra catalogues using $\xi_v(\sigma,\pi)$, Peebles has found $\langle v^2 \rangle^{\frac{1}{2}} \sim$ 500 km/sec, studies in this section have shown these samples may be equally compatible with the figure found for the AARS. The main problem with the KOS survey appears to be its small size, however when combined with the AARS the considerably larger combined sample is consistent with the results from the AARS alone. As well as being small, the Huchra catalogue has the problem it is biased by local inhomogeneities which, if not accounted for, have the effect of over-estimating $\langle v^2 \rangle$ from systematic errors in the selection function used to calculate $\xi_v(\sigma,\pi)$.

Values that lie between the figures 200 and 500 km/sec above have recently been found by Davis and Peebles from $\xi_v(\sigma,\pi)$ estimated from the CfA catalogue. However, a reanalysis of $\xi_v(\sigma,\pi)$ for this sample in part 6, in the same way as for the AARS, shows the estimates from the two samples may be very similar, with $\langle v^2 \rangle^{\frac{1}{2}}$ in the range 200-250 km/sec. The main difference this time between the published results and those discussed in this section is differences in the model for $\xi_v(\sigma,\pi)$.

It is interesting to compare these velocity dispersions with those from other studies, which are discussed in more detail in Chapter 7.2. Assuming the peculiar velocities for the AARS are randomly assigned, the individual rms velocity dispersion is typically $\frac{\langle v^2 \rangle^{\frac{1}{2}}}{\sqrt{2}} \sim$ 140 km/sec. Although this is much lower than the typical figure of $\sim$ 1000 km/sec found in rich clusters, it is rather higher than the typical dispersion 50-100 km/sec in nearby loose groups of galaxies. This latter difference is probably due to the fact $\langle v^2 \rangle$ is a pair weighted statistic and depends quite sensitively on the richness of the clustering sampled. If $\langle v^2 \rangle$ between pairs depends on the abundance of neighbours, as assumed in the CVT, we need

a measure of Q as well as B for the sampled volumes of the AARS, an issue we now turn to.

6.6 THE THREE POINT CORRELATION FUNCTION

Since the quantity Q needed for the Cosmic Virial Theorem depends sensitively on the richness of the clustering sampled, it is important to make an estimate of it for the AARS. This is all the more important since all but one of the previous estimates have come from projected catalogues where Q, like B, depends on an integral over an assumed luminosity function. In part 1 the estimate from the AARS is discussed with part 2 comparing with the results from other catalogues.

6.6.1 Estimation of Q for the AARS

To determine Q for the AARS an estimator was used that was based on a program applied to the Rood catalogue, which P.J.E.Peebles kindly made available.

Since peculiar velocities affect distances along the line of sight, the method estimates an analogue of the angular three point correlation function but uses the redshift information to calculate projected separations along three sides of each triangle defined by galaxy triplets. The shortest side of each triangle $r_1 = \sigma_v$ is defined like σ in section 2.1, with $r_2 = u\sigma_v$ the intermediate side and $r_3 = (u + v)\ \sigma_v$ the longest side, where u and v are the shape parameters discussed in Groth and Peebles (77) (GP). This function $Z_v(r_1,r_2,r_3)$ gives an estimate of Q by a relation similar to eqn. 2.4 in Chapter 2.1 for the spatial function ;

$$Z_v\ (r_1,\ r_2,r_3) = Q(W_z(r_1)\ W_z(r_2) + 2 \text{ x cyclic}) \qquad (6.22)$$

where $W_z(r)$ is an analogue of the angular two point correlation function.

The computation of Z_v and W_z is similar to the prescription outlined in GP for projected catalogues. To reduce noise in Z_v and W_z the redshift information was used to cut out all galaxies with line of sight velocity

separations > 5 MPC along the two shorter edges of each triplet. The background counts of triplets and pairs were estimated by putting down many random points in the redshift volumes, according to the method used in section 2.2. for $\xi_s(s)$, and then scaling to the overall numbers expected in each field. Like the estimates of $\xi_v(\sigma,\pi)$ and $\xi_s(s)$ the results for Q presented are not sensitive to the form of the selection function adopted.

Table 6.5 shows the values found for Q for different triangle sizes σ_v and shape parameters u and v. The mean for all twelve is

$$Q = 0.55 \pm 0.06 \qquad (6.23)$$

Fig 6.22 shows $z_v(\sigma_v, u, v)$ as a function of σ_v(crosses) along with the scaling expected from the model for the spatial three point function in eqn. 2.4, Chapter 2.1.

We see the data is fairly consistent with the model, although it does rise above at the two outer separations, which is perhaps connected with the rise of $\xi(r)$ above a -1.8 powerlaw discussed in the section 4. In a larger sample one should be able to test the model more thoroughly, as has been done for projected samples by GP. In particular, at large separations it may be possible to test more sensitively for linear sturcture evident in the plots of the galaxy distribution by testing the dependence of Q on shape parameter V.

Since the error on eqn. 6.23 is internal and the values of Q in Table 6.5 are not independent, the estimator was tested on some of the simulated catalogues discussed in Chapter 3.7. As Peebles (80a, p.241) discusses, if each clump in the simulations has a fixed number of levels and subclusters per level (as is the case here), we expect $Q \simeq 0.5$, which is about as low as it can be.

The analyses of ten of the first set of simulations with $\langle v^2 \rangle^{\frac{1}{2}} = 200$ km/sec gives a mean $\bar{Q} = 0.49 \pm 0.73$, suggesting the method gives an

TABLE 6.5: Q for the AARS

$\bar{\sigma}_v$ (MPC)		1 < u < 2	2 < u < 3	3 < u < 4
0.125	$0<V<\frac{1}{2}$	0.60	0.63	1.32
	$\frac{1}{2}<V<1$	0.26	0.28	0.02
0.375	$0<V<\frac{1}{2}$	0.14	0.54	0.71
	$\frac{1}{2}<V<1$	0.64	0.51	0.44
0.75	$0<V<\frac{1}{2}$	0.30	0.66	0.72
	$\frac{1}{2}<V<1$	0.56	0.95	0.86
1.5	$0<V<\frac{1}{2}$	0.49	0.54	0.19
	$\frac{1}{2}<V<1$	0.81	0.66	0.22

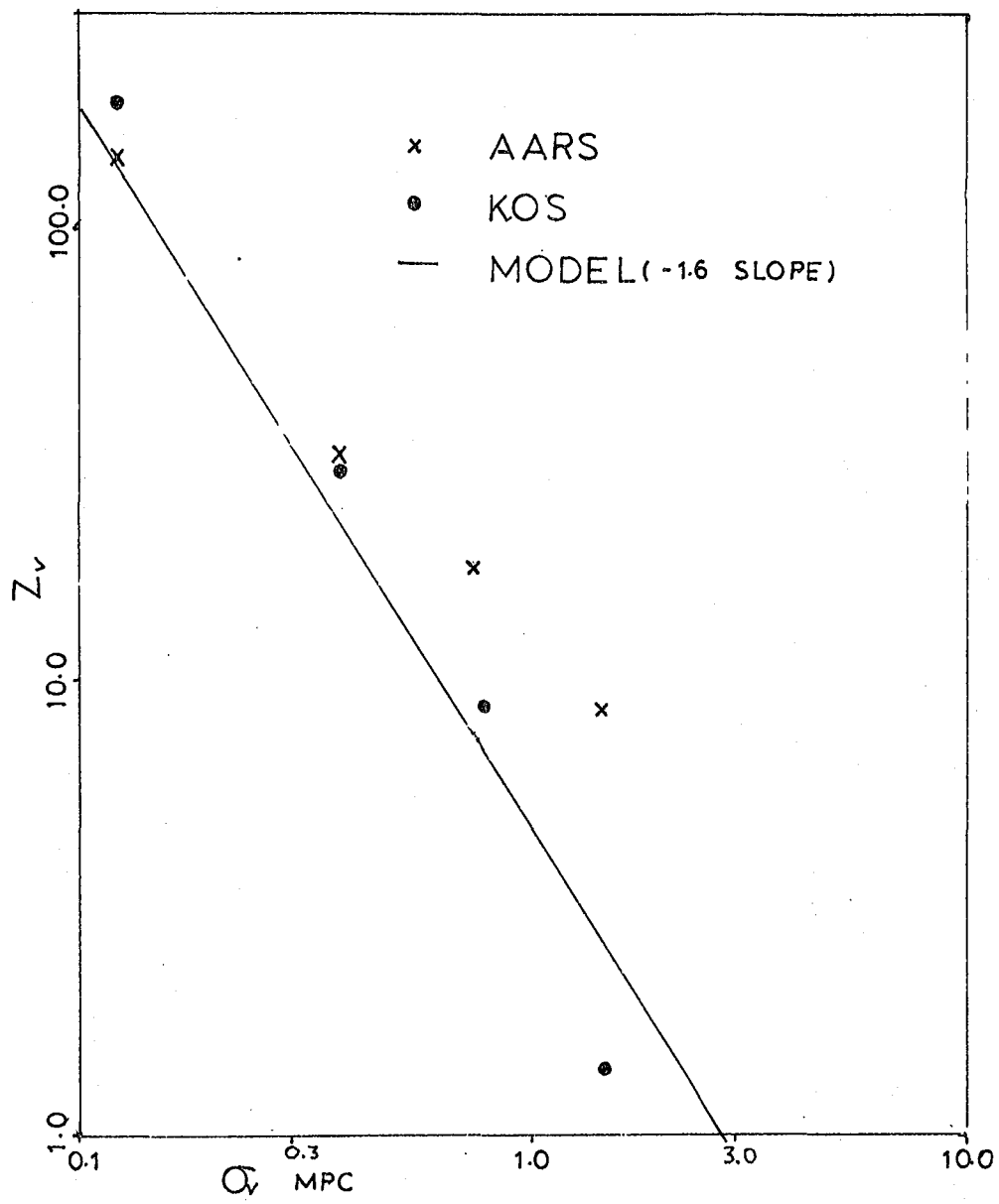

FIGURE 6.22: Projected three point function as a function of projected separation for the AARS and KOS surveys along with expected scaling.

unbiased estimate of Q with internal errors giving a reasonable estimate of the true errors on Q within the sampled volumes.

As an additional test of the fluctuations, Q was estimated in the north and southern subsamples separately. The corresponding values were $Q = 0.64 \pm 0.13$ and $Q = 0.52 \pm 0.09$, the higher value in the north being expected since field GNB has a few groups that appear quite compact when seen in projection (Chapter 5.3).

We see that the estimate in eqn. 6.23 for the total sample lies within the errors for the two subsamples again suggesting the internal errors are reasonable for the sampled volumes.

6.6.2 Comparison with Other Samples

Although Q found for the AARS is about as low as it can be for the model for $\xi(r,r,r)$ in Chapter 2.1 and is considerably smaller than $Q = 1.29$ from the Zwicky and Lick estimates discussed there, the low value is not unexpected because the sample does not contain any rich clusters or many tight groups and so samples only a small spread in cluster richness. Indeed the sensitivity of Q to rich areas can be seen from the dependence of Q on whether Coma is included in the Zwicky catalogue. With Coma included GP found $Q \simeq 1.4$, but when eleven galaxies in the centre were excluded this value fell to $Q \simeq 0.85$.

This sensitivity is also demonstrated by the value of Q found for the KOS sample which was estimated in the same way as for the AARS in part 1. Although Z_V as a function σ_V in Fig 6.22 (filled circles) is quite close to that found for the AARS, the KOS survey gives $Q = 1.50 \pm 0.23$, well above eqn. 6.23. However, as with B and $\langle V^2 \rangle$, most of the contribution to Q in the sample comes from the rich and highly clustered NP4 field, which if removed makes Q fall by nearly a factor of two.

The value $Q = 0.68 \pm 0.05$ found by Peebles (81) for the Rood catalogue is more comparable to the AARS result. However here there is the possibility systematic effects may affect the estimate of Q, although

perhaps to a lesser extent than that found for B and $\langle V^2 \rangle$ in section 5.6.

We may conclude that, while the estimate of Q in eqn. 6.23 is representative of the sampled volumes of the AARS, one would expect considerably larger values from samples with more prominent groups and clusters.

6.7 A MODEL FOR $\xi_s(s)$ AND THE SIMULATIONS

Before concluding this chapter we still need to discuss details of the models used for $\xi_s(s)$, presented in sections 2 and 4, particularly those compared with the results of the simulations in Fig 6.4.

The model for $\xi_s(s)$ is similar to that described in section 5.1 for $\xi_v(\sigma,\pi)$ and is given by a double integral of $\xi(r)$ from eqn. 2.3 convolved with the same peculiar velocity distribution function (eqn. 6.15). The model is

$$\xi_s(s) = \int_0^s \int_{-\infty}^{\infty} 2 \, \sigma \, (\xi((\sigma^2 + y^2)^{\frac{1}{2}}) \, F(W, \langle W^2 \rangle) \, dy) \, d\sigma \qquad (6.23)$$

where W in $F(W, \langle W^2 \rangle^{\frac{1}{2}})$ is replaced by $W = \sqrt{(s^2 - \sigma^2)} - y$.

Since the function is singular at $y = \sigma = 0$ with a powerlaw model for $\xi(r)$, to integrate eqn. 6.23 small cuts y_c and σ_c were introduced and the inner part integrated analytically assuming F constant, ...
Another complication is that, since the fields are narrow, there will be generally fewer pairs at large scales contributing from the transverse direction than from along the line of sight. To crudely allow for this the integration in σ was restricted to $\sigma \lesssim 5.0$ MPC.

A test of the model, and especially the latter approximation, comes from Fig 6.4 for the simulations which was briefly discussed in section 2.3. Here the overall model for $\xi(r)$ was deduced from the results of $\xi_s(s)$ from the low velocity simulations (filled circles) with the small scale amplitude set at B = 15.5. This was set from the estimates of $W_v(\sigma)$ from the four

separations in σ shown in Fig 6.7 and discussed in section 4.2. As noted there, a slightly steeper slope than -1.8 is suggested, which may explain the poorer fit of the dashed curve to the filled circles in Fig 6.4 at small separations. While for a real test of the model one would want to estimate and model $\xi(r)$ for simulated catalogues without peculiar velocities, the general agreement between the models and the results of $\xi_s(s)$ suggest both are consistent with each other.

Finally it might be noted that this model for $\xi_s(s)$ is quite crude. Although the model form for F from the studies in section 5 appears adequate at small scales, at larger separations it may be a poorer approximation to the real distribution function and here streaming motion may be important. Thus, for larger redshift samples more sophisticated models for $\xi_s(s)$ may be worthwhile.

CHAPTER SEVEN

DISCUSSION

7.1 INTRODUCTION

The purpose of this chapter is to bring together the results from the last few chapters to provide information on mass and clustering of galaxies and to discuss how the present distribution of matter may have come about in the expanding universe.

Since the motivation for estimating accurate redshifts in the AARS was for dynamical studies, Section 2 is devoted to a detailed discussion on the mass of galaxies and measurement of Ω on which the statistical data holds valuable information. As well as an application of the Cosmic Virial Theorem and comparison with the more traditional dynamical studies, the data on $\langle V^2 \rangle$ for both the AARS and the CfA is used to provide some of the first possible clues to the way mass is distributed around galaxies.

The distribution of matter is naturally of importance for theories of galaxy formation. In Section 3 the present information here is used along with the forms of the correlation functions found in Chapter 6 to put constraints on the two most popular theories. The second half of the section looks at more general astrophysical constraints on these theories and discusses some new scenarios that may be able to account more naturally for some of the observations discussed earlier in the chapter.

7.2 THE MASS OF GALAXIES AND DISTRIBUTION OF MATTER

Having made an estimate of $\langle V^2 \rangle$, B and Q for the AARS we are now in the position to make a statistical virial estimate of Ω. In the first part of this section we briefly review the data again and apply the 'Cosmic Virial Theorem' to estimate Ω . Since uncertainties in Ω will come from both statistical fluctuations in the sample and uncertainties in the CVT these, especially the latter, are discussed in some detail in the two parts that

follow. In part 4 the results are compared with some more traditional studies and in the final part the relevant data is brought together to discuss possible scenarious for the distribution of matter on small scales and briefly how these may relate to theories of galaxy formation.

7.2.1 Application of the Cosmic Virial Theorem

The important advantage of the statistical virial approach over the usual group studies is that the estimation of the peculiar velocities and potential energies do not require assigning galaxies to particular dynamical units.

From the redshift correlation functions of the AARS in the last chapter a value of $\langle v^2 \rangle^{\frac{1}{2}} \simeq$ 200 km/sec was found at projected separations less than 0.5 MPC, an estimate insensitive to any model assumptions. Although at larger scales the estimates are more uncertain and model dependent the data is not inconsistent with the scaling $\langle v^2 \rangle^{\frac{1}{2}} \sim \sigma^{0.1}$ expected in the theory. The two and three point redshift correlation functions also show the form of $\xi(r)$ and the available data on $\zeta(r,r,r)$ for the AARS are consistent at the smallest scales with the simple powerlaws implied from projected studies and assumed in the statistical virial estimates of the clustering potential energy.

Following the discussion in Chapter 2.2 there are two such dynamical estimates of Ω based on the correlation functions. The first, the cosmic energy equation discussed in Chapter 2.2.2 neither requires the assumption of stability or a model for $\zeta(r,r,r)$ but is sensitive to both the form of $\xi(r)$ and peculiar velocity motions at large scales. As discussed in the last chapter both of these are uncertain even on scales comparable to 1 MPC.

The Cosmic Virial Theorem (discussed in Chapter 2.2.3) on the other hand, although requiring stability, should be insensitive to these factors if applied at small enough scales where the clustering is most likely to be in statistical equilibrium. Indeed the characteristic crossing time $\sim \frac{\sigma}{\langle v^2 \rangle^{\frac{1}{2}}}$

at scales $\sigma < 0.5$ MPC is roughly one tenth of the Hubble time, so by the discussion in Chapter 2.2 this should be consistent with stability.

To apply the CVT to the AARS, eqn. 2.8 of Chapter 2.2.3 is taken with $\langle V^2 \rangle^{\frac{1}{2}} = 200$ km/sec from eqn. 6.20, B = 13 from eqn. 6.10 (with $\gamma = 1.8$) and Q = 0.55 from eqn. 6.23, all estimated consistently from the data. Taking $C_{\gamma = 1.8} = 3.125$ and $r^{0.2} = 1.3\ \sigma^{0.2}$ from Davis and Peebles (83) this gives

$$\Omega = 0.18 \pm 0.05 , \tag{7.1}$$

The error here come from differences in Ω estimated separately from the northern and southern subsamples, the fluctuations of which agree quite well with uncertainties in $\langle V^2 \rangle$, B, and Q found from the simulated catalogues.

Taking the luminosity density, ρ_L for the sample from eqn. 4.13 with eqn. 7.1 gives an overall $\frac{M}{L}$ in the B_J band of

$$\frac{M}{L} \sim 300 \tag{7.2}$$

As noted in Chapter 4.5, the estimate of ρ_L for the AARS may be too small for several reasons, making the value in eqn. 7.2 an overestimate.

7.2.2 Comparison with Other Redshift Samples

Although the simulations and internal errors suggest the values of $\langle V^2 \rangle$, B and Q used in eqn. 7.1 are reasonable for the sampled volumes of the AARS, they need not be representative of the universe as a whole. Indeed the amplitude of B and certainly the amplitude of Q found for the sample appear to be rather lower than found from much larger projected catalogues suggesting the AARS has undersampled dense regions.

While other estimates of $\langle V^2 \rangle$ from the KOS and Huchra catalogues discussed in Chapter 6.5 may be roughly consistent with the AARS result, these samples are either too small or too biased for a convincing comparison. However, combining the AARS and KOS catalogues gives a sample of around 500 galaxies and results similar to the AARS.

A more convincing comparison comes from the large CfA catalogue which may be a more representative sample since it contains three quite prominent clusters at well sampled depths, although the relative shallowness may still lead to biases. Using methods similar to those in Chapter 6.5, Davis and Peebles (82) (DP) have claimed $\langle V^2 \rangle^{\frac{1}{2}} = 340$ km/sec at $\sigma = 1$ MPC and B = 21.5 which, with $Q \simeq 0.7$ taken from the Rood catalogue, gives from eqn. 2.18, $\Omega \sim 0.2$, very close to the estimate in eqn. 7.1.

It might be thought that the larger values of $\langle V^2 \rangle$ and B from the CfA come from the inclusion of the rich clusters ; however DP find the model fits for $\langle V^2 \rangle$ are insensitive to their exclusion. As discussed in Chapter 6.5.6 the biggest reason for the discrepancy of $\langle V^2 \rangle$ with the AARS appears to be the different models used for $\xi_V(\sigma,\pi)$. DP used an exponential velocity distribution function and corrected for large streaming motions both of which seem less physically reasonable than the models used for the AARS. Taking instead $\langle V^2 \rangle^{\frac{1}{2}} = 240$ km/sec at $\sigma = 1.0$ MPC from the discussion in Chapter 6.5.6 and B = 17 from Fig.6.7 we find $\Omega \sim 0.1$, rather lower than above. Since the Rood catalogue is certainly unrepresentative, the value Q = 0.85 assumed here was taken from the Zwicky catalogue excluding Coma (Groth and Peebles, 77), although obviously for a more definite value of Ω one requires a consistent estimate of Q from the CfA.

Taken together the present data suggest a value of $\langle V^2 \rangle^{\frac{1}{2}}$ between 200 and 300 km/sec and a CVT estimate of Ω between 0.1 and 0.2. However the application itself relies on a number of assumptions which we now discuss.

7.2.3 Discussion of the Assumptions

Although the CVT does not depend on group membership assignments it does rest on a number of assumptions. Following the discussion in Chapter 2.2.3 one can summarise these as requirements, (1) the clustering is statistically stable and the velocity dispersions isotropic and (2) the galaxy correlation functions accurately trace out the matter distribution.

One might argue that because the crossing times are short and the scaling of $\langle v^2 \rangle^{\frac{1}{2}}$ is not inconsistent with the slow rise $\sigma^{0.1}$ expected, both seem reasonable by eqn. 2.8 and the discussion following. However as the precise scaling with separation is uncertain they are discussed separately in some detail in (a) and (b) below. In (c) a correction to the usual CVT is also discussed in some detail, that is required if the two body force in eqn 2.6 dominates $\langle v^2 \rangle$ rather than the collective interactions assumed in the CVT.

(a) Stability Assumption

As mentioned above the short crossing times are perhaps the best evidence for the overall stability of the clustering pattern at scales < 0.5 MPC. This is in turn suggested by the anisotropy of $\xi_v(\sigma,\pi)$ in Fig 6.1a where virialised groups make the clustering appear elongated along the line of sight. One might also argue that the fact the dashed histogram is also quite well fitted by a gaussian (Table 6.3) may imply the observed clustering is in a bound and relaxed state (Cf. Rood and Dickel, 78).

At scales > 0.5 MPC where the crossing times are longer we need to consider more seriously the possibility the clustering is expanding or collapsing. For example, some authors have argued that quite high density groups may be freely expanding (Turner and Sargent, 74) if the density in parameter ($\Omega \lesssim 0.03$) is low enough. However, as Peebles (80a,p84) notes, if this is the case it seems hard to understand how they formed at all if gravitational instability is responsible for their existence. Also, if the crossing times are still quite short at say $\sim$ 1 MPC (as found for the AARS) the clustering would dissolve quite quickly if it was not gravitationally bound. If Ω is more comparable to 0.1, as seems reasonable from eqn. 7.1, we might expect from the discussion in Chapter 6.5.4, that the clustering is freely expanding at > 2 MPC but perhaps collapsing at $\sim$ 1 MPC if the spherical model applies.

Even if the clustering is statistically stable there is still the possibility of anisotropy in the velocity dispersions. If the velocity dispersions are predominantly radial, for example, the gravitational acceleration in eqn. 2.6 is reduced through the second term on the left-hand side making the estimate of Ω in eqn. 7.1 too large (see Bean et al, 83).

Although hard to test for observationally, strong anisotropy seems unreasonable from several theoretical considerations. In the spherical model for cluster formation mentioned above, initial radial orbits will become non-radial to allow clusters to relax to their smaller equilibrium radii. In the alternative models of Davis and Peebles (77) transverse velocities are produced through tidal interactions between forming clusters that may 'virialise' the clustering at low density contrast without any physical collapse necessary. Finally, the velocity dispersions are isotropic at small scales in the N body simulations discussed in Chapter 2.2.4.

From the considerations above it seems reasonable to conclude that at scales < 0.5 MPC the clustering is probably stable and the velocity dispersions isotropic so the CVT applies. At slightly larger scales the distribution may be stable or perhaps slowly collapsing on radial orbits, while beyond 2 MPC (where $\langle V^2 \rangle^{\frac{1}{2}} < Hr$) we expect general expansion unless $\Omega >> 0.1$.

(b) Assumptions on Mass Distribution

The accuracy of the models for the correlation functions in tracing out the mass distribution is perhaps a bigger uncertainty than the stability assumption at scales < 0.5 MPC. Although the integral in eqn. 2.7 is insensitive to the form of the correlation functions at large separations the potential depends very sensitively on the form of $\zeta(r,r,r)$ and $\xi(r)$ at the smallest scales and how well these trace out the matter around galaxy pairs. While the available data suggests the powerlaw form of $\xi(r)$ holds down to the optical size of galaxies (Gott and Turner, 79) the behaviour of $\zeta(r,r,r)$ at scales smaller than 50 KPC is unknown.

Since $\sim$ 40% of the integral (Davis and Peebles, 77) in eqn. 2.7 (assuming pure powerlaws) comes from the clustering on scales less than 50 KPC, following Davis and Peebles (82) (DP), Ω in eqn. 7.1 was estimated by replacing the third term in $\bar{\zeta}(r,r,r)$ of eqn. 2.4 with the second in the integral. As DP discuss, this reduces the large (unrealistic) contribution to $\langle v^2 \rangle$ from the singular nature of $\bar{\zeta}(r,r,r)$ at small z. Although this may appear an artificial correction to eqn. 2.7, even if the powerlaws using the usual form for $\bar{\zeta}(r,r,r)$ in eqn. 2.4 hold down to infinitely small scale, we know that because galaxies have a finite size the inverse square force law must break down at some point.

To show that the correction is, indeed, reasonable the force law $\frac{z}{z^3}$ in eqn. 2.7 at z < 50 KPC has been replaced by $\frac{z}{z^2}$, thereby assuming that the mass in galaxies rises linearly with scale to 50 KPC (consistent with isothermal galaxy halos). Assuming the usual model for $\bar{\zeta}(r,r,r)$ in eqn. 2.4 but replacing $\xi(r)$ by $\xi(r + r_c)$ in eqn. 2.3, with r_c = 10 KPC, the left-handside of eqn. 2.7 was numerically integrated to give $\langle v^2 \rangle$ as a function of r.

Fig. 7.1 shows the results of the integration as a dashed curve with B, Ω and Ω for the AARS taken from Part 1. Also shown is $\langle v^2 \rangle^{\frac{1}{2}}$ (solid line) estimated using the modified form of $\bar{\zeta}(r,r,r)$ adopted in eqn. 7.1 and using the usual powerlaw model for $\bar{\zeta}(r,r,r)$ and point mass model for galaxies (dotted line) given by eqn. 2.8 with $C_{\gamma=\ 1.8} = 7.9$ (Peebles,76b).

We see over the scales of interest (100 KPC-1 MPC) the dashed curve and solid line agree well and both are considerably reduced from the dotted line. As noted in Chapter 6.5 this slow rise with scale is not inconsistent with the observations from Fig 6.15 for the AARS or the CfA.

The solid curve on Fig 7.1 shows the result of increasing the galaxy size of 50 KPC in the dashed curve to 1 MPC which, if applicable for the AARS, would raise Ω to $\sim$ 0.4. The scaling from 100 KPC to 1 MPC though, is roughly $\langle v^2 \rangle^{\frac{1}{2}} \sim r^{0.4}$ (Cf eqn. 2.9), apparently fairly well

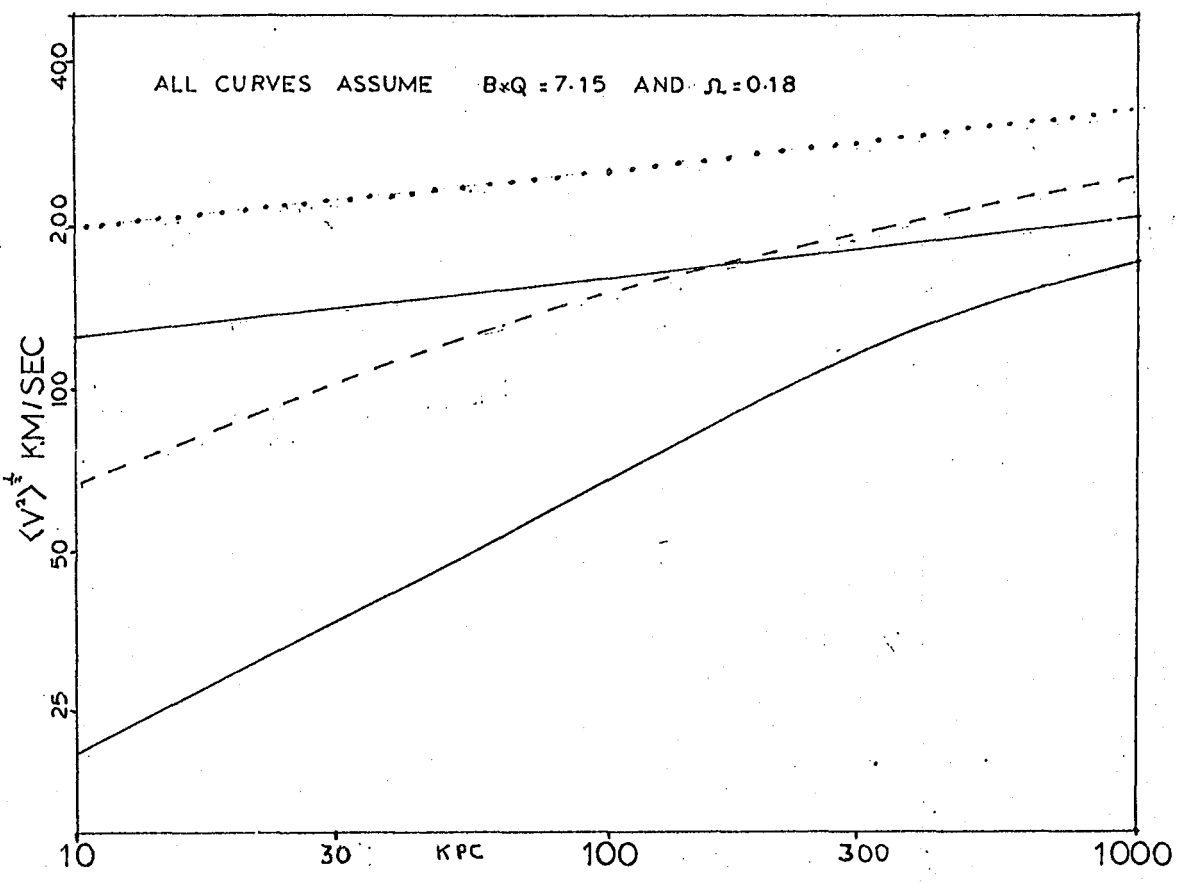

FIGURE 7.1: Expected scaling of $\langle v^2 \rangle^{\frac{1}{2}}$ between pairs as a function of spatial separation assuming purely collective interactions. The dotted line corresponds to point mass galaxies and the usual powerlaw correlation functions with the solid line corresponding to a 'corrected' powerlaw three point function. The dashed and solid curves are the scaling expected if galaxies have halos of extent 50 KPC and 1MPC respectively.

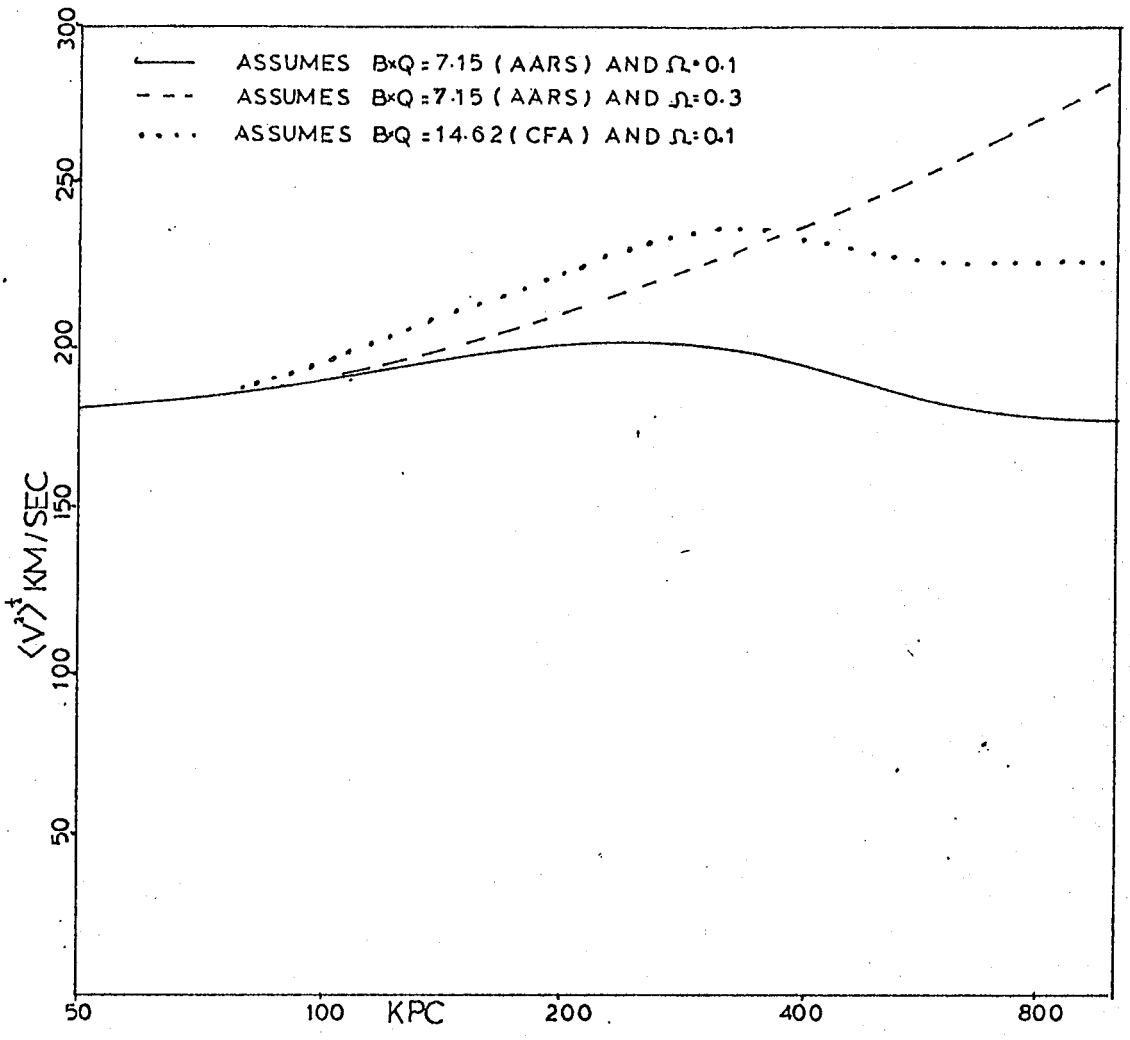

FIGURE 7.2: Expected scaling of $\langle v^2 \rangle^{\frac{1}{2}}$ between pairs as a function of spatial separation assuming collective and discreteness interactions. The solid and dotted curves assume halos of 300 KPC extent with the dashed corresponding to 1MPC halos.

excluded by the present observations (But see Fig 4, Davis, 82).

Another picture excluded by the present data is the idea that bright galaxies and their halos fit into a continuous spectrum of clustering extended from their optical regions out. As Peebles (76a) notes, this can be modelled by assuming a pure inverse powerlaw force in eqn. 2.7, but replacing the powerlaw form of $\xi(r)$ in $\bar{\zeta}(r,r,r)$ by $\xi(r + r_c)$ to allow for the distribution of matter within galaxies. In this way one finds that typical mass elements within galaxies should have relative velocities :

$$\langle V^2 \rangle_{INT} \simeq \frac{2}{3} r_c^{2-\gamma} B Q \Omega \ , \qquad (7.3)$$

However for $\langle V^2 \rangle_{INT}$ to be consistent with the typical internal velocities within galaxies of $\sim$ 200 km/sec, with r_c = 10 KPC and B and Q from Part 1 we require $\Omega \sim 2$ in eqn. 7.3, well excluded by the data.

(c) Binary Interactions

In (b) it was argued that very extended galactic halos (>> 50 KPC) appear to be excluded by the present velocity data. However the assumption up until now has been that galaxy pairs at scale r move in collective force of all other galaxies and material clustered similarly, so that the number of 'discrete' objects is very high. As mentioned in Chapter 2.2.3, if instead the mass is mainly associated with the brightest galaxies that are selected in an apparent magnitude limited sample (as assumed in the usual virial group studies) the interaction term in eqn. 2.6 may dominate. However to assess the importance of this we first need an estimate of n, the mean number density of these objects per MPC^{-3}.

From the luminosity studies in Chapter 4 we see from eqn. 4.12 that the luminosity density for the AARS (since $\alpha = -1$) is given by $\rho_L \sim \phi^* L^*$. From Fig 4.9 we see further that 80% of this light comes from galaxies brighter than -18.5 which have a number density of $\phi^* \sim 0.01\ MPC^{-3}$. As Schecter (74) notes, for some dynamical purposes, galaxies drawn from a

Schecter function with $\alpha = -1$ and a constant $\frac{M}{L}$ can be considered as consisting of ϕ^* equal points of mass $L^* \times (\frac{M}{L})$. Thus it seems reasonable to assume the mass is in galaxies of mass m with number density $n \simeq 0.01$ MPC^{-3}.

Following Davis and Peebles (82) now, the ensemble average number of neighbours in a sphere of radius βr, centred on a pair of separation r is

$$N = 8\pi \; Qn \; \frac{B(\beta r)^{3-\gamma}}{3-\gamma} \qquad (7.4)$$

Taking B and Q from Part 1, we find a pair at separation 0.5 MPC in the AARS will, on average, have only 0.65 bright neighbours within a radius the size of their separation, so that at these and smaller scales their collective contribution to $\langle v^2 \rangle$ should be quite small. This behaviour seems intuitively reasonable from plots of the galaxy distribution in Chapter 5.3 where the typical loose groups on scales of 0.5 MPC generally consist of only two or three bright galaxies.

To make more qualitative estimates of the effect of this interaction term on the CVT, eqn. 2.6 was integrated assuming the modified form of $\zeta(r,r,r)$ discussed in (b) above. Ignoring the second term on the left-hand side and taking $\rho = nm$ we find

$$\langle v^2 \rangle \simeq \frac{2}{3} \; \frac{Gm}{r} \; (1 + 0.4 \; B \; Q \; r^{1.2}) \qquad (7.5)$$

Taking B and Q from section 2.1 as usual, we see the discreteness term on the right-handside dominates at scales < 300 KPC at which scales we would expect $\langle v^2 \rangle^{\frac{1}{2}} \sim \frac{1}{r^{\frac{1}{2}}}$.

Since the available data suggests $\langle v^2 \rangle$ is independent of scale here one might conclude eqn. 7.5 does not apply. However if the mass m rises linearly with radius to 300 KPC, as DP discuss, we could get a more acceptable scaling of $\langle v^2 \rangle$ with separation. More specifically, if this mass is

considered to be an extension of the halos needed to account for the flat rotation curves of bright spirals, from the discussion in Chapter 1.3, we see a halo of extent 300 KPC with $n = 0.01$ MPC^{-3} corresponds to $\Omega \doteq 0.1$.

To assess in more detail the form of $\langle V^2 \rangle$ with scale expected in this picture, the collective force in the right-handside of eqn. 2.6 was calculated numerically by extending the halo of the dashed curve in Fig. 7.1 to 300 KPC for $\Omega = 0.1$. In addition, the solid curve with 1 MPC halos was set to correspond to a density parameter of $\Omega = 0.35$. The interaction term in eqn. 2.6 was then calculated assuming

$$m = 10^{11} M_\odot \left(\frac{R}{10 \text{ KPC}} \right)^{1.0} \qquad (7.6)$$

where the halo scale is given in MPC's, truncated at the two radii above.

The results of these two integrations added to the corresponding interaction terms are shown in Fig.7.2 as solid and dashed curves respectively. We see the solid curve with $\Omega = 0.1$ gives good agreement with the observations for the AARS (Fig. 6.15), although the dashed curve lies about within the errors at larger scales.

While the present data from the AARS cannot discriminate between these models for the mass distribution and those in Fig.7.1 in (b) earlier, some support for the scenario here may come from the CfA data. As noted in section 6.5.6, if the same procedure as used for the AARS is followed, the estimates of $\langle V^2 \rangle$ are very similar from the two samples despite the product B Q being probably a factor of two larger than for the AARS. In turn this may suggest that at scales of one or two hundred KPC's the relative motions of galaxy pairs are not strongly influenced by collective interactions (as in eqn 7.5).

This can be seen by the dotted curve in Fig 7.2, which corresponds to the solid curve for the AARS with Ω = 0.1 but with B = 17 and Q = 0.85 for the CfA taken from the discussion in part 2. Here we see that the model estimates of $\langle v^2 \rangle^{\frac{1}{2}}$ are in fair agreement with those for the sample in Fig. 6.15 (open triangles) and at scales smaller than 100 KPC the expected relative motions are in reasonable agreement with the estimates from Turners binaries discussed with the CfA in Chapter 6.5.6. Indeed, since the selection of the binary sample was biased to lower denser* regions than a fair sample, we might also use the agreement between $\langle v^2 \rangle$ for it and the CfA at the same scales to support the idea that binary interactions dominate here.

Although the present data and models discussed here are still too crude for any firm conclusions to be drawn, it is suggestive that the observed relative velocities at small scales are about consistent with those expected if bright galaxies have extended halos ; if $\langle v^2 \rangle^{\frac{1}{2}}$ had been much less than 150 km/sec or greater than 250 km/sec this picture would have been unacceptable. At larger scales the observed estimates of $\langle v^2 \rangle$ are more uncertain and model dependent and at these scales the stability criterion in (a) above might not apply. For these reasons we cannot exclude the possibility that these halos are very extended (e.g. the dashed curve in Fig. 7.2) and $\Omega >> 0.1$; most of the mass being less clustered than the visible galaxies on scales of MPC's. Indeed, in this case we would expect the large correction for streaming motion in the estimates of $\langle v^2 \rangle$ discussed in Chapter 6.5.4 to be appropriate, making $\langle v^2 \rangle^{\frac{1}{2}}$ in Fig 6.15 rise at large σ (filled circles) as expected in the theory.

* Although DP argue that at small scales ($\sim$ 25 KPC) the Turner pairs should be a fairly representative sample of close bright pairs, due to the selection criterion, pairs at larger separations ($\sim$ 100 KPC) will have fewer bright neighbours than a fair sample so that B Q is lower here than for the CfA.

In Part 5 we consider further relevant data that may put constraints on the distribution of matter on small scales and discuss several particular scenarios suggesting briefly how each may relate to theories of galaxy formation.

7.2.4 Comparison with Other Dynamical Studies

It is naturally of importance to compare the cosmic density measurements from the CVT with other mass estimates. Below are discussed recent results from three different types of studies ; galaxy groups, rich clusters and estimates of Ω from large scale motions.

(a) Galaxy Group Studies

It is particularly relevant to compare the statistical estimates of Ω in part I with more direct group virial studies, since loose groups seem to be a typical environment for galaxies in the general distribution. As discussed in Chapter 2.2.1 one approach to calibrate out systematic effects in these analyses is to repeat the group analysis on catalogues prepared from N body simulations.

One recent study has come from the CfA catalogue where Press and Davis (82) (PD) have used an elaborate procedure to find groups with short crossing times. Although a direct summation of the masses yield $\Omega \simeq 0.15$, noting a strong linear trend of mass per galaxy with radius of group from tens of KPC's to 6.0 MPC, these authors have suggested that all bright galaxies be embedded in isothermal halos to the upper radius ; in which case $\Omega = 0.6$.

While this appears to support the idea of bright galaxies (with mean density $n \overset{\sim}{} 0.01$ MPC^{-3}) having extended halos, discussed in section 2.3 above, the halo densities implied by this study and given by

$$m = 3.24 \times 10^{10} M_{\odot} \left(\frac{R}{10 \text{ KPC}} \right)^{1.01}$$ (PD eqn.33) are a factor of three or so lower than that assumed in eqn. 7.6, that was chosen to account for the observed flat rotation curves at scales $<$ 50 KPC.

Although similar correlations of mass with scale have been noted by several authors (e.g. Rood and Dickel, 78), most should be treated with caution since they may just reflect the way galaxy groups are selected and the results plotted (Burbridge, 75). In the PD algorithm the larger groups all require high velocity dispersions to satisfy the crossing time criterion so the high $\frac{M}{L}$ here may not be surprising. If the trend is real, as Davis (82) notes, it may partly just reflect the long suspected, high $\frac{M}{L}$ of early type galaxies in large clusters. However the trend (especially at large scales) could be artificial because, although no strong artificial trend in $\frac{M}{L}$ is seen in a similar analysis of the simulated catalogues, the N body simulations used here are much less clustered at large scales than in the real universe. For this reason we may expect contamination from Hubble velocities in the real groups to be much worse at large radii than in the simulations, leading to spuriously high velocity dispersions and $\frac{M}{L}$.

In another recent study, Huchra and Geller (82) have defined groups in the Huchra catalogue (to B = 13.2) by means of a projected density criterion with a relative velocity cutoff intended to remove interlopping galaxies. These authors have found at large density contrasts the $\frac{M}{L}$ estimates from the groups were insensitive to both the actual contrast limit chosen and the velocity cutoff, suggesting contamination may not be a problem. The median rms velocity of 92 groups detected in this way was $\sigma \sim$ 140 km/sec, in good agreement with the AARS results if it assumed that peculiar velocities are randomly assigned so that $\sigma_{AAT} = \frac{\langle V^2 \rangle}{\sqrt{2}} \sim$ 140 km/sec. The mean $\frac{M}{L}$ was $\sim$ 170 which with a luminosity density for the sample of $1.1 \times 10^8 \ L_\odot \ MPC^{-3}$ (Davis et al, 78) gives $\Omega \sim 0.07$.

It should be noted that comparison of the CVT with the individual group approach is not straightforward since the former gives weight to galaxies in dense patches whereas in the latter, groups tends to be given equal weight, so galaxies in loose groups contribute more to the results.

As discussed in Chapter 2.2.1, the problem here is that it is these systems where problems of contamination, small numbers, instability and measurement error are most prevalent. Also, as Bahcall and Tremaine (81) (BT) have shown recently, even if membership appears well defined, projection effects in a group along with the point mass model for galaxies can lead to the ordinary virial theorem overestimating the potential and thus underestimating the group mass by, in some cases, a factor of two or three.

Some mass estimates that get around this bias and other problems come from studies of the relative motions of the numerous faint galaxies distributed around nearby bright spirals. Here independent distant indicators are also becoming available to help distinguish real satellites from accidentals (de Vaucouleurs, 78). Preliminary estimates from the galaxy, M31, M81, M101 (Hartwick and Sargent 78, BT), all of which have at least four or five probable satellites, yield masses of around 1-2 x 10^{12} $M_{\odot}$ within 1-200 KPC, not inconsistent with a continuation of the steady rise of mass with scale from the rotation curves. Similar masses for the galaxy and M31 are found from local group timing arguments using their present relative velocities and distances and also from the dynamics of outlying members of the group (Lynden-Bell, 81).

We see that the typical masses of bright galaxies implied from these studies are in good overall agreement with the conclusions from the CVT, despite the different data and techniques used. This gives support for the values of Ω between about 0.1 and 0.2 in part 3 from the small scale dynamics.

(b) Rich Clusters

The most reliable mass estimates are still, perhaps, those found from the application of the virial theorem to the corés of rich clusters whose short crossing times and smooth profiles are strong support for an equilibrium situation. The large velocity dispersions responsible for the high $\frac{M}{L}$ are

almost certainly real because the clusters are so prominent both on the sky and in redshift space, so contamination (or redshift error) cannot be to blame. A clue to membership in these environments can also come from the morphology of the galaxies and Yahil and Vidal (77) have also used a velocity criterion to eliminate non-members on the reasonable physical assumption that the velocity distributions are gaussian. As mentioned in Chapter 1.3, typically we find $\frac{M}{L} \sim 650$ for these systems, considerably larger than eqn. 7.2 for the AARS or the group studies in (a) above. Independent evidence for these high $\frac{M}{L}$ comes from measurements of the X-ray temperature of cluster gas assumed to be heated from the gravitational potential of the clusters (see Faber and Gallagher, 79).

A possible clue to this discrepancy with group galaxies comes from the observed predominance of early type galaxies in these dense environments, a correlation which also appears to hold outside rich clusters (Davis and Geller, 76). Of course if galaxy masses are correlated with morphology and abundance of neighbours this implies the number correlation functions are not strictly mass functions, which in turn could affect the CVT application in Part 1. In this case Ω would be overestimated since $\langle v^2 \rangle$ is weighted to richer areas where the mass per bright galaxy is higher.

Apart from improving the group and statistical studies, a test of this correlation will be to see how the velocity dispersions and $\frac{M}{L}$ vary at 2-3 MPC from rich cluster cores where the distribution should still be close to equilibrium and the galaxy types more representative of the field. Statistical virial tests similar to the CVT and those applied to the cores of Abell clusters (Seldner and Peebles, 77b) may be useful here when more redshift data around clusters becomes available. An observational project of this type is at present underway at the AAT by R.S.Ellis and others using multi-object spectroscopic techniques of several fairly distant clusters.

(c) Large Scale Estimates

It seems appropriate to finally discuss estimates of Ω based on large scale distortions of the Hubble flow because this is the only dynamical way of estimating the mean mass density of any component more weakly clustered than galaxies on scales greater than several MPC's.

Most studies here are based on an estimate of the infall velocity of the galaxy towards Virgo which is related to the mean overdensity within the radius of the local group, through linear perturbation theory, to provide an estimate of Ω. Recent determinations by several observers (e.g. Davis and Huchra, 82, Yahil et al, 80) lie in the range $0.1 < \Omega < 0.7$. The lower bound is consistent with the previous estimates discussed in this chapter from small scale stable systems, but the range of larger values implies considerable weakly clustered mass around Virgo.

While the large infall velocity implied by the dipole anisotropy in the microwave background (Smoot and Lubin, 79) tends to support the higher values of Ω from this Virgo Supercluster test, using a small redshift sample of Abell clusters Ford et al (81) have found little obvious distortion of the Hubble flow in several external superclusters of high density contrast, in turn implying $\Omega << 1$.

Other constraints on Ω at still larger scales can be made by relating estimates of large anisotropies in the Hubble flow with the potential associated with density fluctuations on these scales as measured by the integral* $J_3 = \int_0^\infty \xi(r)\, r^2\, dr$ (Chapter 6.3). Calculating J_3 from $\omega(\theta)$ taken from projected catalogues, Clutton-Brock and Peebles (82) have recently

* This relation involving J_3 is similar to the cosmic energy equation in Chapter 2.2.2., eqn. 2.5. Although the latter is less sensitive to the form of $\xi(r)$ at large scales than J_3, the velocity $\langle v_p^2 \rangle$ in eqn. 2.5 is more sensitive to contributions from complicated non-linear motions at small scales and so is harder to apply.

concluded that the large motion currents on scales of 60 MPC claimed by Rubin et al (76) are not unreasonable if the universe has high density. While the low value of J_3 above implied by Fig 6.2 of the AARS could be used as support for their conclusions, the reality of the Rubin velocity has been questioned (Fall and Jones, 76). It should also be noted that the anticorrelation in Fig 6.2, if a general feature of the galaxy distribution, may suggest peculiar velocities on these scales may be, at least in part, non-gravitational in origin. Although, by the stability criterion, this possibility should not affect the virial estimates of Ω at small scales, all the estimates of Ω described above from large scale measurements will be spurious.

If the velocities are in fact gravitational in origin, when much larger redshift samples of both galaxies and Abell clusters become available it should be possible to greatly improve these estimates of the potential at the largest scales. Also, these samples should provide statistical estimates of the peculiar motions through the expected flattening in the relative velocity distributions along the line of sight; as hinted at large σ in $\xi_v(\sigma,\pi)$ for the AARS in Figs 6.1 (a-c) (see Peebles, 80a, p.289).

7.2.5 The Distribution of Matter at Small Scales

The virial arguments discussed in the last parts have shown the evidence is increasing that the amount of dark matter per typical bright galaxy is at least a factor of tens times more than the conventional masses and consistent with an extension of the halos needed to account for the flat rotation curves around spirals. Indeed the masses are comparable to those needed to bind rich clusters, with the cosmic density parameter Ω typically in the range 0.1 to 0.2.

Of course similar conclusions have been presented by many authors (e.g. Ostriker et al, 74) using different data and techniques. However, the statistical methods applied to the AARS and CfA have shown fairly conclusively that the peculiar velocities responsible for these large masses are not the

result of contamination by Hubble velocities or measuring error that have been blamed for some of the high masses reported in the past. Also the crossing times are short enough that the clustering at the smallest scales should be in a bound and probably, on average, stable state so the cosmic virial theorem should apply.

While the need for at least some dark matter is now generally accepted amongst astronomers it should be still regarded as a hypothesis since there is, as yet, no convincing independent evidence apart from gravity of its existence. The possibility of new physics has occasionally been invoked as an alternative explanation for the virial mass discrepancy. For example Tifft (80) and others have persistently argued that the observed red-shift difference between close galaxy pairs may not reflect their true relative velocities. Alternatively, the relative velocities may be real but induced by the gravitational attraction of neighbouring matter by a force that departs from the usual inverse square law on greater than galactic scales. Although hard to test for observationally, both the flat rotation curves of spirals and the observed profiles and velocity distributions in rich clusters are, within the present observations, consistent with the isothermal distribution of matter expected if matter has relaxed and virialised under the usual Newtonian gravity. Also, as we discuss below, the data from the statistical studies is consistent with physically reasonable dynamics and distribution of matter. Thus it seems reasonable to assume the usual physics and cosmology and consider possible alternatives only as a last resort.

Assuming the usual physics, if there is much more mass implied by the dynamics as seen in the visible galaxies, we can ask if the galaxy distribution is actually a good tracer of the majority of the mass. While on the one hand there is an indication that the mass per galaxy may be larger in rich, compact clusters, the Virgo flow studies suggest most of the mass may be less clustered than the galaxies on scales of many MPC's. As Davis

and Peebles 83 (DP) discuss and as Part 3 demonstrated, the present data from the statistical studies is about good enough to allow consistency tests that provide constraints on how mass is distributed around galaxies at small scales. Below we list four possible scenarios considered by Peebles (78) and discuss how the present and future data can constrain each and discuss finally how they may relate to theories of galaxy formation. The mass may be :

(a) In the visible parts of galaxies, with mass proportional to light.

(b) In many lumps, with individual mass less than that of a galaxy, distributed around galaxies.

(c) Associated with galaxies faint and bright.

(d) In smoothly distributed halos around bright galaxies.

(a) As discussed above, the conventional masses of galaxies are excluded by the rotation curves and relative velocities of close galaxy pairs if the conventional physics apply. Furthermore the rotation curves and the amplitude and scaling of $\langle v^2 \rangle$ for close Turner galaxy pairs (see DP and Chapter 6.5) both imply the dark matter is distributed beyond the optical radii of bright galaxies with mass rising about as fast as radius.

(b) This picture is based on the attractive idea by Peebles (78) that lumpy halos around bright galaxies form a natural extension of the clustering hierarchy to scales of galactic scale. Superficial support for this may appear to come from the remarkable powerlaw form of $\omega(\theta)$ to projected scales of KPC's (Gott and Turner, 79) and the good agreement between the internal velocities of galaxies and the relative velocities of the close galaxy pairs. However as Peebles (74) discusses, to get reasonable continuity between $\xi(r)$ and the observed densities in galaxies and between $\langle v^2 \rangle$ and the star velocity dispersions (see Peebles, 76a and Part 3c) we require Ω to be at least unity. Furthermore, the smooth rotation curves in some bright

spirals suggest the mass around these galaxies is in fairly smooth halos out to (in some cases) 50 KPC, even in quite isolated galaxies. In this picture though we would expect the matter distribution to be lumpy and the halo density to be related to the abundance of neighbouring galaxies (Peebles, 80a, p.392).

(c) Although bright galaxies do appear to have halos at least to several tens of KPC's, DP have recently argued that most of the mass may still be associated with faint galaxies. Some support for this, they argue, comes from a more detailed statistical study of the Turner binary sample by White et al (83). These authors have found the masses from the relative velocities of pairs are only weakly related to their luminosities and the masses are reduced if pairs with fainter neighbours are culled from the sample. Although this suggests light and mass are only weakly correlated for these fairly bright pairs, this study provides no real evidence that this also applies to much fainter galaxies. As White et al (83) discuss, the culling often removes galaxies that are little fainter than the pair and so may be expected to have comparable mass. Even if the masses appear to fall when much fainter galaxies are removed, it may just reflect that more massive pairs tend to have satellite galaxies.

Other support, claimed by DP, comes from the observed scaling of $\langle v^2 \rangle$ for the CfA and binary sample (discussed in Chapter 6.5.6) that is close to that expected in the CVT in eqn. 2.8 and which extends to the optical radii of galaxies. However, as mentioned in (c) of Part 3, the fact that the binary sample (at the larger separations at least) is likely to be underdense relative to the CfA may actually support the idea that most of the mass is associated with the bright galaxies whose relative velocities are due to their motion around each other. Also, at the larger separations the data in the fit to $\langle v^2 \rangle$ with separation comes from the CfA where the fitting estimates are sensitive to the model assumptions. For these reasons it seems likely

the agreement of the observed scaling with theory is fortuitous. Also it is possible that features in $\langle V^2(r) \rangle$ may exist that could be smoothed out in $\langle W^2(\sigma) \rangle$ in a similar fashion to that discussed for $\xi(r)$ in Chapter 6.4.

If most of the mass is associated with faint galaxies it might be wondered where most of the matter lies. From the discussion of the luminosity density in Chapter 4.5, the optical parts of faint galaxies contribute little to the overall luminosity and presumably mass density of the universe. If these galaxies have halos to 50 KPC like bright galaxies, as suggested by DP, we require by the arguments in Chapter 1.3 that if $\Omega \sim 0.2$, their mean number density is at least 0.1 MPC^{-3}. However extrapolating the Schecter luminosity function found for the AARS in Chapter 4.2, we find that only down to luminosities comparable to dwarf spheroidal galaxies is the galaxy density as large as this. Although observations by Faber and Lin (83) have recently suggested such galaxies may have larger than conventional masses, there is as yet no evidence that the total $\frac{M}{L}$ here are much higher than for bright galaxies, which is required if they are to contribute significantly to the mean density. An alternative possibility is that the mass is in dead galaxies that may have little or no detectable luminosity. Condensed objects like massive black holes are a possibility although these cannot be too massive or else they would probably have been detected by their tidal and accretion effects on the visible parts of galaxies.

(d) The remaining possibility is that the mass is in the extended and smooth isothermal halos that extend beyond the scales spanned by the present rotation curves. This has been the normal assumption in most virial studies and is the usual interpretation of the rise of mass with scale around nearby spirals (Ostriker et al (74)). In the local group study mentioned in Part 4a for example, it is assumed that the mass is in and around the galaxy and M31 rather than the twenty or so much fainter galaxies in the group.

Although DP argue that this interpretation is a more artificial explanation of the observed scaling of $\langle v^2 \rangle$ for the CfA than that in (c) above, the discussion in (c) above and in (c) of Part 3, suggests the amplitude and scaling of $\langle v^2 \rangle$ for the AARS and CfA and Turner samples are compatible with a simple extension of the halos needed to support the flat rotation curves of bright spirals. Indeed the present data may be consistent with halos extending beyond the usual individual galaxy halos postulated, with most of the matter lying beyond (or infalling into) the visible confines of small groups and so undetectable in the small scale dynamics. As Davis et al (80) discuss, this very extended halo hypothesis may be consistent with the large scale Virgo flow measurements, the masses of galaxies only eventually converging on scales of many MPC's, allowing $\Omega > > 0.1$. Alternatively halos may truncate at smaller scales and the dark matter on larger scales may be smoothly distributed in envelopes around clusters like Virgo rather than around bright galaxies.

Although we see the present data strongly exclude (a) and the particular scenario discussed in (b), the position as regards (c) and (d) is uncertain ; here further statistical analyses are necessary as well as dynamical studies of individual objects.

It is also possible that some combination of (b)-(d) is, in reality closer to the truth. Indeed one might expect tidal effects in tight groups may have disrupted any original extended halos and the galaxies may be moving in some common envelope as is probably the case in rich clusters (White,76). If dynamical drag with the dark material then causes galaxies to spiral together one may have a natural mechanism for decoupling most of the mass and light in small groups (Hoffman et al, 82). One problem here though is how close pairs of galaxies can persist in their observed numbers where the drag force should cause galaxies to quickly coalesce (White and Sharp, 77).

Perhaps these galaxies have small halos or are on circular orbits (White et al, 83) or relaxation is slowed by a lumpy distribution as envisaged by Peebles, (78) in (b) above.

Some tests of these effects will be to see how $\xi_v(\sigma,\pi)$ varies between galaxies of different luminosity (and morphology) since bright galaxies should be more tightly bound than fainter ones if significant relaxation is operating. A further clue to the distribution of matter may come from a better understanding of the form of the velocity distribution function between galaxy pairs. The present data, at least for the AARS, fits a gaussian quite well, perhaps suggesting the presence of isothermal halos around galaxies and groups and clusters of galaxies as discussed by Yahil (77).

Understanding the distribution further may, as well as providing information on the nature of the dark matter, provide insights into the processes by which galaxies and clusters form.

In the usual isothermal theory discussed in Chapter 2.1 the dark matter is assumed to cluster to form galactic halos and galaxy clusters with any residual gas forming the visible galaxies. If gas dynamics and relaxation only occurs on scales of galactic size and smaller, as Groth and Peebles (76) discuss, one can form galaxies and clusters as a continuous process as envisaged in (b) above. However, as noted above, this requires Ω to be of order unity and also that galaxies closely trace out the mass distribution which together are strongly excluded by the present data.

An alternative discussed by White and Rees (78) is that disruption and dissipation occurs on larger scales ; the formation of galaxy halos and groups following a continuous clustering and disruption sequence in which the visible galaxies survive disruption because dissipation has increased their binding energy. In this picture one might expect the more luminous galaxies to form in the deeper gravitational potential wells, so that most of the mass would be associated with the brighter galaxies as in

(d) above. However if the gas processes that determine the rate of star formation and hence luminosities are not coupled to the large scale dynamics on scales much greater than 10 KPC the luminosity and mass of galaxies need not be strongly correlated (Yahil, 77), as in (c).

One problem with the White and Rees picture is that relaxation and disruption tend to give rise to profiles much steeper than those needed to support flat spiral rotation curves. One possibility for creating a slower fall off is a tidal shearing mechanism occurring between forming galaxy halos (Dekel et al, 80). In a different picture (Gunn, 77) galaxies form first and accrete their halos later. This can give rise to a roughly correct profile but demands rather special initial conditions if the model is to be realistic.

In the very different adiabatic scenario discussed in Chapter 2.1 large scale dissipation is expected to occur on scales of supercluster size, the pancakes fragmenting to form objects of subgalactic mass. The gravitational clustering of these objects to form galaxy halos and galaxies could then follow in a similar fashion to the White and Rees picture above. If the pancake scale is instead comparable to a galaxy halo consisting of non-interacting fermion particles (as we discuss later), the baryonic gaseous material can fall into the potential of the halo and dissipate its energy providing a natural process of segregating visible galaxies from their dark halos as in (c) and (d) above.

We now discuss some of these scenarios in more detail using other results from the redshift data.

7.3 THEORIES OF GALAXY FORMATION

In Chapter 2.1 we considered how the observations of the angular correlation functions have been used to discriminate between theories of galaxy formation and used as a probe of Ω. In the first part of this section we consider how both the more direct estimates of $\xi(r)$ at small

and large scales in Chapter 6 and the dynamical studies discussed in section 2 may provide stronger constraints on the two most popular theories. Also of relevance here are plots of the galaxy distributions in Chapter 5 and the form of the luminosity function in Chapter 4. The second half of the section is still more speculative and points to the possible role that massive non-interacting particles may have in explaining both the small and large scale distributions of galaxies and matter.

7.3.1 Constraints from Redshift Samples

Of all the present observations, perhaps the most important feature still to explain is why the angular correlation functions are good approximations to powerlaws at small angular scales, even down to galactic size in the case of $\omega(\theta)$. The usual interpretation is that $\xi(r)$ itself is a good approximation to a -1.8 powerlaw out to scales of several MPC and galaxies are distributed in a clustering hierarchy that has developed by gravitational clustering. At larger scales projected catalogues and the AARS and CfA redshift samples indicate a break away from a powerlaw at scales 3-10 MPC. As discussed in Chapter 2.1.2, since this feature occurs at around the transition between characteristically linear and non-linear fluctuations, the traditional interpretation is that the universe has high density. This scenario is especially attractive because of its simplicity in that it assumes that the galaxy distribution is a result of simple gravitational clustering of subgalactic seed masses that are randomly distributed at recombination. If Ω is close to unity one may also be able to form galaxies as a natural part of the clustering process, as envisaged in scenario b, of the last part of section 2.

The obvious difficulty though, that almost certainly excludes this picture, is that the dynamics of bound galaxy systems discussed in the last section, all imply $\Omega \ll 1$ unless matter is considerably less clustered than galaxies in which case the usual theory doesn't apply anyway. If instead $0.1 \lesssim \Omega < 0.2$, one can be consistent with the small scale dynamics but in this

case one would have expected the shoulder in $\xi(r)$ to occur at considerably smaller scales than observed. As noted in Chapter 2.1.2 one way out of this is to adjust the initial powerlaw spectrum to have a break upwards in slope to compensate the tendency of $\xi(r)$ to break downwards too soon. As Davis et al (77) discuss, though, this appears artificial in that $\xi(r)$ would only then approximate a powerlaw at this epoch. However, deviations from the powerlaw behaviour may be present that are hidden by projection effects in $\omega(\theta)$ (Chapter 6.4.3).

While the angular correlation functions are still most easily interpreted as evidence for a clustering hierarchy and the isothermal theory, other statistics applied to projected catalogues and projected clustering hierarchy simulations show poor agreement. Shanks (79), for example, has shown that 'Meads analysis' applied to simulated catalogues in which galaxies lie in symmetric Abell-like clusters give better agreement with the real data than hierarchy simulations. In contrast, Kuhn and Uson (82) have recently found a new statistic , sensitive to linear structure, shows evidence for filamentary structure present in the Lick catalogue but not in the hierarchy simulations.

As discussed in Chapter 5.3.2, chain-like structure is seen quite vividly in plots of the galaxy distributions in redshift space, the general appearance quite different from N-body simulations suggesting the real universe may have an 'unknown ingredient' not present in the simple gravitational clustering process. More statistical evidence for this structure comes from a recent study of a shallow redshift sample by Zeldovich et al (82) using a 'cluster analysis', reminiscent of the multiplicity function of Gott and Turner (77a). The authors find the results from the real universe match more closely catalogues based on numerical simulations of the 'pancake theory' than clustering hierarchy simulations suggesting, among other things, the presence of significant cellular features in the real galaxy distribution.

Since the pancake theory discussed in Chapter 2.1.2 predicts a preferred mass and length scale one would expect to find some corresponding feature in $\xi(r)$ that in turn reflects Ω. The most obvious candidate is the shoulder in $\xi(r)$ discussed above which, if occurring at 5-10 MPC implies $0.2 < \Omega < 0.4$, just about consistent with small scale estimates. One serious problem here though is that at these scales and smaller the clustering at present appears to be still in expansion (Chapter 6.5.4) and it is hard to see how galaxies could have formed from the recent collapse of pancakes on this scale. One possible way to reduce this difficulty is lower the length scale and consider the possibility of some feature in $\xi(r)$ that is hidden in $\omega(\theta)$ by projection effects. As discussed in Chapter 6.4 there do appear to be significant deviations from simple powerlaw behaviour over scales 1 to 5 MPC both in $\xi(r)$ from the AARS and CfA ; in the former case a 'wiggle' at 2 MPC being visible. The problem here is that, although the collapse time problem above is reduced, a feature at say 2 MPC requires a cosmic density parameter of near unity, excluded by the small scale relative velocities.

We see that the available clustering data provides strong constraints on both the standard isothermal and adiabatic theories, especially for the case of a low density universe implied by the virial studies. If further we take seriously the possibility of a high infall velocity of the local group towards Virgo, as discussed in section 2.4, we may have to abandon the usual assumption that galaxies trace out the matter distribution. In this case we require a theory that can account for the mechanism by which large scale segregation of light and mass occurred, perhaps on scales of tens of MPC. Of course the testing of such theories is complicated by the fact that the correlation functions can no longer be regarded as good traces of the mass distribution.

Alternatively there is the possibility that such large scale motions may be non-gravitational in origin as envisaged by Ostriker and Cowie (81). These authors have proposed that explosions of first generation objects have formed the large scale structure we see, crude calculations suggesting galaxies should lie on sheets and in filaments of typical widths 2 MPC, surrounded by large holes. Since such features do appear prominent in plots of the galaxy distribution in redshift space, this picture appears from these observations to be as plausible as the standard theories. Although (as discussed later) the presence of anti-correlation in $\xi(r)$ for the AARS need not require dissipation, such non-gravitational forces may have been needed to create some of the particular holes discussed by several observers, since the present observed large scale motions do not appear to be large enough to have cleared them in the age of the universe (Davis et al, 82).

The discussion up until now has been concerned with providing constraints on the standard theories of galaxy formation from clustering and dynamical studies of projected and redshift catalogues. However, luminosity function studies of redshift catalogues and clusters on the sky can provide some information on the processes at work early on in the universe. For example, preliminary comparison of the LF with the multiplicity function (based on group catalogues at high density contrast : Gott and Turner, 77a), suggests considerable small scale dissipation is needed to explain the compact nature of galaxies compared with the overall clustering distribution.

In another study, Sandage et al (76) has noted that as one proceeds from sparse groups dominated by an E or SØ to rich clusters the variation in the absolute magnitude of the dominant galaxy is very small, suggesting these dynamic systems are built around a more or less standard object with a highly variable number of fainter companions that may have fragmented

out of the same gas cloud. However, in the alternative 'statistical hypothesis' (Schecter and Peebles (76)) galaxy luminosities are assumed to be drawn from a universal distribution, independent of environment, with the small dispersion in magnitude merely reflecting the steep slope of the LF; as seen in fits to the Schecter function in Chapter 4.

Finally comparison of the LF of the general distribution with that found in rich clusters may provide insight into any different formation or evolutionary processes operating in the different environments. However, as discussed in Chapter 4, more data is needed before such comparisons can be believed.

7.3.2 Other Astrophysical Constraints

We have seen that the observations discussed in part 1 strongly constrain the two most popular theories of galaxy formation. The isothermal theory, although apparently able to explain the powerlaw form of $\xi(r)$ at the small scales, seems less naturally to account for the nature of the large scale structure. The pancake picture on the other hand explains the latter more easily but is hard pressed to explain the small scale structure, in particular the formation of galaxies in regions where the clustering is generally expanding.

Apart from these dilemmas, the confrontation of other theoretical aspects of the two scenarios with observations provide further constraints and possible clues to more all embracing theories.

Recent theoretical work on GUTS (Grand Unified Theories) by Weinberg (79) suggest adiabatic are more natural than isothermal perturbations, (see Press and Vishniac, 80). However, in the adiabatic case the density fluctuations needed at recombination to account for the present large scale structure are orders of magnitude larger than allowed by the observed fluctuations in the microwave background (Silk, 82).

Further clues to the most plausible theory comes from a knowledge of the redshift epoch z_f at which galaxies formed. Arguements based on the present binding energy and mean densities of galaxies imply in the isothermal theory $z_f > 10$, whereas Binney (77) has given arguments to suggest massive galaxies formed at smaller redshifts. In the pancake theory one might expect that galaxy formation is an ongoing process so there should be clusters of young galaxies forming today. However we require generally $z_f \gtrsim 3$ or else galaxies would be evolving too fast today.

The indication from these constraints is that we look for a compromise theory whose characteristic mass scale is that of individual galaxies and perhaps their halos rather than much smaller or larger units. If, for example, galaxies have typical radii of 50 KPC, implied by the outer rotation curves seen in some spirals, comparison of the outer halo density with the mean density at their formation suggest $3 \lesssim z_f \lesssim 6$, which is interestingly close to the maximum abundance of quasars (Peebles, 80a, p.391). As discussed in section 2, though, the characteristic mass (and radii) per galaxy is still highly uncertain with any masses in the range 10^{12}-10^{13} $M_\odot$ possible, the higher values requiring that much of the mass is much more broadly clustered than visible galaxies. Of course in such a theory one requires a mechanism for segregating the visible components of galaxies from the dark material.

Perhaps the most plausible idea at present is that the mean mass density is dominated by some species of weakly interacting particles (Tremaine and Gunn, 79) that, as well as providing an ideal candidate for the yet undetected dark matter, being non-baryonic allow $\Omega \gtrsim 0.1$ without violating constraints from the observed deuterium abundance (Wagoner, 73). A further attractive feature of such matter within the adiabatic scenario is the ability of perturbations to grow early in the universe without

interacting with the radiation and violating the microwave constraints mentioned above. Also, when the perturbation fragments out of the universe, since the particles cannot dissipate energy but baryons can, one can quite naturally segregate the visible baryonic galaxies from their dark halos.

Of the most likely particle candidates, the most obvious are the neutrinos left over from the big bang that recent experiments in high energy physics (Lyubimov et al, 80) suggest may have a small mass. However, estimates with neutrino masses in the required range of 30 - 100 eV predict characteristic mass scales 10^{15}-10^{16} $M_\odot$ (Doroshkevich et al, 80) similar to the pancake masses from the standard theory, but well above the masses of individual galaxies.

A more plausible candidate at present is the postulated gravatino (Weinberg, 82), a supersymmetric partner of the graviton, which, if it exists, has been shown to have a mass $\lesssim$ 1 KeV. Since these particles (or any others with $\sim$ 1 KeV) are more massive than the neutrinos above, they have the advantage that they become non-relativistic earlier so the characteristic masses are comparable to galaxy masses of 10^{12} $M_\odot$ (Blumenthal et al, 82). Furthermore, since they do not dominate the mean density until long after they have become non-relativistic, the mass scales can extend to scales of supercluster mass. Finally these higher mass particles are more consistent with phase constraint arguments in fermionic halos around dwarf galaxies implied by the recent observations of Lin and Faber (83).

In one particular scenario, Peebles (82) has considered a 1 KeV particle in a closed universe assuming adiabatic fluctuations with scale invariant spectrum $P \sim K$. Apart from the attractive features discussed above, the choice of this initial spectrum produces anticorrelation at large separations which is consistent with the low quadrupole measurements for the background radiation and $\xi(r)$ for the AARS, both discussed in Chapter 6.3,

At smaller scales gravitational clustering on scales greater than $\sim 10^{12}$ $M_\odot$ is expected to give rise to the observed clustering distribution, similar to that predicted by the isothermal theory with white noise initial spectrum.

Naturally theories such as the particular one discussed above will eventually have to explain all features of the observed universe. However, it is interesting that the picture described above can, without undue contrivance, naturally explain the masses of galaxies and some of the observed details of the clustering distribution. Further constraints will come when we understand better the mass and galaxy distribution through larger complete redshift samples.

CHAPTER EIGHT

CONCLUSIONS

8.1 INTRODUCTION

It seems appropriate at this stage to present conclusions of the present work and indicate further areas for study. In the first section of this chapter are summarised the most important findings from the analyses of the AARS, indicating how well the results are reproduced in other samples. In Section 2 we consider other areas of study, apart from redshift catalogues, that may be used to provide independent information on some of the findings of the redshift data. Included here is some work by the author on related topics and recent studies of cosmology from deep observations, where again, complete redshift samples have a role.

8.2 CONCLUSIONS FROM THE REDSHIFT DATA

As we discussed in Chapter 1, up until recently estimates of the galaxy field luminosity function and statistical three dimensional clustering and velocity studies have all come from shallow catalogues that have been both unrepresentative and poorly controlled. Although the deeper KOS sample was the first attempt to get around these problems, more believable results are likely to come from the recently compiled and larger CfA and AARS catalogues, the large size of the former and depth of the latter together providing useful complimentary information on different aspects of the topics above.

In this thesis the main aim has been to report on the compilation and analyses of the AARS and repeat, where possible, the analyses on other catalogues in order to understand possible discrepancies in the results. In addition, studies using the simulated catalogues have tested the methods for random and systematic errors.

Although the results from the analyses of the program discussed in Chapter 1.5 have been extensively discussed in previous chapters, below are presented the main conclusions and findings from the studies of the AARS that are discussed after.

(1) The luminosity function is well fitted by a Schecter function with faint end slope -1.0. The characteristic magnitude $M^{*} = -19.75$though, is around one half magnitude brighter than found from most previous studies when transformed into the appropriate systems.

(2) Both the number magnitude and redshift counts are consistent with galaxies in the volumes being homogeneously distributed on scales comparable to the sample depth.

(3) The clustering of galaxies is very apparent in redshift plots of the fields on scales of 10 MPC or so and smaller with non-spherical structure and some prominent voids visible. No rich Abell-type clusters are visible in the fields and no visual evidence for large virial motions is present.

(4) The two point correlation function $\xi_s(s)$ at scales greater than 10 MPC is roughly consistent with galaxies being distributed homogeneously, although over the region 10 to 20 MPC there is evidence for some anti-correlation.

(5) The three dimensional two point correlation function projected into angular coordinates agrees well in amplitude and form with the observed powerlaw behaviour of $\omega(\theta)$ from projected catalogues. However there is strong evidence for a considerable rise above the usual -1.8 powerlaw in the spatial function between scales 1 and 6 MPC. At the latter scale a sharp break in $\xi(r)$ occurs, consistent with the feature found in projected catalogues.

(6) At small scales peculiar velocities are detectable in $\xi_v(\sigma,\pi)$ and are significantly larger than the measuring error. The models of $\xi_v(\sigma,\pi)$

are well fitted with reasonable velocity distribution functions with dispersion $\langle v^2 \rangle^{\frac{1}{2}} \simeq$ 200 km/sec, roughly independent of separation for projected separations less than 2.0 MPC.

(7) The three point correlation function at the smallest scales is, within the uncertainties, consistent with the model in eqn. 2.4, Chapter 2.1 with $Q = 0.55$.

(8) Application of the Cosmic Virial Theorem with $\langle v^2 \rangle$, B and Q estimated consistently from the sample yields $\Omega \simeq 0.2$. The biggest uncertainty in this figure is probably our ignorance of how well galaxies trace out the mass distribution.

The question of how representative these results are of the universe of a whole of course depends on how representative the sample is. Although examination of the plots (3) and the low value for Q in (7) suggest the AARS under-samples rich regions of the universe, the overall homogeneity (2) and agreement of $\omega(\theta)$ with projected catalogues in (5) suggest the survey should be adequate for most purposes.

While some of the results in (1-8) are reasonably consistent with previous analyses, several are in strong disagreement with previous conclusions. However, the new results are hard to explain away by statistical errors.

For example, the bright value of M^* for the AARS (1) is closely reproduced in both subsamples and the discrepancy is well outside the random errors for the sample estimated from the simulations, and outside expected errors on the magnitudes. Furthermore similar results appear to come from a preliminary analyses of the CfA, if infall and clustering is accounted for (Chapter 4.4).

The other main, unconventional finding is the rise of $\xi(r)$ above the usual powerlaw (5). Here again the behaviour is reproduced in both sub-

samples, appears significant from the simulations and is seen to a lesser extent in the CfA catalogue. As discussed in Chapter 6.4, if the sharp break at $\sim$ 6.0 MPC (5) and anticorrelation in $\xi(r)$ (4) are real features of the galaxy distribution, a considerable rise above a powerlaw in $\xi(r)$ is necessary to maintain the observed powerlaw slope of $\omega(\theta)$ from projected catalogues (5).

As well as helping our understanding of the small scale form of $\xi(r)$ in this way, the behaviour of $\xi(r)$ at large scales is of interest in itself and here, the AARS, due to its depth, may provide as yet the most reliable estimate. Independent evidence for a break at around this scale (5) comes from the various scaled estimates of $\omega(\theta)$ from Schmidt catalogues discussed in Chapter 6,4, while at larger scales the overall amount of anticorrelation (4) is consistent with that needed to explain the recent observations of the microwave background, discussed in Chapter 6.3. At these scales the correlations of order unity claimed to be present in the KOS survey are strongly excluded by (4), the results from the CfA and by a reanalysis of the KOS survey in Chapter 6.3.

Turning to the dynamical studies, the estimates of $\langle V^2 \rangle$ for the AARS (6) are much lower than found previously from the KOS and Huchra catalogues. However the reanalyses of these surveys in Chapter 6.5 suggest the discrepancy can be satisfactorily explained by large sampling fluctuations in these two small catalogues. Again support for the AARS results come from the CfA which, if analysed by the same procedure as the AARS (Chapter 6.5), gives very similar results.

Although we may at last be obtaining believable and consistent estimates of $\langle V^2 \rangle$, B and Q from redshift samples, the value of Ω found from the CVT (8) is still highly uncertain due to several uncertainties about the way matter is distributed. For example, at the smallest scales

where the data on $\langle v^2 \rangle$ is most reliable and the clustering is most likely to be stable, it is not clear if the relative velocities of pairs is due to the collective force of neighbouring faint galaxies or due simply to their motion around each other. Also there could be a bias in the CVT if the mass of galaxies is correlated with abundance of neighbours, as suggested by comparison of the results with rich clusters. Perhaps the biggest uncertainty though comes from the possibility most of the mass may be considerably less clustered than the visible galaxies and so undetected from small scale dynamics. As discussed in Chapter 7.2, the present data on $\langle v^2 \rangle$ is not inconsistent with galaxies having large halos that are a natural extension of those needed to account for the flat rotation curves of spirals at smaller scales. If very extended, Ω could be comparable to unity as suggested by estimates of the large scale motion of the galaxy towards Virgo. As discussed in Chapter 7.3 such a distribution of matter may be consistent with the dark matter being in the form of non-baryonic material which may provide alternative theories of galaxy formation to the standard isothermal and adiabatic scenarious which appear to be severely constrained by the recent data.

8.3 CODA

Throughout this thesis we have seen the need for larger redshift samples, in particular to provide a better understanding of the clustering and peculiar velocities of galaxies. In turn consistency tests can provide better constraints on the distribution of matter and how it has evolved in the expanding universe. From the discussion in Chapter 5.2 samples similar to the AARS are well suited for such studies with well separated and deep but fairly small fields providing the best chance of sampling a fair volume of the universe. For the luminosity function accurate photometry is essential and for future dynamical studies velocities with errors generally lower than 50 km/sec are still required.

Although complete redshift samples have an important role in these fields other studies are relevant to some of the topics discussed in this thesis. For example, deep projected catalogues can provide information on the clustering of galaxies at earlier epochs (Phillips et al, 78) provided the selection function (including the LF) is well understood. Recent analysis by Shanks et al, (83c) suggest a model in which clusters have collapsed at a fairly recent epoch.

In this context studies of the lyman alpha absorption lines in quasars may provide information on the clustering of galaxies at a still earlier epoch if the lines are due to hydrogen clouds distributed along the line of sight in a similar fashion to galaxies. Although Sargent et al (80) have concluded the lines from several quasars are consistent with clouds being homogeneously distributed, work by the author using the same data suggests the lines are weakly clustered in a manner expected if the clustering has been stable since that epoch with $q_o = 0.5$. However, the sample of lines is too small and the resolution too poor for any firm conclusions to be drawn.

A very different study is that of searching for independent evidence and candidates for the hidden mass implied by the rotation curves and relative velocities of galaxies. The most traditional candidate here has been low mass stars assumed to be distributed around bright galaxies in low luminosity halos of profile $\frac{1}{r^2}$.

Although the deep star counts of Shanks et al (80b) could be consistent with a star density of similar fall off to this around the galaxy, models by the author on these and other counts bear out the conclusions of Bahcall and Sonera (80) that considerably deeper surveys at different galactic latitudes, and pass bands and probably requiring the space telescope are needed to distinguish between the usual star populations and a dark halo population. Other possibile tests of the low mass star hypothesis in our own galaxy could come from better measurements in the near infra red or by

searching for high proper motion faint objects in the galaxy. For external galaxies sitting in front of quasars, observations over several years could put constraints on the existence of low mass stars through gravitational lensing effects (Gott, 81).

Since light element synthesis in the big bang (Schramm and Steigman, 81) puts strong constraints on the amount of mass distributed in such stars, the main remaining possibility is the dark matter is non-baryonic and in the form of primaeval blackholes or elementary particles. As discussed in Chapter 7.3.2 the latter possibility has some attractive aspects and there are several theoretical candidates but the possibility of actual experimental confirmation of their existence is highly uncertain. If such a candidate were found experimentally or theoretically various constraints, such as phase space constraints in fermionic galaxy halos, (Tremaine and Gunn, 79), could put limits on the mean density which could be compared with the density implied from dynamical arguments.

The actual amount of dark matter and hence Ω is naturally of fundamental interest in discriminating between Friedmann models. The just closed model is especially attractive for a number of essentially non-observational rasons however, although not inconsistent with the data on Ω discussed in section 2, it does require that mass is less clustered than light on scales of many MPC's. Perhaps a bigger constraint though comes from observations of the Hubble constant and the age of the universe, the preferred range of the former 50-100 km/sec/MPC (see Hodge, 81, for a review) being inconsistent with the age $t_o = 1.5 \times 10^{10}$ yrs (Demarque, 80) found for globular cluster stars if $\Omega \leq 1$. Indeed if $H_o \simeq 100$ km/sec/MPC, as repeatedly claimed by De Vaucouleurs (e.g. De Vaucouleurs & Bollinger, 79), and t_o is as above, we require a positive cosmological constant for any value of Ω.

Another consistency test comes from comparing estimates of q_o with the value $\frac{\Omega}{2}$, equality being expected if the cosmological constant is zero. Estimates here generally come from studies of the Hubble diagram using bright galaxies in rich clusters as standard candles, and from models of deep number counts. However in recent years q_o estimated in these and other ways vary from values of 2 to negative values (see Fang et al, 82), this vast range partly indicating our lack of understanding of galaxy evolution and the properties of galaxies in nearby volumes of the universe.

These studies lead us back to complete redshift samples and the role they have to play in our understanding of fundamental aspects of cosmology. As noted in Chapter 5.2, interpretation of deep counts to provide information on galaxy evolution and q_o requires an accurate understanding of the LF of the general galaxy distribution which, by the discussion in Chapter 5.4, is still remarkably uncertain. Clearly larger samples of redshifts are needed if we are to be able to interpret still deeper data available when the space telescope becomes available.

Very deep complete redshift surveys, such as the multi-object spectroscopic study at present underway by R.S.Ellis and others at the AAT, may be useful in providing constraints on galaxy evolution and q_o. Possibilities here include a deep application of the redshift magnitude test of Soneira (79) or testing the q_o dependence of models of the number redshift distribution curve with the observed distribution. Such studies have the advantage over the usual Hubble diagram in that they do not rely on standard candles in rich clusters which may be affected by special evolutionary processes operating.

Apart from the possibility of a non-zero cosmological constant, the assumption up until now has been the standard Friedmann models describe the universe. However other possible cosmologies have been discussed by several authors.

One idea advocated by Segal (76) is that the Hubble law is fitted better by a square than a linear law. However Soneira (79) has shown from local

redshift catalogues that the redshift magnitude test mentioned above supports the Hubble law and indeed the expected relation also holds well for the CfA (Peebles- private communication) and the AARS, if the usual K corrections are accounted for.

Other possibilities for non-conventional physics and cosmologies include non-velocity redshifts between close pairs of galaxies (Tifft, 80) and non-Newtonian gravity on scales of galactic scale and larger that could even eliminate the need for dark matter. Although no external evidence for the dark matter does exist and these possibilities have not yet fully been tested, the present results from the dynamics do appear to be physically reasonable and self-consistent.

Apart from further consistency tests of the small scale dynamics, once the form of the missing mass has been isolated it may be hoped that independent constraints on Ω may become available (as noted above) that can be compared with the mean density from the dynamics. These along with better constraints on q_o, H_o and t_o should eventually lead to a consistent cosmological model for the universe.

Of course this is the long term expectation of cosmology and it may be many years before any believable estimates of any of these basic cosmological parameters become available. In the short term it is hoped that the results from both the AARS and CfA redshift surveys may encourage astronomers to start the task of measuring accurate redshifts in still larger volumes of the universe to allow more detailed studies of some of the topics discussed in this thesis.

APPENDIX A

TRANSFORM OF B_J TO OTHER SYSTEMS

The final J_{PDS} magnitudes for the AARS discussed in Chapter 3.4 are measured in an isophotal photoelectric J band which we will denote as $B_J^{24.1}$. This is related to the UBV system by

$$B - B_J = 0.23\ (B-V) \tag{1}$$

Provisional J_{COSMOS} magnitudes were measured in an isophotal photographic J band $b_J^{25.7}$ given by

$$B - b_J = 0.12\ (B-V) \tag{2}$$

which was found to hold for stars by Kron (78) who used the same pass band.

To transform between the two systems a correction for the difference between the two isophotes is required. From Metcalfe (private communication) we shall adopt

$$J^{24.1} \approx J^{24.25} \approx J^{25.7} + 0.18 \tag{3}$$

and

$$J^{25.7} \approx J^{Total} + 0.05 \tag{4}$$

Taking eqn. (3) and assuming typically

$$\langle B-V \rangle = 0.8 \tag{5}$$

we get from eqns. (1) and (2)

$$B_J^{24.1} = b_J^{25.7} + 0.27 \tag{6}$$

This is fairly close to the empirical transform found in Chapter 3.4:

$$B_J^{24.1} = b_J^{25.7} + 0.15 \tag{7}$$

As described in KOS (78), the J system used in the KOS survey is related to the UBV system by

$$B - J_{KOS} = 0.65\ (B-V) \tag{8}$$

KOS(78) find that through a comparison of a sample of their magnitudes with Zwicky magnitudes and via the B_T system of the SRC that

$$J_{KOS} = J_{KOS}^{Total} + 0.1 \tag{9}$$

Adopting this equation with the transformation to total B_J, taken from eqns. (3) and (4) as

$$B_J^{24.1} = B_J^{Total} + 0.25\ , \tag{10}$$

we find with eqns (1), (5) and (8)

$$B_J^{24.1} = J_{KOS} + 0.49 \tag{11}$$

This is reasonably close to the empirical transform found in Chapter 3.4

$$B_J^{24.1} = J_{KOS} + 0.45 \tag{12}$$

Adopting this latter relation with the empirical transform found by KOS (78)

$$J_{KOS} = B_z - 0.66 \tag{13}$$

gives a transformation between the Zwicky and PDS system of

$$B_J^{24.1} = B_z - 0.21 \tag{14}$$

Following the assumption of Davis et al (78) that $B_z \simeq B(0)$ we get the same relation between the B(0) system of the Reference Catalogue (de Vaucouleurs et al, 64).

$$B_J^{24.1} = B(0) - 0.21 \tag{15}$$

Eqns (1),(5) and (10) finally give a relation between the J_{PDS} system and the total B_T system of the SRC

$$B_J^{24.1} = B_T + 0.07 \qquad (16)$$

These transforms are summarised in Table 3.2 and discussed briefly in Chapter 3.4.

APPENDIX B

THE CATALOGUE

ENTRY (LEFT TO RIGHT)

1 GALAXY NAME

2 RIGHT ASCENSION (EPOCH 1950.0)

3 DECLINATION (EPOCH 1950.0)

4 J MAGNITUDE = 111 A-J PLUS SCHOTT GG395

* INDICATES CONTAMINATION CORRECTED

5 REPRESENTATIVE ABSORPTION VELOCITY IN km/sec (HELIO CORRECTED)

ϕ INDICATES VELOCITY WAS DETERMINED FROM A LOW DISPERSION SPECTRUM

ε INDICATES VELOCITY ERROR ASSUMED TO BE > 50 km/sec

6 R FACTOR AS IN TONRY AND DAVIS (79)

7 TEMPLATE USED (SEE TABLE BELOW)

8 OBSERVING QUARTER IN FORMAT 792 = 1972 Q2.

9 COUNTS IN UNITS OF 1. E+4 PHOTONS PER SPECTRUM

10 EMISSION LINE VELOCITY IN km/sec.

ERROR BAR IN BRACKETS PROVIDED FOR MANY-LINED SPECTRA

11 ABBREVIATED MORPHOLOGICAL TYPES FROM H CORWIN (EXCEPT GNB)

TEMPLATES AND ADOPTED VELOCITIES WITH ERRORS (i = INFERRED)

1	NGC 253 (794)	249 (7)
2	NGC 24 (794)	561 (10)
3	SRS 3523 (793)	-57 i
4	SAO 192972 (793)	15 i
5	K (HR 353) (792)	55 i
6	SAO 254650 (792)	55 i
7	NGC 253 (792)	249 (7)
8	NGC 157 (793)	1657 (12)
9	SAO 143673 (801)	-3 i

A	SAO 246853 (802)	31	*i*
C	NGC 1532 (794)	1212(10)	
D	SAO 143673 (803)	-3	*i*
E	SRS 3523 (803)	-57	*i*
F	SAO 192972 (803)	15	*i*
G	NGC 24 (803)	561(10)	
H	NGC 1291 (803)	829(7)	
J	NGC 253 (803	249(7)	
K	HD 6655 (804)	16	*i*
L	SRS 3523 (804)	-85	*i*
M	NGC 253 (804)	249(7)	
N	NGC 1291 (804)	829(7)	
P	SAO 143673 (804)	-3	*i*
Q	HD 34510 (804)	21	*i*
R	HD 25570 (804)	36	*i*
S	HD 199213 (804)	33	*i*
T	HD 101266 (811)	-16	*i*
U	HD 114762 (811)	50	*i*
V	HD 171391 (812)	7	*i*

\+ EMISSION LINE VELOCITY PREFERRED

GSA BOUNDARY 0048100 -295410 0105150 -260930

GSA001	0102319	-274154	14.23	5595	4.3	6	792	13.0				SBC
GSA002	0055217	-274618	14.31	5609	9.4	3	793	16.0				SC
GSA004	0049210	-294456	14.41	32237	2.0		792	3.6			&	SO
GSA003	0049489	-273559	14.53	12110	5.9	7	792	19.0	11655			SBC
GSA005	0051175	-271915	14.60	5608	4.7	6	792	16.0	5301			SB
GSA007	0102497	-290359	14.67	5706	4.7	6	792	5.3	5656			SBC
GSA006	0101221	-280120	14.81	5361	4.2	7	792	5.1	5070		&	COLL?
GSA008	0056275	-283424	15.35	17510	3.1	6	792	4.9			&	SO
GSAN02	0049556	-265037	15.46*	9718	7.7	1	794	9.1	9741			SBC
GSA009	0052475	-263534	15.50	17668	6.4	3	793	9.0				SPEC
GSAN04	0055459	-293538	15.60	10226	6.2	1	794	7.9	10209			SAB
GSA012	0058416	-261937	15.61	5841	-0.0	+	793	4.5	5841		&	SBPEC?
GSA015	0050527	-270409	15.62	10797	5.7	3	793	7.4	10877			SB
GSA016	0049496	-273714	15.69	12039	4.0	3	793	6.5	12124			SBPEC
GSA010	0059467	-284108	15.72	17336	5.1	3	793	7.5				SO
GSA011	0053548	-292124	15.86	22650	1.8	4	793	5.6	22684		&	SAB
GSA017	0056501	-290441	15.88	10709	2.9	4	793	10.0	10655			SB
GSA014	0056469	-264444	15.92	17310	5.3	3	793	5.0				SO
GSA020	0056528	-262329	15.94	12359	5.2	1	794	7.1	12400			SPEC
GSA021	0052231	-263831	15.96	17625	4.1	3	793	6.6	17582			SA
GSA013	0051111	-293046	15.99	11325	6.6	3	793	5.9				SO
GSA019	0100157	-291731	15.99	17166	3.7	3	793	7.1	17229			SBC
GSA024	0100236	-294307	16.00	17403	4.6	3	793	4.9	17521			SA
GSAN05	0048133	-270508	16.02	19440	7.2	1	794	11.9	19356			SB
GSA023	0055221	-283313	16.03	15627	3.0	3	793	7.5	15574			PEC-INTT
GSA046	0050255	-273548	16.15	1919	3.5	1	794	7.4				SDM
GSA025	0048550	-271538	16.16	22445	4.0	1	794	5.0				SO
GSA022	0101284	-275003	16.20	5533	3.3	4	793	6.5	5351		&	SO
GSA035	0101380	-264712	16.20	12064	7.4	1	794	9.6				SA
GSA032	0049530	-273702	16.23	11833	4.0	1	794	8.4	11804			SPEC
GSA027	0050097	-270122	16.26	14903	6.1	1	794	7.2				SO
GSA033	0057274	-275710	16.29	17276	2.8	1	794	9.9	17451			SAB
GSA018	0051189	-275233	16.29	22561	4.6	3	793	4.9				SO
GSA039	0057360	-274053	16.31	17333	3.1	1	794	8.1	17148			SB
GSA043	0050455	-262155	16.32	20970	4.7	1	794	5.6	20767			PEC
GSA052	0057226	-272328	16.33	20808	5.1	1	794	6.9	20855			SC
GSA037	0056310	-283541	16.36	17290	3.0	1	794	4.8				SA
GSA026	0050208	-280954	16.36	14432	2.4	4	793	5.8	14157		&	SA
GSA023A	0053372	-274642	16.37*	12794	7.1	3	793	7.3				SO/E?
GSA028	0059326	-283857	16.37*	17387	4.2	1	794	9.6	17511			SA
GSA047	0103098	-285346	16.39	17221	4.7	J	803	8.9				SC
GSA034	0054575	-294306	16.39	23169	6.1	F	803	7.6				E1
GSA038	0048475	-264359	16.40	15382	5.2	1	794	5.2				SO
GSA031	0049018	-275440	16.41	12066	7.9	H	803	9.5				SO
GSA030	0058203	-274359	16.42*	17361	3.9	1	794	7.3	17459			EO+?
GSA053	0055059	-281448	16.42	12349	3.8	F	803	10.5	12371			S
GSA034A	0103140	-294810	16.44	14608	5.1	F	803	9.1				SO
GSA067	0048598	-293639	16.44	13605	4.0	E	803	8.0	13577			SC
GSA048	0054571	-263306	16.44	33811	2.5	C	794	4.1			&	CD
GSA036	0056282	-271602	16.47	32126	3.4	F	803	8.9	32134			SPEC
GSA079	0048240	-264549	16.48	5649	3.0	F	803	7.2	5689			SC
GSA041	0057482	-294834	16.49	10217	5.2	F	803	6.2				SB
GSA131	0055459	-282250	16.51	12463	2.0	K	804	10.0	12211(61)		$ &	SB
GSA040	0055077	-282626	16.52	21497	3.9	L	804	10.1			$ &	SO
GSA064	0057246	-291739	16.53	30071	3.4	P	804	7.7			$ &	SC
GSA056	0049136	-284606	16.53	32191	3.4	P	804	4.6	32303		$ &	SB
GSA090	0051332	-272453	16.55	6101	2.4	R	804	3.6			$ &	PEC
GSA069	0054205	-291857	16.60	22897	3.8	P	804	9.1	22843		$ &	SBC
GSA051	0055593	-274536	16.60	29296	5.2	P	804	13.2	29334		$ &	SB
GSA058	0103322	-292057	16.60	29874	2.7	P	804	5.9			$ &	SO
GSA049	0101257	-294315	16.61	19172	5.0	P	804	15.2			$ &	SB
GSA087	0103594	-271205	16.62	15970	2.8	P	804	6.7	16137		$ &	SBC
GSA062	0103052	-271821	16.62	22766	3.1	P	804	9.9			$ &	SA
GSA078	0101411	-271907	16.63	17543	2.3	P	804	5.2			$ &	SC
GSA045	0049229	-272033	16.64	22178	5.3	P	804	10.7			$ &	SO
GSA084	0048165	-270338	16.65	6846	-0.0	+	804	3.3	6846(160)		$ &	SPEC
GSA050	0100222	-293547	16.67	17441	3.4	Q	804	8.2			$ &	SO
GSA070	0054542	-270550	16.68	21843	-0.0	+	804	5.0	21843(72)		$ &	SB
GSAN01	0100278	-275359	16.69*	20692	4.6	1	794	4.5				SB
GSA060	0100560	-292817	16.69	19371	3.3	P	804	7.1			$ &	SO
GSA135	0053082	-264047	16.71									SO
GSA091	0051414	-284510	16.71	20320	1.9	R	804	3.8	12777?		$ &	S2?
GSA061	0103279	-270428	16.71	16239	7.2	P	804	4.5			$ &	SA
GSA074	0048521	-262623	16.72	11317	1.7	P	804	0.0			$ &	SA
GSA071	0054129	-265439	16.74*	12101	3.4	Q	804	8.6			$ &	SO
GSA099	0103053	-290616	16.74									IM

GSD BOUNDARY 0149572 -513258 0213154 -475029

GSD001	0200391	-511022	13.76*	6439	9.8	3	793	18.6					S0
GSD002	0151162	-494824	13.83	6298	6.6	3	793	12.0	6197				S0
GSD004	0157241	-505746	14.32	6202	8.3	3	793	12.0					S0
GSD006	0150489	-490817	14.54	6347	5.4	3	793	5.9	6346				SBC
GSD005	0152340	-494717	14.90*	6432	11.2	3	793	10.0	6428				S0
GSD007	0152256	-493020	15.16	5958	3.7	3	793	6.5	5927				SCD
GSD012	0151335	-475259	15.17	14541	8.1	3	793	9.0					S0
GSD008	0211171	-504433	15.25	6403	8.1	3	793	8.0	6418				SA
GSD014	0156110	-475836	15.27	11226	6.6	4	793	8.9	11269				S0
GSD010	0210124	-503109	15.32	6611	2.2	4	793	7.7	6428			&	S
GSD011	0209014	-495603	15.35	14303	3.8	3	793	7.2	14356				SB
GSD013	0201113	-504237	15.42	6537	3.9	3	793	4.9	6673				SB
GSD015	0157092	-494252	15.67	17764	3.4	4	793	5.7					SAB
GSD016	0205143	-503318	15.87	6345	3.3	3	793	6.8	6327				S0
GSD025	0153241	-480840	15.90	14621	2.4	3	793	4.8	15098				SC
GSD017	0157471	-505554	15.90	6306	5.2	3	793	5.2	6429				SPEC
GSD031	0206167	-483055	15.92	14520	4.3	1	794	10.5				&	SCD
GSD030	0152194	-491147	15.93	6265	4.2	1	794	11.8					SB
GSD018	0202468	-510941	15.93	5971	2.2	8	793	5.2	6015			&	SBC
GSD019	0208434	-492833	15.94	11122	3.0	4	793	5.3	11334			&	SBC
GSD020	0204363	-492457	15.95	19483	6.1	3	793	7.6					S0
GSD021	0154305	-511957	16.07	6278	5.0	F	803	8.9	6280				SD
GSD038	0204087	-484255	16.09	11045	5.4	1	794	5.8					SB
GSD022	0212445	-500741	16.09	14038	3.4	3	793	4.4	14204				SA
GSD034	0156308	-475657	16.11	10976	7.6	1	794	11.3	10981				SA
GSD023	0206578	-501423	16.11	20158	3.8	3	793	4.0	19956				S0+?
GSD024	0206238	-510546	16.14	8701	5.5	3	793	5.9					S0
GSD027	0156450	-505146	16.16	9104	4.7	4	793	5.5					SA
GSD026	0153565	-502224	16.17	19662	3.4	4	793	3.6	19806				SA
GSD028	0208102	-503139	16.17	19945	3.8	3	793	3.6					S0
GSD029	0153295	-504927	16.19	23074	5.7	1	794	8.0					SBC
GSD044	0202182	-491015	16.23	14281	6.1	1	794	10.0	14212				SPEC
GSD042	0158490	-482624	16.24	14645	6.2	1	794	12.1					S0
GSD003	0156128	-482210	16.27	14476	4.5	3	793	4.7	14557				SAB
GSD047	0150038	-484822	16.27*	7725	5.7	F	803	8.9	7746				SC
GSD053	0209193	-485013	16.30	19396	4.0	F	803	7.6	19359				SBC
GSD032	0151145	-495535	16.32	6093	9.1	F	803	11.5					S0
GSD033	0155205	-510247	16.33	6333	3.4	F	803	6.4	6376				SC
GSD036	0157037	-502644	16.34	14422	6.2	F	803	13.1					S0
GSD037	0210253	-501842	16.35	14326	7.5	F	803	8.0					S0
GSD054	0208459	-484747	16.36	21732	5.4	F	803	8.2	21859				SB
GSD051	0157333	-485201	16.41	14583	3.6	D	803	6.4	14647				S0
GSD039	0155460	-513027	16.42	9289	2.0	F	803	6.8	9202				SBC
GSD040	0210327	-491537	16.47	13774	5.2	F	803	6.3					S0
GSD041	0156452	-500557	16.48	14464	5.5	K	804	5.6					S0
GSD045	0159163	-493708	16.55	29849	5.0	L	804	9.3				$ &	S0
GSD046	0156568	-512729	16.56	26583	-0.0	+	804	5.7	26583(21)			$ &	SC
GSD048	0152478	-510439	16.57	14585	-0.0	+	804	7.0	14585(63)			$ &	S0
GSD035	0153418	-505005	16.59*	30646	5.6	K	804						S0
GSD049	0210473	-491136	16.59	13880	4.7	L	804	9.0				$ &	S0
GSD050	0154198	-501405	16.60										S0
GSD074	0158559	-484443	16.62	27061	4.8	Q	804	9.8				$ &	S0
GSD052	0153090	-502356	16.65	8972	-0.0	+	804	4.0	8972(44)			$ &	SB
GSD088	0203134	-491107	16.66	14764	2.3	P	804	4.0				$ &	SB
GSD078	0158577	-485701	16.67	27532	3.4	P	804	5.5				$ &	S0
GSD055	0150563	-504442	16.68	20010	1.4	Q	804	5.6				$ &	S0
GSD057	0151026	-502132	16.69	19743	4.5	P	804	6.7	19530			$ &	SB
GSD056	0153458	-495905	16.69	16316	1.5	S	804	3.5				$ &	SD
GSD085	0159501	-492927	16.71	26770	3.3	L	804	4.1				$ &	S0
GSD094	0207184	-484126	16.71	19226	2.6	P	804	4.2				$ &	IM
GSD090	0159480	-483000	16.71	10585	1.1	M	804	0.0				$ &	S0+?
GSD058	0211080	-501221	16.72	14432	3.5	P	804	5.5	14492			$ &	SB
GSD084	0201592	-491529	16.75	14444	3.5	P	804	4.6				$ &	S0
GSD059	0151268	-495615	16.75										

GSF BOUNDARY 0333045 -430221 0355178 -465638

GSF001	0342527	-444805	11.64	1172	11.6	F	803	16.7						SCD
GSF002	0337039	-441544	12.13	983	14.6	F	803	127.2						SO
GSF003	0334498	-440716	12.79	1245	10.1	F	803	16.2	1277					SA6
GSF004	0350305	-444051	13.89*	1786	4.0	J	803	8.6	1658				&	SPEC
GSF005	0336182	-452236	14.54	23133	3.2	K	804	5.0	23240				&	SC
GSF009	0352519	-445357	15.02	1272	6.2	F	803	8.3						S
GSF007	0339088	-443739	15.18	11042	6.9	F	803	9.4	11036					SBC
GSF028	0338570	-453057	15.32	1827	1.0	J	803	3.4	1554					IM
GSF013	0352339	-435411	15.36*	1078	2.3	F	803	6.8						SD
GSF023	0334429	-432854	15.37	18725	4.9	F	803	6.9	18687					SBC
GSF012	0344011	-462652	15.46	19130	8.6	J	803	10.3	19010					SBC
GSF044	0334347	-452038	15.47	20258	4.5	K	804	5.0	19440					SA
GSF008	0352589	-455429	15.51	16008	8.9	F	803	12.3						SO
GSF006	0351085	-433243	15.56*	1475	2.3	F	803							SC
GSF041	0353261	-465237	15.56	16057	6.6	K	804	5.4						SO
GSF011	0350154	-440520	15.62	16113	8.0	F	803	8.2						SO
GSF029	0342231	-454207	15.66	21537	5.6	F	803	7.6						SO
GSF010	0353347	-463936	15.67	16117	8.8	F	803	15.2	16014					SO
GSF018	0333493	-451942	15.73	20548	4.8	F	803	7.6						SO
GSF062	0341013	-432736	15.79	1161	2.7	K	804	6.1					&	IM
GSF056	0345316	-455604	15.84	20831	4.7	K	804	4.0						SA6
GSF021	0343151	-462753	15.90	15054	7.1	F	803	9.8						SA
GSF015	0351201	-452243	15.92	18633	8.8	J	803	10.8	18593					SA
GSF017	0353095	-450705	15.93	15313	5.2	G	803	9.8						PEC
GSF020	0339036	-455057	15.94*	20826	4.7	F	803	6.1						SO
GSF025	0345449	-450514	15.95	18212	4.6	F	803	6.6						E2
GSF027	0346431	-454152	15.96	20704	4.3	F	803	6.2						E+?
GSF046	0335402	-431816	15.98	16349	6.9	K	804	5.4						SO
GSF032	0343572	-463103	15.99	19353	5.0	D	803	11.0	19193				&	SB
GSF054	0341592	-455339	16.03*	20186	4.2	K	804	6.0	20080					SBC
GSF016	0349588	-464442	16.03*	1109	5.4	F	803	11.0						IM
GSF053	0345040	-450905	16.11	21886	2.8	N	804	4.2	1195?					IM
GSF031	0347282	-452955	16.14*	21019	7.6	F	803	9.6						SO
GSF030	0351088	-452205	16.14	18382	6.5	F	803	7.4						SO
GSF035	0345493	-454055	16.15	20062	7.6	F	803	7.9	.					SO
GSF024	0354360	-460403	16.16	12716	6.6	F	803	7.4						IM
GSF039	0338042	-452329	16.18	23350	4.8	M	804	7.5	23470					SB
GSF093	0336362	-440754	16.21	819	3.9	P	804	7.2					$ &	SO
GSF060	0336159	-441541	16.24	1074	-0.0	+	804	3.6	1073(25)				$ &	SO
GSF052	0341507	-455031	16.25	20665	6.7	L	804	5.2						EO
GSF100	0334175	-452123	16.29	681	-0.0	+	804	3.3	681(19)				$ &	IM
GSF058	0347249	-442450	16.32	16099	3.8	P	804	9.3					$ &	SB
GSF038	0353487	-461253	16.33	21357	5.7	F	803	8.9	21348					SA
GSF075	0347206	-464821	16.39	22137	3.8	M	804	10.8					$ &	E
GSF084	0334346	-451226	16.40	23232	5.4	K	804	5.0	23232					SC
GSF050	0345401	-450330	16.41	18524	6.5	K	804	4.4						SO
GSF065	0348362	-452540	16.41	18496	3.3	P	804	6.6					$ &	SB
GSF069	0345048	-430420	16.43	27094	3.2	K	804	4.2	27169					SA
GSF036	0354043	-461823	16.45	20435	11.3	F	803	10.6						SO
GSF049	0353430	-440501	16.46	873	2.3	K	804	5.3					&	SA

GNA BOUNDARY 1333173 -015239 1348115 +015206

GNA002	1337246	010506	13.04	6793	9.9	9	801	14.8	6836				SA-INT
GNA001	1337197	010533	13.06	6869	6.5	9	801	12.3	6797				SB-INT
GNA003	1335522	000134	14.13	3782	9.3	9	801	19.4	3775				SAB
GNA005	1335588	004738	14.61	6752	9.3	9	801	11.4	6740				SA
GNA004	1335515	014400	15.06*	12106	2.8	7	792	9.5	11615			&	SBC
GNA006	1334148	012430	15.07	14237	4.6	9	801	7.7	14173				SBC
GNA008	1336391	-005204	15.22	4454	3.3	6	792	4.0	4369				SB
GNA009	1342374	002210	15.24	14380	8.3	9	801	10.6					SO
GNA007	1334194	012633	15.35*	14195	3.2	7	792	3.0				&	SB
GNA010	1333399	-004701	15.38	17859	3.1	9	801	6.0	18000				SB-INT
GNA011	1339257	005113	15.41	14411	4.7	6	792	3.8					SO
GNA012	1333303	-012013	15.52	4596	2.1	9	801	3.5	4370			&	SC
GNA013	1334250	002847	15.52	6589	5.1	9	801	5.1	6619				SO
GNA014	1336116	-000949	15.53	3825	3.9	9	801	3.2	3954				SB
GNA015	1336200	010031	15.60	11916	2.9	9	801	3.1					SO DIST
GNA016	1341121	004303	15.82	21763	2.2	9	801	2.9	21738		P	&	SB COM
GNA017	1334330	003720	15.86	14246	4.1	V	812	4.0	14362				SBC
GNA018	1340465	013426	15.87	6731	8.8	V	812	6.6					SO
GNA019	1335068	-012516	15.88	17146	5.2	V	812	5.6					SO
GNA020	1335327	001626	15.93	6653	2.9	6	792	13.0	6521				SA
GNA021	1337156	-000438	15.93	6625	3.7	V	812	8.3	6778(	84)			SO
GNA022	1335414	-000843	15.99	6658	2.6	V	812	10.5	6614(	70)			SA
GNA023	1334477	-012921	16.03	6555	3.9	V	812	7.3	6647				SA
GNA025	1338565	-001007	16.06	21399	1.9	V	812	4.1	21509			&	SAPEC
GNA026	1345225	010150	16.07	27506	1.1	V	812	3.1	27560				SC
GNA027	1333279	003101	16.08	18477	3.3	V	812	6.2	18671				SC
GNA028	1342041	004844	16.10	23236	3.0	V	812	7.9	23265				SO
GNA029	1345485	-003105	16.10	7791	3.8	V	812	8.3	7985				SO
GNA031	1333472	-001221	16.17	3810	2.8	V	812	6.4	3816				SA
GNA032	1337581	001532	16.19	3674	1.2	V	812	4.3	3696				SCD
GNA033	1339342	-000125	16.19	26563	3.7	V	812	6.5					SO
GNA034	1335226	-012754	16.21	17305	4.0	V	812	9.2	17374				SB(+IM)?
GNA035	1333381	-004637	16.23	18006	3.1	V	792	3.5	17353			&	SPEC
GNA030	1336586	-013544	16.25*	26899	4.8	V	812	5.7					SO+SO?
GNA039	1339410	004325	16.28	22025	5.2	V	812	6.5	23237				SB
GNA040	1342111	002534	16.28	27557	2.2	V	812	5.3					SO
GNA041	1347464	004743	16.29	14351	2.9	V	812	7.3	14452				SB
GNA042	1336150	-012625	16.30	4030	7.0	6	792	6.6	3419			&	SC
GNA043	1342078	003322	16.33	27099	2.2	V	812	4.6	27080				SCD
GNA044	1344430	003809	16.33	26583	5.0	V	812	4.1	26561				SO
GNA045	1339038	-001047	16.33	18125	3.2	V	812	7.3	18102				S
GNA046	1333387	-001524	16.35	16099	-0.0	+	812	7.3	16099(	74)		&	SA
GNA047	1341363	000206	16.35	21397	1.9	V	812	5.8	21594				S
GNA048	1339113	000447	16.38	26918	2.3	V	812	6.7	27197				SBC
GNA049	1340240	-003050	16.39	21176	4.6	V	812	6.6	21194				SO
GNA050	1337173	-003001	16.40	6679	2.4	V	812	4.7	6771				S
GNA051	1337070	001735	16.42	25254	2.6	V	812	6.1	25464				SBC
GNA052	1337186	-002129	16.42	18431	2.4	V	812	4.5	18555				SBC
GNA053	1343525	-010205	16.42	26695	2.8	V	812	5.6					SO
GNA054	1340486	005249	16.43	7461	3.7	V	812	5.6	7444				SCD
GNA055	1341342	-004922	16.43	26563	2.4	V	812	5.9	26563				SO
GNA056	1342225	-005336	16.44	22944	3.2	V	812	4.9	23034				SO
GNA057	1334116	013353	16.46	26015	3.7	V	812	4.4					SO
GNA058	1339014	003434	16.46	21559	2.3	V	812	7.7	21498				SPEC
GNA059	1342462	-014305	16.47	22847	2.5	V	812	3.4	22778				SC
GNA038	1347140	-002849	16.48*	23526	3.0	V	812	4.9					SO
GNA060	1340048	005611	16.50	22015	3.5	V	812	4.7					SO
GNA061	1337183	-005643	16.50	15752	1.9	V	812	5.5	15899				S
GNA062	1333511	000758	16.51	11841	5.3	V	812	5.2					SO
GNA063	1334044	013052	16.53	6969	3.1	V	812	1.2	6995				SBC
GNA064	1334449	-010228	16.53	17394	1.9	V	812	3.5	17554				SD
GNA065	1339051	003413	16.53	17499	1.6	V	812	3.3	17459				SCD
GNA067	1345550	-011653	16.55	22642	3.0	V	812	3.6					SO
GNA068	1344400	003152	16.59	26287	1.3	V	812	3.3	26324				SCD
GNA069	1333226	-010649	16.60	4879	1.0	V	812	4.1	4645				SB
GNA070	1337583	-001113	16.61	26250	1.4	V	812	2.9					SCD
GNA071	1346063	014113	16.61	21433	3.5	V	812	4.2					SO
GNA073	1339113	014749	16.61	23634	1.9	V	812	1.2					SO
GNA072	1339166	003549	16.61										SO
GNA074	1344395	-002519	16.61										S

GNB BOUNDARY 1032500 -015000 1047290 +015100

GNB001	1039443	-000654	14.11	5605	7.5	9	801	19.7	5686				SCD
GNB002	1036467	000338	14.17	5658	9.4	9	801	31.1	5696				E
GNB003	1045449	010616	14.47	4832	7.2	9	801	14.1	4848				SAB
GNB006	1044181	-010740	14.51	11468	7.0	9	801	11.9	11506				SCb
GNB005	1046279	-002235	14.69	1906	4.8	9	801	6.8	1888				SCD
GNB010	1041193	-010156	14.74	8291	2.0	9	801	18.7	7894			&	SO COMP
GNB015	1036502	-000741	14.85	5959	1.4	9	801	12.5	5649			&	SDM
GNB004	1046475	-002412	14.95	11669	6.2	9	801	16.9					E/SO
GNB014	1039194	010317	15.01	5580	2.9	9	801	4.0	5789			&	SDM
GNB009	1047249	003514	15.07	11747	5.2	9	801	12.9					E
GNB013	1044573	-011344	15.12	11399	5.0	9	801	8.5					SBC
GNB012	1047073	003739	15.15	11656	5.9	9	801	14.9					E
GNB018	1042305	002204	15.23	11791	5.7	9	801	5.2	11769				SCD
GNB019	1046430	003538	15.24	12240	6.0	9	801	6.7	12354				SCB
GNB008	1036380	-000857	15.27	5665	9.0	9	801	9.7	5729				SAB
GNB016	1045316	-013947	15.36	11299	7.8	9	801	9.3	11295				SBC
GNB024	1045206	010436	15.51	4835	1.9	A	802	5.2	4937			&	SAb
GNB020	1047160	012809	15.51	11673	4.5	9	801	5.7	11709				SCD
GNB021	1042298	004152	15.52	7923	2.7	A	802	8.0	7920			&	S PEC
GNB017	1041013	-004019	15.62	11680	4.6	9	801	8.8					SO
GNB022	1034005	-010007	15.73	10984	4.6	A	802	13.4				&	SO
GNB023	1039124	013857	15.83	21692	2.8	A	802	10.8				&	SDM+HII?
GNB031	1043423	-012724	15.84	15776	2.1	T	811	19.4			$	&	SBC
GNB026	1033405	000600	15.87	8031	3.5	T	811	12.3			$	&	S
GNB050	1047290	012521	15.87	11745	5.8	V	812	6.2					SCD
GNB075	1042427	014350	15.92	5019	2.7	V	812	10.7	4962				S
GNB029	1038002	010441	15.92	13493	2.4	T	811	14.1			$	&	SCD
GNB034	1045337	002551	15.94	11842	4.2	T	811	14.8			$	&	SAB
GNB030	1046505	002947	15.95	11979	1.9	T	811	15.4			$	&	E/SO
GNB025	1046184	010703	15.96	11558	3.9	A	802	9.0				&	SAb
GNB041	1046374	003837	15.96	2368	2.5	T	811	10.2			$	&	SBC
GNB036	1041114	-000938	15.99	11439	2.1	U	811	20.7			$	&	SAB?
GNB027	1044179	000919	16.00	12053	5.4	T	811	20.1			$	&	SBC
GNB032	1047254	003703	16.01	11115	4.0	T	811	14.5			$	&	SCD
GNB033	1045110	-000648	16.02	11610	3.0	T	811	15.8			$	&	SCD
GNB028	1041257	-001933	16.04	18291	2.9	T	811	15.1			$	&	PR ?
GNB040	1038012	-003855	16.04	11721	5.0	T	811	21.0			$	&	SO
GNB035	1046511	-000955	16.04	11466	6.1	T	811	20.0			$	&	SBC
GNB011	1045009	004533	16.09*	8423	6.4	9	801	5.5	8255				SAb
GNB038	1042505	-005957	16.11	11608	-0.0	+	811	21.0	11608(	56)	$	&	COMP?
GNB039	1034171	-012319	16.12	8071	2.5	T	811	13.8			$	&	SAB
GNB037	1047285	-013610	16.15	11112	4.7	T	811	13.7			$	&	SO
GNB043	1040090	-000510	16.17*	5481	-0.0	+	811	11.9	5481(	34)	$	&	S PEC
GNB062	1037008	000026	16.18	5654	3.2	V	812	9.2	5734				S
GNB046	1039480	012319	16.27	21368	4.0	T	811	15.6			$	&	SCD
GNB044	1038179	-003941	16.30	11403	4.0	T	811	20.5			$	&	SA
GNB059	1043300	-004953	16.32	10983	3.7	V	812	7.6	11273				SAB
GNB048	1047086	-013112	16.34	11240	6.3	V	812	7.1	11545				SBC
GNB047	1036443	010601	16.37*	19745	4.7	V	812	9.4					SBC
GNB051	1045030	-011615	16.39	11984	4.2	V	812	9.7	12227				SC
GNB069	1040586	011654	16.45	21700	2.4	V	812	5.9	21721				SBC
GNB052	1047229	-013657	16.45	11159	7.2	V	812	6.2	11414				SAB
GNB053	1039011	-014923	16.47	17849	4.8	V	812	5.7	17889				SB
GNB055	1033319	-001536	16.53	10699	5.2	V	812	5.3	10901				SA
GNB057	1040485	011418	16.55	21457	2.9	V	812	4.2	21752				SAB
GNB045	1033318	002140	16.56	28971	2.9	T	811	9.5			$	&	SCD
GNB090	1042484	012313	16.58										
GNB056	1046311	-002415	16.58	11593	2.5	V	812	4.6					SAB
GNB076	1040411	-004932	16.59*	11420	3.0	V	812	5.0	11628				SAB
GNB054	1043558	-012315	16.59	18038	4.8	V	812	4.9					SA
GNB074	1045292	004952	16.60	13803	7.2	V	812	9.8					SA
GNB049	1038551	004049	16.61	24657	3.2	V	812	3.1					SCD
GNB068	1042452	013410	16.66	18541	4.2	V	812	4.3					SPEC
GNB091	1047149	-014109	16.71	11119	4.0	V	812	5.1	11155				SB
GNB073	1037093	-002650	16.71	8114	5.3	V	812	5.2	8112				SO/SA
GNB065	1037196	011435	16.73*	20080	2.8	V	812	2.2					SA
GNB093	1047197	-000743	16.76	11463	3.2	V	812	6.5	11546				SAB
GNB058	1046310	-012938	16.76	15931	3.8	V	812	5.3					SA
GNB063	1043500	-001714	16.76	22914	4.3	V	812	5.5					SPEC

REFERENCES

Abell, G.O, 1962. In problems of Extragalactic Research, ed. G.C.McVittie (New York ; McMillan).

Allen, C.W, 1973. Astrophysical Quantities, 3rd edition (London:Athlone Press).

Bahcall, J., and Soneira, R.M., 1980. Ap.J., 238, L17.

Bahcall, J., and Tremaine, S., 1981. Ap.J., 244, 805 (BT).

Bahcall, N.A., and Soneira, R.M., 1982. Ap.J., 258, L17.

Bean, A.J., Efstathiou, G., Ellis, R.S., Peterson, B.A., and Shanks, T., 1983. M.N.R.A.S. submitted.

Binney, J., 1977. Ap.J., 215, 483.

Boksenberg, A., 1972. In Auxiliary Instrumentation for Large Telescopes. Proc. of the ESO-CERN Conference, ed. S. Lausten and A.Reiz, p.295.

Blumenthal, G.R., Pagels, H., and Primack, J.R., 1982. Nature, 299, 2nd Sept.

Burbidge, G., 1975. Ap.J., 196, L7.

Burbidge, E.M., and Burbidge, G., 1975. In Galaxies and the Universe, ed. A.Sandage, M. Sandage and J.Kristian, p.81.

Clutton-Brock, M., and Peebles, P.J.E, 1982. A.J. 86, 1115.

Davis, M., 1982. Phil. Trans. R.Soc.Lond. A 307, 111.

Davis, M., and Geller, M.J., 1976. Ap.J. 208, 13.

Davis, M., Geller, M.J., and Huchra, J., 1978. Ap.J. 221, 1.

Davis, M., Groth, E.J., and Peebles, P.J.E., 1977. Ap.J. 212, L107.

Davis, M., and Huchra, J., 1982. Ap.J. 254, 437.

Davis, M., Huchra, J., Latham, D., and Tonry, J., 1982. Ap.J. 253, 423.

Davis, M., and Peebles, P.J.E., 1977. Ap.J. Suppl. 34, 425.

Davis, M., and Peebles, P.J.E., 1982. Preprint (DP).

Davis, M., Tonry, J.,Huchra, J., and Latham, D., 1980. Ap.J. 239, L113.

Dekel, A., Lecar, M., and Shaham, J., 1980. Ap.J. 241, 946.

Demarque, P., 1980. In Star Clusters. J.E.Hesser, Ed: 281. Reidel Publ. Dordrecht, Holland.

de Vaucouleurs, G., 1978. Ap.J., 224, 710.

de Vaucouleurs, G., Bollinger, G., 1979. Ap.J. 233, 433.

de Vaucouleurs, G., and de Vaucouleurs, A., 1964. Reference catalogue of Bright Galaxies (Univ.of Texas: Austin).

de Vaucouleurs, G., de Vaucouleurs, A., and Corwin, H, G., 1976. Second Reference Catalogue of Bright Galaxies (Univ.of Texas: Austin) (SRC).

Doroshkevich, A.G., Khlopov, M.Y., Junyaev, R.A., Szalay, A.S, and Zeldovich, Y.B., 1980. Proc.10th Texas Symp. Rel. Astrophys.

Doroshkevich, A.G. and Shandarin, S.F., 1978. M.N.R.A.S. 182, 27.

Doroshkevich, A.G., Sunyaev, R.A, and Zeldovich, Y.B., 1974. I.A.U. Symposium. 63, 213.

Efsthathiou, G., 1979. Ph.D.Thesis, University of Durham.

Efsthathiou, G., and Bean, A.J., Ellis, R.S., Shanks, T., and Peterson, B.A., 1983. In preparation.

Efsthathiou, G., and Eastwood, J.W., 1981. M.N.R.A.S. 194, 503.

Einasto, J., Joeveer, M., and Saar, E., 1980. M.N.R.A.S. 193, 353.

Ellis, R.S., 1981. In the origin and evolution of galaxies. Proc. of the NATO Advanced Study Institute, ed. B.J.T. Jones and J.E.Jones,p.255.

Faber, S.M., and Gallagher, J.S., 1979. Ann.Rev.Astr.Ap., 17, 135.

Faber, S.M., and Lin, O.N.C., 1983. Ap.J. 266, L17.

Fall, S.M., 1976. M.N.R.A.S. 176, 181.

Fall, S.M., and Jones, B.J.T., 1976. Nature. 262, 457.

Fall, S.M., and Tremaine, S., 1977. Ap.J. 216, 682.

Fang, L.Z., Kiang, T., Cheng, F.H., and Hu, F.X., 1982. Quarterly Journal of the R.A.S, 23, 363.

Felten, J.E., 1977. A.J. 82, 861.

Fisher, J.R., and Tully, R.B., 1981. Ap.J. Suppl. 47, 139.

Fong, R., Godwin, J.G., Green, M.R., and Shanks, T., 1983. In preparation.

Ford, H.C., Harms, R.J., Ciardullo, R., and Bartko, F., 1981. Ap.J. 245,L53.

Geller, M.J., and Peebles, P.J.E., 1973. Ap.J. 184, 329.

Godwin, J., 1976. Ph.D.Thesis, University of Oxford.

Gott, J.R., 1981. Ap.J. 243, 140.

Gott, J.R., and Rees, M.J., 1975. Astron and Astrophys. 45, 365.

Gott, J.R., and Turner, E.L., 1976. Ap.J. 209, 1.

Gott, J.R., and Turner, E.L., 1977a, Ap.J. 216, 357.

Gott, J.R., and Turner, E.L., 1977b. Ap.J. 213, 309.

Gott, J.R., and Turner, E.L., 1979. Ap.J. 232, L79.

Gott, J.R., Turner, E.L., and Aerseth, S.J., 1979. Ap.J. 234, 13.

Gregory, S.A., and Thompson, L.A., 1978, Ap.J. 222, 784.

Groth, E.J., and Peebles, P.J.E., 1976. Astron. and Astrophys. 53, 131.

Groth, E.J., and Peebles, P.J.E., 1977. Ap.J. 217, 385 (GP).

Gunn, J.E., 1977. Ap.J. 218, 592.

Harrison, E.R., and Noonan, T.W., 1979. Ap.J. 232, 18.

Hartwick, F.D.A., and Sargent, W.L.W., 1978. Ap.J. 221, 512.

Hauser, M.G., and Peebles, P.J.E., 1973. Ap.J. 185, 757.

Hewett, P.C., 1982. M.N.R.A.S. 201, 867.

Hewett, P.C., MacGillivray, H.T., and Dodd, R.D., 1981. M.N.R.A.S. 195, 613.

Hodge, P.W., 1981. Ann.Rev.Astr. Ap., 19, 357.

Hoffman, Y., Shaham, J., and Shaviv, G., 1982. Ap.J. 262, 413.

Hubble, E., 1929. Proc. Nat.Acad.Sci. 15, 168.

Hubble, E., 1934. Ap.J. 79, 8.

Huchra, J., 1976. Ap.J. 81, 952.

Huchra, J., Davis, M., Latham, D., and Tonry, J., 1983. Ap.J.Suppl. in Press.

Huchra, J., Geller, M.J., 1982. Ap.J. 257, 423.

Jackson, J.C., 1972. M.N.R.A.S. 156, 1P.

Jones, J.E., and Jones, B.J.T., 1980. M.N.R.A.S. 191, 685.

Kiang, T., and Saslaw, W., 1969. M.N.R.A.S. 143, 129.

Kirshner, R.P., Oemler, A., and Schecter, P.L., 1978. A.J. 83, 1549 (KOS(78)).

Kirshner, R.P., Oemler, A., and Schecter, P.L., 1979. A.J. 84, 951 (KOS(79)).

Kirshner, R.P., Oemler, A., Schecter, P.L., and Schectman, S.A., 1981. Ap.J. 248, L57. (KOS(81)).

Kron, R.G., 1978. Ph.D. Thesis, University of California, Berkeley.

Kuhn, J.R., and Uson, J.M., 1982. Ap.J. 263, L47.

Lampton, M., Margon, B., and Bowyer, S., 1976. Ap.J. 208, 177.

Limber, D.N., 1954, Ap.J. 119, 655.

Lin, D.N.C., and Faber, S.M., 1983, L21.

Lubin, P.M., 1982. Paper presented at the 86th course of the International School of Physics, Varenna.

Lynden Bell, D., 1981. The Observatory, 101, 111.

Lyubimov, V.A., Novikov, E.G., Nozik, V.Z., Tretyakov, E.F., and Kowsik, V.S., 1980. Preprint from the Institute of Theoretical and Experimental Physics.

Melott, A.L., 1983. M.N.R.A.S. 202, 594.

Oke, J.B., 1974. Ap.J. Suppl. 27, 21.

Oemler, A., 1974, Ap.J., 194, 1.

Öpik, E., 1922. Ap.J. 155, 406.

Ostriker, J.P., and Cowie, L., 1981. Ap.J. 243, L127.

Ostriker, J.P., Peebles, P.J.E., and Yahil, A., 1974. Ap.J. 193, L1.

Ostriker, J.P, and Tremaine, S.D., 1976. Ap.J. 202, L113.

Partridge, R.B., and Wilkinson, D.T., 1967. Phys. Rev. Letters, 18, 557.

Peebles, P.J.E., 1974. Ap.J. 189, L51.

Peebles, P.J.E., 1976a, Ap.J. 205, L109.

Peebles, P.J.E., 1976b. Ap.Space Sci. 45, 3.

Peebles, P.J.E., 1978. Astron and Astrophys. 68, 345.

Peebles, P.J.E., 1979. A.J. 84, 730.

Peebles, P.J.E., 1980a. In the Large Scale Structure of the Universe (Princeton: Princeton University Press).

Peebles, P.J.E., 1980b. In Cosmologie Physique, eds. R.Balian, J.Audouze and D.N.Schramm (Amsterdam: North Holland)p. 216.

Peebles, P.J.E., 1981. Proc. 10th Texas Symp. rel. Astrophys.

Peebles, P.J.E., 1982. Ap.J. 263, L1.

Peebles, P.J.E., and Groth, E.J., 1975. Ap.J. 196, 1.

Pence, W.D., 1976. Ap.J. 203, 39.

Penzias, A.A., and Wilson, R.W., 1965, Ap.J.142, 419.

Peterson, B.A., 1973. I.A.U. Symposium. 58, 75.

Peterson, B.A., Bean, A.J., Efstathiou, G. , Ellis, R.S., Shanks, T. and Zou, Z.L., 1983. In preparation.

Phillipps, S., Fong, R., Ellis, R.S., Fall, S.M. and MacGillivray, H.T., 1978. M.N.R.A.S. 182, 675.

Pratt, N.M., Martin, R., Alexander, L.W.G., Walker, G.S., and Williams,P.R., 1975. In Image Processing Techniques in Astronomy (Dordrecht:Reidel).

Press, W.H., and Davis, M., 1982. Ap.J. 259, 449.

Press, W.H., and Lightman, A.P., 1978. Ap.J. 219, L73.

Press, W.H., and Vishniac, E.T., 1980. Ap.J. 236, 323.

Rood, H.J., 1982. Ap.J. Suppl. 49, 111.

Rood, H.J., and Dickel, J.R., 1978. Ap.J. 224, 724.

Rubin, V.C., Ford, W.K., Thonnard, N., Roberts, M.S., and Graham, J.A., 1976. A.J. 81, 687.

Sandage, A., 1978. A.Ji 83, 904.

Sandage, A., 1976. Ap.J. 205, 6.

Sandage, A., and Tammann, G.A., 1975. Ap.J. 196, 313.

Sandage, A., Tammann, G.A., and Yahil, A., 1979. Ap.J. 232, 352.

Sanduleak, N., and Pesch, P., 1982. Ap.J. 258, L11.

Sargent, W.L.W., and Turner, E.L., 1977. Ap.J. 212, L3.

Sargent, W.L.W., Young, P.J., Boksenberg, A., and Tytler, D., 1980. Ap.J. Suppl. 42, 41.

Saslaw, W., 1980. Ap.J. 235, 299.

Schecter, P., 1974. Ph.D. Thesis. California Institute of Technology.

Schecter, P., 1976. Ap.J. 203, 297.

Schecter, P., and Peebles, P.J.E., 1976. Ap.J. 209, 670.

Schecter, P., and Press, W.H., 1976. Ap.J. 203, 557.

Schmidt, M., 1968. Ap.J. 151, 393.

Schramm, D.N., and Steigman, G., 1981. Ap.J. 243, 1.

Segal, I.E., 1976. in Mathematical Cosmology and Extragalactic Astronomy (New York: Academic Press).

Seldner, M., and Peebles, P.J.E., 1977a, Ap.J. 215, 703.

Seldner, M., and Peebles, P.J.E., 1977b, Ap.J. 214, Ll.

Seldner, M., and Uson, J.M., 1983. Ap.J. 246, 1.

Shane, C.D., and Wirtanen, C.A., 1967. Publ. Lick. Obs., 22, Part 1.

Shanks, T., 1979. M.N.R.A.S. 186, 583.

Shanks, T., 1983. M.N.R.A.S. 202, 1245.

Shanks, T., Bean, A.J., Efstathiou, G., Ellis, R.S., Fong, R., and Peterson, B.A., 1983b, Submitted to Ap.J.

Shanks, T., Fong, R., Ellis, R.S., and MacGi llivray, H.G., 1980a, M.N.R.A.S. 192, 209.

Shanks, T., Phillipps, S., and Fong, R., 1980b. M.N.R.A.S. 191, 47p.

Shanks, T., Stevenson, P.R.F., Fong, R. and MacGillivray, H.T., 1983a, Submitted to M.N.R.A.S.

Shanks, T., Stevenson, P.R.F., Fong, R., and MacGillivray, H.G., 1983c, In preparation.

Shapley, H., 1935. Proc. Nat.Acad.Sci. 21, 587.

Shapley, H., and Ames, A., 1932. Ann. Harvard Obs., 88, 43.

Shostak, G.S., and Rogstad, D.H., 1973. Astron and Astrophys. 24, 405.

Silk, J., 1981. Proc. 10th Texas Symp. rel. Astrophys., 188.

Smoot, G.F., and Lubin, P.M., 1979. Ap.J. 234, L83.

Soneira, R.M., 1979. Ap.J. 230, L63.

Soneira, R.M., and Peebles, P.J.E., 1978. A.J. 83, 845.

Tammann, G.A., and Kraan, R., 1977. I.A.U. Symposium 79, 71.

Tammann, G.A., and Yahil, A., and Sandage, A., 1979, Ap.J. 234, 775.

Tifft, W.G, and Gregory, S.A., 1977. I.A.U. Symposium 79, 267.

Tifft, W.G., 1980. Ap.J. 236, 70.

Tinsley, B.M., and Danly, L., 1980. Ap.J. 242, 435.

Tonry, J., and Davis, M., 1979. A.J. 84, 1511.

Tremaine, S., and Gunn, J.E., 1979. Phys. Rev. Letters, 42, 407.

Tully, R.B., 1980. Ap.J. 237, 390.

Tully, R.B., 1982, Ap.J. 257, 389.

Turner, E.L., 1976. Ap.J. 208, 304.

Turner, E.L., and Gott, J.R., 1976. Ap.J. 209, 6.

Turner, E.L., and Sargent, W.L.W., 1974.Ap.J. 194, 587.

Tyson, J.A., and Jarvis, J.F., 1979, Ap.J. 230, L153.

Wagoner, R.V., 1973. Ap.J. 179, 343.

Weinberg, S., 1979. Phys. Rev. Letters. 42, 850.

Weinberg, S., 1982. Phys. Rev. Letters. 48, 1303.

White, S.D.M., 1976. M.N.R.A.S. 174, 19.

White, S.D.M., and Rees, M.J., 1978. M.N.R.A.S. 183, 341.

White, S.D.M., Huchra, J., Latham, D., and Davis, M., 1983.
M.N.R.A.S. 203, 701.

White, S.D.M., and Sharp, N.A., 1977. Nature. 269, 395.

Yahil, A., 1977. Ap.J. 217, 27.

Yahil, A., Sandage, A., and Tammann, G.A., 1980. Ap.J. 242, 448.

Yahil, A., Vidal, N.V., 1977. Ap.J. 214, 347.

Zeldovich, Y.B., Einasto, J., Shandarin, S.F., 1982. Nature. 300, 407.

Zwicky, f., 1933. Helv.Phys.Acta. 6, 110.

Zwicky, F., Herzhog, E., Wild, P., Karpowicz, M. and Kowal, C.T.,
1961-68. Catalogue of galaxies and clusters of galaxies, in
6 vols., California Institute of Technology, Pasadena.

ACKNOWLEDGEMENTS

I wish to thank first Dr. R. Fong for the supervision of this thesis and for many helpful discussions over the past four years.

Special thanks also go to my colleagues and collaborators in the Cosmology group at Durham, Drs. R.S. Ellis and T. Shanks and at the Institute of Astronomy, Cambridge, Dr. G. Efstathiou, all of whom had a large influence on the work in this thesis.

I am also indebted to Drs. B.A.Peterson and Zou Zhen Long for their work on the final photometry of the redshift survey and for Dr. D. Carter for his help at the Anglo Australian Telescope. Dr.H.Corwin is thanked for classifying most of the galaxies in the survey as well as Professor P.J.E. Peebles for providing a useful computer program and for a very good suggestion (the maximum likelihood estimator of the luminosity function).

I should also wish to thank my other colleagues at Durham, I. Inglis, B.Mobasher, P.F.Stevenson, for useful discussions over the years.

I acknowledge the receipt of an S.E.R.C. studentship and a University of Durham grant for the period of the research.

Finally, I thank my dear wife, Flora, for her patience and understanding without which this thesis would never have been completed.